Project No. 11-2988

# Ag Transport Through Non-Irradiated and Irradiated SIC

---

## Reactor Concepts

**Izabela Szlufarska**
University of Wisconsin, Madison

Madeline Feltus, Federal POC
Paul Demkowicz, Technical POC

NEUP Nuclear Energy University Programs
U.S. Department of Energy

# Final Report

| | | |
|---|---|---|
| **Project Title:** | **Ag Transport Through Un-irradiated And Irradiated SiC** | |
| **Covering Period:** | October 1, 2011 – September 30, 2015 | |
| **Date of Report:** | January 11, 2016 | |
| **Recipient:** | University of Wisconsin<br>Madison, WI 53706 | |
| **Contract Number:** | 00089350 | |
| **Project Number:** | 11-2988 | |
| **Subcontractors:** | N/A | |
| **Other Partners:** | N/A | |
| **Contact(s):** | Principal Investigator: | Izabela Szlufarska<br>szlufarska@wisc.edu |
| | Co-Principal Investigators: | Dane Morgan (ddmorgan@wisc.edu)<br>James Blanchard (blanchard@engr.wisc.edu) |
| | Collaborators: | Kumar Sridharan (kumar@engr.wisc.edu)<br>Isabella Van Rooyen<br>(isabella.vanrooyen@inl.gov) |

**Technical point of contact:** Paul Demkowicz, Idaho National Laboratories

**Table of Content**

**1 Introduction ..... 4**

**2 Diffusion Couple Experiments ..... 4**

- ***2.1 Development of Ion Implantation Diffusion Couple System ..... 4***
  - **2.1.1 Overview of Diffusion Couple Design Approach ..... 4**
  - **2.1.2 Diffusion Couple Exposures ..... 5**
- ***2.2 Analysis of Ion Implanted Diffusion Couples ..... 6***
  - **2.2.1 Overview of Analysis Approach ..... 6**
  - **2.2.2 STEM Analysis of Ion Implanted Diffusion Couples ..... 8**
  - **2.2.3 SIMS Analysis of Ion Implantation Diffusion Couples ..... 11**
- ***2.3 Discussion of Measured Ag Transport ..... 16***
  - **2.3.1 Defects Contributing to Non-equilibrium Diffusion ..... 16**
  - **2.3.2 Discussion of Mechanisms Contributing to Enhanced Diffusion ..... 18**
  - **2.3.3 Diffusion Analysis of Polycrystalline 3C-SiC Diffusion Couples ..... 20**
  - **2.3.4 Discussion of Diffusion in Polycrystalline 3C-SiC: Role of Microstructure ..... 22**
  - **2.3.5 Comparison of Ag Diffusion Energetics with Literature ..... 23**
  - **2.3.6 Comparison of Diffusion Energetics with TRISO Fuel Release ..... 25**
- ***2.4 Summary of Observations ..... 26***

**3 Diffusion Studies in Irradiated SiC ..... 27**

- ***3.1 Overview of Ag Diffusion in Irradiated SiC ..... 27***
- ***3.2 Effect of Carbon Ion Irradiation on Ag/SiC Diffusion Couple Experiment ..... 28***
  - **3.2.1 Materials and Method ..... 28**
  - **3.2.2 Radiation/Implantation Damage ..... 29**
  - **3.2.3 SIMS Profiles ..... 30**
  - **3.2.4 Comparison of Effective Diffusion Coefficient in Unirradiated and Irradiated SiC 34**
  - **3.2.5 GB Diffusion and Lattice Diffusion in Irradiated SiC ..... 39**
- ***3.3 Analysis of Neutron-Irradiated TRISO Fuel Particles ..... 41***
  - **3.3.1 Materials and Method ..... 41**
  - **3.3.2 STEM Analysis of Distribution of Ag and Other FP ..... 42**
  - **3.3.3 Possible Mechanism of Ag Transport in Neutron Irradiated TRISO Fuel Particle ..... 46**
- ***3.4 Summary of Experimental Work in the Project ..... 47***

**4 Co-incorporation of Ag with Other Elements ..... 48**

**5 Atomistic simulations of Ag diffusion ..... 48**

- ***5.1 Ag Diffusion along High Energy Grain Boundary ..... 48***
  - **5.1.1 Methods ..... 49**
  - **5.1.2 DFT Calculations of Ag Energetics ..... 53**
  - **5.1.3 Kinetic Monte Carlo Model for Ag Diffusion ..... 58**

**5.1.4 Discussion on the Impact of Ag HEGB Diffusion ... 63**
*5.2 Radiation Enhanced Diffusion ... 67*
**5.2.1 Kickout Reactions as a Possible RED Mechanism ... 68**
**5.2.2 Self-Interstitial as a Source for KickoutRreactions ... 69**
**5.2.3 Kickout Reaction Rates ... 72**
**5.2.4 Discussion on Radiation Enhanced Diffusion Mechanism ... 76**
*5.3 Summary of Results from Atomistic Simulations ... 77*

**6 Continuum model of diffusion through polycrystalline SiC ... 78**

**7 Publications resulting from this project ... 79**

**8 References ... 79**

**9 Appendices ... 88**

# 1 Introduction

Silicon carbide is the main barrier to diffusion of fission products in the current design of TRistuctural ISOtropic (TRISO) coated fuel particles and Ag is one of the few fission products that have been shown to escape through this barrier. Because the SiC coating in TRISO is exposed to radiation throughout the lifetime of the fuel, understanding of how radiation changes the transport of the fission products is essential for the safety of the reactor. The goals of this project are: (i) to determine whether observed variation in integral release measurements of Ag through SiC can be explained by differences in grain size and grain boundary (GB) types among the samples; (2) to identify the effects of irradiation on diffusion of Ag through SiC; (3) to discover phenomena responsible for significant solubility of Ag in polycrystalline SiC. To address these goals, we combined experimental analysis of SiC diffusion couples with modeling studies of diffusion mechanisms through bulk and GBs of this material. Comparison between results obtained for pristine and irradiated samples brings in insights into the effects of radiation on Ag transport.

# 2 Diffusion Couple Experiments

## *2.1 Development of Ion Implantation Diffusion Couple System*

### *2.1.1 Overview of Diffusion Couple Design Approach*

Numerous experimental challenges influence investigation of silver (Ag) diffusion in silicon carbide (SiC). The primary issues are the expected low solubility limits (S(T)) ($<1\text{x}10^{17}$ at/cm$^3$) at the temperatures of interest to TRISO fuel operation and accident conditions (900-1600°C) [1] and limited diffusion length scales at the time and temperatures associated with reported diffusion experiments. These constraints influence the design of diffusion couples appropriate for investigation of the Ag-SiC system as well as the necessary analysis techniques needed to measure diffusion in the Ag-SiC system.

This work utilized ion implantation diffusion couples to investigate the diffusion behavior in the Ag-SiC system. Ion implantation overcomes critical issues associated with high temperature diffusion couples of Ag-SiC, namely it provides a consistent Ag source at the temperatures of interest where Ag is a liquid with a high vapor pressure, and as such many traditional diffusion couple designs are not applicable under these conditions. The approach also provides a planar well-defined planar interface, which allows for application of high sensitivity depth profiling techniques. This work revisited Ag-SiC ion implantation diffusion couple approaches, which had been previously reported in the literature [2] and modified the design approach to limit the influence of implantation effects.

The ion implantation diffusion couples were constructed using polycrystalline CVD 3C-SiC from Rohm and Haas (3C-SiC) and single crystal 4H-SiC wafers 4° off (1000) from Cree, Inc. (4H-SiC). Polycrystalline 3C-SiC samples were prepared from bulk samples and were polished to an arithmetic surface roughness (Ra) < 10 nm. The single crystal 4H-SiC wafers were obtained from Cree, Inc. with a Ra < 10 nm. Roughness values were measured using a Zygo optical profilometer. The polycrystalline 3C-SiC substrates were implanted with two separate dose conditions, 400 kV Ag+ to $1\text{x}10^{14}$ ion/cm$^2$ and $5\text{x}10^{14}$ ions/cm$^2$, at 300ºC at the Michigan Ion Beam Laboratory (MIBL) through the Advanced Test Reactor National User Facility (ATR-NSUF) program. The single crystal 4H-SiC substrates were implanted to a dose of $5\text{x}10^{14}$ ions/cm$^2$ at identical conditions to the polycrystalline 3C-SiC substrates. The implantation dose and the 300ºC implantation temperature were selected to avoid amorphization of the SiC substrate during implantation, while the two dose conditions for the 3C-SiC substrates were selected to understand potential dose dependence on the diffusion behavior. Following Ag implantation a 200-250 nm diamond-like-carbon (DLC) coating was deposited on the SiC's implanted surface to protect the sample during thermal exposure.

### *2.1.2 Diffusion Couple Exposures*

Individual samples, ~8 mm × ~8 mm, were cut from the bulk implanted substrates for thermal exposure. Individual samples for thermal exposure were mated with an as-polished 3C-SiC sample using graphite paste to further protect the implantation surface. The samples were sealed in a thick-walled quartz ampoule with excess coarse SiC powder to limit surface decomposition, as shown in Fig. 2.1. Approximately, 0.05 g of Ag foil was encapsulated in the isolated sample chamber along with the diffusion sample to limit Ag out-diffusion from the Ag implanted SiC substrates. This diffusion couple exposure system was developed based on observations made from earlier ion implantation diffusion couple studies where samples that were thermally exposed in a W-mesh vacuum furnace exhibited significant surface decomposition which completely consumed the implantation layer in select samples [3]. Samples were exposed to 1500-1569ºC in an MTI GSL 1600X-80 tube furnace and at 1625ºC in a Lindberg Blue tube furnace. The self-contained samples were inserted and removed at temperature followed by a quenched step to limit diffusion contributions during transient heating and cooling. Temperatures were monitored with an external Type-B thermocouple placed in the center of the tube furnace hot zone. Table 2.1 shows the ion implantation diffusion couples investigated in this stage of the study.

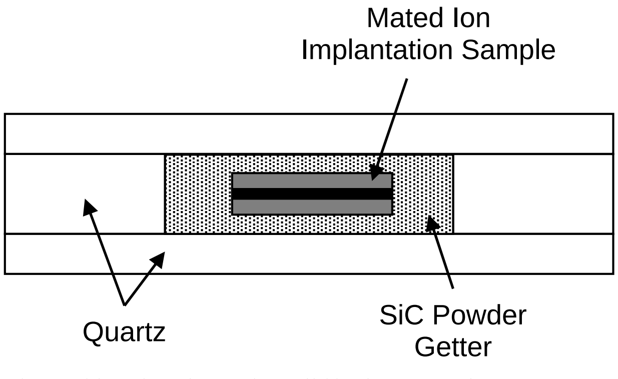

**Figure 2.1** Schematic illustration of ion implantation diffusion couple exposure system.

**Table 2.1** Ion implantation diffusion couple exposure conditions for Ag implantation doses of 5x$10^{14}$ ions/cm$^2$, *indicates 1x$10^{14}$ ions/cm$^2$ also included

| *Temp. (ºC)* | *1500ºC* | *1535ºC* | *1569ºC* | *1625ºC* |
|---|---|---|---|---|
| *Time (hours)* | *5,10,20 hours** | *10 hours** | *5,10,20 hours* | *1 hour* |

## *2.2 Analysis of Ion Implanted Diffusion Couples*

### *2.2.1 Overview of Analysis Approach*

Diffusion couple analysis focused on measurement of the change in Ag distribution of implanted Ag after thermal exposure to understand the nature and magnitude of thermal diffusion in the samples. Bulk changes in the Ag distribution were determined through the use of secondary ion mass spectroscopy (SIMS), while changes in the spatial distribution of Ag in the SiC substrate were investigated by scanning transmission electron microscopy (STEM).

SIMS analysis was preferred over other depth profiling measurements, such as Rutherford Backscatter Spectroscopy (RBS), due to the large dynamic range in Ag sensitivity gained from SIMS. This aspect is imperative as the signature of impurity diffusion in SiC is expected to be observed below the solubility limits of the Ag-SiC system, that is, when the ion implantation diffusion couple is exposed to temperature, impurity diffusion is driven into the bulk past the implantation peak at approximately the *S(T)* of the system. This is displayed in Fig. 2.2, which shows a schematic of the ion implantation diffusion scenario which satisfies the constant source approximation, where the impurity concentration extends into the bulk below the *S(T)* of the system and is observed as a shoulder or “tail” off of the Gaussian distribution extending into the bulk substrate. Because the signature of impurity diffusion is tied to the solubility limit of the Ag-SiC a high sensitivity depth profiling technique capable of measuring concentrations below 1x$10^{17}$ at/cm$^3$ is required - for this reason SIMS was identified as an ideal analytical technique.

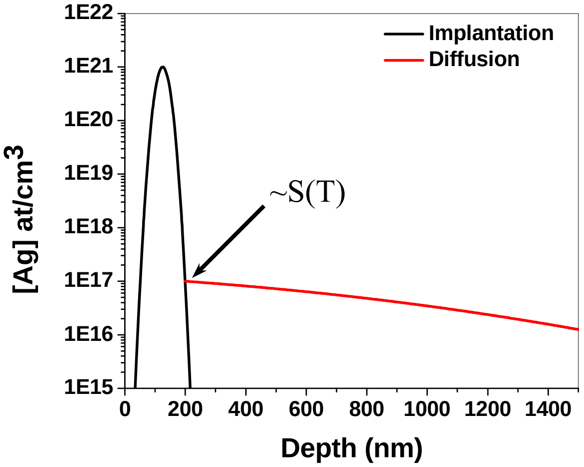

**Figure 2.2** Schematic illustration of the ion implantation diffusion couple depth profile.

SIMS analysis was conducted using a Cameca IMS 7f-GEO magnetic sector SIMS. Depth profiles were obtained for Ag in SiC by rastering a 5 keV $O_2^+$ ion beam over a 200 × 200 µm area with a 33 µm diameter optically gated analysis area. The SIMS analysis was performed at the Institute of Critical Technology and Applied Science Nanoscale Characterization and Fabrication Laboratory at Virginia Tech. $^{107}$Ag intensity was measured as a function of time and the measured intensity was correlated to Ag concentration using a relative sensitivity factor of $1.10\text{-}1.32\times10^{23}$ at/cm$^3$ calculated from of the as-implanted (AI) SiC substrates using the isotope $^{28}$Si as the bulk SiC reference intensity. Relative sensitivity factors were determined for all AI substrates (polycrystalline 3C-SiC $1\times10^{14}$ ions/cm$^2$ and $5\times10^{14}$ ions/cm$^2$, and single crystal 4H-SiC $5\times10^{14}$ ions/cm$^2$), where the range in relative sensitivity factors is representative of minor experimental variations for each AI substrate. Crater depths were determined by measuring the SIMS sputter crater using a Zygo optical profilometer to correlate sputtering time with depth.

STEM was employed to observe the initial state of the implanted substrate and the change in Ag spatial distribution after thermal exposure. STEM samples for investigation were prepared by traditional focused ion beam (FIB) lift-out techniques using a Zeiss CrossBeam Dual Beam FIB/SEM at the University of Wisconsin-Madison Materials Science Center (UWMSC). The FIB lift-out technique provided cross-sectional TEM samples of the SiC structure along the implantation and diffusion direction. Bright Field (BF) TEM analysis was performed using a Technai TF-30 at 300 kV. Selected area diffraction (SAD) patterns of the implantation layer and unaffected SiC beyond the implantation layer were obtained using a 300 nm aperture. Annular Dark Field (ADF) micrographs were obtained using a FEI Titan aberration-corrected STEM at the UWMSC to provide additional mass-contrast to aid in resolving the nature of the Ag after implantation and thermal exposure

### *2.2.2 STEM Analysis of Ion Implanted Diffusion Couples*

Figure 2.3 shows a BF-TEM comparison of the implantation zone for the polycrystalline 3C-SiC $5\times10^{14}$ ions/cm$^2$ as-implanted (AI) and 1569ºC 20 hour exposure samples. SAD patterns, inset in Fig. 2.3, indicate the implantation zone remained crystalline and suggests the implanted Ag remained in solution after implantation as no segregated features are observed in the implantation zone, which is identified as a darker band parallel to the implantation surface. Post thermal exposure, a fine structure is observed in the primary implantation region, indicating implanted Ag redistributes after thermal annealing in the crystalline substrate. Figure 2.4 shows the BF-TEM micrographs of the single crystal 4H-SiC $5\times10^{14}$ ions/cm$^2$ AI and 1569ºC 20 hours exposure samples. Similar to the polycrystalline 3C-SiC substrates, no evidence of amorphization is apparent as the SAD pattern indicates a crystalline substrate remains after implantation. Following thermal exposure fine scale segregated Ag features are observed. No insight on the structure of the fine scale segregated Ag features was determined from the SAD analysis of the thermally exposed samples.

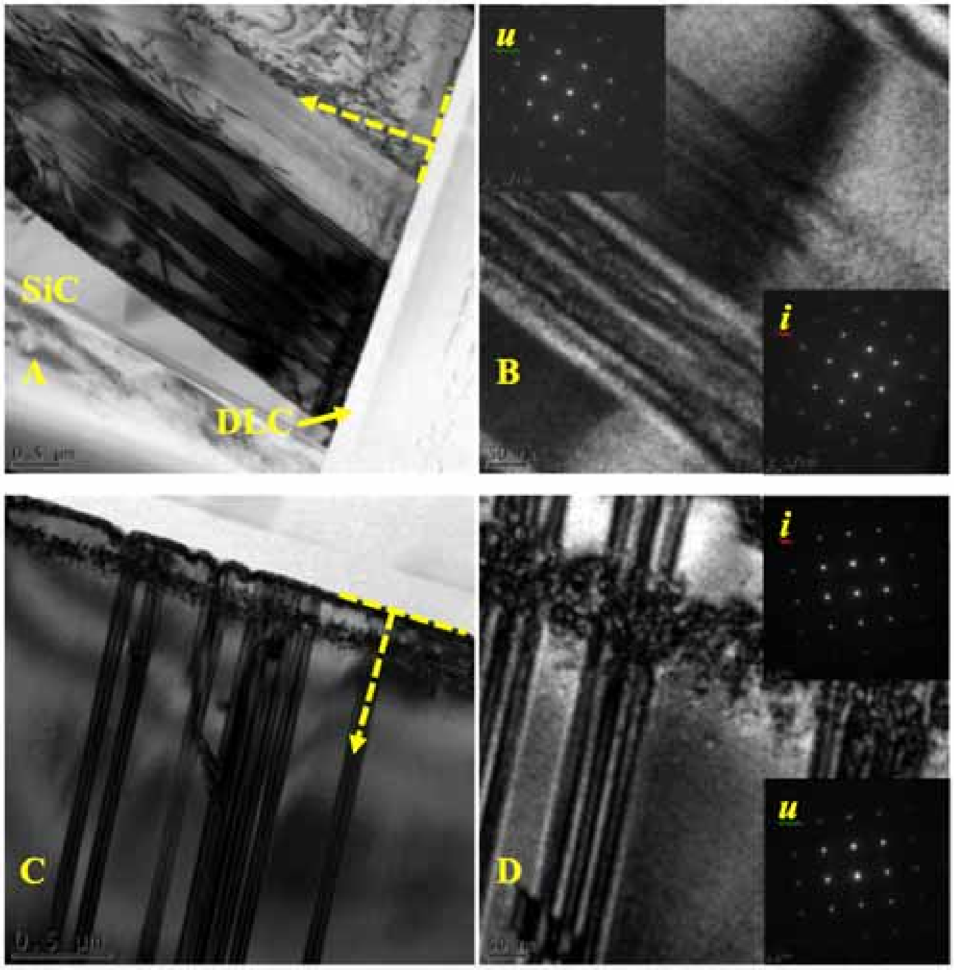

**Figure 2.3** BF TEM micrographs of polycrystalline 3C-SiC 5×10$^{14}$ ions/cm$^2$ AI (A-B) and 1569ºC 20 hours (C-D) conditions, inset SAD of (200) zone axis, dashed line indicates implantation surface while arrow indicates implantation direction, *i*) shows SAD from implanted region, *u*) indicates SAD from undamaged region.

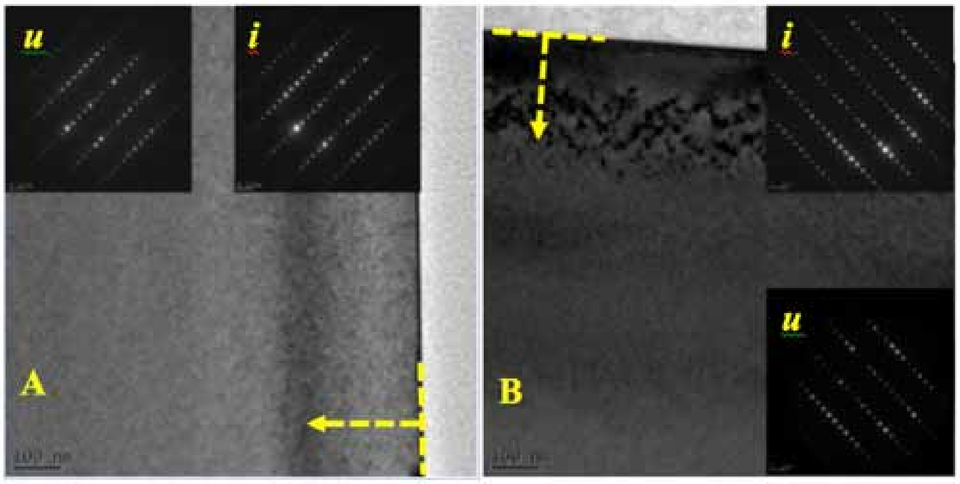

**Figure 2.4** BF TEM micrographs of single crystal 4H-SiC 5×$10^{14}$ ions/cm$^2$ AI (A) and 1569ºC 20 hours (B) conditions, inset SAD of (11-20) zone axis, dashed line indicates implantation surface while arrow indicates direction implantation direction, *i*) shows SAD from implanted region, *u*) indicates SAD from undamaged region.

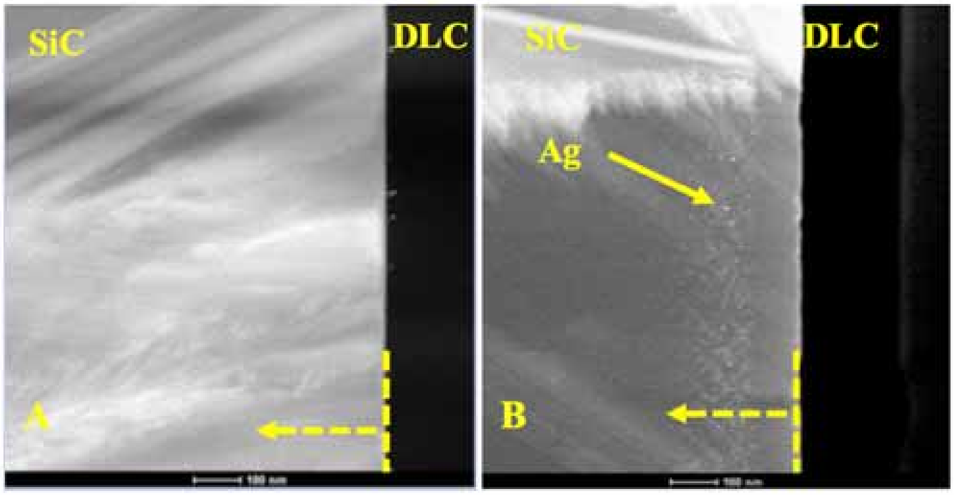

**Figure 2.5** ADF micrographs of polycrystalline 3C-SiC 5×$10^{14}$ ions/cm$^2$ AI (A) and 1500ºC 10 hours (B) conditions identifying fine structure after thermal exposure, dashed line indicates implantation surface while arrow indicates direction of ion implantation.

ADF provides diffraction contrast and mass contrast for imaging Ag impurities in the low atomic mass SiC matrix. Figure 2.5 shows a comparison of the polycrystalline 3C-SiC 5×$10^{14}$ ions/cm$^2$ AI and 1500ºC 10 hours thermal exposure, confirming fine scale Ag features form after thermal exposure in the region associated with the implantation zone. The affected depth is measured to be ~300-350 nm with no obvious features observed at greater depths. No obvious indicators of Ag segregation to microstructural features were noted.

The primary observation from the STEM analysis was that the substrate remained crystalline after ion implantation. This was a targeted attribute of the experiment as amorphization of the implantation region has been shown to influence the transport and redistribution of the implanted Ag due to recrystallization of the SiC substrate [2]. Maintaining a crystalline implantation region is expected to mitigate the influence of substrate recrystallization on Ag transport. Additionally, STEM analysis indicated the implantation surface remained intact with no deleterious surface decomposition, such that changes in the Ag distribution would not be influenced by SiC substrate decomposition.

### *2.2.3 SIMS Analysis of Ion Implantation Diffusion Couples*

SIMS analysis provided insight into the bulk redistribution of the implanted Ag after thermal exposure through depth profile measurements. Figure 2.6 shows an isochronal comparison of Ag depth profiles for single crystal 4H-SiC substrates exposed to temperatures of 1500-1569ºC for 10 hours. The AI Ag profile measured in the single crystal 4H-SiC substrate presents a singular Ag concentration peak at ~140 nm with a skewed Ag concentration past the primary peak away from the surface into the bulk substrate. This is expected from ion straggling during implantation. The thermally exposed single crystal 4H-SiC substrates indicate a bi-modal Ag distribution for all thermally exposed samples, with the primary peak remaining at ~140 nm and a secondary peak at a depth of ~500 nm. Figure 2.7 shows Ag depth profiles for the isothermal exposures of 1569ºC 5-20 hours. The isothermal comparison presents a similar observation in that no significant variation in the Ag concentration profile past the primary implantation peak is observed as a function of time, which implies that the observed redistribution of the implanted Ag concentration past the primary implantation peak is independent of the exposure time and temperature for the conditions investigated.

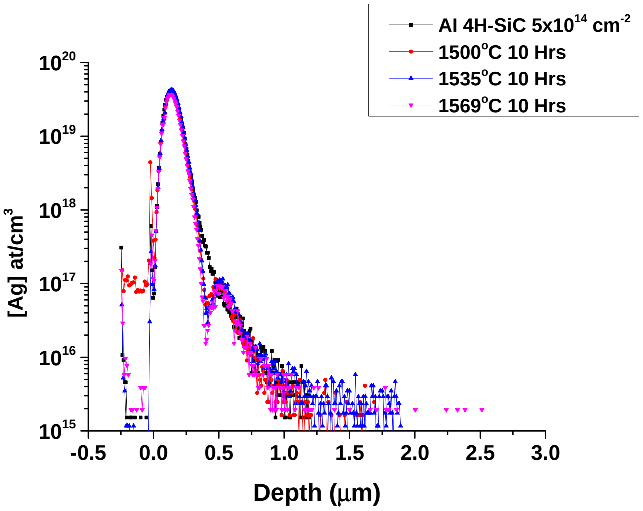

**Figure 2.6** SIMS depth profiles of Ag in SiC for single crystal 4H-SiC (dose of $5\times10^{14}$ ions/cm$^2$) in AI condition followed by 1500-1569ºC 10 hours isochronal exposures identifying redistribution of Ag past the primary implantation peak.

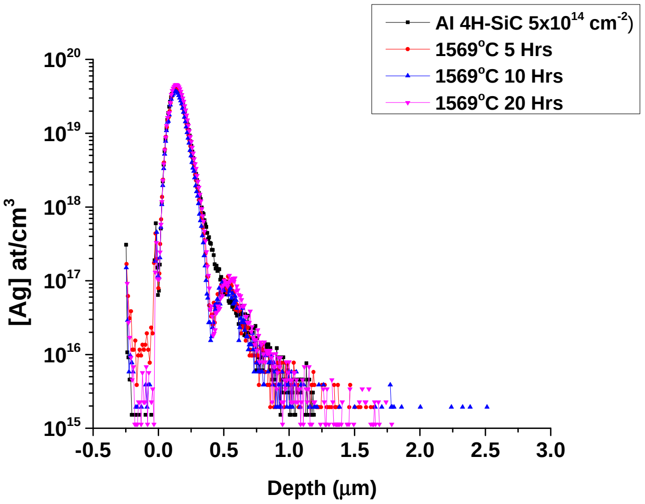

**Figure 2.7** SIMS depth profiles of Ag in SiC for single crystal 4H-SiC (dose of $5\times10^{14}$ ions/cm$^2$) in AI condition followed by 1569ºC 5-20 hours isothermal exposures identifying redistribution of Ag with minimal variation past the primary implantation peak.

The correlation of the Ag depth profile with the SRIM damage profile is shown in Fig. 2.8. A scaling factor of 1.28 was used to account for the underestimation of the heavy ion interaction with SiC in SRIM [4]. The observed Ag concentration minimum and secondary peak, as seen in Fig. 2.6 and Fig. 2.7, coincides with the reduction in implantation induced damage estimated in SRIM and is beyond the depth containing end-of-range defects identified by BF-

TEM. The consistent Ag depth profiles suggest the redistribution of Ag past the primary implantation peak is due to diffusion annealing of a finite population of implantation induced defects in the single crystal 4H-SiC substrate.

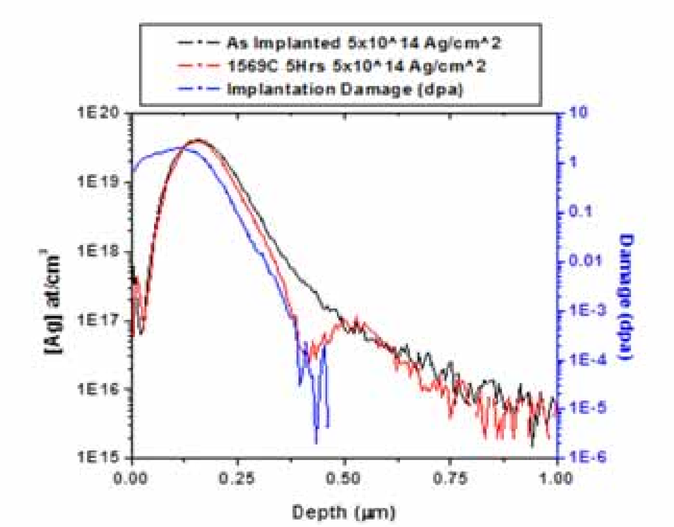

**Figure 2.8** SIMS Ag depth profile of single crystal 4H-SiC (dose 5x$10^{14}$ ions/cm$^2$) in AI conditionand 1569°C 5 hours exposure overlaid with damage profile estimated from SRIM.

SIMS depth profiles for the polycrystalline 3C-SiC substrates indicated a different behavior than the 4H-SiC single crystal substrates. SIMS Ag depth profiles for the 5×$10^{14}$ ions/cm$^2$ polycrystalline 3C-SiC substrates exposed to isochronal conditions of 1500-1569ºC for 10 hours are shown in Fig. 2.9. Ag concentration is observed to penetrate into the bulk SiC beyond the primary implantation peak with increasing penetration as a function of exposure temperature, suggesting a temperature dependence on the Ag penetration. Figure 2.10 shows a comparison of 5×$10^{14}$ ions/cm$^2$ polycrystalline 3C-SiC substrates exposed to 1500ºC for 10 and 20 hours with the AI condition. From Fig. 2.10 a minimal variation in the Ag concentration between the 1500ºC 10 and 20 hours exposures is observed implying the observed profiles at 1500ºC are due to Ag transport influenced by finite non-equilibrium point defects generated during implantation. Figure 2.11 shows the Ag concentration depth profiles for isothermal 5×$10^{14}$ ions/cm$^2$ polycrystalline 3C-SiC substrates exposed to 1569ºC for 5-20 hours and indicate that the Ag penetration into bulk SiC increases as a function of time. This observation suggests the Ag concentration “tail” extending into the bulk past the primary implantation peak is due to a thermally dependent transport mechanism. A comparative Ag concentration penetration depth was determined at a reference Ag concentration of 2×$10^{16}$ at/cm$^3$ in the Ag penetration “tail”. The magnitude of the observed Ag penetration past the AI profile is approximately 0.19 µm, 0.44 µm and 0.66 µm for 1500ºC, 1535ºC, and 1569ºC, 10 hour exposures, respectively, while the 1625ºC 1 hour exposure indicated an Ag concentration penetration of 0.34 µm past the AI profile. From this behavior, evidence of thermal Ag diffusion is indicated by the extended Ag penetration past the consistent 1500ºC 10 and 20 hour profiles. For the 1500ºC profiles, the consistent profiles imply no Ag transport is measurable beyond the signature of the implantation-induced transport. Figure 2.12 shows a Ag dose comparison for polycrystalline 3C-SiC $1\times10^{14}$ ions/cm$^2$ and 5x10$^{14}$ ions/cm$^2$ AI and 1535ºC 10 hour exposures - the profiles indicate a similar Ag concentration penetration profile extending into the bulk SiC offset by the variation in independent AI profiles, suggesting minimal implantation dose dependence.

A reduction of the primary peak for Ag implanted concentration was noted for most exposures and this is consistent with previously reported observation of thermally exposed Ag/SiC implantation diffusion couples and is expected to be due to loss to the implantation surface [5-8]. For the 1569ºC 10 hours and 20 hours exposures a peak shift skewed away from the implantation surface was observed. This phenomenon was also reported by Friedland *et al.* [5] and was suggested to be due to grain boundary diffusion effects.

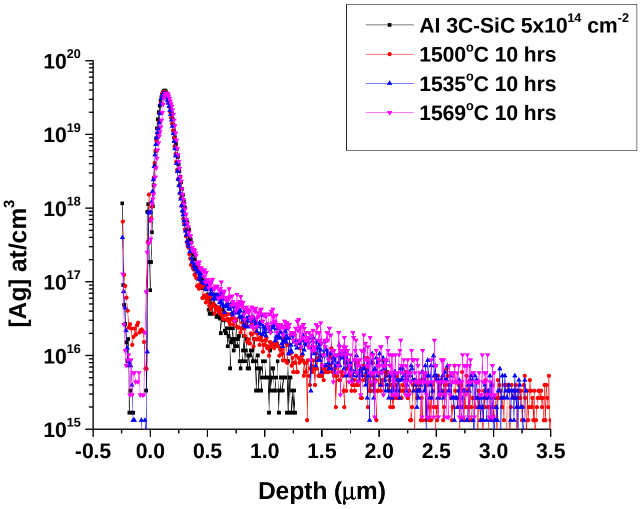

**Figure 2.9** SIMS depth profiles of Ag in SiC for polycrystalline 3C-SiC (dose 5x10$^{14}$ ions/cm$^2$) in AI condition followed by1500-1569ºC 10 hour isochronal exposures identifying extension of Ag concentration past the primary implantation peak.

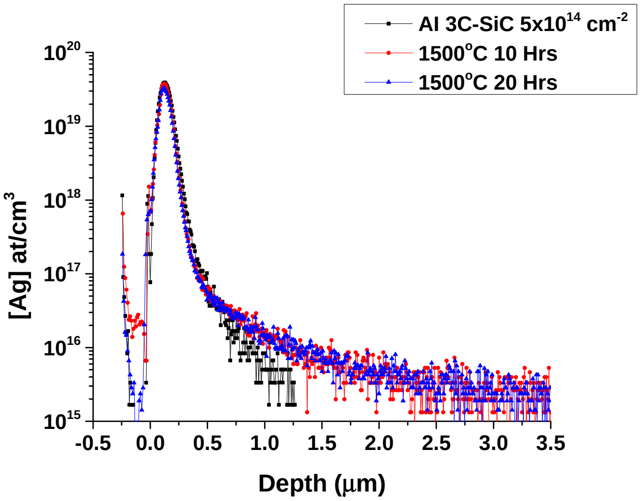

**Figure 2.10** SIMS depth profiles of Ag in SiC for polycrystalline 3C-SiC 5×10$^{14}$ ions/cm$^2$ AI, followed by 1500ºC 10 hours and 20 hours. The comparison identifies limited variation in Ag concentration between exposure conditions show no significant Ag concentration penetration into bulk SiC.

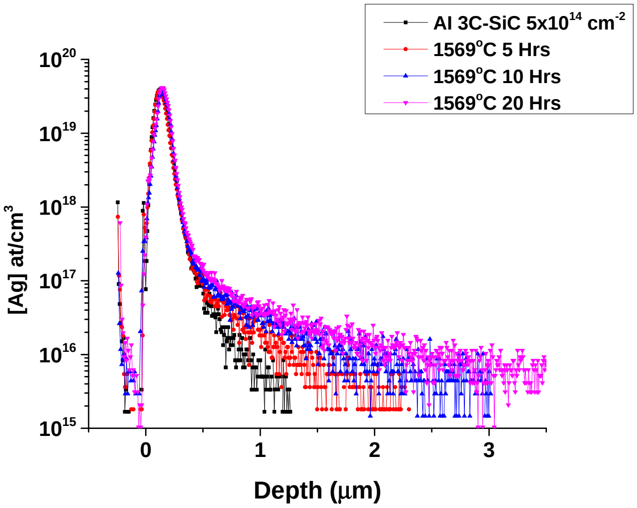

**Figure 2.11** SIMS depth profiles of Ag in SiC for polycrystalline 3C-SiC 5×10$^{14}$ ions/cm$^2$ AI followed by 1569ºC 5-20 hours isothermal exposures. An extension of the Ag concentration is measured in bulk SiC past the primary implantation peak for all conditions with the magnitude of penetration dependent on exposure time.

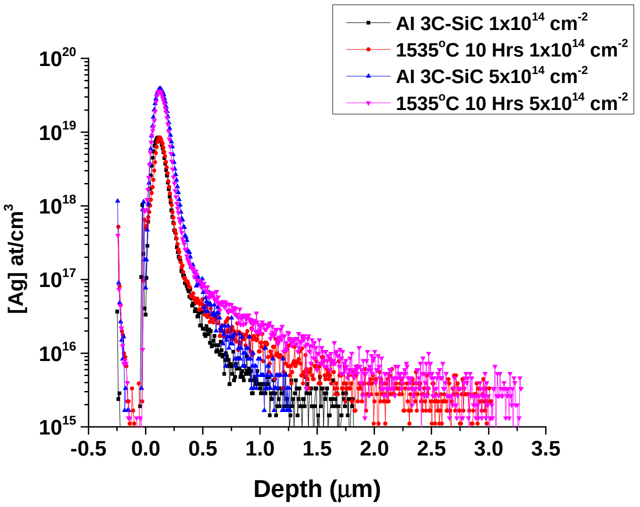

**Figure 2.12** SIMS depth profiles for implantation dose comparison of Ag in SiC for polycrystalline 3C-SiC $1\times10^{14}$ ions/cm$^2$ AI followed by 1535ºC 10 hours and polycrystalline 3C-SiC $5\times10^{14}$ ions/cm$^2$ AI and 1535ºC 10 hours exposures. An extension of the Ag concentration is measured in bulk SiC past the primary implantation peak for both implantation conditions.

## *2.3 Discussion of Measured Ag Transport*

### *2.3.1 Defects Contributing to Non-equilibrium Diffusion*

The SIMS observations from both 4H-SiC single crystal and 3C-SiC polycrystalline diffusion couples imply residual point defects from the ion implantation influence the measured Ag profiles after thermal exposure. This effect is manifested as enhanced diffusion relative to thermal diffusion. The following section discusses the nature of the observed diffusion based on the SIMS and STEM analysis. Discussion focuses primarily on the analysis of the single crystal 4H-SiC samples as the single crystal nature of the microstructure isolates the contributions from grain boundary effects.

The diffusion coefficient, $D$, for equilibrium impurity diffusion is described by an Arrhenius relationship shown in Equation 2.1. In Equation 2.1, $D_o$ (m$^2$/s) is a pre-exponential term which describes the physical nature of the diffusion mechanism, $k$ is Boltzmann's constant (eV/K), $T$ is temperature (K) and $Q$ is the activation energy (eV). The activation energy, $Q$, is composed of a migration energy barrier, $E_m$, and a formation energy barrier, $E_f$ . Here $E_m$, in general terms, describes the energy barrier for a specific mechanism to proceed forward, while $E_f$ describes the probability that a specific defect is present to participate in the diffusion process. The activation energy, $Q$, is approximated as the sum of both $E_m$ and $E_f$.

**Equation 2.1**

$$D = D_o exp\left(\frac{-Q}{kT}\right)$$

In simple cases, enhanced diffusion can occur from irradiation effects when non-equilibrium point defect concentrations contributing to the diffusion mechanism are present after implantation. Under enhanced diffusion conditions resulting from non-equilibrium point defects, the activation energy for diffusion is not dependent on $E_f$ and is dominated by $E_m$ and trapping effects [9]. When trapping effects are limited, the enhanced diffusion coefficient, $D^{enh}$, is increased proportionally to the concentration of non-equilibrium point defects remaining after implantation where the barrier to diffusion becomes dominated by $E_m$ for the specific mechanism. Equation 2.2 demonstrates this principle for a specific mechanism, in this example, a direct interstitialcy diffusion mechanism [10]. In Equation 2.2, $D^{enh.}$, is the enhanced diffusion coefficient, $[A_I]$, is the impurity interstitial concentration, $[A_I^{eq.}]$ is the equilibrium impurity interstitial concentration and $D_A^{eq.}$ is the equilibrium diffusion coefficient. $[A_I^{eq.}]$ depends on the $E_f$, as described by Equation 2.3 [11], leading to the enhanced diffusion coefficients dependence on $E_m$.

**Equation 2.2**

$$D_A^{enh.} = D_A^{eq.} \frac{[A_I]}{[A_I^{eq.}]}$$

**Equation 2.3**

$$[A_I^{eq.}] \approx {}^{\#\, defect\ sites}\!/_{unit\ volume} \times exp\left(\frac{-E_f}{kT}\right)$$

For enhanced diffusion to be active after ion implantation, residual point defects must be present. Residual point defects generated during implantation are expected to be present in the SiC substrate after the implantation process at 300°C in this study and as such would be available to contribute to enhanced diffusion. However, the availability of specific defects is expected to vary as self-interstitials and vacancies have different annealing temperatures in SiC. The annealing temperatures of vacancies in the Si and C sublattices are expected to be 800°C and 450-500°C, respectively [12]. The corresponding migration barriers, $E_m$, for vacancy motion are 5.2-6.5 eV for Si sublattice vacancies, $V_{Si}$, and 3.5–5.2 eV for C sublattice vacancies, $V_C$ [12]. The effective diffusion length for intrinsic vacancy diffusion is estimated from $x = \sqrt{Dt}$, where $x$ is an approximation of the diffusion length scale. For the implantation conditions, ~40 min implantation at 300°C, the effective vacancy diffusion length are $\sim 4.3 \times 10^{-26}$ nm and $\sim 1.5 \times 10^{-29}$ nm using reported diffusion coefficients of $V_C$ and $V_{Si}$, respectively [13-15]. This highlights the limited vacancy mobility at 300°C. The picture of remaining interstitials generated by implantation damage is less clear. The insight on the nature of self-interstitials in SiC as determined by *ab initio* simulations suggest several interstitial configurations are possible [16],[13]. The mobility of self-interstitial defects is expected to be greater than vacancies in SiC. The expected prevalent migration pathway for C interstitials is associated with a $E_m$ between 0.91–1.68 eV [12] while the barrier for Si self-interstitial diffusion is expected to range from 3.4-3.56 eV [12],[17]. A comparison of the magnitude of the $E_m$ for vacancies and interstitials suggests that Si self-interstitials may remain after implantation as the $E_m$ is equivalent to the low end of the C vacancy $E_m$, which corresponds to a defect annealing temperature of 450-500°C. The $E_m$ of C self-interstitials is ~2 eV lower, implying that the defects are likely mobile at 300°C and may anneal out. The energetics of defects formed by the implantation process suggests excess point defects, notably Si and C vacancies and Si self-interstitials, are available to participate in the Ag diffusion process after the implantation is halted.

The nature of the implantation induced point defects for the Ag-SiC system is not explicitly known, and as such direct confirmation of the mechanism responsible for the Ag diffusion in 4H-SiC and initial diffusion in 3C-SiC (as indicated by the 1500°C 10 and 20 hour samples) is not possible. No direct measurement of the nature of the impurity Ag after implantation has been made in this study. A previous ion implantation study by Xiao *et al.* [8] reported that implanted Ag exists interstitially after implantation at 377°C as determined by RBS channeling experiments. Alternately, *ab initio* simulations by Schrader *et al.* [16] suggest the most stable Ag defect in the lattice is the $Ag_{Si}$-$V_C^{-1}$ complex, implying Ag prefers to sit in a complex-substitutional site after implantation. TEM analysis indicates trapping of implanted Ag at end-of-range large scale defects, as shown in Fig. 2.3 and Fig. 2.4, which are formed due to a super-saturation of point defect in the primary implantation peak.

The distributions of implantation induced vacancy and self-interstitial point defects are expected to vary as a function of depth in the implanted substrate. Excess vacancies are expected to be present in the regime from the surface to the projected end-of-range and excess interstitials begin to dominate beyond the projected end-of-range [18, 19]. In Si substrate implantations, this difference in point defect populations is expected to influence enhanced impurity diffusion [20]. The observed Ag diffusion, associated with the Ag concentration minima in the single crystal 4H-SiC depth profiles, occurs in the regime where there is excess of interstitials. This suggests that excess vacancies provide sufficient trapping sites to immobilize implanted Ag from the implantation surface to the end-of-range. The redistribution of Ag past the transition from excess vacancies to excess interstitials implies that the observed Ag diffusion is dependent on mobile interstitials. The secondary segregation peak occurs beyond the primary implantation peak and is expected to be the result of Ag gettering at implantation induced impurity sinks in the irradiated substrate. This implantation induced gettering in the trans-end-of-range region has been observed in Si ion implantations and is attributed to trapping of mobile interstitials at small interstitial features [21-23]. The suggested dependence of the observed enhanced Ag diffusion on the vacancy and interstitial populations provides evidence for two potential mechanisms: direct interstitial diffusion and a kick-out diffusion mechanism.

### *2.3.2 Discussion of Mechanisms Contributing to Enhanced Diffusion*

A direct interstitial diffusion mechanism describes the scenario where implanted Ag resides interstitially after implantation, as suggested by Xiao *et al.* [8]. Here, the excess implanted Ag interstitials would be expected to be mobile at the exposure temperatures until reaching an interstitial sink, due to the expected low $E_m$ for Ag interstitials, ~0.89 eV [16]. This would account for the observed bi-modal distribution as an increased sink density is present at the near-surface due to excess vacancies, at the end-of-range implantation peak due to large scale defects, and in the region past the primary peak (trans-end-of-range defects).

In the simplified kick-out process an excess self-interstitial ($I$) replace an Ag substitutional atom ($Ag_S$) yielding a Ag interstitial atom ($Ag_I$), shown in Equation 2.4. The Ag interstitial is then available to diffuse by a direct interstitial mechanism or by the reverse reaction. However, this simplified process is likely more complicated in SiC due to the multiple sublattices and the presence of anti-site defects.

**Equation 2.4** $$Ag_S + I \Leftrightarrow Ag_I$$

Based on Equation 2.2 impurity diffusivity is dictated by the Ag impurity concentrations, which are coupled to the self-interstitial concentration. For systems where the kick-out mechanism is active, under equilibrium conditions the concentration of substitutional impurities can be significantly greater than that of the interstitial impurities, however, the vacancy diffusivity can be much lower than the interstitial diffusivity [24]. This holds for the energetics of Ag defects in SiC where $E_f$ is lower for substitutional defects compared to interstitials and $E_m$ of interstitials is expected to be lower than $E_m$ of substitutional defects [16]. Thus after implantation, the kick-out mechanism effectively mobilizes a non-equilibrium fraction of the implanted impurity atoms leading to enhanced diffusion.

For the kick-out mechanism, [$Ag_I$] cannot be estimated directly as insight on the reaction constant for Equation 2.4 must be known in addition to trapping effects. We define the "+1 model" as one that assumes a self-interstitial, $I$, is formed for every incident ion [25]. Assuming the reaction in Equation 2.4 proceeds completely to the right (with limited trapping effects), an upper bounds estimate of [$Ag_I$] ~$1\times10^{-4}$ to $1\times10^{-8}$ can be made from the +1 model. The same estimate for [$Ag_I$] is also obtained if we assume all implanted Ag resides interstitially after implantation. The estimated value for [$Ag^{eq.}_I$] is ~$1\times10^{-30}$ at 1500ºC based on the $E_f$ ~ 10.49 eV from *ab initio* calculations [16]. This equates to a [$Ag_I$]/[$Ag^{eq.}_I$] ~ $1\times10^{22-26}$, leading to a proportional increase in $D^{enh}$ and represents an upper bound in the magnitude of $D^{enh.}$ (as the role of trapping is not considered). The single crystal 4H-SiC depth profiles indicate that the mobile point defects are annealed out after 1500ºC at 10 hours. A lower bound on $D^{enh.}$ is estimated from the observed diffusion length from the Ag concentration minima to the trans-end-of-range peak of ~100 nm. The estimated lower bound of $D^{enh.}$ for the shortest exposure time (1625ºC for 1 hour) is ~$1\times10^{-18}$ $m^2/s$. This value is reasonable in comparison to the calculated $D^{Ag}$ for interstitial lattice diffusion from *ab initio* simulation of ~$2.5\times10^{-30}$ $m^2/s$ at 1625ºC as it represents an ~$1\times10^{11}$ increase in $D^{Ag,}$ which is below the estimated bound for $D^{enh}$.

Ultimately, the extent of the enhanced diffusion and responsible mechanism observed in single crystal 4H-SiC exposures is unknown due to a limited understanding of the residual point defects after implantation and magnitude of the specific defect concentrations. However, the correlation of the damage profile with bi-modal Ag redistribution indicates the non-equilibrium interstitial point defects, which remain after ion implantation, contribute to the observed diffusion of Ag in single crystal 4H-SiC. The constant Ag concentration profile past the primary peak at 1569ºC for 5, 10, 20 hours exposures for single crystal 4H-SiC implies that the redistribution was due to the annealing out of a finite mobile point defect population which is indicative of an enhanced diffusion by ion implantation [10].

### *2.3.3 Diffusion Analysis of Polycrystalline 3C-SiC Diffusion Couples*

The time and temperature dependence of the Ag profiles in the polycrystalline 3C-SiC diffusion couples allowed for analysis of the diffusion kinetics of the system. For ion implantation diffusion experiments, the main implantation peak serves as a constant source approximation when the peak concentration is greater than the solubility limit, $S(T)$, of the system. A modified expression for diffusion dependence of ion implanted impurity species is presented in Equation 2.5. In Equation 2.5, $C_o$ is the concentration at which the impurity species extends into the bulk, $d_o$ is the depth at which the impurity concentration deviates from the implantation peak at $C_o$, $d$ is the depth at $C(d,t)$, $t$ is time in seconds of the thermal exposure, and $D$ is the diffusion coefficient [26].

**Equation 2.5**

$$\boldsymbol{C = C_o erfc\left(\frac{d-d_o}{\sqrt{4Dt}}\right)}$$

The magnitude of the Ag concentration penetration "tail", $C_o$, was estimated by extrapolating a linear fit of the Ag concentration "tail" in the bulk to the primary implantation peak. Table 2.2 shows the magnitude for the observed Ag penetration, $C_o$, for each implantation sample.

**Table 2.2** $C_o$ values for polycrystalline 3C-SiC diffusion profiles

| ***Time*** | ***Dose*** | ***1535°C*** | ***1569°C*** | ***1625°C*** |
|---|---|---|---|---|
| **1 hour** | $5\times10^{14}$ $cm^{-2}$ | - | - | $6.47\pm0.57\times10^{16}$ $at/cm^3$ |
| | $1\times10^{14}$ $cm^{-2}$ | - | - | - |
| **5 hours** | $5\times10^{14}$ $cm^{-2}$ | - | $6.33\pm0.83\times10^{16}$ $at/cm^3$ | - |
| | $1\times10^{14}$ $cm^{-2}$ | - | - | - |
| **10 hours** | $5\times10^{14}$ $cm^{-2}$ | $6.13\pm0.43\times10^{16}$ $at/cm^3$ | $6.26\pm0.69\times10^{16}$ $at/cm^3$ | - |
| | $1\times10^{14}$ $cm^{-2}$ | $4.81\pm0.43\times10^{16}$ $at/cm^3$ | - | - |
| **20 hours** | $5\times10^{14}$ $cm^{-2}$ | - | $6.03\pm0.70\times10^{16}$ $at/cm^3$ | - |
| | $1\times10^{14}$ $cm^{-2}$ | - | - | - |

Diffusion coefficients for Ag in polycrystalline 3C-SiC, $D^{Ag}$, were estimated from the exposures above 1535°C, as at 1500°C no change in Ag profile was observed due to thermal diffusion, by numerically solving Equation 2.5 using the $C_o$ values in Table 2.2. Estimated values for $D^{Ag}$ from the SIMS profiles are presented in Table 2.3. Fitting the $D^{Ag}$ to an Arrhenius relationship, Equation 2.1, using a least squares fit equates to an activation energy, *Q*, of 5.89±0.99 eV and a pre-exponential term, $D_o$ of $2.08\text{x}10^{-1}$ m$^2$/s. The range of the pre exponential term error is $4.04\times10^{-4}$ to $1.07\times10^{2}$ m$^2$/s. Error is estimated from the standard deviation of the linear regression fit.

**Table 2.3** Estimated Ag diffusion coefficients in SiC ($D^{Ag}$) from SIMS diffusion profiles

| ***Time*** | ***Dose*** | ***1535°C*** | ***1569°C*** | ***1625°C*** |
|---|---|---|---|---|
| **1 hour** | $5\times10^{14}$ cm$^{-2}$ | - | - | $5.17\pm0.56\times10^{-17}$ m$^2$/s |
| | $1\times10^{14}$ cm$^{-2}$ | - | - | - |
| **5 hours** | $5\times10^{14}$ cm$^{-2}$ | - | $1.40\pm0.42\times10^{-17}$ m$^2$/s | - |
| | $1\times10^{14}$ cm$^{-2}$ | - | - | - |
| **10 hours** | $5\times10^{14}$ cm$^{-2}$ | $9.72\pm8.63\times10^{-18}$ m$^2$/s | $1.27\pm0.19\times10^{-17}$ m$^2$/s | - |
| | $1\times10^{14}$ cm$^{-2}$ | $8.19\pm1.92\times10^{-18}$ m$^2$/s | - | - |
| **20 hours** | $5\times10^{14}$ cm$^{-2}$ | - | $1.41\pm0.15\times10^{-17}$ m$^2$/s | - |
| | $1\times10^{14}$ cm$^{-2}$ | - | - | - |
| ***Average*** | | $8.95\times10^{-18}$ m$^2$/s | $1.36\times10^{-17}$ m$^2$/s | $5.17\times10^{-17}$ m$^2$/s |
| ***Error*** | | $\pm4.42\times10^{-18}$ m$^2$/s | $\pm1.63\times10^{-18}$ m$^2$/s | $\pm5.62\times10^{-18}$ m$^2$/s |

SIMS depth profiling in the polycrystalline 3C-SiC substrates gives rise to the possibility that the observed Ag penetration is due to SIMS artifacts from preferential sputtering and roughness effects. The peak-to-valley roughness of the SIMS crater surface is an indication of the magnitude of the crater surface roughness. Peak-to-valley roughness was measured by optical profilometery to be 0.05±0.02 µm. This correlates to penetration depths ~4-13 times greater than the peak-to-valley roughness as measured at the reference Ag concentration of $2\times10^{16}$ at/cm$^3$ past the AI profile for 1500-1625ºC. Additionally, the peak-to-valley roughness did not correlate with measured Ag concentration penetration differences observed in the isothermal 1569ºC comparison, implying that the variation in observed Ag penetration is not primarily due to a SIMS artifact.

Additional caution is noted for the diffusion analysis in this study as the contributions of enhanced diffusion from annealing of excess point defects during the initial stages of Ag defect diffusion are unknown and will likely influence the observed diffusion. Furthermore, secondary diffusion phenomena associated with peak broadening may also influence the diffusion analysis of $C_o$. The contribution of these effects on the diffusion analysis error is not explicitly known. To mitigate concerns about the influence of implantation effects, higher temperatures and longer annealing times should be investigated to drive diffusion lengths past the primary implantation peak and the magnitude of the Ag penetration to concentrations above the influence of the enhanced Ag diffusion and SIMS detection limits.

### *2.3.4 Discussion of Diffusion in Polycrystalline 3C-SiC: Role of Microstructure*

Comparison of the change in Ag concentration past the primary implantation peak between the single crystal 4H-SiC and polycrystalline 3C-SiC substrates suggests polycrystalline 3C-SiC accommodates excess Ag and facilitates impurity diffusion into bulk SiC. Ideally, the single crystal 4H-SiC substrate serves to isolate lattice diffusion contributions while the polycrystalline 3C-SiC substrate serves to mimic the TRISO fuel layer by introducing GB diffusion to contribute to Ag transport.

The absence of Ag extending into bulk SiC in the single crystal 4H-SiC substrates suggests that Ag is not accommodated in single crystal SiC above the detection limits of the SIMS analysis technique ($1\times10^{15}$ at/cm$^3$), whereas an extension of the Ag concentration is observed at approximately 4-7$\times10^{16}$ at/cm$^3$ for the polycrystalline 3C-SiC substrates. In the single crystal 4H-SiC substrates implanted defects are annealed out after 1500ºC 10 hours. The extension of Ag into the bulk of the polycrystalline 3C-SiC and similar diffusion profiles for the polycrystalline 3C-SiC $5\times10^{14}$ ions/cm$^2$ 1500ºC 10 and 20 hours exposures suggests that GBs act as Ag impurity sinks for the mobile implanted Ag defects during the initial stages of the thermal annealing, while the presence of GBs facilitates measurable impurity diffusion above 1535ºC. No experimental values of the solubility limits of Ag in single crystal or polycrystalline SiC are reported in literature. Solubility limits, $S(T)$, for impurities with atomic numbers greater than 37, have a maximum value of $2.5\times10^{17}$ at/cm$^3$ at temperatures greater than 2150ºC [1]. The observation of $S(T) < 1\times10^{15}$ at/cm$^3$ for the single crystal 4H-SiC substrate follows this trend. The presence of GBs likely accounts for an increase in the $S(T)$ of the system as Ag is expected to strongly segregate to GBs with an estimated GB segregation factor, $s$, of $\sim1\times10^{8}$ at 1500ºC where $s$ is defined as the ratio of the impurity concentration at the GB to the impurity concentration in the lattice [11]. This analysis implies that most Ag is expected to be segregated to GBs. Electron backscatter diffraction analysis of the polycrystalline 3C-SiC substrate in this study estimated the total GB volume fraction to be $\sim4\times10^{-4}$. Under a bounding condition of complete GB saturation, an upper estimate for $S(T)$ of $\sim4\times10^{19}$ at/cm$^3$ is possible. The measured $C_o$ for the observed Ag concentration penetration correlates to Ag GB concentration of approximately 0.1 at% and a bulk Ag concentration $<< 1\times10^{15}$ at/cm$^3$, for $s \sim 1\times10^{8}$. For both scenarios the peak implanted Ag concentration is above the expected $S(T)$ of the 4H-SiC and 3C-SiC systems implying that the constant source approximation assumed in Equation 2.5 was satisfied.

The presence of GBs implies that the measured Ag penetration in 3C-SiC is due to GB diffusion and is more significant than impurity lattice diffusion. This conclusion is supported by experimental observations, which suggest C self-diffusion along GBs in polycrystalline 3C-SiC is 5-6 orders of magnitude faster than lattice diffusion [14] and *ab initio* results which suggest $D^{Ag}$ along Σ3 GBs is greater by 10 orders of magnitude than lattice diffusion [11]. Again, this analysis suggests the observed diffusion in polycrystalline 3C-SiC is due primarily to GB diffusion, however, other microstructural features may contribute to the observed diffusion, including differences in dislocation density, stacking fault density, and extrinsic defect populations. The presence of stacking faults (SF) and GBs are confirmed in the BF-TEM analysis of the polycrystalline 3C-SiC substrates (Fig. 2.3), while no such features are observed in the BF-TEM analysis of the single crystal 4H-SiC substrates (Fig. 2.4).

### *2.3.5 Comparison of Ag Diffusion Energetics with Literature*

Table 2.4 shows a comparison of the pre-exponential term, $D_o$, and activation energy, $Q$ from ion implantation studies, computational studies, release from TRISO fuel and self-diffusion in of Si and C in polycrystalline 3C-SiC. Figure 2.13 graphically illustrates the magnitude of the reported diffusion coefficients.

**Table 2.4** $D_o$ and Q values for Ag/SiC diffusion and Si and C tracer self-diffusion from ion implantation, computational simulations, and TRISO release.

| Type | Mechanism | $D_o$ ($m^2/s$) | Q (eV) | Note | Ref. |
|---|---|---|---|---|---|
| This work | GB* | $2.08\times10^{-1}$ | $5.89\pm0.99$ | *Exact mechanism unknown | - |
| Implantation | GB | $4.30\times10^{-12}$ | 2.50 | | [5] |
| Implantation | Lattice | $D < 1\times10^{-21}$ | | Upper bound (1400°C) | [5] |
| Implantation | GB | $2.40\times10^{-9}$ | 3.43 | | [6] |
| Implantation | --- | $D < 5\times10^{-21}$ | | Upper bound (1500°C) | [27] |
| Simulation | Lattice | $6.30\times10^{-8}$ | 7.88 | Fastest calc. mechanism | [16] |
| Simulation | GB | $1.60\times10^{-7}$ | 3.95 | (210) $\Sigma3$ tilt GB, fastest mechanism along $[0\bar{1}1]$ | [11] |
| Simulation | GB | - | $3.35\pm0.25$ | (120) antiphase $\Sigma5$ tilt GB | [28] |
| TRISO Release | - | $D > 1\times10^{-16}$ | | Lower Bound (1500°C) | [29] |
| TRISO Release | - | $6.76\times10^{-9}$ | 2.21 | | [30] |
| TRISO Release | - | $4.50\times10^{-9}$ | 2.26 | | [31] |
| TRISO Release | - | $9.60\times10^{-6}$ | 4.22 | “Good SiC” | [32] |
| TRISO Release | - | $4.50\times10^{-5}$ | 4.16 | “Medium SiC” | [32] |
| TRISO Release | - | $2.50\times10^{-3}$ | 4.24 | “Poor SiC” | [32] |
| TRISO Release | - | $3.60\times10^{-9}$ | 2.23 | | [33] |
| TRISO Release | - | $6.80\times10^{-11}$ | 1.83 | | [34],[35] |
| TRISO Release | - | $3.50\times10^{-10}$ | 2.21 | | [36] |
| TRISO Release | - | $1.14\times10^{-13}$ | 1.13 | | [37] |
| Tracer | Lattice | $2.62\pm1.83\times10^{4}$ | $8.72\pm0.14$ | C Self-Diff. | [14] |
| Tracer | GB | $4.44\pm2.03\times10^{3}$ | $5.84\pm0.09$ | C Self-Diff. | [14] |
| Tracer | Lattice | $8.36\pm1.99\times10^{3}$ | $9.45\pm0.05$ | Si Self-Diff | [15] |

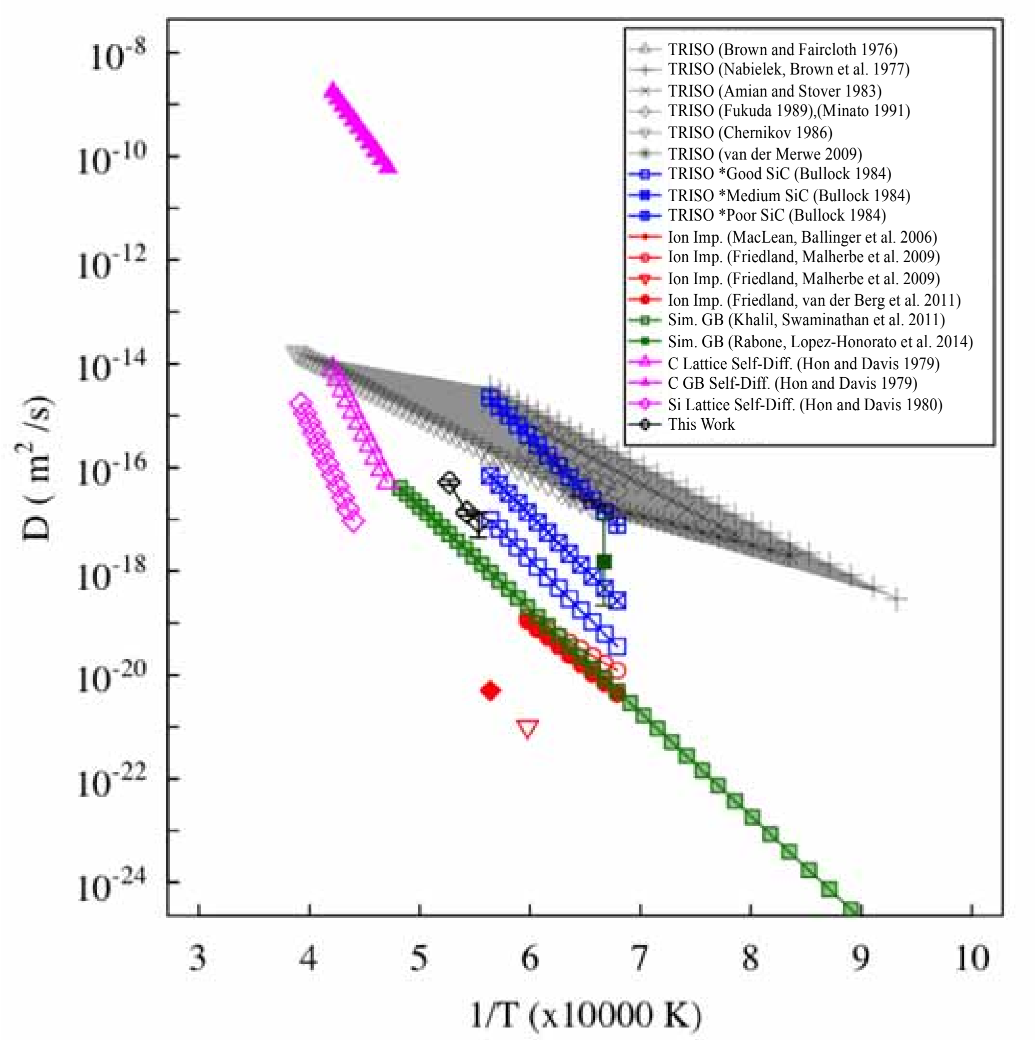

**Figure 2.13** Comparison of diffusion coefficients, $D^{Ag}$, in SiC from surrogate experiments, release from TRISO fuel, computational simulations, and this work. Si self-diffusion, C self-diffusion, and C grain boundary self-diffusion coefficients are presented for reference. The shaded régime represents $D^{Ag}$ with $Q$ = 1.13-2.26 eV and is associated with historic Ag release measurements from TRISO fuel.

The Si and C lattice self-diffusion coefficients and the C GB self-diffusion coefficient bracket the estimated $D^{Ag}$ from this study, while the calculated activation energy of 5.89±0.99 eV is similar to that of C self-GB diffusion [14]. This comparison suggests a similar mechanism may be active for the observed Ag diffusion. Additionally, the magnitude of $D^{Ag}$ in this work is approximately one order of magnitude greater than the reported effective $D^{Ag}$ for GB diffusion along Σ3 GBs [11]. The observed deviation may be accounted for in that diffusion along Σ3 GBs is expected to be a limiting case relative to diffusion along general GBs. With Σ3 GBs representing limiting GB diffusion pathways, contributions from additional GB types, namely high angle grain boundaries, could possibly lead to an increased effective $D^{Ag}$ [38]. An increase in the effective $D^{Ag}$ for GB dependent diffusion with the inclusion of additional GB types is supported by the findings of Rabone *et al.* [28] who report a $D^{Ag}$ along Σ5 GBs approximately two to three orders of magnitude greater than the fastest mechanism along the Σ3 GB [11]. Because the $D^{Ag}$ measured in this work is an average of all GB types present in the SiC layer, the inclusion of general GBs would be expected to increase the effective $D^{Ag}$ over the calculated $D^{Ag}$ for the Σ3 GB. These observations give additional validation to the measured Ag diffusion being dominated by GB diffusion.

The root of the deviation in $Q$ between the experimental work reported here and GB diffusion simulation results reported in the literature is not explicitly known. The variation may be accounted for by the influence of microstructural defects (such as defect trapping, GB segregation, and GB character effects), implantation effects, and the contributions from multiple potential contributing diffusion mechanisms (dislocations, SFs, GBs). The cumulative influence of these effects is captured by the SIMS depth profiling technique employed in this study. Anisotropy effects may also contribute to the variation as the reported $Q$ for Ag diffusion along the Σ3 GB is reported to vary as a function of direction along the GB plane, with $Q_{eff.}$ for the fastest mechanism along the [111] direction equal to 7.56 eV compared to 3.95 eV for the fastest mechanism along the [0-11] direction [11]. Additionally, in this work diffusion analysis at short thermal exposures may be influenced by the initial rapid irradiation enhanced diffusion from the annealing out of ion implantation induced defects as observed in the single crystal 4H-SiC conditions. This effect may lead to an overestimation of $D^{Ag}$ as the depth profile may be dominated by the initial rapid enhanced diffusion at short time scales before thermal diffusion dominates and influencing the magnitude of $Q$. This effect would lead to a possible elevated calculation of Q in this study, as the 1625°C 1 hour exposure, was the only condition with a "short thermal exposure time".

### *2.3.6 Comparison of Diffusion Energetics with TRISO Fuel Release*

The reported activation energies, $Q$, for TRISO fuel release range from 1.13-2.26 eV, as presented in Table 2.4 (see table for citations). The work by Bullock [32] represents a deviation from the historical release data and reports a $Q$ ranging from 4.16-4.24 eV with $D_o$ varying from $9.60\times10^{-6}$ to $2.50\times10^{-3}$ $m^2/s$ based on the perceived quality of the SiC layer. The variation in magnitude and energetics between these TRISO release studies and the surrogate systems, which includes this work, suggest the observed diffusion responsible for release in actual TRISO fuel is augmented relative to the Ag diffusion observed in surrogate systems. The magnitude of reported $D^{Ag}$ in this work is approximately one to three orders of magnitude lower relative to the reported $D^{Ag}$ from historic TRISO fuel release, and other surrogate studies report similar deviations in magnitude of measured $D^{Ag}$ [5, 6, 11]. The difference in reported diffusion coefficients and energetics implies a significant variation between diffusion behavior of the observed diffusion in TRISO fuel and the observed diffusion studied in surrogate systems. A first order approximation attributes the observed discrepancies to the inherently complex irradiation effects present TRISO fuel service.

In this work, enhanced Ag diffusion was observed in single crystal 4H-SiC under conditions expected to be interstitial rich, while the implantation enhanced diffusion was observed to be limited in regimes with excess vacancies and high interstitial sink densities. The variation in behavior is likely dependent on the nature of non-equilibrium point defects and defect sink density. The microstructure of neutron and self-ion irradiated SiC varies as a function of temperature and dose [39] and at elevated temperatures, ~1200ºC, the defect density decreases with a corresponding mean defect size increase [40]. This suggests a complex microstructure with varying defect sink densities and point defects populations exists over the life-time of the TRISO irradiation. STEM analysis of the SiC layer in irradiated TRISO fuel particles identified fission products segregated to nano-scale features in the interior of SiC grains [41], suggesting diffusion of fission products into the SiC grain interior. A comprehensive understanding of the residual point defects and irradiated SiC microstructure is not fully presented for the irradiated TRISO SiC in Ag release studies. However, this study indicates that parallels may exist between the observed implantation enhanced Ag diffusion and Ag diffusion measured from TRISO fuel release. This implies the potential for enhanced lattice diffusion to contribute to Ag release under irradiation conditions where excess non-equilibrium point defects are present and able to contribute to diffusion.

The suggested GB diffusion in polycrystalline 3C-SiC presents an alternative or co-operative mechanism to describe the deviation between TRISO release and surrogate systems. The comparison of single crystal 4H-SiC and polycrystalline 3C-SiC implantation samples confirms Ag segregates to GBs and because point defects are stable in GBs the same opportunity for irradiation enhanced diffusion exists. Recent STEM/EDS studies of the SiC layer of TRISO fuel from the AGR-1 irradiation campaign has identified Ag and other select fission products segregating to GBs and triple points [42]. This suggests SiC grain boundaries play a role in accommodating Ag and may serve as diffusion pathways. Additionally, modification of the local GB structure through the nucleation of cavities at GBs has been observed for Si self-ion irradiations [40]. Similar modification of the GB structure in the SiC layer of TRISO fuel may influence the effective diffusion length scale for Ag release. These effects may result in the observed higher $D^{Ag}$ for TRISO release relative to surrogate experiments.

### *2.4 Summary of Observations*

The use of SIMS for depth profiling of Ag/SiC ion implantation diffusion couples provided an increased dynamic range allowing for the identification of multiple diffusion régimes not previously observed. This aspect was critically important when considering the physical constraints on the Ag/SiC system such as solubility limits of Ag in SiC. Ag diffusion was observed to be active via enhanced diffusion of implantation-induced defects in the single crystal 4H-SiC single crystal substrates under perceived interstitial rich conditions, while thermal diffusion past the primary implantation peak was measured in the polycrystalline 3C-SiC substrates. The comparison of single crystal 4H-SiC and polycrystalline 3C-SiC diffusion couples confirmed that GBs act as Ag impurity sinks and suggests that GB diffusion contributed to the observed diffusion in the polycrystalline 3C-SiC substrate. The magnitude and energetics of the suggested GB diffusion implies impurity diffusion in annealed, ion-implanted polycrystalline 3C-SiC does not account for the measured Ag release from TRISO fuel as determined from Ag release experiments. This observation, coupled with the measured implantation-enhanced diffusion in single crystal 4H-SiC, suggests that irradiation effects likely contribute in some capacity to the Ag release. The observations in this work also provided additional confirmation of active Ag diffusion in polycrystalline 3C-SiC and presented new insights on enhanced Ag diffusion in single crystal 4H-SiC suggesting irradiation enhanced lattice diffusion may also contribute to Ag release in the TRISO fuel system.

# 3 Diffusion Studies in Irradiated SiC

## *3.1 Overview of Ag Diffusion in Irradiated SiC*

While diffusion coefficients measured in laboratory diffusion couple experiments [6, 43, 44] are in a very good agreement with values predicted by computer simulations [16, 45-47], these diffusion coefficients are orders of magnitude lower than those observed in actual fuel release experiments [32, 37, 48, 49]. The reason(s) for these discrepancies is not explicitly known, but one important difference between the in-pile and out-of-pile experiments is the presence of radiation in the former measurements. The effect of radiation damage on Ag release has been hypothesized in previous studies [6, 49-52], yet the magnitude of the enhancement and the mechanism remain largely unknown.

As discussed in section 2.3.1 and 2.3.2, evidence shows that radiation defects induced by Ag implantation caused enhanced Ag diffusion in single crystal 4H-SiC. However, the main purpose of implantation in diffusion couple experiments described earlier was to introduce Ag into SiC and therefore the radiation damage produced was short-ranged and not intentionally controlled. Furthermore, the implantation temperatures in those studies (room temperature to 600°C) are also different from the operating temperatures of TRISO particles (800°C to 1400°C [53]), which may result in different types of radiation-induced defects between the two temperature ranges. Connell *et al.* [51] investigated transport of Ag-Pd mixture in well-controlled neutron irradiated 3C-SiC and showed that Ag-Pd transport was significantly enhanced in the high temperature and high dose irradiated samples. However, it remains unclear whether these conclusions are valid for Ag diffusion in the absence of Pd.

In this section, two approaches are introduced to better understand the radiation effects on Ag diffusion in SiC. The first one is well controlled diffusion couple experiment with pre-irradiated SiC to quantitatively investigate the effects of carbon ion irradiation. The second approach is a STEM post irradiation examination of neutron irradiated TRISO fuel particle to unveil the most possible release mechanism.

## 3.2 *Effect of Carbon Ion Irradiation on Ag/SiC Diffusion Couple Experiment*

### *3.2.1 Materials and Method*

The same polycrystalline CVD 3C-SiC and single crystal 4H-SiC as described in section 2.1.1 were used in this study. Before carbon ion irradiation, samples were polished to an arithmetic surface roughness ($R_a$) of less than 10 nm using successively finer diamond polishing media culminating in a final polishing step with 0.05 µm colloidal silica. We prepared three 3C-SiC and three 4H-SiC bulk samples. For each type of material, two samples were subjected to carbon ion irradiation to introduce radiation damage, and the third unirradiated bulk sample was used as a reference (control) system. Carbon ion irradiation was conducted at the University of Wisconsin-Madison Ion Beam Laboratory (UW-IBL). Samples were irradiated at 950°C with 3.15MeV $C^{2+}$ beam using a tandem accelerator equipped with Source of Negative Ions via Cesium Sputtering (SNICS). The irradiation current was ~2.5µA and the total fluence was $1.1\times10^{17}$ ions/cm$^{-2}$. Following this, both $C^{2+}$ irradiated and unirradiated 3C-SiC samples were simultaneously implanted with 400keV $Ag^{+}$ at 300°C to a dose of $5\times10^{14}$ ions/cm$^{-2}$ at the Michigan Ion Beam Laboratory (MIBL). Similarly, the irradiated and unirradiated 4H-SiC samples were simultaneously implanted with 400keV $Ag^{2+}$ at the same temperature and dose at the INNOViON Corporation. Following Ag implantation, a ~220 nm thick diamond-like-carbon (DLC) films were deposited on the surface of the samples for surface protection during subsequent high temperature exposures. The DLC films were deposited using the plasma immersion ion implantation and deposition (PIIID) process [54] at the University of Wisconsin, Madison. Deposition was performed using the acetylene plasma generated by the glow discharge method at a pressure of 12 mTorr, and at near-room temperature.

After Ag implantation, individual samples (each approximately 8 mm × 8 mm in size), were cut from the bulk control and carbon ion irradiated samples for thermal exposures at various temperatures and times, as listed in Table 3.1. Detailed procedures of thermal exposure are described in Section 2.1.2. Here, the irradiated and unirradiated samples were sealed in the same quartz tube during thermal exposure to ensure that they have the same temperature history. After thermal exposure, samples were investigated by SIMS to understand the change in Ag concentration profile as a function of depth. Details for SIMS analysis are described in Section 2.2.1.

**Table 3.1** Thermal exposure conditions for various diffusion couples.

| Temperature | | 1400 °C | 1500°C | 1535°C | 1569°C |
|---|---|---|---|---|---|
| Time | $C^{2+}$ irradiated 3C-SiC | - | 10 hours | 10 hours | 5,10,20 hours |
| | Unirradiated 3C-SiC | - | 10 hours | 10 hours | 10 hours |
| | $C^{2+}$ irradiated 4H-SiC | 10 hours | 10 hours | - | 1,10 hours |
| | Unirradiated 4H-SiC | 10 hours | 10 hours | - | 10 hours |

### *3.2.2 Radiation/Implantation Damage*

Figure 3.1 shows the distribution of radiation damage in an irradiated 3C-SiC sample after 1569°C thermal exposure. STEM analysis was performed using a 300kV Technai TF-30 at the University of Wisconsin-Madison Materials Science Center. STEM samples were prepared by traditional focused ion beam (FIB) lift-out techniques using a Zeiss Augria FIB/SEM. FIB lift-out technique provided cross-sectional TEM samples of the SiC structure along the implantation and diffusion directions. SRIM code [55] was used to calculate the damage profile. In these calculations we assumed SiC density of 3.21 g/cm$^3$ and threshold displacement energies of 35 and 20 eV for Si and C, respectively. The calculated SRIM profile is overlaid with STEM image in Figure 3.1.

The visible radiation damage extends to the distance of approximately 2750 nm from the implantation surface. This damage consists of both black spot defects (BSD) and dislocation loops, an observation that is consistent with other reports [56]. The amount of damage increases with implantation depth and has an approximately 250 nm wide highly damaged band at the end-of-range. The difference between damage range predicted by SRIM (2550 nm) and the one measured experimentally (STEM visible damage range, approximately 2750 nm) is approximately 7.8%, indicating that the SRIM prediction is applicable in this study. Selected Area Electron Diffraction (not shown here) carried out on as-irradiated samples and on irradiated and Ag-implanted samples showed no evidence of amorphization within the entire irradiation/implantation range.

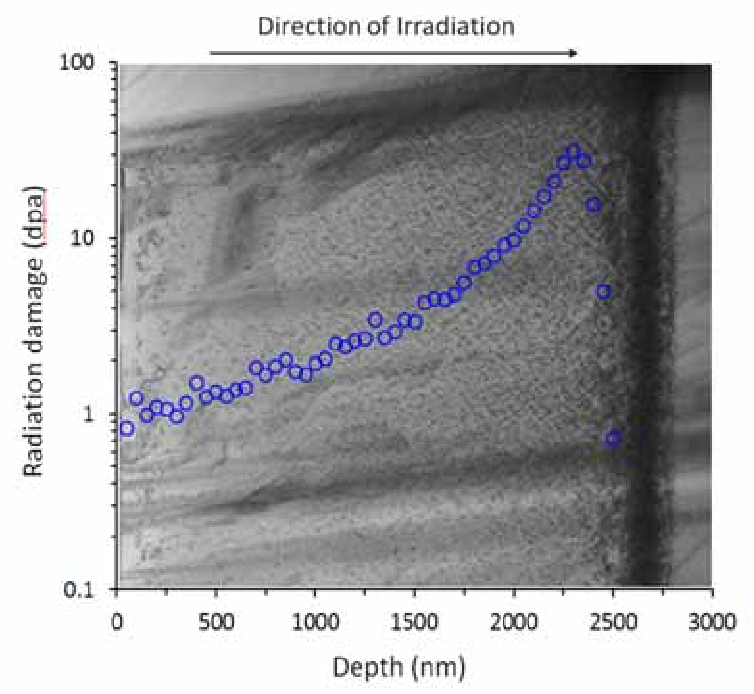

**Figure 3.1** STEM image showing the range of radiation induced damage in a $C^{2+}$ irradiated polycrystalline 3C-SiC followed by Ag implantation and thermal exposure at 1569°C for 20hours, overlaid with damage profile calculated using SRIM software.

### *3.2.3 SIMS Profiles*

Figure 3.2 shows Ag concentration profiles for unirradiated 3C-SiC samples exposed for 10 hours to a constant temperature (different for each sample) in the range 1500-1569°C. The Ag concentration in all exposed samples is observed to penetrate into the bulk SiC past the AI peak, indicating thermal diffusion of Ag into SiC. This penetration depth for unirradiated 3C-SiC samples was determined to be approximately 0.41 μm at 1500°C, and 0.64 μm at 1535°C and 1569°C.

Figure 3.3 shows the Ag depth profiles for irradiated polycrystalline 3C-SiC samples exposed to temperatures 1500-1569°C for 10 hours. Similar to unirradiated samples, Ag penetration "tail" is also observed in the samples that were first irradiated and then annealed. The Ag penetration depth determined for irradiated samples is approximately 2.08 μm for 1500°C and 1535°C, and 1.86 μm for 1569°C. These depths are significantly higher than those observed in an unirradiated sample. This result provides evidence that carbon ion irradiation enhances the diffusion of Ag in 3C-SiC. As is discussed in Sections 2.2.3 and 2.3.4, for Ag implanted polycrystalline 3C-SiC at 1569°C from 5-20 hours, the Ag penetration depth increased with exposure time and this effect was suggested to be due to GB diffusion mechanism. The penetration depths calculated from unirradiated 3C-SiC thermal exposed at 1569°C for 5, 10 and 20 hours are 0.47, 1.07 and 1.58μm, respectively (Fig. 2.11). These depths are higher in the case of the irradiated 3C-SiC. Specifically, as shown in Figure 3.4, the Ag penetration depths in irradiated samples exposed at 1569°C for 5, 10 and 20 hours are approximately 1.36μm, 1.86μm and 1.92μm, respectively. It can be seen that the diffusion depth still shows time dependence, although the diffusion rate seems to slow down after 10 hours. This result indicates that a more complicated radiation enhanced diffusion mechanism is active in carbon irradiated polycrystalline SiC.

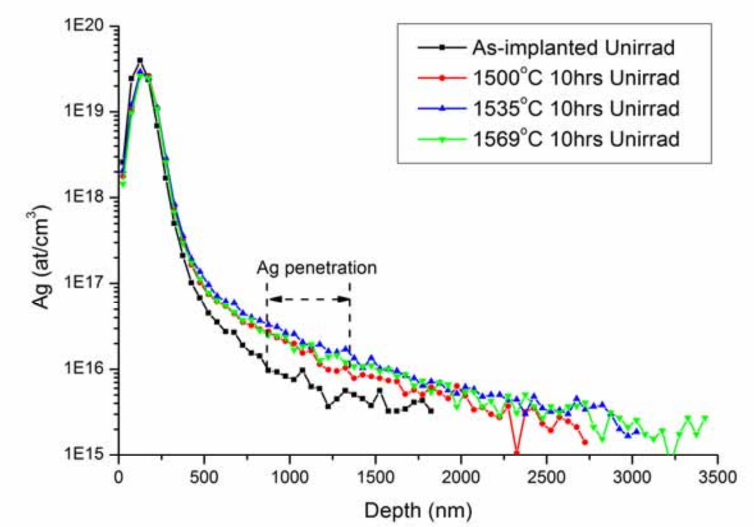

**Figure 3.2** SIMS Ag profiles of as-implanted and isochronally annealed unirradiated polycrystalline 3C-SiC.

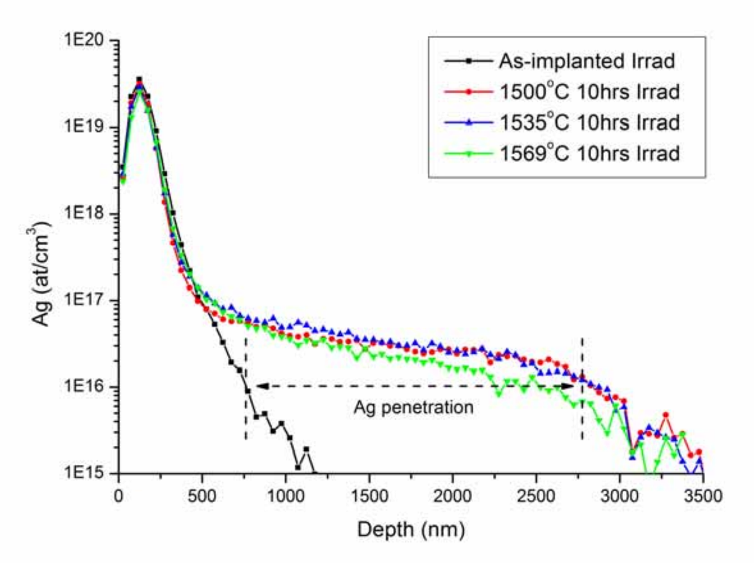

**Figure 3.3** SIMS Ag profiles of irradiated polycrystalline 3C-SiC, showing data for as-implanted and isochronally annealed samples.

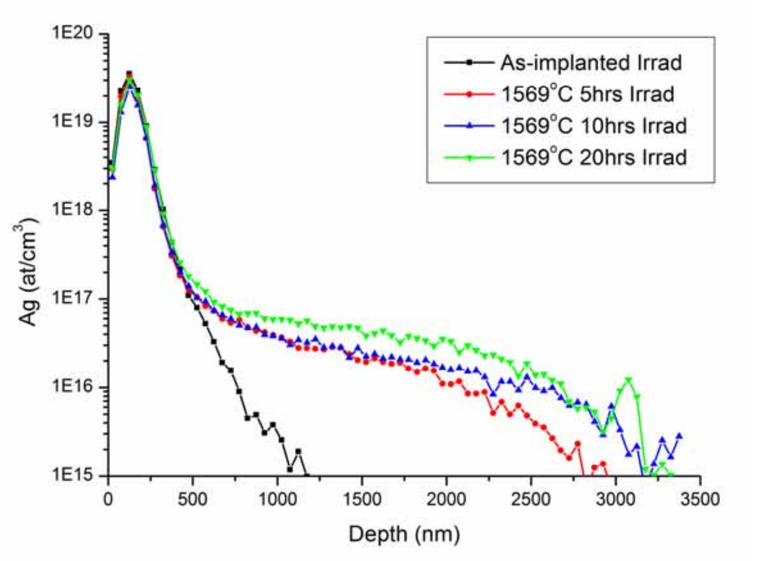

**Figure 3.4** SIMS Ag profiles for irradiated polycrystalline 3C-SiC. Data is shown for as-implanted sample as well as for sample isochronally annealed at 1569°C for 5, 10, and 20 hours.

The SIMS profiles determined in this study for unirradiated single crystal 4H-SiC samples are shown in Figure 3.5. These profiles also lack Ag penetration "tail" and show a bi-modal distribution, which is consistent with the SIMS profile of 4H-SiC in Section 2.2.3. While AI 4H-SiC substrate has a singular Ag concentration peak in the diffusion profile at ~140 nm, all thermal exposed samples show a bi-modal Ag distribution with the primary peak remaining at

~140 nm and a secondary peak at ~500 nm (see inset in Figure 3.5). Interestingly, the secondary peak becomes more pronounced as the exposure temperature increases. This may indicate a weak defect annihilation at lower temperature (1400°C), which is driven by interstitial diffusion of Ag [44]. Within the implantation induced damage range, Ag mobility was enhanced by radiation damage, which led to the observed redistribution of Ag.

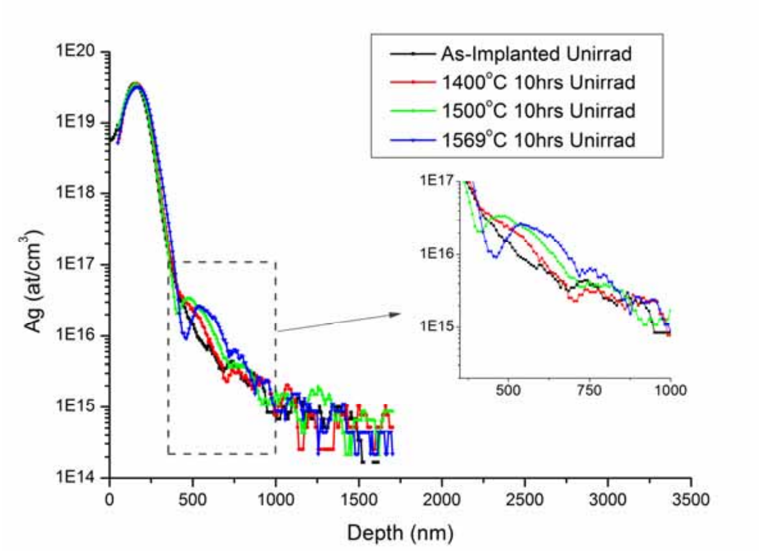

**Figure 3.5** SIMS Ag profiles of as-implanted and isochronally annealed unirradiated single crystal 4H-SiC.

The SIMS profiles of irradiated single crystalline 4H-SiC are shown in Fig. 3.6. Figure 3.6 (a) shows the Ag depth profiles for carbon irradiated samples exposed to temperatures 1500 and 1569°C for 10 hours and Fig. 3.6 (b) shows Ag concentration profile for irradiated samples that were exposed at 1569°C for 1 and 10 hours. In all of our single-crystal 4H-SiC data we found no significant diffusion of Ag. Since radiation did not enhance Ag diffusion in 4H-SiC (in contrast to a significant radiation effect observed for 3C-SiC), one can conclude that the Ag transport in 3C-SiC is mediated by GB diffusion and this type of diffusion can be accelerated by radiation. For the $C^{2+}$ irradiated single crystal 4H-SiC, a single peak is seen for all samples. Assuming that the bi-modal profile in thermally exposed unirradiated samples was due to the annealing of implantation induced defects in a confined region, it is plausible that the $C^{2+}$ irradiation followed by Ag implantation introduced trapping sites at an effective enough density so as to immobilize the implanted Ag. A similar behavior of suppressed diffusion of boron near the damage region was reported in boron ion implanted Si [57] and SiC [58]. Further microstructural analysis will be needed to confirm the hypothesized origin of the bi-modal distribution.

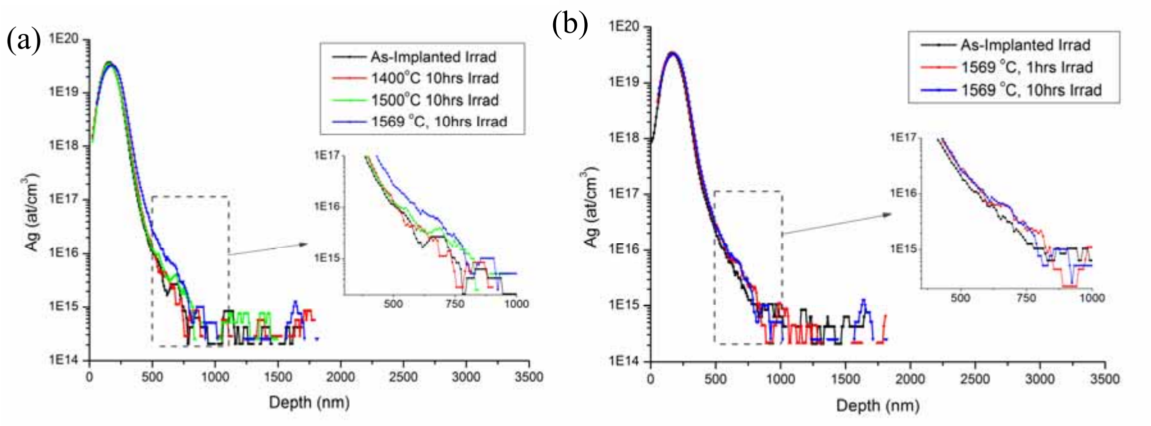

**Figure 3.6** SIMS Ag profiles of as-implanted and isochronally annealed irradiated single crystal 4H-SiC. The annealed samples were exposed (a) to different temperatures for a period of 10 hours and (b) to a temperature of 1569°C for different times.

By comparing SIMS profile results for 3C and 4H SiC, it could be concluded that the Ag transport is mediated by GB diffusion. To be more specific, for unirradiated samples, a clear Ag penetration was observed in 3C-SiC (Fig. 3.2), but not in 4H-SiC (Fig. 3.5). The results are similar for irradiated samples where Ag diffusion was only seen in 3C-SiC (Fig. 3.3) but not in 4H-SiC (Fig. 3.6). In addition an enhancement of Ag diffusion is also observed in irradiated 3C-SiC (Fig. 3.3) as compared to the unirradiated 3C-SiC sample (Fig. 3.2), indicating that GB diffusion can be accelerated by radiation.

It should be noted that the polycrystalline SiC and single crystal SiC samples have different polytypes, which are 3C and 4H, respectively. However, we do not believe that the polytype will alter our conclusions for the following reasons: (i) diffusion through 3C and 4H is not expected to be significantly different because of the same short-range order in the two polytypes and, (ii) the polytype would primarily affect bulk diffusion. However, Ag diffusion through bulk has been shown to be very slow both in the case of 3C (based on the DFT calculations [16]) and in 4H or 6H (based on the lack of observation of Ag diffusion in experiments [5, 59]). For these reasons it is commonly assumed that the difference in polytype does not have a significant effect on diffusion.

### *3.2.4 Comparison of Effective Diffusion Coefficient in Unirradiated and Irradiated SiC*

In order to quantitatively analyze the effect of carbon irradiation on enhancing Ag diffusion, the diffusion coefficients for both unirradiated and irradiated samples were determined from the SIMS results discussed in the previous sections.

A direct discrimination of the contributions from lattice diffusion and GB diffusion to the observed Ag diffusion in 3C-SiC is not possible as the lattice diffusivity cannot be quantitatively assessed due to the slow diffusion of Ag in single crystal 4H-SiC and due to the spatial/mass resolution limit at the "tail" of the concentration profile. Therefore, we only report an effective diffusion coefficient $D$, which is a combination of GB diffusion $D_{gb}$ and lattice diffusion $D_l$ coefficients.

As described in Section 2.3.3, for ion implantation diffusion experiments, the main implantation peak serves as a constant source approximation when the peak concentration is greater than the solubility limit, $S(T)$, of the system. An effective diffusion coefficient $D$ of a Fickian type diffusion can be determined by the following equation

**Equation 3.1**
$$\boldsymbol{C(d,t) = C_0 \mathrm{erfc}\left(\frac{d-d_0}{\sqrt{4Dt}}\right)}$$

where $C_o$ is the concentration at which the impurity diffuses into the bulk and it is usually equal to the solubility of the impurity. $d_o$ is the depth at which the impurity concentration equals to $C_o$, $d$ is the depth where the concentration is measured and $t$ is time in seconds [60]. This equation assumes a constant concentration ($C_0$) at the source during the time of the experiment. In these experiments, the peak Ag concentration is ~$3\times10^{19}$ and the solubility (the highest Ag concentration in the Ag "tail") is less than $1\times10^{17}$, which suggests that the implanted Ag is more than enough to pin the concentration at its solubility limit for the duration of the experiment, justifying the use of Equation 3.1.

By subtracting the AI Ag profile from the thermal exposed Ag profile, we can obtain Ag diffusion profiles (symbols in Fig. 3.7) for different exposure conditions. In this study, our aim is to compare the diffusion of Ag in pristine SiC and in carbon irradiated SiC. Therefore, $d_o$ is chosen as 500 nm to avoid the region damaged by Ag implantation as identified in Ref. [44] for the same implantation conditions. If the experimental data follows the trend described by Equation 3.1, a plot of $\mathrm{erfc}^{-1}(C/C_o)$ vs. $(d- d_o)$ will yield a straight line with the slope equal to $(4Dt)^{-1}$. An example of such plot for 3C-SiC samples irradiated and heat treated at 1569°C for 10 hrs is shown in Fig. 3.8. We first fit a linear function based on all the points from depth 575 to 2675 nm (for unirradiated samples from 575 to 1725 nm) and then adjust $C_o$ until the intercept of the linear fit equals to zero. The slope obtained from the linear fit is finally used to calculate $D$.

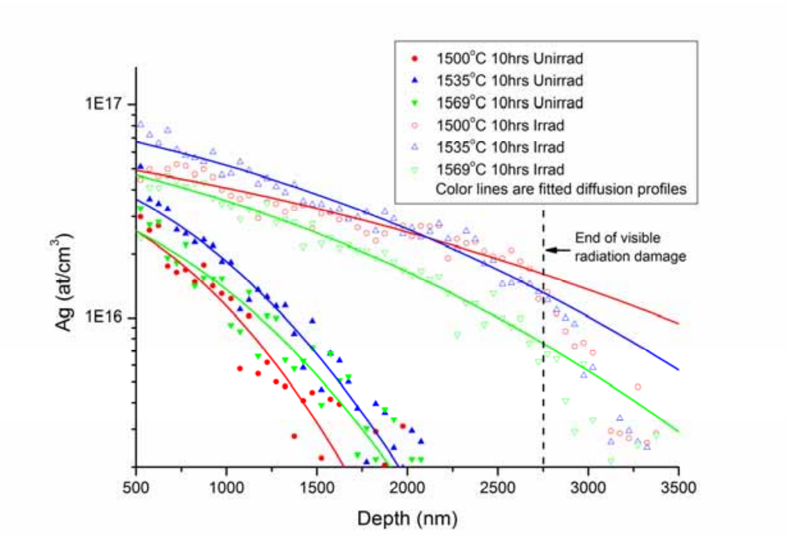

**Figure 3.7** Measured Ag diffusion profiles (symbols) and fitted diffusion profiles (lines) for polycrystalline 3C-SiC. Reference profiles for as-implanted samples were subtracted from the profiles shown in the figure.

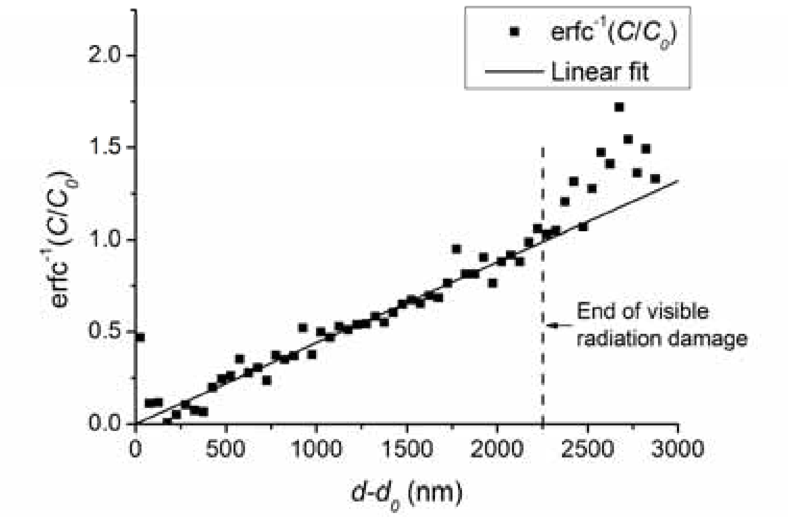

**Figure 3.8** Linear fit of $\mathrm{erfc}^{-1}(C/C_0)$ to determine diffusion coefficient of 1569°C/10hrs exposed irradiated 3C-SiC.

By plugging in the calculated $D$ values into Equation 3.1, we can plot the fitted Ag concentration profile, $C(d,t)$, for each sample (see colored lines in Fig. 3.7). The fitted $C(d,t)$ profiles align well with the experimental SIMS data for unirradiated samples, whereas in irradiated samples they align well until ~2750 nm, which is the termination point of visible radiation damage as identified by TEM. Beyond the end of radiation damage, the fitted $C(d,t)$ profiles have a higher Ag concentration than the SIMS measured data points, consistently with the hypothesis that radiation damage is the underlying reason for enhanced Ag diffusion.

The calculated $C_o$ and $D$ values for different exposure conditions in unirradiated and irradiated 3C-SiC samples are summarized in Table 3.1, where the reported error is derived from the standard deviation of the slope of the linear fit. From Table 3.1 we can see that the effective diffusion coefficients in irradiated samples are 12.3, 5.3 and 4.1 times higher than that in unirradiated samples at 1500, 1535 and 1569°C, respectively, demonstrating that carbon ion irradiation can appreciably enhance Ag diffusion in polycrystalline SiC. Although still lower than most reported $D$ values from TRISO integral release experiments, $(1.5\text{-}35.9)\times10^{-16}\,\text{m}^2/\text{s}$ at 1500 °C [48, 49, 61, 62], $D$ value of irradiated sample at 1500°C is similar to the $D$ value of $7.1\times10^{-17}\,\text{m}^2/\text{s}$ reported by Bullock [32] for "medium SiC" from a TRISO post-irradiation annealing experiment. Considering that the SiC layer in a real TRISO fuel is subjected to more severe neutron radiation than this ion irradiation study, the radiation enhanced diffusion coefficient is expected be higher than the values reported here, and radiation could be responsible for the observed increased Ag release from TRISO particles.

The magnitude of the diffusion coefficient, $D$, in unirradiated 3C-SiC increases with thermal exposure temperature (see Figure 3-9), and it can be fitted to an Arrhenius relationship

**Equation 3.2**

$$\boldsymbol{D = D_o \exp\left(\frac{-Q}{kT}\right)}$$

where $D_o$ ($\text{m}^2/\text{s}$) is a pre-exponential term which describes the physical nature of the diffusion mechanism, $k$ is the Boltzmann's constant (eV/$T$), $T$ is temperature (K) and $Q$ is the activation energy (eV). The fitted $Q$ and $D_o$ values of unirradiated 3C-SiC are 1.84±0.40 eV and $(1.04\pm0.10)\times10^{-12}\,\text{m}^2/\text{s}$, respectively. One should treat these values only as approximate estimates because the experiments were carried out over a relatively narrow range of annealing temperatures and only one sample was investigated at each temperature.

**Table 3.2** $C_o$ and $D$ values for unirradiated and irradiated Ag/3C-SiC diffusion couples.

| | | 1500°C 10hrs | 1535°C 10hrs | 1569°C 10hrs | 1569°C 5hrs | 1569°C 20hrs |
|---|---|---|---|---|---|---|
| $C_o$(at/cm$^3$) | Unirradiated | $2.56\times10^{16}$ | $3.61\times10^{16}$ | $2.56\times10^{16}$ | - | - |
| | Irradiated | $4.92\times10^{16}$ | $6.71\times10^{16}$ | $4.68\times10^{16}$ | $5.70\times10^{16}$ | $7.81\times10^{16}$ |
| $D$(m$^2$/s) | Unirradiated | $5.93\pm0.31\times10^{-18}$ | $7.99\pm0.74\times10^{-18}$ | $8.84\pm1.19\times10^{-18}$ | - | - |
| | Irradiated | $7.32\pm0.74\times10^{-17}$ | $4.21\pm0.30\times10^{-17}$ | $3.60\pm0.21\times10^{-17}$ | $3.53\pm0.16\times10^{-17}$ | $1.80\pm0.11\times10^{-17}$ |

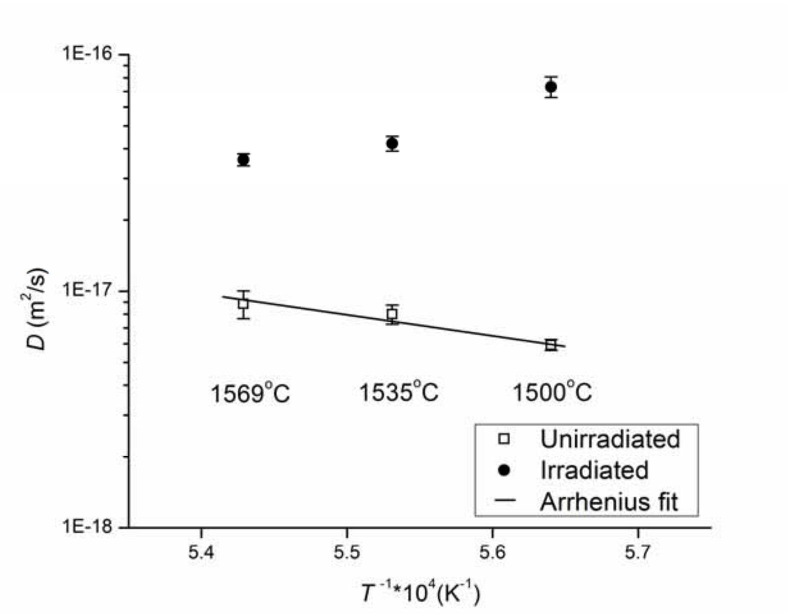

**Figure 3.9** Comparison of Ag diffusion coefficient D in unirradiated and irradiated polycrystalline 3C-SiC (error bars are derived from standard deviation of linear fit in Figure 3.8).

Unlike the unirradiated samples, the *D* values of irradiated samples do not show even an approximate Arrhenius temperature dependence (Figure 3.9). The lack of Arrhenius dependence could be due to the narrow range of thermal exposure temperatures or to the large grain size (~18μm) used in this study. Specifically the grain size exceeds the Ag penetration depth of 3.5 μm and it is likely that only few GBs are involved in the observed Ag diffusion. As GB diffusion is expected to be dominant, the measured *Ds* will largely depend on the local microstructure (e.g., the type and network of GBs), an effect which may obscure the temperature dependence of diffusion. Nevertheless, the trends in *D* with temperature of unirradiated and irradiated samples do appear to be qualitatively different, indicating that other mechanisms may contribute to Ag diffusion in the presence of radiation damage. It is possible that Ag diffusion in the irradiated samples, though higher, is less sensitive to temperature than in unirradiated samples. It is likely that effects from radiation damage significantly overwhelm temperature effects in the temperature range investigated in this study. The observation of decrease in diffusion coefficient with increasing temperature in irradiated samples may be due to the annealing of radiation-induced defects. The radiation-induced defects, a probable source for the observed radiation enhanced diffusion (RED), will annihilate faster at higher temperatures, which in turn suppresses Ag diffusion. More experiments are needed to test this hypothesis and to investigate radiation-induced defects and their annihilation during thermal exposure. *D* values determined from 1569°C isothermal exposure are consistent for samples that were annealed for 5 and 10 hours, but *D* estimated from a 20 hour thermal exposure is lower. This observation may be ascribed to greater annealing of radiation damage with exposure time. However, caution is needed with this interpretation since the measurement error for these results is not explicitly known.

The $C_o$ values in both unirradiated and irradiated samples do not show a clear temperature dependence. This is likely due to the narrow range of temperatures investigated in our experiments. This observation is consistent with lack of temperature dependence found for penetration depth discussed in Section 3.2.3. However, it is clear that the $C_o$ values in irradiated samples are about two times larger than in unirradiated samples. Therefore, the irradiated 3C-SiC is able to accommodate more Ag than its unirradiated counterpart.

It is interesting to compare the value of $C_0$ to the total number of SiC atoms in the GBs to assess the GB solubility of Ag. Using a lattice parameter of 4.36Å one can estimate the total concentration of atoms in SiC to be about $9.7\times10^{22}$ bulk-atoms/cm$^3$. Assuming the GBs are about 0.5 nm thick and approximately 18 μm grain size, yields an estimated density of GB atoms in SiC of $2.7\times10^{18}$ GB-atoms/cm$^3$. Taking the ratio of $C_0 \sim 3\times10^{16}$ Ag-atoms/cm$^3$ to this GB atom density suggests a density of Ag in the GB of about $1.1\times10^{-2}$ atom fraction (Ag as a fraction of total number of Si and C atoms) for unirradiated conditions, and about twice this value for irradiated material. Thus our results suggest the GB solubility for Ag is about 1-2% atomic fraction.

### *3.2.5 GB Diffusion and Lattice Diffusion in Irradiated SiC*

In polycrystalline materials, diffusion is a complicated phenomenon that involves several fundamental processes, such as direct lattice diffusion from the surface, diffusion along the GBs, partial leakage from the GBs to the lattice, and the subsequent lattice diffusion near the GBs [63]. Depending on the relative contributions of such processes, one can observe essentially different regimes of kinetics. Harrison has classified the diffusion kinetics in polycrystalline materials into three regimes identified as Types A, B and C [64]. Here, we apply different kinetic regimes to our experimental results to provide insights into the underlying mechanisms. In the calculations below we will use data obtained for samples 1569°C 10 hours exposed sample as an example, but other samples show qualitatively similar results.

Type A regime is observed when the lattice diffusion length, $(D_l t)^{1/2}$, is greater than the average grain diameter, $d_{gb}$. Usually $D_l<D<D_{gb}$, thus in this study $(D_l\, t)^{1/2}<(Dt)^{1/2} = 1.14$ μm, smaller than the average grain diameter of 18 μm. Therefore Type A regime is not applicable to this study. Type C is applicable when the diffusion takes place only along the GBs, without any substantial leakage to the lattice. It occurs when $(D_l t)^{1/2}<0.2s\delta$, where $s$ is the GB segregation factor and $\delta$ is the effective GB width. By applying our data and using $\delta = 0.5$ nm, we can deduce that Type C can be applicable if $s > 1.11\times10^3$. The segregation factor in irradiated SiC is not explicitly known, but atomistic simulations from Ref. [45] showed that segregation factor of Σ3 GB in unirradiated SiC at 1200°C is $3.1\times10^8$. Unless carbon irradiation greatly reduces this value, Type C kinetics may be applicable for irradiated samples in this study. If Type C applies, the effect of lattice diffusion is negligible and $D_{gb} = D$. In this case, the significant difference in the diffusion coefficient between unirradiated and irradiated samples is solely ascribed to the enhanced GB diffusion caused by carbon irradiation. However, if the carbon irradiation greatly changes *s* value so that Type C is no longer applicable, both lattice diffusion and GB diffusion need to be taken into account and one needs to consider Type B diffusion.

Type B regime is applicable when the following conditions are satisfied

**Equation 3.3**

$$\beta = \frac{s\delta D_{gb}}{2D_l(D_l t)^{1/2}} > 10$$

**Equation 3.4**

$$\alpha = \frac{s\delta}{2(D_l t)^{1/2}} < 0.1$$

Under these conditions, $D_{gb}$ can be calculated, using known values of $D_l$ and *s* and the following equation [65]

**Equation 3.5**

$$\boldsymbol{s\delta D_{gb} = 1.322\left(\frac{D_l}{t}\right)^{1/2}\left[-\frac{\partial lnC}{\partial(d-d_o)^{6/5}}\right]^{-5/3}}$$

In Figure 3.10 we plot ln*C* vs $(d\text{-}d_o)^{6/5}$ for an irradiated sample. By obtaining the slope from a linear fit, the relation between $D_l$, $D_{gb}$, and, *s* can be defined using Equation 3.5. Then applying Equations 3.3 and 3.4 we find that $1.74\times10^{-22}$ ($m^2$/s) < $D_l$<$3.41\times10^{-18}$ ($m^2$/s), 1< *s* <140, and $3.41\times10^{-16}$ ($m^2$/s) < $D_{gb}$<$4.78\times10^{-14}$ ($m^2$/s). From these calculations we conclude that Type B kinetics is applicable when segregation factor in the irradiated samples is lower than 140. Although $D_l$ and $D_{gb}$ cannot be determined exactly, these calculations would suggest that both GB diffusion and lattice diffusion coefficients are greatly enhanced as compared to the unirradiated samples if Type B kinetics were accurate, for which $D_l \approx 10^{-29}$ ($m^2$/s) [16] and $D_{gb} \approx 10^{-18}$ ($m^2$/s) at 1569°C.

From the lattice diffusion coefficient extracted by assuming Type B diffusion, the one-dimension diffusional distance ($x_l$) can be estimated by $x_l = (D_l t)^{1/2}$. For 1569°C 10 hours exposed 4H-SiC sample, we can estimate 2.5 nm < $x_l$ < 349.9 nm. As can be seen in Fig. 3.10, hundreds of nanometer penetration of Ag is not observed in these single crystal samples. This result suggests that either Ag atoms are trapped in the implantation damage region, or $D_l$ lies near the lower bound of the $1.74\times10^{-22}$ ($m^2$/s) <$D_l$< $3.41\times10^{-18}$ ($m^2$/s) regime. In the latter case, the $D_l$ will lead to few (or tens of) nanometers of penetration and such penetration cannot be discerned experimentally.

While both type B and C kinetics are applicable, our result clearly suggests that the ion irradiation enhances Ag diffusion in either case.

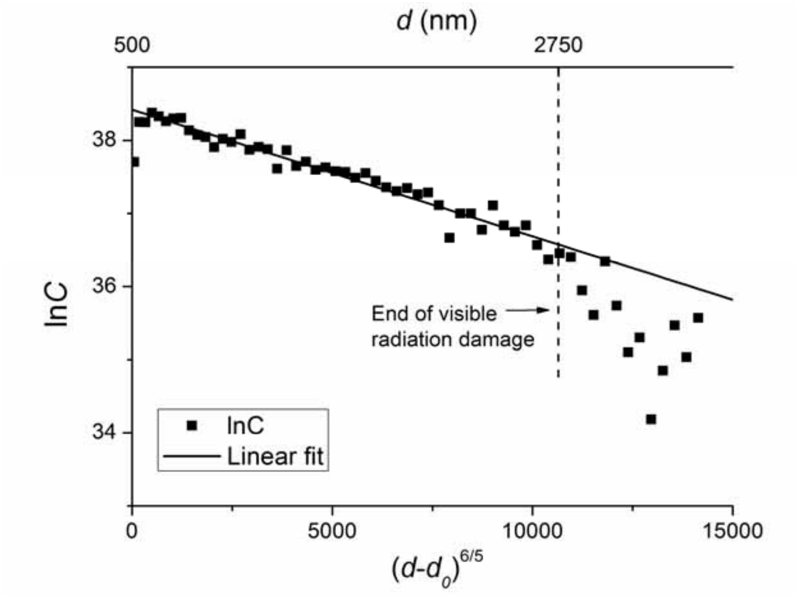

**Figure 3.10** A plot of logarithm of concentration ln$C$ vs. $(d\text{-}d_o)^{6/5}$ for 1569°C/10hrs exposed irradiated 3C-SiC. Diffusion coefficient can be determined by fitting the data to Type B kinetics (Equation 3.5)

## *3.3 Analysis of Neutron-Irradiated TRISO Fuel Particles*

Research described in this section was carried out in collaboration with Dr. Isabella Van Rooyen from Idaho National Laboratories. Dr. Van Rooyen co-wrote the text presented in this section. The experiments were supported by a rapid turn-around proposal (RTE 13-412). The results of this work have been submitted for publication ("STEM EDS Analysis of Fission Products in Neutron Irradiated TRISO Fuel Particles from AGR-1 Experiment", B. Leng, I. van Rooyen, Y. Q. Wu, I. Szlufarska, K. Sridharan, Submitted).

### *3.3.1 Materials and Method*

The TRISO fuel particle examined in this study was CP35 from Compact 6-3-2 from the AGR-1 experiment, which had an estimated Ag retention of 80%. Details of this fuel particle and the rationale for its selection for this study are described elsewhere [41]. Two STEM lamellae (identified as 6a and 6b) were prepared by a focused ion beam near the IPyC-SiC interlayer as shown in Fig. 3.11. The purpose of using two lamellae was to provide larger areas for investigation and no specific microstructural differences were expected in these two lamellae.

The fission products (FPs) produced during irradiation consist of relatively heavy elements compared with coating material layers used in TRISO fuel particles. Therefore, the High Angle Annular Dark Field (HAADF) detector in STEM, of which contrast in the image is sensitive to atomic number differences (so-called Z-contrast imaging), was chosen to reveal the distribution of FPs. The compositional analysis of these fine FP precipitates was performed by standardless EDS analysis in STEM mode.

The STEM-EDS analyses were conducted with an FEI Tecnai G2 F30 STEM at the Microscopy and Characterization Suite, Center for Advanced Energy Studies, in Idaho Falls where low-activity irradiated materials can be examined. Pd, U, and Ag were identified using Pd Kα1 peak (21.175 keV), U Lγ1 peak (20.163 keV), and Ag Kα1 peak (22.162 keV), respectively, to avoid uncertainties associated with peak overlaps. An EDS line scan was used for the qualitative identification of FP using an acquisition time of 10–40 secs/point. Transmission Electron Microscopy images and analysis software were used for quantitative EDS analysis, and furthermore longer 480 secs/point area analysis was used for quantitative measurements to increase the signal-to-noise ratio.

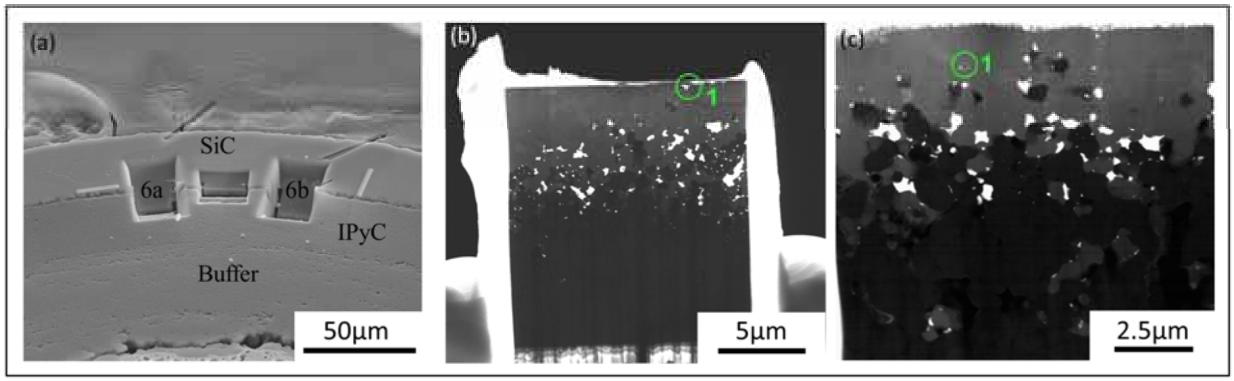

**Fig. 3.11** Images showing: (a) positions in a post-irradiated TRISO fuel particles from where STEM lamellae were fabricated, (b) position investigated in lamella 6b (Position 1:SiC layer) and (c) position investigated in lamella 6a (Positions 1: SiC layer).

### *3.3.2 STEM Analysis of Distribution of Ag and Other FP*

Using HAADF imaging and combined EDS measurements, various FP precipitates were identified, and categorized based on their size, shape, and location in the microstructure.

**Micron-sized Precipitates (≥100 nm)**

As shown in Fig. 3.11, micron-sized precipitates with irregular shape were mainly located at IPyC-SiC interlayer, but some of these precipitates were also observed inside the SiC and IPyC layers. The size of these precipitates varied from approximately 100 nm up to 2μm, and the precipitates in SiC and IPyC layers were smaller than those in IPyC-SiC interlayer (Fig. 3.11). Additionally, micron-sized precipitates in the SiC layer and the IPyC-SiC interlayer had sharp protrusions connecting them to SiC grain boundaries which indicates that their formation may be associated with GB transport of FP. Figure 3.12 shows the EDS spectrum of a micron-sized precipitate located at the SiC layer ~5μm away from the interlayer. These precipitates consist of mainly Pd and U, while other minor FPs, such as Cs, Eu, and Ce, were also identified. No Ag was identified within the micro-sized precipitates. EDS analysis showed that the ratio of U, Pd, and Si in micron sized precipitates in the SiC layer is close to 1:2:2, suggesting that they may be $UPd_2Si_2$ ternary silicides, as indicated by selected area diffraction pattern in the previous transmission electron microscopy study of another particle from AGR-1 [52].

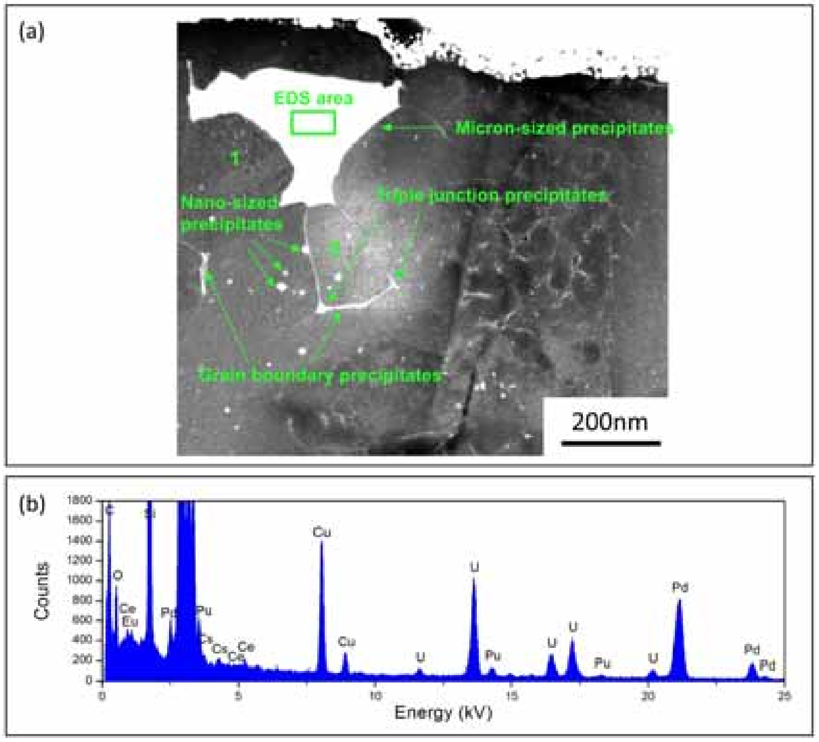

**Fig. 3.12** (a) Distribution of various FP precipitates in the SiC layer ~5um from SiC-IPyC interlayer of sample 6b (position1 in Fig 3 .11[b]), numbers are used for marking different regions to provide context to higher magnification images in other figures, and (b) EDS area scanning spectrum inside the micron-sized precipitate (within the green box) (Cu is an artifact from transmission electron microscopy grid).

## Nano-sized Precipitates (5 to 20 nm)

Unlike the micron-sized precipitates, which have long been observed by the scanning electron microscopy and transmission electron microscopy studies [52, 66-68], nano-sized FP precipitates were not observed until STEM was introduced as an advanced characterization technique [41]. Nearly spherical-shaped nano-precipitates, 5 nm to 20 nm in size, were identified mainly located inside the SiC grains at the SiC-IPyC interlayer and further inside the SiC layer

(Fig. 3.13(a)). Most of these nano-precipitates were identified to be Pd-rich with no detectable Ag and U (Fig. 3.13(c)), which is consistent with the previous work [41]. Further examination in this study indicated a small amount of Ag in one EDS site (Fig. 3.13 (b)).

Figure 3.13(b) shows an example of the Pd-Ag nano-sized particle, which is found in the SiC layer ~5 μm away from the interlayer. The EDS spectrum clearly showed peaks corresponding to Pd and Ag. Among 10 nano-sized precipitates evaluated in this study, only two contained Ag. These Ag-Pd containing nano-precipitates should be further investigated to determine if they are intergranular or intragranular.

The semi-quantitative analysis results of selected nano-sized precipitates are shown in Table 3.3. The Si content in precipitates is higher, whereas C content is lower than in the SiC matrix, indicating the precipitates to be FP silicides. The concentration of FP measured in nano-sized precipitates is much smaller than Si or C. This is because the collected EDS signal emanates mainly from SiC matrix (~100 nm size, comparable to sample thickness) rather than from small size of precipitates (<20 nm).

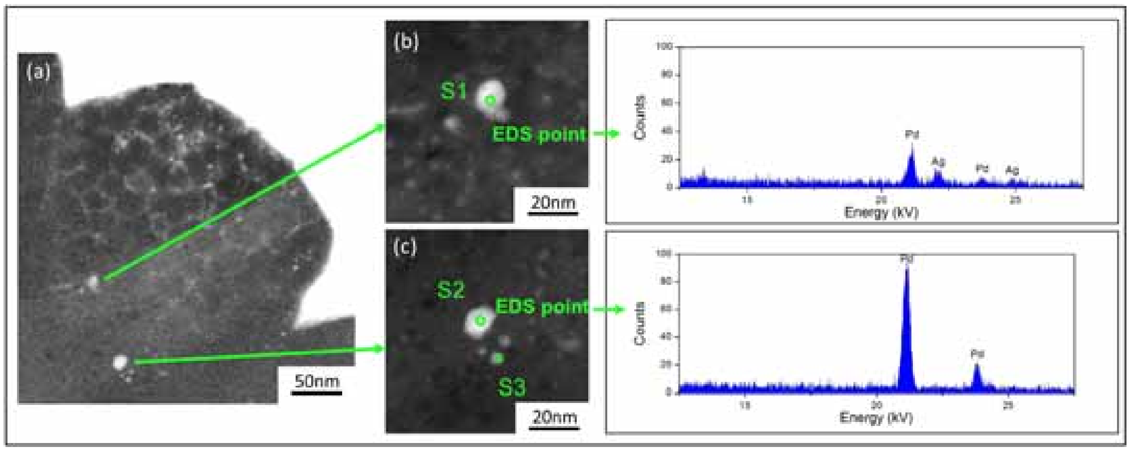

**Figure 3.13** (a) Different types of nano-precipitates identified inside a SiC grain (position1 in Fig. 3.12(a)), (b) EDS spectrum indicates S1 is a Pd-Ag precipitate and (c) EDS spectrum indicates S2 is a Pd-rich precipitate.

**Table 3.3** Quantitative EDS results showing the composition of Pd-Ag (Fig. 3.13(b)) and Pd-rich (Fig. 3-13(c)) nano-sized spherical precipitates.

| **Elements** | **Concentration (at.%)** | | | |
|---|---|---|---|---|
| | **SiC matrix** | **S1** | **S2** | **S3** |
| **C(K)** | 47.14 | 31.30 | 26.21 | 32.37 |
| **Si(K)** | 52.79 | 66.36 | 66.51 | 62.38 |
| **Pd(K)** | 0.00 | 1.88 | 7.04 | 5.25 |

|  |  |  |  |  |
|---|---|---|---|---|
| **U(L)** | 0.07 | 0.46 | 0.06 | 0.00 |

**GB precipitates (Width <5nm) and Triple Junction Precipitates (10 to 20 nm)**

Nano-sized FP at triple junctions and boundaries of SiC grain was revealed by STEM-High Angle Annular Dark Field (ADF) imaging (Fig. 3.14 and Fig. 3.15). These triple junction precipitates are connected by hair-line shaped GB precipitates. In the previous study [41], these intergranular precipitates were found to be either Pd-rich (identified up to 4μm from SiC-IPyC interlayer) or Ag-rich (up to 0.5μm from the interlayer). This work confirmed the results of the previous study by analyzing more areas.

Pd-rich intergranular precipitates were identified up to 5 μm from SiC-IPyC interlayer as shown in Fig. 3.14. Quantitative results in Table 3.4 suggest the Pd-rich triple junction precipitates to be Pd silicides with no detectable U or Ag. Variation in Pd concentration may be influenced by the matrix signals, the extent of which depends on different precipitates' sizes.

Ag-rich intergranular precipitates were identified up to 1.5 μm from SiC-IPyC interlayer (Fig. 3.15) providing evidence of Ag can transport along SiC grain boundaries. EDS spectrum shows that no U or Pd exist inside the Ag-rich precipitates, but a small amount of Cd was identified.

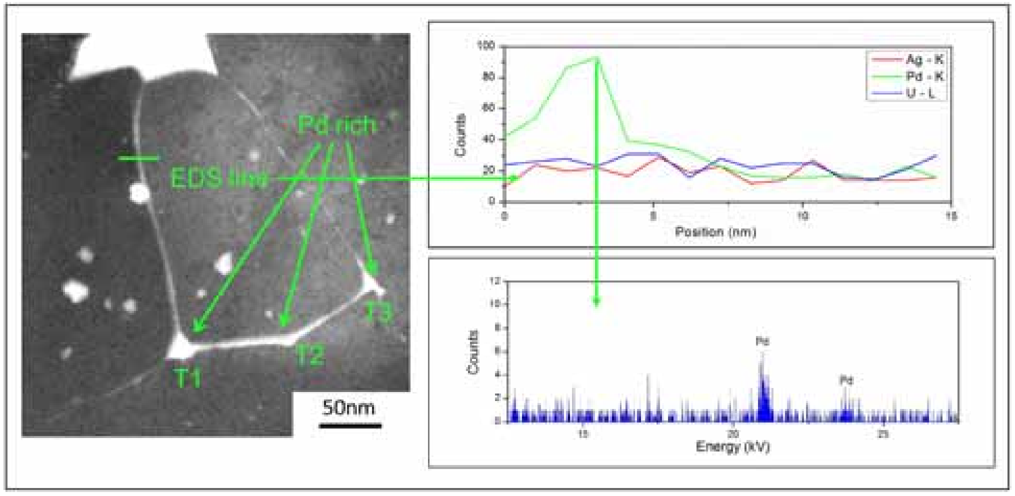

**Figure 3.14** High magnification image of position.2 in Fig. 3.12(a), showing Pd-rich GB precipitates and triple junction precipitates.

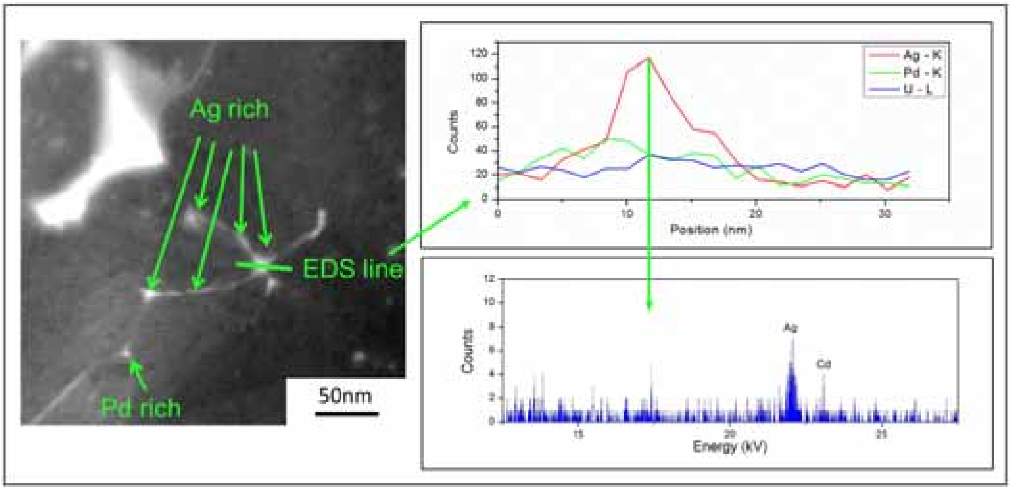

**Figure 3.15** Ag-rich GB and triple junction precipitates in SiC layer of sample 6a, ~1.5 um from SiC-IPyC interlayer (position 1 in Fig. 3.11 (c)).

**Table 3.4** Quantitative EDS results showing the composition of different three Pd-rich triple junction precipitates (T1,T2,T3) (shown in Fig.3.4)

| Elements | Concentration (at.%) | | | |
|---|---|---|---|---|
| | SiC matrix | T1 | T2 | T3 |
| **C(K)** | 47.14 | 41.13 | 36.0 | 33.43 |
| **Si(K)** | 52.79 | 51.40 | 58.98 | 55.75 |
| **Pd(K)** | 0.00 | 7.47 | 4.83 | 10.77 |
| **U(L)** | 0.07 | 0.00 | 0.19 | 0.05 |

### *3.3.3 Possible Mechanism of Ag Transport in Neutron Irradiated TRISO Fuel Particle*

In this study, Ag was found in SiC GBs and triple junctions up to 1.5 µm from the SiC-IPyC interlayer, providing direct evidence of Ag GB diffusion. Compared with Pd rich GBs and triple junctions, which were identified up to 5µm in SiC layer from SiC-IPyC interlayer, the intergranular Ag was identified within a shorter range. This may imply that Ag GB transport is slower than Pd. However, more GB precipitates need to be examined to confirm this hypothesis. It is worth noting that in this study, no Pd was identified in Ag-rich grain boundaries and triple junctions and no Ag was identified inside the micron- sized Pd-U-Si precipitates. This may suggests that the Pd assisted Ag transport through "mobile Pd- silicide nodules" as proposed in [67] and [69] is not likely to be the main mechanism for Ag GB transport. However, it should be noted that atomic migration along the grain boundaries, below the STEM and EDS detection limits, is possible and likely. From this study, it seems that Pd is not required for Ag intergranular transport. The single instance where an Ag-Pd nano-sized precipitate was found inside the SiC grains suggests a possible Pd-assisted intragranular transport mechanism for Ag. Similar to the intragranular Pd precipitates, Ag-Pd intragranular precipitates were not observed in the surrogate experiment [69], indicating a possible relation with radiation effects. Further high-resolution STEM work is needed to investigate the intergranular Ag-Pd precipitate formation. Small amounts of Cd were also seen in the Ag-rich GB precipitates and triple junction precipitates, which suggest that it can transport with Ag by an intergranular mechanism.

### *3.4 Summary of Experimental Work in the Project*

The effects of radiation damage in SiC on diffusion of Ag have been studied with the goal of advancing the understanding of the transport of Ag fission product through the SiC diffusion barrier layer in TRISO fuel particles.

Polycrystalline 3C-SiC and single crystal 4H-SiC were irradiated with 3.15MeV $C^{2+}$, followed by Ag ion implantation with 400KeV Ag ions. The samples were annealed at 1500°C, 1535°C, and 1569°C for durations of up to 20 hours, followed by analysis of Ag distribution profile by SIMS analysis. For 3C-SiC polycrystalline material, the damage introduced by carbon ion irradiation significantly enhanced the diffusion coefficient of Ag as compared to the unirradiated samples, with the difference decreasing with increasing temperature (likely due to defect annealing). The diffusion of Ag in unirradiated samples followed the expected Arrhenius law, whereas for the irradiated samples a nearly 'flat-line' behavior was observed and was speculated to stem from the counteracting effects of temperature and defect annealing. The Ag diffusion coefficient was $(1.8\text{-}7.3)\times10^{-17}\text{m}^2/\text{s}$ for ion irradiated 3C-SiC, and $(5.9\text{-}8.8)\times10^{-18}\text{m}^2/\text{s}$ for unirradiated 3C-SiC. The $C^{2+}$ irradiated 4H-SiC single crystal, on the other hand, showed no visible Ag diffusion due to slow lattice diffusion (even under irradiation conditions). The increased effective diffusion coefficient in 3C-SiC was attributed to enhanced GB diffusion in the irradiated region.

Carbon irradiation experiment provided strong support for the hypothesis that ion radiation can significantly enhance Ag diffusion in polycrystalline SiC. However, the observed enhancement in diffusion coefficient in itself could not account for the integral release measurements ($(1.5\text{-}35.9)\times10^{-16}\text{m}^2/\text{s}$ at 1500°C). In addition to irradiation, the release of Ag can be affected by many other factors, such as the presence of nanocracks and voids [27, 70, 71], change in the microstructure (including degradation) of SiC [72, 73], the effect of other fission products/impurities [42, 74-77], and possibly combined effects of these factors with irradiation.

The work also represents one of first few studies on high resolution TEM/EDS examination of fission product in TRISO fuel after in-pile neutron irradiation testing. Previous PIE study [41] has illustrated the potential of STEM-EDS method to identify Ag at the SiC- IPyC interlayer in a neutron irradiated TRISO fuel particle during post-irradiation examination. In the PIE study presented in this section, we further examined FP precipitates inside SiC layer (0.5μm to 5μm from the interlayer), along with a quantitative assessment of size, shape, preferential location, and composition of those FP precipitates.

Ag was found in SiC grain boundaries and triple junctions up to 1.5μm from the SiC-IPyC interlayer, providing direct evidence of Ag GB diffusion. No Pd was found in those nano-sized Ag GB and triple junction precipitates, which suggests that Pd may not be required for Ag GB transport. The co-existence of Cd with Ag in triple points reported previously [41] was confirmed by the present study. The presence of Pd rich nano-sized intragranular precipitates was further investigated. In one instance an Ag-Pd nano-sized precipitate was found inside the SiC grains, which suggests a possible Pd-assisted intragranular transport mechanism for Ag. Further high-resolution STEM work is needed to confirm the intergranular Ag-Pd precipitate formation. Nano-sized precipitates were not observed in the surrogate Pd/Ag-SiC diffusion experiments [69, 75], indicating that the precipitates are associated with neutron radiation effects.

# 4 Co-incorporation of Ag with Other Elements

We have considered the possibility that solubility of Ag in SiC could be increased if Ag was co-incorporated with other species. To test this hypothesis, we have performed *ab initio* calculations based on the Density Functional Theory of formation energies of defects comprised of Ag bound to iodine or oxygen. We found that for crystalline SiC, Ag co-incorporation with I or O into SiC is not energetically favorable. The results have been published in (*Londono-Hurtado et al. J. Nucl. Mater. 2013*) and are summarized in Appendix A.

# 5 Atomistic simulations of Ag diffusion

## *5.1 Ag Diffusion along High Energy Grain Boundary*

Despite the efforts to understand the Ag release through SiC in past decades, the release mechanism yet remains largely unknown. Recently, a number of studies have provided strong evidence supporting the hypothesis that GB diffusion is a dominant pathway for the Ag transport in high-quality CVD-SiC. For example, Friedland *et al.* [5, 6] and Gerczak *et al.* [78] recently carried out Ag implantation in a single crystal SiC (sc-SiC) and a polycrystalline CVD-SiC (pc-SiC) at 1300°C. The Ag diffusion was only observed in pc-SiC, but not in the sc-SiC. Lopez-Honorato *et al.* [79, 80] designed a diffusion couple model where a layer of silver was trapped between two stoichiometric SiC layers then heat treated up to 1500°C. Significant Ag diffusion into SiC was observed in the samples and transmission electron microscopy images confirmed Ag particles along the columnar GB structure. Most recently, a study by Van Rooyn *et al.* [41] used scanning transmission electron microscopy-energy dispersive X-ray spectroscopy to observe Ag in both GBs and the triple junctions from irradiated TRISO coated particles.

The above considerations suggest that GB diffusion is a preferred mechanism for Ag transport, yet it remains unclear which GBs transport the Ag and how quickly, how this transport occurs at the atomistic level, and if there is any coupling to irradiation effects. To better elucidate the fundamentals of Ag diffusion in SiC, atomistic simulation studies have modeled Ag diffusivity through bulk [16], ∑3-GBs [45], and ∑5-GBs [81] of 3C-SiC. The diffusion coefficients ($D$) were predicted to be $D_{\mathrm{Bulk}}= 3.9\times10^{-29}$ $\mathrm{m^2s^{-1}}$ at 1600°C in bulk SiC (the fastest mechanism being Ag interstitials, where the Ag residues on a site tetragonally coordinated by four Carbon atoms), $D_{\sum3\text{-GB}} = 3.7\times10^{-18}$ $\mathrm{m^2s^{-1}}$ at 1600°C in ∑3-GBs (for the fastest direction, which was along the $[0\bar{1}1]$), and $D_{\sum5\text{-GB}} = 0.22 - 10.5\times10^{-18}$ $\mathrm{m^2s^{-1}}$ at 1227°C in the ∑5 (120) tilt GB. These results strongly suggest that the bulk diffusion cannot account for the experimentally observed release rates of Ag from TRISO particles, which are summarized in Table 5.2. Additionally, the higher $D$ values found for GBs provide further evidence that GB diffusion is a dominant mechanism responsible for Ag release.

Despite the higher $D$ values predicted for select GBs compared to bulk, the predicted $D$ in ∑3 and ∑5 GBs are still from one to three orders of magnitude lower than the lowest values measured from integral release measurement [37, 48, 49, 61, 62, 82, 83] at similar temperatures, and therefore they cannot be simply invoked as the explanation for the observed diffusion. A major missing part of present understanding is that high-energy GBs (HEGBs) have not yet been modeled or measured explicitly, but are expected to play a significant role in Ag transportation in pc-SiC. The HEGBs are often highly disordered structures and represent > 40% of GBs in TRISO prototype materials [78, 84]. The high fraction of HEGBs allow them to provide a percolating path for Ag transportation, and HEGBs are the one of few GB types that are present in high enough concentration to form a percolating path [45]. More importantly, it is often found that disordered (amorphous) materials provide a faster transportation pathway for extrinsic defects [85-87] compared to crystalline materials. Therefore, we expect HEGBs are the most likely GB type to dominate Ag transport, and the Ag diffusion coefficient in HEGBs to be faster than those in other GBs or bulk, which possibly bridges the remaining discrepancies with integral release measurements. In this work, we used an *ab initio* based stochastic modeling approach to predict the Ag diffusion coefficient in HEGBs.

### *5.1.1 Methods*

The HEGB is modeled as an amorphous SiC (a-SiC) region, as the local environments in HEGBs of covalent materials are known to be similar to amorphous phases [88, 89] and a bulk amorphous phase is computationally more tractable to model than a full GB structure. We prepared an a-SiC structure from classical molecular dynamics with the Tersoff interatomic potential using the melt-quench method [90]. A supercell containing 128 atoms with a perfect stoichiometry (but allowing antisite and coordination defects) was arbitrary cut out from the bulk, then fully relaxed using Density Functional Theory (DFT) with periodic boundary conditions and under constant zero pressure and zero K temperature. The resulting cell vectors were [11.21, 0.17, -0.37; 0.17, 11.57, 0.15; -0.38, -0.15, 11.03] (non-cubic) and the final density of the cell was 2.98 g/cm$^3$, which is comparable with the simulated density by Tersoff potential (3.057 and 2.896 g/cm$^3$) in Ref [90], and is, as expected, lower than the DFT calculated sc-SiC density, 3.18 g/cm$^3$. It is true that some features of real amorphous structures may depend on cooling and processing conditions, but we make the assumption that the present method captures local environments adequately enough to approximate the diffusion rates of Ag through an amorphous-like GB region.

The Vienna Ab-Initio Simulation Package (VASP) [91-94], an *ab initio* DFT code, and projector-augmented plane-wave (PAW) method [66, 95] were used to relax the final a-SiC and to explore Ag diffusion in the a-SiC structure. The exchange-correlation was treated in the Generalized Gradient Approximation (GGA), as parameterized by Perdew, Burke, and Ernzerhof (PBE) [96]. A single Γ-point *k*-point mesh was used to sample reciprocal space. While this is not highly converged it was necessary to use few *k*-points to enable the large number of required calculations. The Γ-point *k*-point mesh had an error about 15 meV/atom for 128 atom cell compared to 2×2×2 *k*-point mesh, which is expected to be well-converged. Tests on at least five barriers showed that error in energy barrier with respect to *k*-points for a Γ-point vs. 2×2×2 *k*-point mesh is within an acceptable error range of 200 meV/Ag (this corresponds to about a factor of 5× error at 1500K). The energy cut-off was set at 450eV. The convergence for the electron self-consistency cycle was set to $10^{-4}$eV. For the formation energy ($\Delta E_f$) of defects, we use the following expression [97] : $\Delta E_f = E_{def} - E_{undef} + \Sigma_I \Delta n_I \mu_I$. The $E_{def}$ and $E_{undef}$ are energies of the defected and the undefected cell, $\Delta n_I$ is the change in the number of the atomic species $I$ in the defected cell from the number of same species in the undefected cell, and $\mu_I$ is the chemical potential of atomic species $I$ relative to its reference energy. The reference states for Si and C are taken as the bulk Si and C VASP energies (which are referenced to their pseudopotential reference energies) in their groundstate structures (diamond lattice for Si and graphite for C). Throughout this study, Si-rich condition chemical potentials are used for silicon and carbon ($\mu_{Si}$ = -5.44 and $\mu_C$ = -9.65 eV) for consistency. The *ab initio* formation energy of bulk solid phase Ag metal ($\mu_{Ag}$ = -2.82eV) is set to be the chemical potential for Ag. No charged supercells or explicitly charged defects were considered in this study. We believe this approximation is a reasonable as the neutral state for Ag interstitials (which are our focus in this study, as discussed in Section 5.1.2) is stable charge state for Ag in n-type crystalline SiC, as predicted by Shrader, *et al* [16]. Furthermore, even if the Ag were charged, at least some of the impact of the changes in energy as compared to the neutral state would cancel between initial and activated states during the migration barrier calculation, further reducing its impact on the predicted value of *D*.

To obtain diffusion pathways and the corresponding minimum energy path, the climbing nudged elastic band (CNEB) method was employed. Typically, three images were used in the CNEB calculations. The initial estimate for the transition state was set as a center image, and additional images are linearly interpolated between Ag site and the center image. The transition states are first estimated by putting the Ag at the centroid of the sites consisting of the initial and final Ag sites and all Si and C sites within 1.89 Å (the nearest neighbor bond length of SiC) (this approach is similar to that use in Ref. [98]). Calculations starting from this initial Ag position converged into a stable transition state in more than 80% of cases during the CNEB optimization. However, in the remaining cases the initial Ag position was too close to a Si or C atom and the CNEB calculation did not converge. For these cases a new candidate activated state was estimated by using a two step process. First, a linearly interpolated image halfway between the initial and final Ag configurations is determined. Then, if in this image the Ag and any other atom were less than 1.45 Å apart, the Ag and this other atom were moved by 1.0 Å each in opposite directions to assure their separation. The displacement was done in the plane normal to the line connecting the initial and final Ag states. Displacements were attempted along lines every 45 degrees within the normal plane until all interatomic distances in the candidate activate state were greater than or equal to 1.42 Å (which is 75% of a SiC nearest-neighbor bonding length). The calculations starting from these candidate activated states showed robust convergence.

In order to represent Ag migration barriers independently of the initial and final state energies we use the Kinetically Resolved Activation (KRA) Barrier [99, 100] to represent the barrier value. In the KRA the saddle point migration energy ($E_m^{saddle}$) is determined by the energies of the initial and final sites ($E_f^{initial}$ and $E_f^{final}$) and KRA energy ($E_{KRA}$), which is used to as in Equation 5.1 and illustrated in Fig. 5.1. The KRA approach provides a compact way to represent the migration energy of a hop in either a forward or backward direction. Furthermore the approach defines $E_{KRA}$ so as to remove the contributions of the initial and final energy to $E_m^{saddle}$, and $E_{KRA}$ is therefore likely to vary less and be easier to represent than $E_m^{saddle}$.

**Equation 5.1**

$$E_{KRA} = E_m^{saddle} - (E_f^{initial} + E_f^{final}) / 2$$

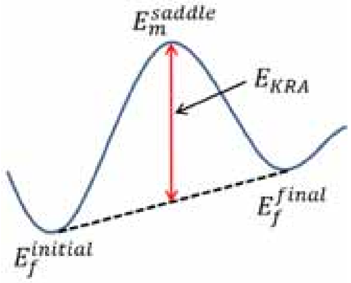

**Figure 5.1** A schematic representation of the Kinetically Resolved Activation (KRA) barrier.

In order to explore the diffusion in a disordered lattice we use the effective medium approximation (EMA) [101], which has been applied previously to model diffusion in an amorphous system [102, 103]. In this model, a single Ag atom diffuses under the assumption that Ag atoms do not interact with each other while diffusing along HEGB. The main idea of this scheme is to replace the actual system jump frequencies by an effective energy surface with an equal frequency distribution (fitted to DFT calculations), but stochastically sampled. The effective energy surface (effective medium) can be mapped out by creating Ag interstitial sites (lattices), and calculating Ag interstitial formation energies (energy assigned to lattice) and the KRA barriers (transition state energies relative to lattices, which will determine the jump frequency). These parameters are then stochastically sampled until the distributions (μ and σ) in the EMA model are within the standard error from DFT calculations (Table 5.2).

In the EMA model used in this study, the connectivity between interstitial sites is simulated by adopting the randomly blocked sites approach [104] as depicted in Fig. 5.2(a). A virtual face centered cubic (*f.c.c.*) lattice was used as an effective medium where each lattice site represents a position of an Ag interstitial in a locally stable state and the number of neighbors on the lattice represent number of nearby minima for Ag interstitial that are connected to the original minimum by a single hop. Then the lattice sites of *f.c.c* are randomly blocked (about 63.33% of sites) until the distribution of remaining nearest-neighbor sites reaches the mean (μ) and standard deviation (σ) of the distribution we obtained from fitting to DFT values. The blocked lattices are marked as inaccessible and not used in the simulation. The hop distance is taken from the distance between Ag interstitial, sampled from DFT calculations (Section 5.1.2). Since there was no significant correlation between the migration barriers and Ag interstitial site distances found in the calculations (Section 5.1.2) we assumed that the site energies and the KRA barriers can be chosen independently of site distances. Subsequently each site (e.g., A, B, and C in Fig. 5.2) was assigned a random site energy that is sampled from a fitted distribution of the formation energy (Section 5.1.2). The $E_{KRA}$ (e.g., $E_{KRA}^{*}$ and $E_{KRA}^{**}$ in Fig. 5.2(b)) is also sampled from a fitted distribution of DFT barrier values (Section 5.1.2). Now the sampled site and $E_{KRA}$ energies are used to determine the saddle point migration energies (e.g., $E_{A\leftrightarrow B}^{saddle}$ and $E_{B\leftrightarrow C}^{saddle}$) and hop barriers for KMC.

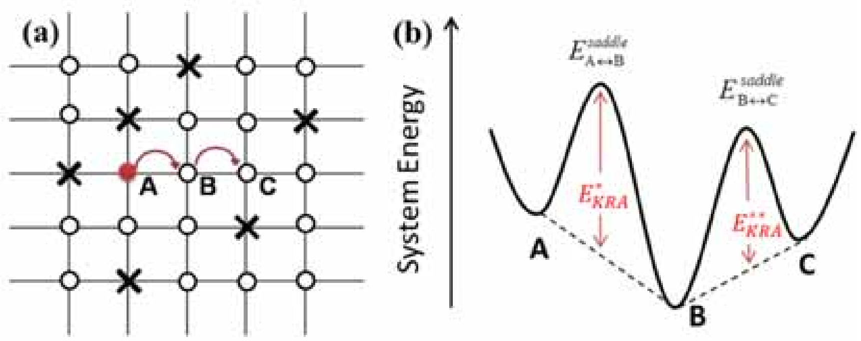
(a)
A
B
C
(b)
System Energy
$E_{A\leftrightarrow B}^{saddle}$
$E_{B\leftrightarrow C}^{saddle}$
$E_{KRA}^{*}$
$E_{KRA}^{**}$
A
B
C

**Figure 5.2** (a) A schematic of the randomly blocked sites model, where cross represents blocked (inaccessible) sites and open circle represents open (accessible) sites. (b) A schematic of the combined scheme of random site energies and random barriers (with KRA) models used to construct the energy landscape when the system evolves from A to B to C. See text for details.

The kinetic Monte Carlo (kMC) method was employed to time-evolve the system and observe Ag interstitial diffusion. The simulation was performed on a virtual lattice, using parameters fitted to DFT calculations as described above. Experimentally measured GB dimensions were used for the simulation cell of the virtual lattices (which we will refer to as a virtual HEGB). The virtual HEGB structure should match a typical grain size and HEGB width. With this goal in mind the HEGB structure is set to be a rectangular plate with side of approximately 980nm (~1 μm) and thickness of 1 nm (z-direction) [78, 84] in this work. Owing to the low formation energies of Ag defects in HEGB (Section 5.1.2), Ag is assumed to stay within the assumed constant finite thickness of the GBs. Therefore, PBC were applied on the virtual lattice except along the z-direction. The Bortz-Kalos-Liebowitz [105] algorithm was used in the kMC model. The hopping rates (Γ) for Ag atoms are given by the transition state theory as $\Gamma = \omega \exp(-E_A/k_B T)$, where $\omega$ is attempt frequency and $E_A$ is the migration barrier of the hop. The $\omega$ value is assumed to be equal to a typical phonon frequency for a heavy atom, which we take as $1.0\times10^{-12} s^{-1}$. The activation barrier ($E_A$) for each hop is estimated by the formalism of $E_{KRA}$ energy associated with energies of two equilibrium sites. In each step of kMC, Ag migrates from the current lattice site ($i$) to one of $Z$ neighbor lattices. The probability for Ag to migrate from lattice site $i$ to $j$ is determined stochastically by $P_{ij} = \Gamma_{ij} / \Sigma_{n=1}^{Z} \Gamma_{in}$, where $j$ is a positive integer from an interval $(0,Z]$. Next, the system is updated to the $j$ state with an increment of time forward, $\Delta t$, given by $\Delta t = \left(\sum_{n=1}^{Z} \Gamma_{ij}\right)^{-1} \ln(u^{-1})$), where $u$ is a uniform random number between 0 and 1. The Ag diffusion coefficient is determined by the Einstein relation, $D_{Ag} = < r^2_{Ag}(t) > / 2dt$, from the calculated mean square displacement as a function of time [106], where $d$ is the dimensionality of the system in which Ag diffuses (here $d = 2$), $t$ is time, and $< r^2_{Ag}(t) >$ is the mean square displacement of Ag as a function of time. We evaluate the average using the multiple time origin method [107]. For the quasi-two dimension HEGB of interest, $< r^2_{Ag}(t) > = 1/N_t \, [\, \Sigma_{j=1}^{N_t} [[\, r_x(o_{j+(N/2)}) - r_x(o_j)]^2 + [r_y(o_{j+(N/2)}) - r_y(o_j)\,]^2]$ where $N_t$ is the number of time origins, and the quantity $r_x(o_{j+(N/2)}) - r_x(o_j)$ is the displacement along the x-direction over the time span between time origin $o_j$ and $o_{j+(N/2)}$ (analogous quantities for the y-direction). The diffusion along the z-direction is negligible within the geometry of HEGB (1nm in thickness with no PBC vs. effectively infinite diffusion in the x-y direction due to PBCs) and therefore is not considered for simplicity. For statistical reliability we choose the number of time origins $N_t$ to be half the total number of time steps, $N/2$. For the given $N$ time-steps, $< r^2_{Ag}(t) >$ is computed for $N/2$ possible time origins between $j$ and $(j + N/2)$ time steps. The kMC simulation is allowed explore the system across multiple periodic boundaries along $x$ and $y$ directions. The converged diffusion coefficient values were extrapolated from a linear fit to a plot of $< r^2_{Ag}(t) >$ vs. $t$. Each simulation was typically performed for 10 billion kMC steps to obtain a well-converged fit.

### *5.1.2 DFT Calculations of Ag Energetics*

In order to understand the transportation behavior of Ag in the a-SiC, it is important to determine which Ag defect is stable and will contribute to the diffusion. To determine the dominant Ag diffusion species in a-SiC, first the formation energies of the point defects (vacancies, Ag substitutionals on Si and C lattices, and Ag interstitials) were studied. These defects were sampled over a wide range of local environments and the results are summarized in

Table 5.1. Note that values for a-SiC (part (b)) of Table 1 are the average values over many defect sites, along with a standard deviation to represent the spread in values. The sampled set includes 30 vacancies, 30 substitutionals, and 153 interstitials, where this latter set is quite comprehensive and discussed in Section 5.1.2. All the defect types in a-SiC, on average, had lower $E_f$ than those in the single crystal SiC (sc-SiC). Particularly, Ag interstitials showed a dramatic difference in formation energy in a-SiC compared to sc-SiC. For most of the interstitial sites, Ag interstitials in a-SiC had 7-8eV lower $E_f$ than the most stable Ag interstitial (10.49 eV [16]) in sc-SiC (a tetrahedral site surrounded by four carbons), although a few interstitial sites in the a-SiC had energies as high or higher than $E_f$ in sc-SiC. Some of the Ag interstitial formation energies were near zero or negative in energy, i.e. the Ag was more stable in the a-SiC than as bulk metallic Ag. This result suggests that Ag will segregate strongly to HEGBs, consistent with what has been found in previous GB studies [45].

**Table 5.1** Formation energies of neutral defects (*Vac* = Vacancy, *Sub* = Substitutional, and *Int* = Interstitial) in (a) sc-SiC [16] and in (b) a-SiC. In part (b), the average (AVG) and standard deviation (STD) of defect formation energies are listed. Energies are given in eV and are for Si-rich conditions and referenced to Ag metal.

| **(a)sc-SiC** | ***Vac*** | | ***Ag Sub*** | | ***Ag Int*** | |
|---|---|---|---|---|---|---|
| | C site | Si site | C site | Si site | TC[a] | TSi [b] |
| | 4.19 | 7.63 | 7.39 | 6.60 | 10.49 | 11.38 |
| **(b) a-SiC** | ***Vac*** | | ***Sub*** | | ***Int*** | |
| | C site | Si site | C site | Si site | - | |
| AVG | -0.23 | 2.34 | 0.96 | 2.71 | 3.50 | |
| STD | 1.24 | 1.38 | 1.18 | 1.01 | 1.91 | |

[a] Tetragonally coordinated between four C atoms

[b] Tetragonally coordinated between four Si atoms

Based on the stability of Ag defects, the dominant diffusion mechanism in the a-SiC can be constrained by the following the arguments. We have considered vacancy-mediated substitutional diffusion and interstitial diffusion mechanisms. First, a substitutional diffusion mechanism is considered, as the formation energy of vacancies and substitutionals are energetically more favorable than interstitial in general. However, substitutional diffusion requires a migration of a vacancy [16], and this process is even less favorable in the amorphous system than the crystalline. We have found that to migrate a vacancy around Ag in a-SiC has a barrier typically in the range of 4-7eV, and migration of a vacancy in a-SiC without Ag has an energy barrier of 3.0-4.5 eV from test on five barriers for each cases. These values are both quite high, and will lead to slow vacancy mediated Ag diffusion. Secondly, an interstitial diffusion mechanism is considered. Table 5.1 shows that that the average formation energy of Ag interstitials are > 2 eV more than Ag substitutionals so it might be expected that Ag in HEGB exists primarily as substitutionals, not interstitials. However, in the most stable substitutional and interstitial sites we studied, Ag formation energies were -0.84 and -0.59 eV, respectively, which are about equal. This result suggests that for the most stable cases, which might be expected to dominate the behavior of small amounts of Ag, both substitutional and interstitial Ag may be approximately equally stable. The migration barriers, however, were typically around 1-3 eV for Ag interstitials, which is considerably lower than the typical barriers for vacancies. Given these energy trends, Ag transportation via interstitial mechanism is expected to be dominant mechanism and is the mechanism which we focus on in this paper. We note that the above qualitative argument is insufficient to rule out the possibility of a fast vacancy mediated path, and such transport mechanisms are a useful topic for further study.

To model Ag interstitial diffusion in a-SiC, the energy landscape of Ag interstitials was first investigated. In an amorphous material, locating extrinsic interstitial defect sites is challenging because of lack of long-range order. Many approaches to identify interstitial sites have been proposed in other amorphous systems [108-111]. To achieve a complete list of possible Ag interstitial sites, we have taken a brute force but comprehensive approach to identify possible sites. Specifically, we identified all existing interstitial sites by gridding our entire supercell with a fine uniform grid and relaxing a Ag interstitial at every grid point in the cell. A similar approach was used to study Li diffusion in amorphous oxides [111]. When necessary, gridding points were shifted so that they were at least 1.5 Å from any adjacent host atoms to avoid a numerical instability. The ideal grid density was tested for ¼ of the simulation cell to verify a maximum grid size that could still to capture all existing minima. It was determined that a grid size of 1 Å on a side was adequate to find all the interstitials.

For the a-SiC sample, we investigated $11^3$ grid points and identified 247 apparently distinct Ag interstitial sites. However, many of these sites were found to be close to each other, both energetically and geometrically. These similar sites may fail to relax to a single site due to the fact that the calculations are at zero temperature and have a complex energy landscape with many weakly separated local minima. At finite temperature, on the other hand, the Ag will likely thermalize into just one effective site, even if a number of very nearby ones are found at zero temperature. Therefore the hierarchical clustering approach [110] was employed to group the close configurations into clusters while having the lowest energy state represent the cluster. All Ag within a cut-off distance were grouped together. The cut-off distance was set to be 0.5 Å, which is about 1/4 of the shortest bonding length between Ag and host atom for a bulk interstitial (the bonding length of Ag and C in the bulk sc-SiC interstitial position is 2.076 Å). Thus we are making the approximation that sites within this cut-off distance are essentially equivalent. The following observations support the idea that the clustering will not have a significant effect on the Ag interstitial diffusion at the temperature range of the interest (1200-1600°C). Firstly, the energy variation within a cluster was typically found to be no larger than 50 meV, 100 meV at most. Also the migration barriers between configurations in clusters were found to be less than 200 meV in all the 10 cases checked. These results suggests that within a cluster the Ag will easily move between sites at high temperatures, which will cause the cluster to behave like a single effective local minimum for Ag.

The distribution of formation energies is shown in Fig. 5.3 (a). The formation energies of Ag interstitials in a-SiC had an average value of 3.50 eV and this value is ~7 eV more stable than the most stable Ag interstitial in sc-SiC (10.49eV [16]). The values range from -0.59 to 8.21 eV, with a standard deviation of 1.91 eV. The Ag, which is an impurity with a relatively larger size than those studied in similar amorphous systems [108-110, 112-115], turned out to be highly stable as interstitial in a-SiC. Figure 5.3 (b) shows the Ag distance from one interstitial site to the nearest neighbor site. The figure shows that 95% of interstitial sites have a nearest-neighbor interstitial site within 2.0Å and 100% within 2.75Å.

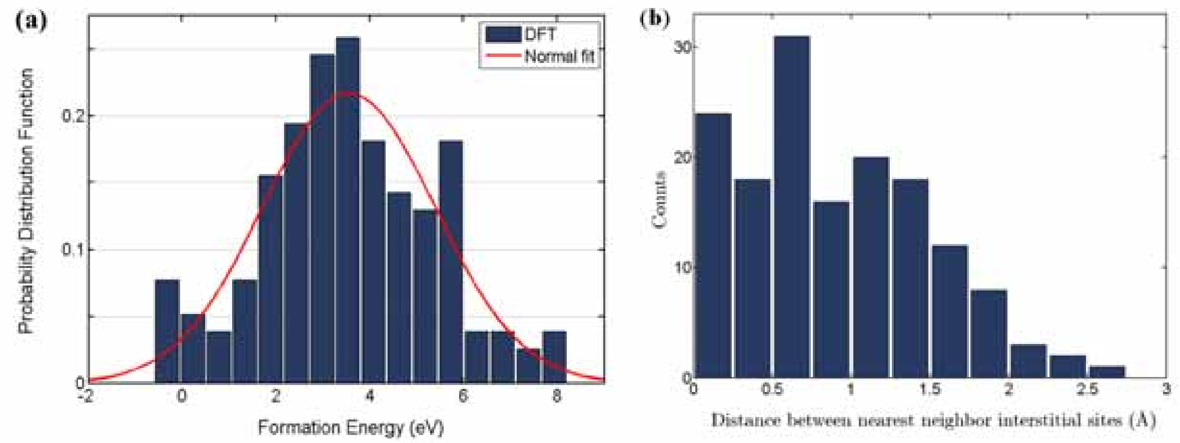

**Figure 5.3** Gridding approach results after clustering (a) Distribution of formation energy with a bin size of 0.5 eV. Comparison to Gaussian distribution parameterized by mean and standard deviation from gridding method. (b) Distribution of Nearest-Neighbor cluster distance from one cluster to the other with a bin size of 0.5 Å.

Migration barriers that are needed for a diffusion analysis of Ag in a-SiC are calculated using the CNEB. A number of migration barrier calculations are performed to achieve a statistically robust dataset. Instead of gathering barrier energies for all possible migrations, we focused on elucidating the systematic features of barriers as the sampling size increase. Fifty pairs of minima, approximately 1/6 of the total number of transition states, are randomly sampled. The distribution of migration barriers as a function of the relative Ag distance is shown in Fig. 5.4(a). The energy barrier for a hop is dependent on the energy state of two endpoints and thus two values (barrier from low energy state to high energy state (L-H) and vice versa (H-L)) are plotted for each reaction. It is observed that there is no correlation between the barrier and the Ag hop distance. However, most of the CNEB calculations between sites with distance larger than 2.5Å failed to discover a single saddle point (not shown in Fig. 5.4). They either showed a convergence failure, likely due to significant difference in local ordering that requires movement of multiple atoms, or found two saddle points, which is not a single hop and involves another minimum between them. Therefore 2.5 Å was used as a cutoff distance to determine the number of neighbor interstitial sites (*Z*) from an interstitial site. The *Z* distribution and the normal fit to *Z* are shown in Fig. 5.5. On average, interstitial sites had *Z*=4.4, which represents the average number of sites to which Ag can migrate by a single hop.

The $E_{KRA}$ values as shown in Fig. 5.4(b) are distributed normally in the range of 0.4-2.2 eV. Table 5.2 gives the results of fitted normal distributions for Ag interstitial sites for both coordination and energetics. With the KRA formalism and values in Table 5.2 and Equation 5.1 the number of possible hops and their migration energies associated with leaving a given site can be sampled. Therefore, now we can stochastically generate the Ag atom hop energetics that are needed at each kMC step.

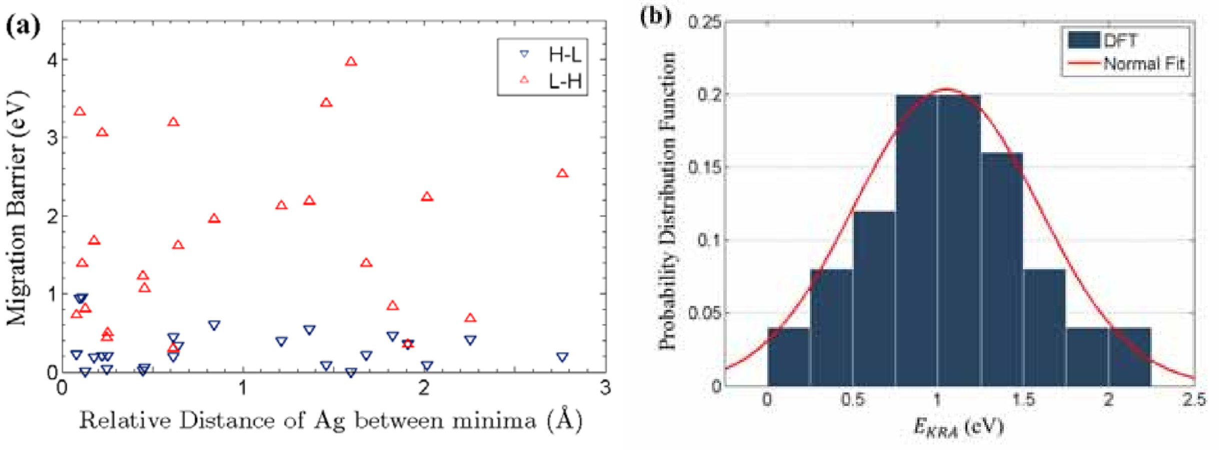

**Figure 5.4** Result of migration barrier calculations for Ag in a-SiC: (a) Energy barriers between two minima plotted as a function of relative distance of minimum. The barrier from high to low and low to high energy state is marked with "H-L" and "L-H" respectively. (b) A histogram of $E_{KRA}$ values from calculated migration barriers in (a).

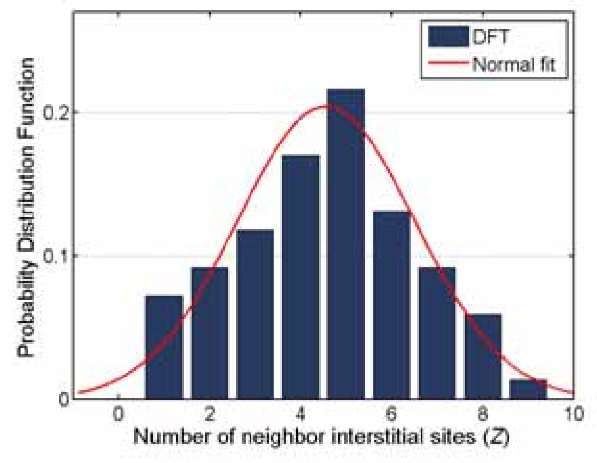

**Figure 5.5** A histogram of the number of neighbor interstitial sites (*Z*) from an interstitial site within the cutoff distance of 2.5 Å of relative Ag positions. A normal distribution fit to the data is shown with red line.

**Table 5.2** Mean (μ) and Standard deviation (σ) of diffusion related parameters from *ab initio* calculation. All three parameters were fitted to normal distributions (FIG. 5.3(a), FIG. 5.4(b), and Fig. 5.5). SE$\mu$ and SE$\sigma$ are the standard errors of mean and standard deviation (($SE_{\mu} = \sigma / \sqrt{n}$, and $SE_{\sigma} \approx \sigma / \sqrt{2(n-1)}$ [116])) from the distribution.

| | μ | σ | SE$\mu$ | SE$\sigma$ |
|---|---|---|---|---|
| **$E_f$ (eV)** | 3.50 | 1.91 | 0.15 | 0.11 |
| **$E_{KRA}$ (eV)** | 1.05 | 0.54 | 0.08 | 0.05 |
| **$Z$ (sites)** | 4.4 | 2.1 | 0.17 | 0.12 |

### *5.1.3 Kinetic Monte Carlo Model for Ag Diffusion*

With the statistical distributions from Table 5.2 we performed a kMC simulation as described in Section 5.1.1. To be more specific, we first constructed a virtual medium of *f.c.c.* lattice sites where *f.c.c.* sites correspond to Ag interstitial sites. The single Ag hop distance (lattice distance in EMA) is taken as $\sqrt{\overline{h^2}}$ = 2.1 Å, where $h$ is Ag hop distance sampled from DFT calculation, and $\overline{h^2}$ is the mean of $h^2$ for all sampled Ag hops. Then sites are randomly removed (i.e. become inaccessible) until the distribution of number of remaining nearest neighbor sites agrees with the mean and standard deviation of $Z$, sampled from a-SiC (Table 5.2). The formation energies are randomly assigned to remaining sites by sampling from the fitted normal distribution of $E_f$ in Table 5.2. The migration barriers between sites are computed by Equation 5.1, where $E_{KRA}$ is sampled from the normal distribution in Table 5.2. After the Ag interstitial site network has been established, a single Ag is randomly placed on one of the sites and its movement is determined by the rates of migration using kMC.

It is important to carry out the sampling correctly and to generate a realistic energy landscape. We have identified two factors that in general may lead to an unrealistic (or inefficient) sampling and that were adjusted for in our model. First, we considered if there might be a relation between a minimum that has a low number of possible hops, and its surrounding energy landscape. Physically this might correspond to there being a particular tendency for a site far from any others to be unstable and have a low barrier for migration. Since the long time steps (where $\Delta t$ is much larger relative to those of typical steps) are most likely to occur when Ag sits on a site that has small number of neighbors and is the bottom of the potential well, this type of correlation could play a critical role. We found in our *ab initio* calculations that all the minima with low number of nearest neighbors ($Z$=1 or 2) are higher in their energy than energies of neighboring minima. In fact, low $Z$ minima were found to be higher in formation energy than the average of neighboring energy minima by 1-2eV. This correlation implies that Ag atoms are less likely to be found at these meta-stable low $Z$ minima under equilibrium condition of dilute solution. This correlation is included in our model by setting the energy of low $Z$ sites (Z=1 or 2) to 1.5 eV higher than the average energies of their neighboring minima.

Another important consideration related to the possibility of generating an unrealistic energy landscape is the sampling of parameters from tails of Gaussian distributions. Although we have shown that it is a reasonable approach to take parameter distributions as Gaussian, the analysis was based on considering the middle regions of the Gaussian, not the tail regions. However, a significant number of samples from the Gaussian distributions during the kMC runs include many points in the far tail regions of the Gaussians, which may not be representative of the real system. Considering that our actual *ab initio* results are all within two standard deviations from mean value, the sampling is likely accessing many values that are far from the *ab initio* observations. Thus we constrained the minimum and maximum values from sampling to be consistent with those obtained from the *ab initio* calculations. The values are still sampled from the Gaussian distributions (Table 5.2), but values outside those limiting cases seen in the *ab initio* calculations are not used.

It is possible that the diffusion of impurities in a disordered material can be different in different regions. To account for possible spatial deviation of the distribution parameters, we have explored 1/8 volume fraction of another 128 atom a-SiC test structure (prepared in the same manner as described in Section 5.1.1) with DFT calculations and we discovered 31 interstitial minima. The distribution of formation energies followed normal distribution as well. The formation energies distribution from this new data set followed N(3.24, 2.21) with standard error of mean $SE_\mu$ = 0.40 and standard error of standard deviation $SE_\sigma$ = 0.28, where the original distribution was N(3.50, 1.91). For the $E_{KRA}$, about 1/6 of possible transition states within the sub-region were examined. The $E_{KRA}$ also showed a normal distribution of N(1.14, 0.58) with standard error of mean $SE_\mu$ = 0.15 and standard error of standard deviation $SE_\sigma$ = 0.11, where the original distribution was N(1.05, 0.54). The mean and standard deviation values from the distributions associated with the new structure are within the standard error range (Table 5.2) of those computed for the previous structure. As both variables had distribution parameters within their standard error range, we conclude that the distributions are not statistically distinct. This result suggests that the distributions determined from our first cell are adequately general for modeling the energy landscape for Ag in HEGB.

The typical HEGB dimensions are approximately 1μm×1μm×1nm and we will assume that this is large enough that the Ag diffusivity in a given HEGB is indistinguishable from that which would be obtained from an infinite HEGB, denoted $D_{eff}$. In order to determine $D_{eff}$ we model diffusion in a series of cells each with dimensions of 140nm × 140nm × 1nm, as larger cells were too computationally expensive. To obtain the effective infinite cell diffusivity we calculated the $D_{eff}$ for a number of the 140nm × 140nm × 1nm simulation cells in series. Specifically, $D_{eff}$ is estimated as the harmonic mean of diffusion coefficient in each simulation cell, or $D_{eff} = n / [\Sigma_{i=1}^{n} (D_i)^{-1}]$, where $n$ is the number of sampling ($n$=350) and $D_i$ is the diffusion coefficient from each simulation cell.

Due to the significance of $E_{KRA}$ formalism in our model, it is expected that the largest errors will stem from the $E_{KRA}$ distribution. Although we have shown the sampled $E_{KRA}$ distribution can effectively represent the distribution in a-SiC, the effective diffusivity can be sensitive to the change of $E_{KRA}$ within the standard error range. Hence, here we analyze the impact on $D_{eff}$ of the uncertainty in $E_{KRA}$ by considering two extreme conditions for $E_{KRA}$. We assume that the distribution can be shifted within the standard error range of our computed distribution mean and sigma. The standard errors ($SE_\mu$, $SE_\sigma$) of measured distribution mean ($\mu$) and standard deviation ($\sigma$) were summarized in the Table 5.2. We define the total uncertainty due to $E_{KRA}$ sensitivity by setting mean and standard deviation to result in their extreme values and studying the range of $D$. In other words, for the (a) upper bound of D we set $\mu' = \mu - SE_\mu$ and $\sigma' = \sigma + SE_\sigma$ and for the (b) lower bound of $D$ we set $\mu' = \mu + SE_\mu$ and $\sigma' = \sigma - SE_\sigma$. In the kMC simulation, $D_{eff}$ values are predominantly determined by relatively slow hops with large t, which is due to high migration barrier. More sampling of higher values for $E_{KRA}$ will therefore give lower $D$. The upper bound case samples barrier from distribution with lower mean and smaller spread, which barriers are sampled from left tail of parent Gaussian distribution. For the lower bound $D$, barriers are sampled from a distribution with higher mean and larger spread, which distribution center lies near and above the right tail of the parent Gaussian distribution. The $D_{eff}^{total}$ for cases (a) and (b) are calculated as done for the original $E_{KRA}$ distribution at each temperature, but now using the newly determined $E_{KRA}$ distributions to estimate a lower and upper value and corresponding error range for $D_{eff}^{total}$.

Another potentially significant uncertainty stems from the statistical error in $D$ sampling from kMC modeling. For statistical reliability, $D_{eff}$ values were computed from the harmonic mean of 350 of the 140 nm × 140 nm × 1 nm cells at each temperature. The standard error of $D_{eff}$ ($SE(D_{eff})$) is estimated by the equation proposed by Norris, $SE_N(D_{eff}) = (D_{eff})^2 \times [\sigma_{(1/D_i)} / \sqrt{m-1}]$, where the $\sigma_{(1/D_i)}$ is the standard deviation of the reciprocals of the $D_i$, and $m$ is the number of the sampling [117]. We note that this formula effectively relies on a first-order Taylor expansion which may not provide an accurate estimate for our values. We therefore also estimate a bound on this error by blocking the 350 calculations into 10 blocks of 35 and calculating the standard error in the mean of these blocks. This also provides an estimate of our error and we denote this block based approach as $SE_B(D_{eff})$. We found that the statistical error from number of sampling was generally significantly less than the uncertainty from $E_{KRA}$. For example, the $SE_N(D_{eff})$ ($SE_B(D_{eff})$) at 1673 K was found as $5.1\times10^{-19}$ m$^2$s$^{-1}$ ($8.9\times10^{-19}$ m$^2$s$^{-1}$) while the estimated errors (the difference between the upper and lower bound) from $E_{KRA}$ was $4.2\times10^{-18}$ m$^2$s$^{-1}$. The total error from two sources is added in quadrature at each temperature, where we always use the larger of the two values of $SE_N(D_{eff})$ and $SE_B(D_{eff})$, and shown in Fig. 5.6.

The calculated $D_{eff}$ in the range from operating to accident temperature of TRISO fuel particles (from 1200 to 1600 °C) are shown in Fig. 5.6 at each temperature. The diffusion prefactors ($D_0$), the effective activation energies ($Q_A$), and the diffusion coefficient ($D$) at 1300 °C and 1600 °C from the literature are also summarized in Table 5.3 and Fig. 5.6. Ag diffusion simulations were performed in 50 virtual HEGB cells for each temperature. The error bar includes the uncertainty range of $D$ values due to $E_{KRA}$ sampling during kMC (See above for details on the error calculations, where we find that among possible sources of likely error, uncertainty arising from $E_{KRA}$ sampling is the most significant.), and all of the calculated $D$ values are found within the error bars. The diffusion coefficients show Arrhenius type diffusion and the pre-exponential factor ($D_0$) and effective activation barrier ($E_{A,eff}$) are extrapolated from the Arrhenius relation $D_{eff}^{total} = D_0 \cdot \exp(-E_{A,eff} / k_B T)$, where $k_B$ is the Boltzmann constant. The effective activation barrier ($E_{A,eff}$) and diffusion prefactor ($D_0$) predicted by our model are 2.79 ± 0.18 eV and (2.79 ± 1.09) × $10^{-10}$ $m^2s^{-1}$, respectively. This fitted Arrhenius relation is shown in Fig. 5.6 and shows an excellent agreement with the calculated values. In Fig. 5.7, the effective activation barrier is compared with reported experimental values (open symbol=integral release, and filled symbol = ion implantation), and theoretical predictions (filled triangles) in different structures of SiC.

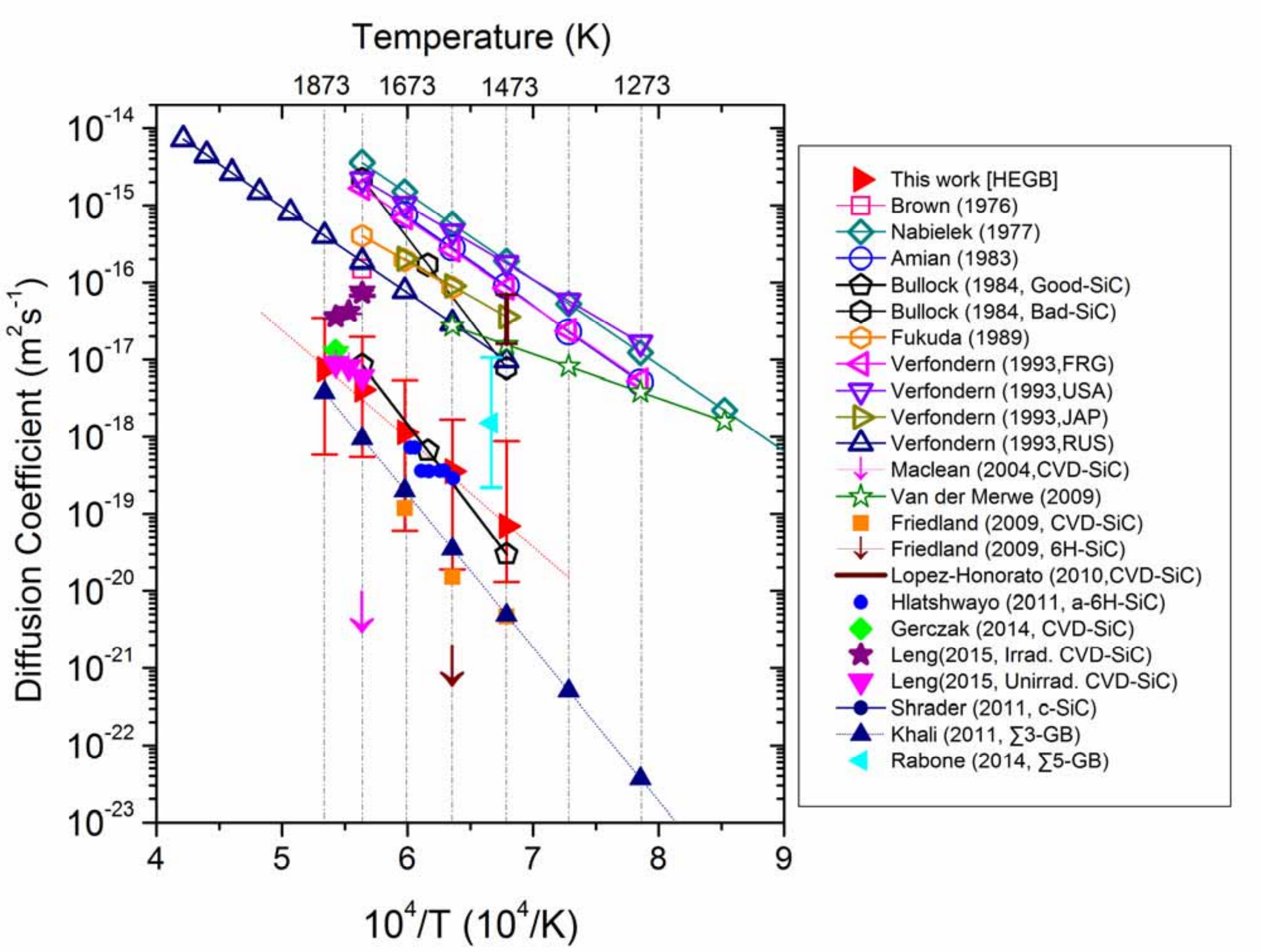

**Figure 5.6** The temperature dependence of Ag diffusion coefficients. Ref [16, 45] are the upper bounds for *D* in crystalline 3C-SiC and ∑3-GB from computational study. Ref [49, 61, 82] are integral release data from irradiated TRISO particles. Open symbols are Arrhenius fit of measurements from irradiated TRISO particles and filled symbols represents reported values from non-irradiated SiC from both surrogate experimental and computational studies. Note the downward arrows are indications that the value is upper limit (i.e. the estimation of *D* is less than this value). The Arrhenius fit for Ag diffusion in a HEGB from this work is shown with red dashed line.

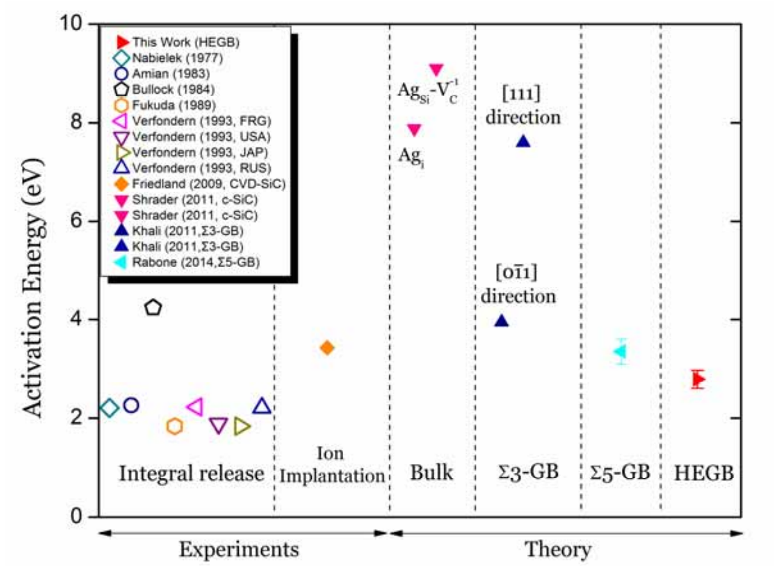

**Figure 5.7** Effective activation energy barrier in this study and literature values [5, 16, 45, 49, 61, 62, 81-83]. Note that values predicted in the bulk and ∑3-GB are activation energies for Ag specific species and directions, respectively.

**Table 5.3** A summary of reported diffusion coefficients for Ag in SiC in the form of an Arrhenius relation $D = D_0 \times \exp\left(-Q_A / k_B T\right)$ when available. The temperature range shown gives the range of temperature values used to fit the Arrhenius relation for *D*.

| **Method and Reference** | **Temp.(°C)** | $D_0(\mathrm{m^2 s^{-1}})$ | $Q_A$ **(eV)** | ***D* (T=1300°C)** | ***D*(T=1600°C)** |
|---|---|---|---|---|---|
| **Experiments** | | | | | |
| ***Integral Release*** | | | | | |
| Brown [48] | $^a1500$ | - | - | - | $^a1.5 \times 10^{-16}$ |
| Nabielek[49] | 800-1500 | $6.8 \times 10^{-9}$ | 2.21 | $5.7 \times 10^{-16}$ | - |
| Amian[82] | 1000-1500 | $4.5 \times 10^{-9}$ | 2.26 | $2.8 \times 10^{-16}$ | - |
| Bullock [83] | 1200-1500 | $9.6 \times 10^{-6}$ | 4.24 | - | - |
| Fukuda [62] | 1300-1500 | $6.8 \times 10^{-11}$ | 1.84 | - | - |
| Verfondern (FRG)[61] | 1000-1500 | $3.6 \times 10^{-9}$ | 2.23 | $2.6 \times 10^{-16}$ | - |
| Verfondern (USA) [61] | 1000-1500 | $5.0 \times 10^{-10}$ | 1.89 | $4.5 \times 10^{-16}$ | - |
| Verfondern (JAP) [61] | 1200-1400 | $6.8 \times 10^{-11}$ | 1.84 | $9.0 \times 10^{-17}$ | - |
| Verfondern (RUS) [61] | 1200-2300 | $3.5 \times 10^{-10}$ | 2.21 | $3.0 \times 10^{-17}$ | $4.0 \times 10^{-16}$ |
| Van der Merwe [37] | 920-1290 | $1.14 \times 10^{-13}$ | 1.13 | $2.7 \times 10^{-17}$ | - |
| ***Ion Implantation*** | | | | | |
| Friedland (CVD-SiC)[6] | 1200-1400 | $2.4 \times 10^{-9}$ | 3.43 | $1.5 \times 10^{-21}$ | - |
| $^b$Friedland (6H-SiC) [5] | 1200-1400 | - | - | $^c< 1.0 \times 10^{-21}$ | - |
| Friedland(CVD-SiC) [5] | 1200-1400 | $4.3 \times 10^{-12}$ | 2.50 | $2.8 \times 10^{-20}$ | - |
| Maclean (CVD-SiC)[118] | $^a1500$ | - | - | - | $^{a,c}<5.0 \times$ |

| | | | | | |
|---|---|---|---|---|---|
| | | | | | $10^{-21}$ |
| Gerczak (CVD-SiC) [78] | [a]1569 | - | - | - | [a]$1.3 \times 10^{-17}$ |
| Leng (CVD-SiC, Unirrad.) [119] | [a]1569 | $1.04 \times 10^{-12}$ | 1.84 | - | [a]$8.8 \times 10^{-18}$ |
| Leng (CVD-SiC, Irrad.) [119] | [a]1569 | - | - | - | [a]$3.6 \times 10^{-17}$ |
| ***Diffusion Couple*** | | | | | |
| Lopez-Honorato[80] | 950, 1150, [a]1500 | - | - | - | [a]$2.99 \times 10^{-15}$ |
| Lopez-Honorato[79] | 1200 | - | - | [a]$(1.0 - 1600) \times 10^{-18}$ | - |
| Gerczak [78] | 1500 | - | - | - | - |
| **Simulations** | | | | | |
| Shrader(c-SiC) [16] | [d]TST | $6.3 \times 10^{-8}$ | 7.88 | $3.6 \times 10^{-33}$ | $3.9 \times 10^{-29}$ |
| Kahlil (∑3-GB ) [45] | [d]TST | $1.6 \times 10^{-7}$ | 3.95 | $3.5 \times 10^{-17}$ | $3.7 \times 10^{-18}$ |
| Rabone (∑5-GB)[81] | [e]1227 | - | 3.35 | [a]$(0.22 - 10.5) \times 10^{-18}$ | - |
| This work (HEGB) | 1200-1600 | $2.7 \times 10^{-10}$ | 2.79 | $5.4 \times 10^{-19}$ | $7.6 \times 10^{-18}$ |

[a] Diffusion coefficient evaluated at specified temperature

[b] Ag diffusion in single crystal SiC, if marked

[c] Upper limit of diffusion coefficient as no detectable Ag diffusion was observed

[d] By Transition State Theory

[e] By Density Functional Theory Molecular Dynamics

### *5.1.4 Discussion on the Impact of Ag HEGB Diffusion*

The above results suggest that HEGBs can provide fast diffusion paths. However, it necessary to discuss their contributions to the Ag release in a more general context of other GB related studies and more general aspects of the Ag release process. In particular, the HEGBs are expected to be the dominant Ag diffusion path not only because of their diffusion rate, but also because of the high prevalence and strong Ag segregation tendencies. Here we discuss each of these properties in relation to other GB studies, Ag release studies, and the general Ag release process.

If HEGBs are to provide a fast Ag release path they must enable a connected (percolating) pathway through polycrystalline material. In pc-SiC, ∑3-GBs and random GBs (HEGBs) are the most abundant type of GBs [41, 78] and the HEGBs constitute a majority (>40%) of GBs in CVD grown SiC [84]. This value is high enough that it is expected to provide a percolating pathway [45]. It should be noted that of the GB types only HEGBs and ∑3-GBs, with their high fraction of all GBs, can provide a percolation path for Ag diffusion in SiC [45]. Thus, while it is possible that mobility of Ag in other non-∑3 CSL GBs are faster than in HEGB, other paths are less likely to explain accelerated diffusivity given that only HEGB can provide a percolating path for Ag transport. Therefore, it is reasonable to assume that HEGBs may provide the dominant pathways for Ag diffusion in SiC.

If HEGBs are to provide a fast Ag release path, they must also provide stable sites for Ag segregation. A strong segregation of Ag to HEGB is expected based on our calculations, and results to date suggest this segregation is even stronger than for other CSL GBs. The formation energies for substitutional and interstitial Ag (Table 5.1) are significantly lower than the most stable states of Ag found for bulk (10.5 eV in $\mathrm{Ag_{TC}}$). Similarly, the most stable interstitials in the HEGB (which are as low as -0.59 eV) are lower than the interstitial sites found in ∑3-GB (5.32 and 2.76 eV (both Ag-V clusters) [45]), and in a ∑5-GB (0.88 eV and 1.19 eV.) Ag therefore appears to be notably more stable in the HEGBs than bulk [16] or in other CSLs [45, 81], and thus Ag is expected to segregate to these GBs. This weak solubility in bulk SiC is consistent with the recent results of Hlatshwayo [59], who observed precipitates of implanted Ag in single crystal 6H-SiC after thermal exposure at T < 1300 °C, suggesting low bulk Ag solubility.

A useful assessment of the solubility energetics in our model is to predict Ag solubility and compare it to values estimated from experiments. The solubility of the Ag in SiC (concentration per unit volume at equilibrium) can be estimated in the non-interacting limit using the calculated formation energies of Ag defects.

**Equation 5.2**

$$C_{\mathrm{Ag}} = \sum_{i=1}^{n} \frac{\exp(-E_F^i / k_{\mathrm{B}} T)}{(1+\exp(-E_F^i / k_{\mathrm{B}} T))} \times \rho_i$$

where $i$ is the type of defect, $\rho_i$ is the site density of defects of type $i$ (number of sites per unit volume), and $E_F^i$ is the formation energy of the defect of type $i$. For $i$ = Ag interstitial in HEGB, the solubility limit ($C_{\mathrm{Ag}}^{\mathrm{HEGB}}$) is calculated by considering the amorphous SiC unit cell studied above and the $n$ = 153 sites and their energies that were determined to be the effective stable Ag interstitial sites in that cell. For each interstitial site, we used a site density ($\rho_i$) value of (1 site / a-SiC cell volume). The Ag solubility limit in the HEGB ($C_{\mathrm{Ag}}^{\mathrm{HEGB}}$) from Ag metal is predicted by this approach to be $4.60\times10^{27}$ $\mathrm{m^{-3}}$ at 1200 °C, and $4.59\times10^{27}$ $\mathrm{m^{-3}}$ at 1535 °C. The use of the Ag metal reference case is relevant for any situation where metallic Ag is in excess, e.g.,during ion implantation. Using the atomic density of the a-SiC cell used in this study, the total concentration of atoms in HEGB can be estimated to be about $8.96\times10^{28}$ GB-atoms/$\mathrm{m^3}$. Taking the ratio of GB Ag solubility to GB atomic density, we can estimate that the Ag solubility is about 5.1 at. % (i.e., about 0.051 Ag for a Si or C) in the HEGB. From Equation 5.2, the Ag solubility limits in sc-SiC and Σ3-GB are calculated as $C_{\mathrm{Ag}}^{\mathrm{Bulk}}$=$3.00\times10^{10}$ $\mathrm{m^{-3}}$ and $C_{\mathrm{Ag}}^{\Sigma3}$ = $3.80\times10^{18}$ $\mathrm{m^{-3}}$ at 1200 °C, and $C_{\mathrm{Ag}}^{\mathrm{Bulk}}$=$7.08\times10^{13}$ $\mathrm{m^{-3}}$ and $C_{\mathrm{Ag}}^{\Sigma3}$ = $2.30\times10^{20}$ $\mathrm{m^{-3}}$ at 1535 °C. The $C_{\mathrm{Ag}}^{\mathrm{Bulk}}$ and $C_{\mathrm{Ag}}^{\Sigma3}$ are calculated based on the neutral defect formation energies in Ref [16, 45], and these values are consistent with reported values [45]. It can be seen that the Ag solubility in GBs are significantly higher than in sc-SiC, specifically $\times10^{8}$ for Σ3-GB and $\times10^{17}$ for HEGB at 1200 °C. These solubility limit differences are consistent with the Ag strongly segregating to GBs, especially to HEGBs.

The GB solubility can be compared to experimentally measured (net) solubility from pc-SiC. In Ag-implanted SiC diffusion studies, the Ag solubility limits measured at 1535 °C are $4.80\times10^{22}$ $\mathrm{m^{-3}}$ [44] and $3.61\times10^{22}$ $\mathrm{m^{-3}}$ [119]. Note that these are the net solubilities, including contributions from crystalline regions and all GBs. The net solubilities ($C_{\mathrm{Ag}}^{net}$) are higher than $C_{\mathrm{Ag}}^{\mathrm{Bulk}}$ by a factor of about $10^9$. This comparison indicates that the net solubility cannot be solely explained by the bulk solubility, and is consistent with our above argument of a strong Ag segregation to GB. If the net solubility is converted into a GB solubility by assuming all the Ag is in GBs, then the GB solubility at 1535 °C is estimated from these experiments as 1-2 % atomic fraction of GB-atoms (as discussed in Ref. [119]). If we further assume all the Ag is in HEGBs, which make up about half the GBs, then this value suggests a HEGB Ag solubility of 2-4%, which is is remarkably good agreement with the estimate from our calculations. While this level of quantitative agreement is almost certainly fortuitous, the qualitative agreement supports the both our *ab initio* energetics and the model that Ag is predominately present in, and therefore transported by, HEGBs, at least in typical ion implantation studies.

It is important to note that the above model for predicting Ag solubilities assumes no Ag-Ag interactions. While such as assumption is not unreasonable at just a few percent concentration, it is not clear this is overall a good approximation. We estimated the qualitative effect of Ag-Ag interaction by examining formation energies of two interstitials in the system and comparing that to their single isolated interstitial energies. Sets of two interstitial sites have been picked so the Ag-Ag distance is within 5.0 Å. For these calculations the presence of another Ag nearby increased the formation energy by about 1.4-2.0 eV/Ag. The increase in formation energy indicates that there is a significant interaction which will reduce Ag solubility relative to the predictions of the non-interacting model above. More work on a Ag solubility model including Ag-Ag interactions is therefore needed for more quantitative predictions of Ag concentrations in HEGBs.

This work has provided the first guidance on the specific transport properties of HEGBs and suggests that these GBs are a good candidate for being the fastest Ag diffusion paths among different GB types. To further explore whether HEGBs are in fact the dominant mechanism, the $D_{\mathrm{HEGB}}$ is compared to previous studies on other mechanisms and rates of Ag diffusion in SiC. A DFT study by Shrader *et al.* [16] showed extremely low $D_{\mathrm{bulk}}$ values ($3.9\times10^{-29}$ m$^2$ s$^{-1}$ at 1600°C), suggesting that the GB diffusion is far more important than bulk diffusion, at least in the unirradiated materials. Study on Ag diffusion in a low angle ∑3 CSL grain boundary by Khalil *et al.*[45] has shown a relatively fast diffusion compared to $D_{\mathrm{bulk}}$, but still slower than our $D_{\mathrm{HEGB}}$ in the range of temperature considered, 1200-1600°C. At 1600 °C, the ratio of $D_{\mathrm{HEGB}}$ to $D_{\Sigma3\text{-GB}}$ is close to one, but our result indicates this ratio will increase as the temperature is lowered due to the difference in activation energies. In contrast, Rabone *et al.*[81] predicted a range of $D_{\sum5\text{-GB}}$ to be higher than $D_{\mathrm{HEGB}}$ as shown in Fig. 5.6, but their results shows inconsistency with both integral release (open symbols) and ion implantation measurements (non-triangle filled symbols). In fact, there are some potential sources of errors in the approach taken by Rabone *et al.* [81]. They extracted a migration barrier from a Ag hop in molecular dynamics, which hop was identified from the trajectory and from the change in potential energy. In this approach a single energy barrier for the Ag interstitial hop is used to extract $D$ from the Arrhenius relation. However, it is not clear that this hop is fully representative given that the total energies of the system before and after the hop were found inconsistent. Thus we take $D$ from Rabone *et al*. to be an upper bound for the diffusion in ∑5-GB, as other larger barriers might exist. Although the data is very limited, from the comparison of reported $D$s, Ag in HEGB is expected to diffuse at similar rates or faster than other GB or bulk mechanism in pc-SiC, except perhaps in the ∑5-GB.

In the above arguments, we showed that the HEGBs can provide percolating, highly soluble and fast pathway for Ag transportation. This hypothesis is also supported by experimental studies on Ag diffusion in sc-SiC and a-SiC. In a 6H sc-SiC [5, 27], no movement of Ag in SiC was detected at 1300°C [5] and 1500°C [27]. It was postulated that the Ag bulk diffusion is not fast enough to be observed on the experimental time scale, thus the upper bound of $D$ values were estimated from the limited time of experiment. The slow Ag diffusion in sc-SiC is consistent with this work and other simulation studies [16, 45]. Particularly encouraging is that the Ag diffusion from amorphized 6H-SiC by Hlatshwayo [59] shows a quantitatively good agreement with our predictions for a-SiC. The agreement with Ag diffusion in amorphized 6H-SiC experiments not only supports the fast diffusion of Ag in disordered HEGBs but also suggests that the stochastic approach utilized in this work is indeed capable of reproducing realistic Ag transport.

It is useful to compare the $D_{\mathrm{HEGB}}$ to net diffusion coefficients in the pc-SiC to assess whether they support HEGB diffusion being the dominant mechanism in pc-SiC. As it can be seen from Fig. 5.6, $D_{\mathrm{HEGB}}$ shows a good agreement with $D$ values of the recent ion implantation experiments (non-triangle filled symbols) [5, 44, 78, 119] on 3C-SiC. The discrepancies with the existing non-irradiated experimental data on pc-SiC are within about a factor of ten, except the diffusion couple studies by López-Honorato *et al.*[79, 80]. They reported $D$ value that is 3 orders of magnitude higher than $D^{\mathrm{HEGB}}$, and in fact these values are close to integral release measurements (Fig. 5.6, open symbols) [37, 48, 49, 61, 62, 82, 83]. In the studies of López-Honorato *et al.* Ag diffusion was observed with SEM in a heat-treated diffusion couple, where a layer of silver was trapped between CVD-SiC layers. The fast diffusion observed perhaps owes to the higher concentration of Ag, which may support some form of accelerated Ag transport, e.g., through a dissolution type mechanism [73]. Similarly in the Ag/SiC vapor diffusion couple at 1500 °C, Gerczak [78] observed localized dissolution of condensed Ag at SiC surface and Ag penetrated into bulk in Ag-Si corrosion form, not by impurity diffusion kinetics. As the Ag concentration in these experiments is much higher than the expected Ag concentration in the SiC layer of TRISO particles [37, 49] the implications of these results for the TRISO particles is not entirely clear.

There is a 2-3 orders of magnitude difference between our predicted $D_{\mathrm{HEGB}}$ and the $D$ from integral release measurements in the relevant temperature ranges of 1200-1600 °C. Compared to integral release measurements, other ion implantation experimental observations of Ag diffusion also exhibit a low value, quite consistent with our calculations. These experiments and our calculations are different from the integral release measurements in multiple ways, but perhaps the most obvious difference is that these experiments and our calculations do not involve irradiation. Therefore, we believe that the predicted $D_{\mathrm{HEGB}}$ is an approximate upper bound for the effective diffusivity in unirradiated pc-SiC.

As just mentioned, integral release measurements show a clear discrepancy in diffusion rates when compared to most of the other studies, including both experiments (typically ion implantation) and modeling. The discrepancies are likely due to a combination of different factors. However a reasonable explanation for the disagreement of $D$ values between integral release measurements, and ion implantation experiments and models is that irradiation affects Ag diffusivity in SiC. In general, radiation enhanced diffusion (RED) has been widely observed in metallic nuclear materials and semiconductors [120-122]. These irradiation effects, if they are occurring, must involve coupling over time as the integral release experiments are generally performed by heating samples that were irradiated previously, so the release is measured long after the irradiation has occurred. It is not clear how the irradiation, especially prior irradiation, might enhance the Ag transport, but below we discuss some possible mechanisms.

Irradiation of SiC not only results elevated point defect concentration but also develops complex defect structures such as interstitial clusters, dislocations, and voids. Irradiation-induced defects may activate different diffusion mechanisms to create radiation enhanced diffusion (RED) of Ag, and this might take place in both bulk and GB regions. In irradiated SiC, however, it is likely that GB RED is responsible for the observed fast diffusion of Ag instead of bulk RED, based on the following argument. From earlier discussion we have shown that the Ag solubility in bulk expected to be low, and an extremely strong segregation towards GBs is predicted. Therefore, even if RED occurs in the bulk, the Ag will quickly end up trapped in GBs, which will then provide the dominant diffusion mechanism. Consistent with the hypothesis that the irradiation effects are dominated by RED in GBs, we showed in Section 3 (also Ref. [119]) that the sc-SiC does not show any enhanced Ag transport after irradiation, while irradiated pc-SiC clearly shows RED of Ag at 1400-1569 °C. These arguments support the hypothesis that GB RED may bridge the discrepancy of Ag diffusivity between integral release and other reported values. However, there is limited understanding in the possible mechanisms for RED in SiC GBs. In the following Section 5.2, we propos a Ag kickout mechanism [119], that can be active in GBs with crystalline qualities.

### *5.2 Radiation Enhanced Diffusion*

Depending on irradiation temperature and fluence, different defect structures (such as vacancies, interstitials, interstitial clusters, dislocation loops, and voids) can develop inside of SiC during irradiation [123]. These irradiation-induced defects may change both bulk diffusivity and GB diffusivity of Ag and lead to radiation enhanced diffusion (RED). In general it is unlikely that the observed RED of Ag is through a bulk mechanism, i.e., although bulk diffusion might be enhanced it is not likely that this mechanism is dominant. First, such a mechanism would require significant amounts of Ag dissolved in the bulk SiC lattice. Calculations from Shrader, *et. al.* [16] showed that Ag solubility in bulk SiC is extremely low, suggesting that Ag in single crystal SiC and in grains within polycrystalline SiC could reside primarily in Ag precipitate clusters. This hypothesis is consistent with recent experimental studies from Hlatshwayo [59], who found precipitates of implanted Ag in single crystal 6H-SiC after thermal exposure at T<1300°C. In addition, the extremely strong GB segregation predicted by *ab initio* studies [45, 124] implies that even if bulk diffusion were accelerated under irradiation, Ag would rapidly become trapped at GBs and the GB diffusion would dominate any transport in a polycrystalline material. The absence of any bulk RED for Ag is consistent with our results in Section 3, where the single crystal SiC does not show any enhanced Ag transport after irradiation.

The possible sources of RED in SiC GBs are difficult to analyze due to their structural complexity, but we here provide some qualitative considerations of possible mechanisms. For GBs with significant crystalline qualities (these are most obviously low angle or coincident site lattice GBs, but also perhaps some regions of more disordered GBs) it is expected that mechanisms can be at least qualitatively described by a model that treats the local structure as crystalline. Within that approximation, we considered what mechanisms might accelerate Ag diffusion in a crystalline environment, with the idea that these mechanisms might provide RED for some types of GBs. We assume at the outset that these crystalline-like GB environments have enough disorder that there is sufficient Ag solubility for it not to cluster into Ag metal precipitates, as it is likely to do in pure bulk. The stability of substitutional Ag and the barriers for Si and C vacancy mediated diffusion [16] suggest that substitutional diffusion of Ag is likely to be slow, and that facile Ag motion in a crystalline environment is most likely through some form of Ag kickout mechanism to access fast Ag interstitial motion. Such a mechanism has been seen previously for other elements in crystalline SiC. For instance, it was shown in Refs [113, 125] that irradiation of SiC may enhance the bulk diffusivity of boron through the kick-out reaction $A_S + I \rightarrow A_I$, where intrinsic interstitials $I$ kick out impurity atoms from substitutional sites $A_S$ to interstitial sites $A_I$. A detailed model of possible kickout mechanisms which might be active during integral release experiments is given in following sections.

### *5.2.1 Kickout Reactions as a Possible RED Mechanism*

Ag integral release experiments to date typically involve heating an irradiated SiC material often hundreds or thousands of hours after irradiation [32, 48, 49, 61, 62, 83, 126]. Therefore, any model to explain Ag integral release experiments in terms of RED must include a mechanism by which irradiation can alter the kinetics after the irradiation has long-since stopped. Excess vacancies are likely available in irradiated SiC after irradiation and commonly lead to RED in metals (e.g., see Ref. [127]). However, a study from Shrader *et al.*[16] has shown that high intrinsic $V_{Si}$ and $V_C$ hopping barriers (approximately 2.70 eV, and 3.66 eV) mean Ag diffusion by vacancy mechanisms is expected to be quite slow even in the presence of greatly enhanced vacancy concentrations, and unlikely to provide the relatively low 2-3 eV activation energy observed in integral release experiments. An alternative possible mechanism of RED is Ag diffusion as an interstitial after being kicked out from its most stable substitutional position by a Self-Interstitial (SI). This mechanism is consistent with the fast Ag interstitial (notated as $Ag_{TC}$, tetragonally coordinated by C) diffusion predicted by Shrader *et al.* [16]. Although few free SI will survive after irradiation, BSDs, which are speculated to be SI clusters, develop during radiation [56]. BSDs are quite stable, and will persist long after irradiation. These BSDs can be dissolved into interstitials [128] at the typical integral release experiment annealing temperature of >1200 °C, providing a source of SIs to kick out Ag in GBs and enable Ag motion. To assess if the kickout model for Ag RED is plausible we need to consider if the following quantities are consistent with the observed Ag diffusion: (i) the number of SIs provided by the BSDs, (ii) the rate SIs are generated by dissolving BSDs, and (iii) the rate of SI kickout reactions.

### 5.2.2 *Self-Interstitial as a Source for KickoutRreactions*

First the concentration of available SIs is taken into consideration. From simple geometric arguments we can approximate the SI concentration when disk-shaped BSDs are fully dissolved into SIs by $\mathrm{C_{SI}(at/m^3) = C_{BSD}(1/m^3) \times 2\pi \bar{d}(m) \times \bar{r}_{SiC}{}^{-1}\ (at/m)}$, where $C_{SI}$ and $C_{BSD}$ are number densities of SI (either a C or a Si) and BSD, $\bar{d}$ is the average diameter of BSD, and $\bar{r}_{SiC}$ is the bond length of SiC in bulk (156 pm). Here we assume that the SI density in BSDs is the same as that of Si and C in SiC. In Table 5.4, TEM observations on BSD concentration and size from Ref [39, 129] are summarized, and the SI concentrations are estimated for each set of data under the assumption that the BSDs are fully dissolved. The $C_{SI}$ for neutron and self ion irradiations are approximately expected to be $1\times10^{24}$-$1\times10^{26}$ at·m$^{-3}$. In particular, $C_{SI}$ for C$^+$ irradiated 4H-SiC, which was irradiated under conditions similar to those used in this study (similar radiation source, temperature, and dpa), is estimated to be $2.6\times10^{24}$ at·m$^{-3}$ [129]. The C$^+$ irradiated 4H-SiC data will be used for the present analysis as it is the available data with the most similar irradiation conditions to the experiments performed here. However, note that all values for $C_{SI}$ in Table 5.4 are larger than this value, so this value provides a lower bound within the data we have collected. This exercise shows that the estimated $C_{SI}$ is greater by two orders of magnitude than the Ag solubility limit measured in our ion implantation experiment (~ $1\times10^{23}$at·m$^{-3}$), and greater by five orders of magnitude than Ag TRISO particle content measured before annealing in integral release measurements ($10^{18}$-$10^{19}$ at·m$^{-3}$) [37, 49]. Also the irradiation condition of post-irradiation experiments [32, 48, 49, 61, 62, 83, 126] and our ion-implantation measurements are within reported BSD forming region reported in Ref. [39]. It is therefore reasonable to surmise that these experiments led to BSD formation and that these BSDs can provide a significant interstitial source during annealing. These results demonstrate that enough SI can be liberated from BSDs during post-irradiation annealing to potentially enable kicking out of every dissolved Ag many times over, supporting our hypothesis of SI enabled RED. It should be noted that the BSD dissolution rate and SI concentration can be different from one experiment to another, since they may have developed differently depending on the irradiation condition.

**Table 5.4** Measured density and size of BSD in neutron and Si ion radiated SiC [39, 129]. The concentration of self-interstitials is estimated based on the geometry of BSD.

| Reference | Implanted particles | Irradiation Temperature (℃) | Fluence (dpa) | BSD Size(nm) | BSD Density $(1/m^3)$ | Estimated $C_{SI}$ $(at/m^3)$ |
|---|---|---|---|---|---|---|
| Katoh, *et al.* [39] | Neutron(3C-SiC) | 300 | 6 | 1.0 | $2.2\times10^{24}$ | $3.7\times10^{25}$ |
| | | 800 | 4.5 | 2.6 | $2.6\times10^{23}$ | $1.1\times10^{25}$ |
| | | 800 | 7.7 | 3.0 | $3.3\times10^{23}$ | $1.7\times10^{25}$ |
| | Silicon(3C-SiC) | 1000 | 10 | 4.0 | $2.6\times10^{23}$ | $1.8\times10^{25}$ |
| | | 1400 | 10 | 10.0 | $2.3\times10^{21}$ | $3.9\times10^{23}$ |
| He, *et al.* [129] | Neutron(3C-SiC) | 300 | 10 | 1.1 | $1.20\times10^{24}$ | $2.2\times10^{25}$ |
| | | 300 | 7 | 1.0 | $2.10\times10^{24}$ | $3.6\times10^{25}$ |
| | | 500 | 7 | 1.9 | $7.80\times10^{23}$ | $2.5\times10^{26}$ |
| | Carbon(3C-SiC) | 600 | 0.5 | 1.3 | $5.00\times10^{23}$ | $1.1\times10^{25}$ |
| | Carbon(4H-SiC) | 1000 | 0.5 | 1.4 | $1.10\times10^{23}$ | $2.6\times10^{24}$ |

Now we estimate the rate of BSD dissolution and associated release of Sis, which is an important factor to determine whether the SI mediated RED of Ag can be active during annealing experiments. The dissolution rate ( $v^{dissolution}$ ) for an *n*-atom cluster can be estimated from a simple model for thermally activated emission and diffusion away of the interstitials in the cluster into an infinite medium with no significant interstitial concentration (see Equation 5.3, taken from Ref. [130]). This model must be parameterized by specific properties of BSD observed in carbon irradiation experiments, and we choose those for the 4H-SiC (Table 5.4) due the similarity of irradiation conditions to this study. The SIA-clusters are assumed to be in the form of a disc plate and to be stoichiometric, which is the most stable composition [131]. Adapting the derivation of geometric reaction factor between a spherical-cluster and point defects, the thermal dissociation rate for disc-shaped clusters to emit *i* (Si or C) interstitial, $v^{dissolution}$, can be written as [128]

**Equation 5.3**

$$v_i^{dissolution}(s^{-1}) = \frac{2\pi \bar{d}^2}{\Omega_i \ln(r_m / r_0)} D_i \exp(-\Delta E_D / (k_B T))$$

where $D_i$ is the diffusion coefficient of interstitial $i$ in matrix, $r_0$ is the dislocation core radius and is the half of the distance between dislocations. $\bar{d}$ is the average diameter of BSD, and $2\pi\bar{d} = n\bar{r}$ is given for the disk-shape cluster where $\bar{r}$ is the covalent bond radii between Si and C. $\Omega_i$ is the atomic size of element $i$, $k_B$ is the Boltzman constant, T is the annealing temperature, and $\Delta E_D$ is the binding energy of an interstitial to an SIA-cluster. The binding energy of interstitial can be calculated as $\Delta E_D = E_F(n-1) + E_F(1) - E_F(n)$ [132] where $E_F(n)$ is the formation energy of $n$-atom SIA cluster and $E_i$ is the formation energy of a single interstitial in a perfect crystal of 3C-SiC (taken as $E_C = -3.24$ eV, and $E_{Si} = -3.17$ eV [132]). The $E_F(n)$ are taken from the atomistic simulations based model developed by Watanabe, Morishita [131], which gave $E_F(n)=0.96n^1+2.37n^{1/2}$. It should be noted that the defect formation energies in SiC, calculated by different potentials, have shown inconsistency with each other. Also a recent first principle calculation work by Jiang *et al.* [133] had shown the empirical potential may not be capable of predicting the correct energetics or structures of small carbon interstitial cluster. Hence, the correct formation energy model, even for larger interstitial clusters, may deviate from what was proposed by Watanabe *et al.* [131]. However, there is very limited knowledge of the free energy of SIA clusters, so we will follow the model from Watanabe, Morishita [131].

The BSD is assumed to maintain the SiC stoichiometry, and we can therefore apply Slezov's multi-component system scheme to Equation 5.3 to get:

**Equation 5.4** $$\bar{\nu}^{\,dissolution}(s^{-1}) = \frac{2\pi\bar{d}^2}{\bar{\Omega}\ln(r_m/r_0)}\bar{D}_{eff}\exp\left(\frac{E_F(n+1)-E_F(n)-\bar{E}_{eff}}{k_B\mathrm{T}}\right)\cdot\left(C_{\mathrm{C}}^{x_{\mathrm{c}}}C_{\mathrm{Si}}^{x_{\mathrm{Si}}}\right)$$

where $\bar{D}_{eff}$ and $\bar{E}_{eff}$ are the effective diffusion coefficient and an interstitial formation energy for Si and C ($\bar{D}_{eff} = 4\left[(x_{\mathrm{C,\,matrix}}D_{\mathrm{C,\,matrix}})^{-1} + (x_{\mathrm{Si,\,matrix}}D_{\mathrm{Si,\,matrix}})^{-1}\right]^{-1}$, and $\bar{E}_{eff} = [x_{\mathrm{C}}E_{\mathrm{C}} + x_{\mathrm{Si}}E_{\mathrm{Si}}]$). $\bar{\Omega}$ is the average atomic volume of Si and C, $C_i$ is the concentration of element $i$ in bulk ($C_C=C_{Si}=0.5$), $C_{i,\text{ matrix}}$ is the $i$ interstitial fraction in matrix, and $D_{i,\text{ matrix}}$ is the diffusion coefficients in the matrix, where $D_C=(9.57\times10^{-8}\ \mathrm{m^2s^{-1}}) \times \exp(-0.78\ \mathrm{eV}/k_B\mathrm{T})$ for C interstitials and $D_{Si}=(9.57\times10^{-8}\ \mathrm{m^2s^{-1}}) \times \exp(-1.58\ \mathrm{eV}/k_B\mathrm{T})$ for Si interstitials. The migration barriers associated with interstitial diffusion are taken from Watanabe, Morishita [132].

In this approach it is assumed that the dissolution process to liberate interstitials from BSDs is a non-equilibrium reaction and is not kinetically hindered at such high annealing temperature. Once interstitials are dissolved they are presumed to diffuse away in this model. The total concentration of dissolved SI in the system is estimated by integrating $\nu^{-1}$ when the irradiated SiC is annealed for a period of time. In Fig. 5.8, the dissolved concentration of SI after 20, 200, and 2000 hrs annealing is predicted. The Ag solubility limit measured in this work is also shown. For SI kickout to enable RED of Ag there must be significantly more SIs than Ag dissolved in the SiC. For the annealing experiment in this work of 10 and 20 hours, the produced SI concentration is predicted to be lower than the Ag solubility limit. The analysis of SI concentration therefore indicates that the RED by Ag kickout reactions may show a very small effect on the Ag distribution in this experimental work, consistent with what is observed. However, in the integral release experiments, the annealing time typically ranges from hundreds to thousands of hours [32, 48, 49, 61, 62, 83, 126]. Therefore SI concentrations in the integral release experiments are expected to be higher than Ag dissolved in SiC under given conditions and RED may occur.

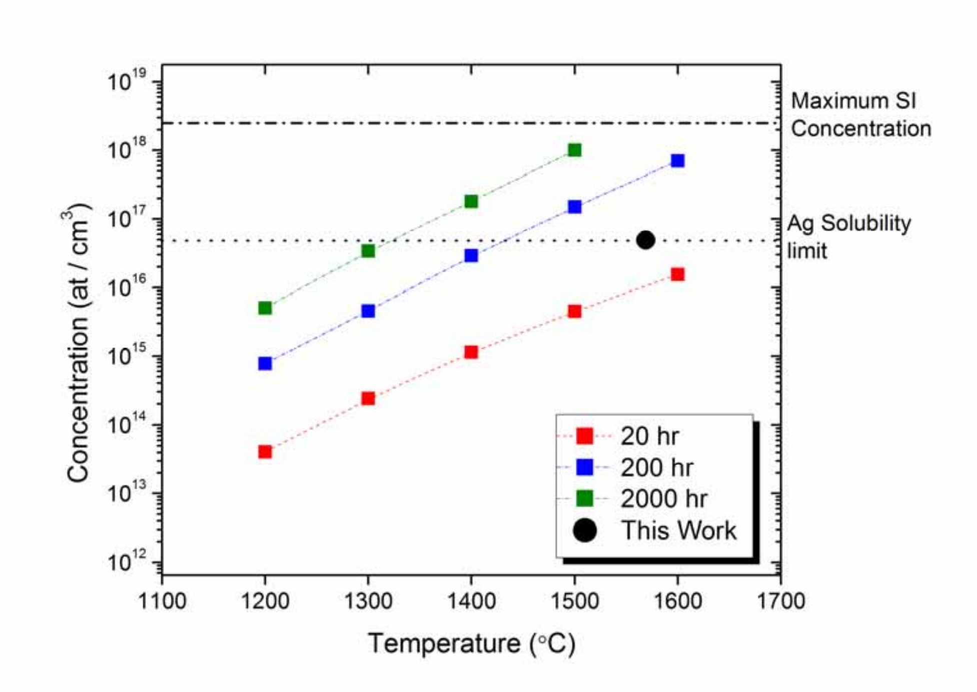

**Figure 5.8** The SI concentration dissolved from BSD as a function of annealing temperature and annealing time (for 20, 200, and 2000 hours). The SI concentration is estimated using properties of BSD measured in $C^+$ irradiated 4H-SiC. The SI concentration when the BSD is fully dissolved is denoted with a dash-dot line. The Ag solubility limit at about 1569°C is shown with black dot, and a guide to the eye is provided by the dotted line.

### *5.2.3 Kickout Reaction Rates*

The next issue to explore in considering SI enabled RED is if the reaction rates for key steps in Ag kickout are fast enough to observe significant diffusion of Ag during annealing integral release experiments. The reaction rates will depend on the reaction barrier and energies of reactants and products. The change in enthalpy ($\Delta E=\sum E_{\text{products}}-\sum E_{\text{reactants}}$) and reaction activation barrier ($E_A$) are shown for each relevant reaction in Table 5.5. Note that enthalpies and energies are taken as interchangeable under the assumption that we are working at 1 atm pressure. In this study, the products of reactions are assumed to be isolated defects that are not bound, and any binding energies of defects are not considered. This approach assumes that binding and unbinding of defects is not rate-liming. One exception to this assumption is binding of kicked out

Ag interstitials to any defects left after the kickout reaction, as this binding could greatly alter the ability of interstitial Ag to diffuse.

In Table 5.5, R.1-4 SI reactions with $Ag_{Sub}$-V, the most stable Ag defect in bulk SiC ($E_f$=5.32 eV) [16], are calculated. These reactions are not to kick out the Ag but merely to assess if the SI can easily and favorably fill a vacancy site, leaving just substitutional Ag ($Ag_{Sub}$). The structure of $Ag_{Sub}$-V (notated as $Ag_{Si}-V_C$ in Ref [16]) is that a Ag sits in between C and Si vacancy. Therefore the reactions are dependent on the orientation of SIs (e.g., C interstitial next to C vacancy (R.1) and C interstitial next to Si vacancy (R.3) will result different reaction energetics). In the R.3, the silicon interstitial relaxed on the carbon vacancy site instantly when two defects began to interact with each other, and formed $Ag_{Si}-Si_C$ with nearly zero reaction barrier. The reaction barriers for R.1, R.2, and R.4 are calculated as 1.07, 0.24, and 1.75 eV respectively. All reactions (R.1-R.4) were exthothermic ($\Delta E< 0$) and substitutional Ag defects are formed, with or without antisite defects depending on the reaction. We found that, for all SI reactions with $Ag_{Sub}$-V, the SI tends to fill a vacancy site to minimize total defect formation energy, with the specific site filled depending on the SI species and orientation. The products of these reactions ($Ag_{Sub}$ from R.1 and R.4, and $Ag_{Sub}$–antisite from R.2 and R.4) cannot be directly related to fast release of Ag as they are largely immobile [16]. However, we found these products can further react with SI through a kickout reaction to create Ag interstitials that can contribute to Ag diffusion.

The Ag kickout reactions by SIs are next investigated. Following Ref [16], we notate the final stable Ag interstitial, which sits in the tetrahedral site surrounded by C, with $Ag_{TC}$. The essential reactions to produce $Ag_{TC}$ are shown as R.5-R.12 in Table 5.5. R.5-R.8 show the reaction between SIs and substitutional type Ag defects, which not only are the next most stable defect type for Ag in SiC [16] but also are products of R.1-R.4, as discussed above. The reactions R.9-R.12 show kickout reactions of substitutional Ag that are bound to antisites, which are also products of R.1-R.4. For all kick-out reactions R.5-R.12 the activation barriers range from about 2-5 eV. The reactions for substitutionals Ag on the carbon lattice (2.11 eV for R.5, and 2.71 eV for R.6) had lower activation barriers than those for substitutionals Ag on the silicon lattice (3.35 eV for R.7, and 5.14 eV for R.8). Except R.8, the formation of $Ag_{TC}$ by kickout of an isolated $Ag_{Sub}$ is overall energetically favorable. For R.9-R.12, where Ag is next to an antisite, the reaction barriers for Ag kickouts are 1.57, 0.88, 0.34, and 0.01 eV. These reaction barriers are calculated to be lower than kickout barrier for substitutional Ag (R.5-R.8). However, it was found that the interstitial Ag next to an antisite defect formed a bound defect cluster of Ag with the antisite defects (a Ag – Antisite cluster). We define the binding energy of these clusters ($E_b$) as the energy of the cluster minus the energy of the antisites in the same positions as in the cluster and the energy of the $Ag_{TC}$ isolated from the antisites (i.e., the products minus reactants for $Ag_{TC}$ + Antisite → $Ag_{Int}$ – Antisite cluster). The $Ag_{Int}$–Antisite cluster binding energies were -3.12 eV for the product of R.9 and -3.83eV for the product of R.12. Therefore, forming these $Ag_{Int}$–Antisite clusters are unlikely to result in mobile Ag. For these cases, Ag atoms are likely to be trapped in a defect cluster and remain immobile. The $Ag_{Int}$–Antisite binding energies are only -0.63eV and -0.45 eV for the product of R.5 and R.10, and positive for the product of R.11 therefore long-term significant Ag trapping would not occur for these reactions.

**Table 5.5** Reactions between SIs and most stable Ag defects in bulk. The reaction activation barriers (EA) and the change in enthalpies ($\Delta E = E_{product} - E_{reactant}$) are calculated for each reaction.

| Reac. # | Reaction | $\Delta E$ (eV) | $E_A$ (eV) |
|---|---|---|---|
| R.1 | $(\mathrm{Ag}-\mathrm{V}) + \mathrm{C_I} \rightarrow \mathrm{Ag_{Si}}$ | -5.63 | 1.07 |
| R.2 | $(\mathrm{Ag}-\mathrm{V}) + \mathrm{C_I} \rightarrow \mathrm{Ag_C}-\mathrm{C_{Si}}$ | -1.66 | 0.24 |
| R.3 | $(\mathrm{Ag}-\mathrm{V}) + \mathrm{Si_I} \rightarrow \mathrm{Ag_{Si}}-\mathrm{Si_C}$ | -3.93 | - |
| R.4 | $(\mathrm{Ag}-\mathrm{V}) + \mathrm{Si_I} \rightarrow \mathrm{Ag_C}$ | -6.63 | 1.75 |
| R.5 * | $\mathrm{Ag_C} + \mathrm{Si_I} \rightarrow \mathrm{Ag_{TC}} + \mathrm{Si_C}$ | -2.09 (-0.63**) | 2.11 |
| R.6 | $\mathrm{Ag_C} + \mathrm{C_I} \rightarrow \mathrm{Ag_{TC}}$ | -3.85 | 2.71 |
| R.7 | $\mathrm{Ag_{Si}} + \mathrm{Si_I} \rightarrow \mathrm{Ag_{TC}}$ | -4.86 | 3.35 |
| R.8 * | $\mathrm{Ag_{Si}} + \mathrm{C_I} \rightarrow \mathrm{Ag_{TC}} + \mathrm{C_{Si}}$ | 0.97 (-3.47**) | 5.14 |
| R.9 * | $(\mathrm{Ag_C}-\mathrm{C_{Si}}) + \mathrm{Si_I} \rightarrow \mathrm{Ag_{TC}}+\mathrm{Si_C} + \mathrm{C_{Si}}$ | 0.77 (-3.12**) | 1.57 |
| R.10 * | $(\mathrm{Ag_C}-\mathrm{C_{Si}}) + \mathrm{C_I} \rightarrow \mathrm{Ag_{TC}}+\mathrm{C_{Si}}$ | -0.99 (-0.45**) | 0.88 |
| R.11 | $(\mathrm{Ag_{Si}}-\mathrm{Si_C}) + \mathrm{Si_I} \rightarrow \mathrm{Ag_{TC}}+\mathrm{Si_C}$ | -3.36 | 0.34 |
| R.12 * | $(\mathrm{Ag_{Si}}-\mathrm{Si_C}) + \mathrm{C_I} \rightarrow \mathrm{Ag_{TC}}+\mathrm{Si_C} + \mathrm{C_{Si}}$ | 1.36 (-3.83**) | 0.01 |

* The products of these reactions actually form bound Ag interstitial – antistite ($\mathrm{Ag_{Int}}$–Antisite) clusters, in some cases with significant movement of Ag off the $\mathrm{Ag_{TC}}$ position and energy stabilization. Please see text for details.

** The binding energy ($E_b$) of Ag interstitial – antistite ($\mathrm{Ag_{Int}}$–Antisite) clusters, defined as products minus reactants for $\mathrm{Ag_{TC}}$ + Antisite → $\mathrm{Ag_{Int}}$–Antisite cluster.

A number of reaction paths to kick out Ag from a substitutional site can be identified from Table 5.5. For all types of stable Ag defects considered here, we have discovered a number of energetically favorable reaction paths to kick out Ag and form $\mathrm{Ag_{TC}}$. For each path, we summarized the rate-limiting barrier ($E_R$) and the total change in the free energy ($\Delta E_t$) when forming $\mathrm{Ag_{TC}}$ from initial point defect energies. Once the unbound Ag interstitial is formed, we are approximating the migration barrier for $\mathrm{Ag_{TC}}$ to be equal to the $\mathrm{Ag_{TC}}$ migration barrier in bulk SiC, which is 0.89 eV. It should be noted that $\mathrm{Ag_{Int}}$–Antisite clusters are often more stable than unbound $\mathrm{Ag_{TC}}$ (i.e., the binding energies ($E_b$) of bound state of $\mathrm{Ag_{Int}}$–Antisite clusters are negative) and the paths which involve these clusters in their reaction are marked with '*' in Table 5.5. In these cases, only paths involving weakly bound Ag-Antisite clusters (R.5* and R.10*) are considered for favorable reaction paths as Ag atoms are rarely trapped.

Here, we explicitly consider the two-step reactions for transforming $\mathrm{Ag_{Sub}}$-V cluster into a mobile $\mathrm{Ag_{TC}}$. These paths involve a first step where vacancy of $\mathrm{Ag_{Sub}}$-V defects are filled (R.1-R.4). The vacancy filling reactions are exothermic and have energy barriers < 1.75 eV, which are small enough that this fist step is never rate limiting. Then these paths have a second step where the substitutional Ag is kickout out. Here we list each possible path, labeled P.1 – P.5.

**(P.1)** C *interstitial reacts with* $Ag_{Sub}$-V *to fill* C *sublattice. Then* Si *interstitial kicks out the* $Ag_{Si}$ *to form* $Ag_{TC}$ (R1→R.7). $E_R$= 3.35 eV. $\Delta E_t$= -10.49 eV.
**(P.2)** C *interstitial reacts with* $Ag_{Sub}$-V *to fill* Si *sublattice. Then* C *interstitial kicks out the* $Ag_C$-$C_{Si}$ *to form* $Ag_{TC}$ (R.2→R.10*).$E_R$= 0.88 eV. $\Delta E_t$= -2.65 eV.
**(P.3)** Si *interstitial reacts with* $Ag_{Sub}$-V *to fill* C *sublattice. Then* Si *interstitial kicks out the* $Ag_{Si}$-$Si_C$ *to form* $Ag_{TC}$ (R.3→R.11). $E_R$= 0.34 eV. $\Delta E_t$= -7.29 eV.
**(P.4)** Si *interstitial reactions with* $Ag_{Sub}$-V *to fill* Si *sublattice. Then* Si *interstitial kicks out the* $Ag_C$ *to form* $Ag_{TC}$ (R.4→R.5*). $E_R$= 2.11 eV. $\Delta E_t$= -8.72 eV
**(P.5)** Si *interstitial reactions with* $Ag_{Sub}$-V *to fill* Si *sublattice. Then* C *interstitial kicks out the* $Ag_C$ *to form* $Ag_{TC}$ (R4→R.6). $E_R$= 2.71 eV. $\Delta E_t$= -10.48 eV

Next, one-step reactions for transforming $Ag_{sub}$, the second stable Ag defect, to form mobile $Ag_{TC}$ are considered. These paths involve a single step where the substitutional Ag is kicked out (analogously to the second step in the above two-step reactions) and they are labeled **P.6** – **P.8.**

**(P.6)** Si *interstitial kicks out* $Ag_C$ *to form* $Ag_{TC}$ (R.5*). $E_R$ = 2.11 eV. $\Delta E_t$= -2.09 eV.
**(P.7)** C *interstitial kicks out* $Ag_C$ *to form* $Ag_{TC}$ (R.6). $E_R$ = 2.71 eV. $\Delta E_t$= -3.85 eV.
**(P.8)** Si *interstitial kicks out* $Ag_{Si}$ *to form* $Ag_{TC}$ (R.7). $E_R$ = 3.35 eV. $\Delta E_t$= -4.86 eV.

From the above discussion, we have shown that there are paths with barriers in the 0-4 eV range (which can be overcome at TRISO integral release experiment temperatures) for $Ag_{Sub}$-V and $Ag_{Sub}$ to be kicked out and to form Ag interstitials, including both types of reacting Ag defect and SI species. Based on the thermal equilibrium concentration of Ag defects, which favor $Ag_{Sub}$-V clusters, (P.1), (P.4) and (P.5) are most likely reaction path to kick out Ag as they all begin with this cluster. When $Ag_{Sub}$-V interacts with SIs it can readily form substitutional Ag with no vacancies nearby, which can then be kicked out. When following this path the $Ag_{Sub}$-V clusters can be kicked out to form interstitial Ag with barriers of 3.35, 2.11 and 2.71 eV for (P.1), (P.4) and (P.5), respectively (see Fig. 5.9). Although there are possible reactions that lead to Ag trapping due to a high reaction barrier (e.g. R.1→R.8) or a strong binding energy as an $Ag_{Int}$-Antisite cluster (e.g., R.1→R.8*, R.2→R.9*, R.3→R.12*, and R.8*), the fraction of kicked out Ag is expected to be greater than trapped Ag as the substitutional Ag concentration is likely much larger than the $Ag_{Sub}$-Antisite concentration. Once $Ag_{TC}$ is formed, Ag can again form substitutional Ag since $Ag_C$ or $Ag_{Si}$ are more stable than $Ag_{TC}$. However the reaction barrier for $Ag_{TC}$ to form substitutional on C site is 3.91 eV and on Si site is 2.98 eV, which is substantially higher than the $Ag_{TC}$ migration barrier of 0.89 eV. Thus Ag kicked out into the interstitials state is expected to diffuse quite far before being trapped again as a substitutional defect. The suggested barriers of 2.11-3.35 eV from reactions (P.1, P.4, and P.5) are comparable with the range of the effective activation barriers measured in integral release measurements, 1.84-4.24

eV [32, 48, 49, 61, 62, 83, 126], and the generally accepted value of 2.28-2.70 eV [134]. While the success of this model is suggestive, the hypothesis is still quite speculative and needs further validation. In particular, the parameters used in this model were taken from 3C SiC as our primary comparisons were to integral release experiments done on 3C material. However, the data in the present paper is taken on 4H SiC and a quantitative assessment of the present results would require evaluating all parameters for 4H. Furthermore, this model treats only processes in a perfect crystalline environment. A generalization of these studies to more realistic GB environments would be necessary to more fully assess the ability of these mechanisms to drive RED of Ag in GBs.

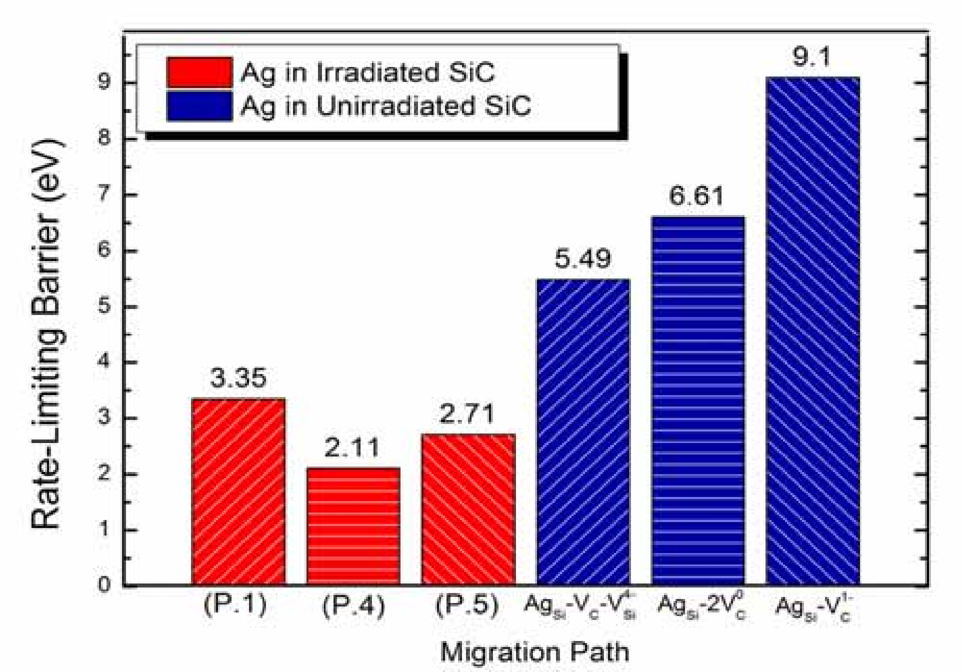

**Figure 5.9** The rate-limiting barriers for Ag migration in the irradiated (Red) and unirradiated (Blue) SiC. Only the most stable Ag defects are shown here. In irradiated SiC, Ag kickout barriers are rate-limiting barriers as the migration barrier of Ag is 0.89 eV. In unirradiated SiC, reorientations of defect complexes are the rate limiting barriers [16].

### *5.2.4 Discussion on Radiation Enhanced Diffusion Mechanism*

In the previous sections we have shown, from both experiment and modeling, that radiation can enhance Ag release through SiC. Based on these results, here we discuss a possible effect of radiation on diffusion mechanism of Ag in single-crystal and polycrystalline SiC.

In the Section 5.2, we discussed a possible mechanism for RED, which is the kickout of substitutional Ag by SIs. This process would be expected to occur in both in GB and crystalline bulk environments. However no RED of Ag is seen in our single crystal 4H-SiC experiments (see Section 3). We interpret the lack of RED in the single crystal as being due to the low solubility of Ag in a crystalline region (see estimations on Ag solubilities in Section 5.1.4) allowing for only insignificant substitutional concentration of Ag ions available for kickout. Thus the present kickout model is relevant for regions where Ag energetics is sufficiently altered from bulk single crystal to allow for significant substitutional Ag, but similar enough to crystalline to allow crystalline energetics to provide qualitative guidance on possible mechanisms.

In Section 5.2.2, we discussed the possibility that interstitial clusters formed under irradiation can dissolve under post-irradiation annealing, providing the source of C interstitials, which in turn kick out substitutional Ag and lead to RED. We have argued that the interstitials from this dissolution process are sufficient in number to enable significant Ag transport, and that the resulting kickout mechanism has a barrier consistent with that seen in integral release experiments. While this picture is all quite speculative, our analysis suggests it is possible that some kind of kickout mechanisms supports RED of Ag through relatively ordered GBs and provides at least a qualitative insight into what processes might be occurring in crystalline-like regions. This mechanism of RED may explain the radiation effects on Ag observed in Section 3.

It is also of interest to consider possible effects of irradiation on highly disordered GBs, where a crystalline picture is unlikely to be a good approximation. For highly disordered GBs that can be considered approximately amorphous (high-angle GBs), the literature on RED in amorphous materials strongly suggests that RED is likely. Diffusivities of impurities in various disordered (amorphous) materials can be enhanced by orders of magnitude due to irradiation [135-141]. Specifically, irradiation may increase the pre-factor [135-137] or decrease the activation energy [138-141] of the impurity diffusivity, depending on the diffusion mechanism. Mechanisms proposed for amorphous RED include changes in mediating point defect concentrations [140], irradiation impacting collective diffusion [142], and coupling to free volume [141]. Any of these mechanisms could potentially enhance Ag diffusion under irradiation in high-angle GBs. Regardless of the difference in the experimental conditions and proposed mechanisms in above studies, the reported diffusivities in irradiated amorphous systems show an enhancement in $D$ of typically by 1-3 orders of magnitude. If we apply this amount of enhancement to the recently calculated $D$ in a model high-angle GB [124] ($1.9\times10^{-18}$ $m^2/s$ at $1500^oC$), the expected diffusion coefficients of Ag in the irradiated high-angle GB is comparable to that reported for integral release measurements (e.g., $(1.5\text{-}35.9)\times10^{-16}$ $m^2/s$ at $1500^oC$). However, this scale of RED is significantly larger than observed in Section 3, and the magnitude of RED of Ag in SiC under different conditions requires further investigation. Although there are still many open questions about magnitudes and mechanisms, these observations on other amorphous systems suggest that RED of Ag through a percolating network of amorphous-like high-angle GBs may explain the observed radiation effects on Ag diffusion in SiC. Overall, we see that for both more crystalline and more highly disordered GBs there are possible mechanisms that could lead to RED for Ag.

## *5.3 Summary of Results from Atomistic Simulations*

To understand Ag diffusion mechanism in SiC layer of TRISO fuel particles, we have assessed two questions with atomistic modeling: (i) "*Is HEGB diffusion is responsible for Ag release through the polycrystalline-SiC?*" and (ii) "*Is there any possible RED mechanism that could account for the enhanced diffusion observed in irradiated SiC?*". To address the first question, Ag diffusion in HEGBs is simulated using a DFT based kinetic Monte Carlo (kMC) model. Ag in a HEGB is predicted to exhibit an Arrhenius type diffusion with diffusion prefactor and effective activation energy of $(2.73 \pm 1.09) \times 10^{-10}\mathrm{m}^2\mathrm{s}^{-1}$ and 2.79 ± 0.18 eV, respectively. The comparison between HEGB results to other theoretical studies suggests not only that GB diffusion is predominant over bulk diffusion, but also that the HEGB is one of fastest grain boundary paths for Ag diffusion in SiC. The Ag diffusion coefficient in the HEGB shows a good agreement with ion-implantation measurements, but is 2-3 orders of magnitude lower than the reported diffusion coefficient values extracted from integral release measurements on in- and out-of- pile samples. This discrepancy between our model and the diffusion observe in integral release experiments involving irradiation drove us to consider the second question above. In response to this question we proposed a possible kickout model for Ag diffusion in GBs with significant crystalline qualities. This model suggests that dissolution of irradiation generated defect clusters could drive mechanisms for Ag interstitial diffusion in crystalline-like GB, with rate-limiting barriers of 2.11-3.35 eV (5.49-9.1 eV in bulk SiC). While this picture is quite speculative, our analysis suggests it is possible that irradiation, even significantly prior to the annealing and Ag release experiment, supports a kickout mechanism that leads to RED of Ag through GBs.

## 6 Continuum model of diffusion through polycrystalline SiC

We have developed of a 3D kinetic Monte Carlo model of impurity diffusion along grain boundaries of a polycrystalline samples. The details of the model have been published in (*Deng et al. Comp. Mater. Sci. 2014*) and can be found in Appendix B. This model has been applied to evaluate diffusivity and release fraction of Ag in polycrystalline SiC. The effects of various grain boundary network properties on transport of Ag across the SiC layer have been examined, including fraction of each grain boundary type, spread in grain boundary diffusivities and distribution of grain boundary types. We found that the effective diffusivity and release fraction of Ag exhibit large variability due to changes in the GB structure of SiC, and this variability is almost independent of temperature fluctuation. Our results suggest that the variation in properties of grain boundary networks in SiC may contribute to the spread in the Ag diffusivity and release fraction measured in TRISO particles. It is also found that the grain boundary diffusion alone may be insufficient to account for the Ag diffusivities and release fractions measured in integral release experiments. Additional factors such as irradiation and temperature distribution may also play an important role in Ag transport across the SiC layer. The results have been published in (*Deng et al J. Nucl. Mater. 2015*) and can be found in Appendix B.

## 7 Publications resulting from this project

[1] *Cs and Ag co-incorporation in cubic silicon carbide*, A. Londono-Hurtado, D. Morgan, I. Szlufarska, ***J. Nucl. Mater.*** 439, p. 65-71 (2013)

[2] *Understanding Ag release from TRISO fuel through surrogate diffusion experiments and fuel analysis*, T. J. Gerczak, PhD dissertation, University of Wisconsin – Madison (2013)

[3] *Kinetic Monte Carlo simulations of effective diffusivities on grain boundary networks*, J. Deng, D. Morgan, I. Szlufarska, ***Computational Materials Science*** 93, 36-45 (2014)

[4] *Grain boundary diffusion of Ag through polycrystalline SiC in TRISO fuel particles*, J. Deng, H. Ko, P. Demkowicz, D. Morgan, I. Szlufarska, ***J. Nucl. Mater.*** 467: 332-340 (2015)

[5] *Effect of exposure environment on surface decomposition of SiC-silver ion implantation diffusion couples*, T.J. Gerczak, G.Zheng, K.G. Field, T.R. Allen, ***J. Nucl. Mater.*** 456, 281-286 (6015)

[6] *Observations of Ag Diffusion in Ion Implanted SiC*, T.J. Gerczak, B. Leng, K. Sridharan, JL Hunter, AJ Giordani, TA Allen, ***J. Nucl. Mater.*** 461, 314-324 (2015)

[7] *Effect of carbon ion irradiation on Ag diffusion in SiC*, B. Leng, H. Ko, T. J. Gerczak, J. Deng, A. J. Giordani, J. L. Hunter, D. Morgan, I. Szlufarska, K. Sridharan, ***J. Nucl. Mater*** To be published (2016)

[8] *STEM EDS Analysis of Fission Products in Neutron Irradiated TRISO Fuel Particles from AGR-1 Experiment*, B. Leng, I. van Rooyen, Y.Q. Wu, I. Szlufarska, K. Sridharan, Submitted

[9] *Ag diffusion in SiC high-energy grain boundaries: kinetic Monte Carlo study with first-principle calculations*, H. Ko, J. Deng, I. Szlufarska, D. Morgan, Submitted

## 8 References

1. Madelung, O., U. Rossler, and M. Schulz, *LN Volumes III/22B-41 A2b: silicon carbide (SiC), solubility of impurities*. 2015, Springer Materials.
2. Malherbe, J.B., *Diffusion of fission products and radiation damage in SiC.* Journal of Physics D: Applied Physics, 2013. **46**(47): p. 473001.
3. Gerczak, T.J., et al., *Effect of exposure environment on surface decomposition of SiC–silver ion implantation diffusion couples.* Journal of Nuclear Materials, 2015. **456**: p. 281-286.
4. Zhang, Y., et al., *Damage profile and ion distribution of slow heavy ions in compounds.* Journal of Applied Physics, 2009. **105**(10): p. 104901.
5. Friedland, E., et al., *Study of silver diffusion in silicon carbide.* Journal of Nuclear Materials, 2009. **389**(2): p. 326-331.

6. Friedland, E., et al., *Investigation of silver and iodine transport through silicon carbide layers prepared for nuclear fuel element cladding.* Journal of Nuclear Materials, 2011. **410**(1-3): p. 24-31.
7. Hlatshwayo, T.T., et al., *Annealing of silver implanted 6H–SiC and the diffusion of the silver.* Nuclear Instruments and Methods in Physics Research Section B: Beam Interactions with Materials and Atoms, 2012. **274**: p. 120-125.
8. Xiao, H.Y., et al., *Near-surface and bulk behavior of Ag in SiC.* Journal of Nuclear Materials, 2012. **420**(1-3): p. 123-130.
9. Kuznetsov, A.Y., et al., *Boron diffusion in Si and SiC during 2.5 MeV proton irradiation at 500–850°C.* Nuclear Instruments and Methods in Physics Research Section B: Beam Interactions with Materials and Atoms, 1999. **148**: p. 279-283.
10. Stolk, P.A., et al., *Physical mechanisms of transient enhanced dopant diffusion in ion-implanted silicon.* Journal of Applied Physics, 1997. **81**(9): p. 6031.
11. Khalil, S., et al., *Diffusion of Ag along Σ3 grain boundaries in 3C-SiC.* Physical Review B, 2011. **84**(21).
12. Bockstedte, M., et al., *The Nature and Diffusion of Intrinsic Point Defects in SiC.* Materials Science Forum, 2002. **389-393**: p. 471-476.
13. Lento, J.M., et al., *Self-interstitials in 3C-SiC.* Journal of Physics: Condensed Matter, 2004. **16**(7): p. 1053-1060.
14. Hon, M.H. and R.F. Davis, *Self-diffusion of14C in polycrystalline β-SiC.* Journal of Materials Science, 1979. **14**: p. 2411-2421.
15. Hon, M.H. and R.F. Davis, *Self-diffusion of 30Si in polycrystalline beta-SiC.* Journal of Materials Science, 1980. **15**: p. 2073-2080.
16. Shrader, D., et al., *Ag diffusion in cubic silicon carbide.* Journal of Nuclear Materials, 2011. **408**(3): p. 257-271.
17. Mattausch, A., M. Bockstedte, and O. Pankratov, *Self Diffusion in SiC: the Role of Intrinsic Point Defects.* Materials Science Forum, 2001. **353-356**: p. 323-326.
18. Lévêque, P., et al., *Vacancy and interstitial depth profiles in ion-implanted silicon.* Journal of Applied Physics, 2003. **93**(2): p. 871.
19. Pellegrino, P., et al., *Separation of vacancy and interstitial depth profiles in ion-implanted silicon: Experimental observation.* Applied Physics Letters, 2001. **78**(22): p. 3442.
20. Pelaz, L., et al., *B cluster formation and dissolution in Si: A scenario based on atomistic modeling.* Applied Physics Letters, 1999. **74**(24): p. 3657.
21. Gueorguiev, Y.M., et al., *High-energy ion-implantation-induced gettering of copper in silicon beyond the projected ion range: The trans-projected-range effect.* Journal of Applied Physics, 2000. **88**(10): p. 5645.
22. Kögler, R., et al., *Cu gettering in ion implanted and annealed silicon in regions before and beyond the mean projected ion range.* Journal of Applied Physics, 2003. **94**(6): p. 3834.

23. Gueorguiev, Y.M., et al., *Impurity gettering by high-energy ion implantation in silicon beyond the projected range.* Applied Physics Letters, 1999. **75**(22): p. 3467.
24. Stolwijk, N.A., et al., *Diffusion and solubility of gold in silicon.* Physica B + C, 1982. **116**(1): p. 335-342.
25. Chao, H.S., et al., *Species and dose dependence of ion implantation damage induced transient enhanced diffusion.* Journal of Applied Physics, 1996. **79**(5): p. 2352.
26. Myers, S.M., *Annealing behavior and selected applications of ion-implanted alloys.* Journal of Vacuum Science and Technology, 1978. **15**(5): p. 1650.
27. MacLean, H.J., et al., *The effect of annealing at 1500°C on migration and release of ion implanted silver in CVD silicon carbide.* Journal of Nuclear Materials, 2006. **357**(1-3): p. 31-47.
28. Rabone, J., E. Lopez-Honorato, and P. Van Uffelen, *Silver and cesium diffusion dynamics at the beta-SiC Sigma5 grain boundary investigated with density functional theory molecular dynamics and metadynamics.* J Phys Chem A, 2014. **118**(5): p. 915-26.
29. Brown, P.E. and R.L. Faircloth, *Metal fission product behaviour in high temperature reactors - UO2 coated particle fuel.* Journal of Nuclear Materials, 1976. **59**: p. 29-41.
30. Nabielek, H., P.E. Brown, and P. Offerman, *Silver release from coated particle fuel.* Nuclear Technology, 1977. **35**(2): p. 483.
31. Amian, W. and D. Stover, *Diffusion of silver and cesium in silicon-carbide coatings of fuel particles for high temperature gas-coolcd reactors.* Nuclear Technology, 1983. **61**(3): p. 475.
32. Bullock, R.E., *Fission-product release during postirradiation annealing of several types of coated fuel particles.* Journal of Nuclear Materials, 1984. **125**: p. 304-319.
33. Moormann, R. and K. Verfondern, *Methodikumfassender probabilistischer Sicherheitsanalysen fur zukunftige HTR-Anlagenkonzepte—Ein Statusbericht Band 3: Spaltproduktfreisetzung Report*. 1986, Research Center Julich
34. Fukuda, K., *Research and development of HTGR fuels Report*. 1989, JAERIM89-007
35. Minato, K., *Diffusion coefficients of fission products in UO2, PyC, SiC, graphite matrix and IG-110 graphite, unification of coated particle performance models and fission product transport data for the HTR IAEA Technical Workshop*. 1991, HTR IAEA Technical Workshop: Julich, Germany.
36. Chernikov, A.S., *Fission Product diffusion in fuel element materials for HTGR, Fission product release and transport in gas-cooled reactors*. 1986, IAEA Specialists Meeting: Berkley, CA.
37. van der Merwe, J.J., *Evaluation of silver transport through SiC during the German HTR fuel program.* Journal of Nuclear Materials, 2009. **395**(1-3): p. 99-111.
38. Fujita, T., Z. Horita, and T.G. Langdon, *Using grain boundary engineering to evaluate the diffusion characteristics in ultrafine-grained Al–Mg and Al–Zn alloys.* Materials Science and Engineering: A, 2004. **371**(1-2): p. 241-250.
39. Katoh, Y., et al., *Microstructural development in cubic silicon carbide during irradiation at elevated temperatures.* Journal of Nuclear Materials, 2006. **351**(1): p. 228-240.

40. Kondo, S., Y. Katoh, and L.L. Snead, *Cavity swelling and dislocation evolution in SiC at very high temperatures.* Journal of Nuclear Materials, 2009. **386-388**: p. 222-226.
41. van Rooyen, I.J., T.M. Lillo, and Y.Q. Wu, *Identification of silver and palladium in irradiated TRISO coated particles of the AGR-1 experiment.* Journal of Nuclear Materials, 2014. **446**(1-3): p. 178-186.
42. Lillo, T.M. and I.J. van Rooyen, *Associations of Pd, U and Ag in the SiC layer of neutron-irradiated TRISO fuel.* Journal of Nuclear Materials, 2015. **460**: p. 97-106.
43. López-Honorato, E., et al., *Silver Diffusion in Silicon Carbide Coatings.* Journal of the American Ceramic Society, 2011. **94**: p. 3064-3071.
44. Gerczak, T.J., et al., *Observations of Ag diffusion in ion implanted SiC.* Journal of Nuclear Materials, 2015. **461**: p. 314-324.
45. Khalil, S., et al., *Diffusion of Ag along $\Sigma 3$ grain boundaries in 3C-SiC.* Physical Review B, 2011. **84**(21): p. 214104.
46. Deng, J., et al., *Grain boundary diffusion of Ag through polycrystalline SiC in TRISO fuel particles.* Journal of Nuclear Materials, 2015. **467, Part 1**: p. 332-340.
47. Méric de Bellefon, G. and B.D. Wirth, *Kinetic Monte Carlo (KMC) simulation of fission product silver transport through TRISO fuel particle.* Journal of Nuclear Materials, 2011. **413**(2): p. 122-131.
48. Brown, P.E. and R.L. Faircloth, *Metal fission product behaviour in high temperature reactors -UO2 coated particle fuel.* Journal of Nuclear Materials, 1976. **59**(1): p. 29-41.
49. Nabielek, H., P.E. Brown, and P. Offermann, *Silver release from coated particle fuel.* Nuclear Technology, 1977. **35**: p. 483-493.
50. Friedland, E., T. Hlatshwayo, and N. van der Berg, *Influence of radiation damage on diffusion of fission products in silicon carbide.* physica status solidi (c), 2013. **10**(2): p. 208-215.
51. O'Connell, J.H. and J.H. Neethling, *Ag transport in high temperature neutron irradiated 3C–SiC.* Journal of Nuclear Materials, 2014. **445**(1-3): p. 20-25.
52. van Rooyen, I.J., et al., *Electron microscopic evaluation and fission product identification of irradiated TRISO coated particles from the AGR-1 experiment: A preliminary review.* Nuclear Engineering and Design, 2014. **271**: p. 114-122.
53. Collins, B.P., et al., *AGR-1 Irradiation Test Final As-Run Report*. 2012, Idaho National Laboratory: Idaho Falls, Idaho 83415.
54. Anders (Ed.), A., *Handbook of plasma immersion ion implantation and deposition*. 2000, New York: Wiley.
55. Devanathan, R., W.J. Weber, and F. Gao, *Atomic scale simulation of defect production in irradiated 3C-SiC.* Journal of Applied Physics, 2001. **90**(5): p. 2303-2309.
56. Snead, L.L., et al., *Handbook of SiC properties for fuel performance modeling.* Journal of Nuclear Materials, 2007. **371**(1): p. 329-377.
57. Stolk, P.A., et al., *Physical mechanisms of transient enhanced dopant diffusion in ion-implanted silicon.* Journal of Applied Physics, 1997. **81**(9): p. 6031-6050.

58. Troffer, T., et al., *Doping of SiC by implantation of boron and aluminum.* Physica Status Solidi a-Applied Research, 1997. **162**(1): p. 277-298.
59. Hlatshwayo, T.T., *Diffusion of silver in 6H-SiC*. 2011, University of Pretoria.
60. Myers, S.M., *Annealing behavior and selected applications of ion-implanted alloys.* Journal of Vacuum Science & Technology, 1978. **15**: p. 1650.
61. Verfondern, K., R.C. Martin, and R. Moormann, *Methods and data for HTGR fuel performance and radionuclide release modelling during normal operations and accidents for safety analysis*. 1993, Forschungszentrum Jülich GmbH.
62. Fukuda, K., et al., *Research and development of HTGR fuels*. 1989.
63. Mishin, Y. and C. Herzig, *Grain boundary diffusion: recent progress and future research.* Materials Science and Engineering: A, 1999. **260**: p. 55-71.
64. Harrison, L.G., *Influence of dislocations on diffusion kinetics in solids with particular reference to the alkali halides.* Transactions of the Faraday Society, 1961. **57**(0): p. 1191-1199.
65. Whipple, R., *CXXXVIII. Concentration contours in grain boundary diffusion.* Philosophical Magazine, 1954.
66. Blöchl, P.E., *Projector augmented-wave method.* Physical Review B, 1994. **50**(24): p. 17953-17979.
67. Pearson, R.L., R. Lauf, and T. Lindemer, *Interaction of palladium, the rare earths, and silver with silicon carbide in HTGR fuel particles*. 1982, Oak Ridge National Lab., TN (USA).
68. Tiegs, T., *Fission product Pd-SiC interaction in irradiated coated-particle fuels.* Nuclear Technology, 1982. **57**(3): p. 389-398.
69. Olivier, E.J. and J.H. Neethling, *The role of Pd in the transport of Ag in SiC.* Journal of Nuclear Materials, 2013. **432**: p. 252-260.
70. Nabielek, H. and P.E. Brown, *The release of silver-110m in high temperature reactors: Technical note*. 1975, OECD Dragon Project. p. 370.
71. Coward, R.A., et al., *Transmission electron microscopy investigation of Ag diffusion mechanisms in β-SiC.* Journal of Nuclear Materials, 2015. **457**(0): p. 298-303.
72. Price, R.J., *Neutron irradiation-induced voids in β-silicon carbide.* Journal of Nuclear Materials, 1973. **48**(1): p. 47-57.
73. Geng, X., et al., *An original way to investigate silver migration through silicon carbide coating in triso particles.* Journal of the American Ceramic Society, 2014. **97**(6): p. 1979-1986.
74. O'Connell, J.H. and J.H. Neethling, *Palladium and ruthenium supported silver migration in 3C–silicon carbide.* Journal of Nuclear Materials, 2015. **456**(0): p. 436-441.
75. Neethling, J.H., J.H. O'Connell, and E.J. Olivier, *Palladium assisted silver transport in polycrystalline SiC.* Nuclear Engineering and Design, 2012. **251**: p. 230-234.
76. O'Connell, J.H. and J.H. Neethling, *Ag transport in high temperature neutron irradiated 3C-SiC.* Journal of Nuclear Materials, 2014. **445**(1-3): p. 20-25.

77. Londono-Hurtado, A., et al., *Cs and Ag co-incorporation in cubic silicon carbide.* Journal of Nuclear Materials, 2013. **439**(1–3): p. 65-71.
78. Gerczak, T., *Understanding Ag release from TRISO fule through surrogate diffusion experiments and fuel analysis*. 2013, University of Wisconsin-Madison.
79. López-Honorato, E., et al., *Silver diffusion in silicon carbide coatings.* Journal of the American Ceramic Society, 2011. **94**(9): p. 3064-3071.
80. López-Honorato, E., et al., *Silver diffusion in coated fuel particles.* Journal of the American Ceramic Society, 2010. **93**(10): p. 3076-3079.
81. Rabone, J., E. Lopez Honorato, and P.V. Uffelen, *Silver and caesium diffusion dynamics at the b-SiC $\Sigma 5$ grain boundary investigated with density functional theory molecular dynamics and metadynamics.* The journal of physical chemistry. A, 2014. **118**(5): p. 915-926.
82. Amian, W.S.D., *Diffusion of Silver and Cesium in SiC coating of TRISO fuel particle for HTGCR.* Nuclear Technology, 1983. **61**: p. 475-486.
83. Bullock, R.E., *Fission-Product release during postirradiation annealing of several types of coated fuel-particles.* Journal of Nuclear Materials, 1984. **125**(3): p. 304-319.
84. Kirchhofer, R., et al., *Microstructure of TRISO coated particles from the AGR-1 experiment: SiC grain size and grain boundary character.* Journal of Nuclear Materials, 2013. **432**(1-3): p. 127-134.
85. Joesten, R., *Diffusion, atomic ordering, and mass transport*. Advances in Physical Geochemistry. Vol. 8. 1991, New York, NY: Springer US. 345-395.
86. Kolobov, I.U.R. and Y.R. Kolobov, *Grain boundary diffusion and properties of nanostructured materials*. 2007: Cambridge International Science Pub.
87. Xu, S., et al., *Lithium transport through lithium-ion battery cathode coatings.* Journal of Materials Chemistry A, 2015. **3**(33): p. 17248-17272.
88. Keblinski, P., et al., *Thermodynamic criterion for the stability of amorphous intergranular films in covalent materials.* Physical review letters, 1996. **77**(14): p. 2965-2968.
89. Szlufarska, I., A. Nakano, and P. Vashishta, *A crossover in the mechanical response of nanocrystalline ceramics.* Science, 2005. **309**(5736): p. 911-914.
90. Rino, J., et al., *Short- and intermediate-range structural correlations in amorphous silicon carbide:A molecular dynamics study.* Physical Review B, 2004. **70**(4): p. 045207.
91. Kresse, G. and J. Furthmüller, *Efficiency of ab-initio total energy calculations for metals and semiconductors using a plane-wave basis set.* Computational Materials Science, 1996. **6**(1): p. 15-50.
92. Kresse, G. and J. Furthmüller, *Efficient iterative schemes for ab initio total-energy calculations using a plane-wave basis set.* Physical Review B, 1996. **54**(16): p. 11169-11186.
93. Kresse, G. and J. Hafner, *Ab initio molecular dynamics for liquid metals.* Physical Review B, 1993. **47**(1): p. 558.

94. Kresse, G. and J. Hafner, *Ab-Initio molecular-dynamics simulation of the liquid-metal amorphous-semiconductor transition in germanium.* Physical Review B, 1994. **49**(20): p. 14251-14269.
95. Kresse, G., *From ultrasoft pseudopotentials to the projector augmented-wave method.* Physical Review B, 1999. **59**(3): p. 1758.
96. Perdew, J.P., K. Burke, and M. Ernzerhof, *Generalized gradient approximation made simple.* Physical Review Letters, 1996. **77**(18): p. 3865-3868.
97. Kohan, A.F., et al., *First-principles study of native point defects in ZnO.* Physical Review B, 2000. **61**(22): p. 15019-15027.
98. Hao, S. and D.S. Sholl, *Using first-principles calculations to accelerate materials discovery for hydrogen purification membranes by modeling amorphous metals.* Energy & Environmental Science, 2008. **1**(1): p. 175.
99. Van der Ven, A., et al., *First-principles theory of ionic diffusion with nondilute carriers.* Physical Review B, 2001. **64**(18): p. 184307.
100. Puchala, B. and D. Morgan, *Atomistic modeling of As diffusion in ZnO.* Physical Review B, 2012. **85**(6): p. 064106.
101. Haus, J.W. and K.W. Kehr, *Diffusion in regular and disordered lattices.* Physics Reports-Review Section of Physics Letters, 1987. **150**(5): p. 263-406.
102. Kronmüller, H., W. Frank, and P. Scharwaechter, *Self-Diffusion and Relaxation Processes in Amorphous Metallic Alloys.* Science and Technology of Rapid Solidification and Processing, ed. M. Otooni. Vol. 278. 1995: Springer Netherlands. 271-289.
103. Schirmacher, W., et al., *Anomalous diffusion of hydrogen in amorphous metals.* Europhysics Letters, 1990. **13**(6): p. 523.
104. Kehr, K.W. and T. Wichmann, *Diffusion coefficients of single and many particles in lattices with different forms of disorder.* Materials Science Forum, 1996. **223-224**: p. 151-160.
105. Bortz, A.B., M.H. Kalos, and J.L. Lebowitz, *A new Algorithm for Monte Carlo simulation of Ising spin system.* Journal of Computational physics, 1975. **17**(1): p. 10-18.
106. Karger, J., et al., *Single-file diffusion and reaction in zeolites.* Journal of Catalysis, 1992. **136**(2): p. 283-299.
107. Barnard, L. and D. Morgan, *Ab initio molecular dynamics simulation of interstitial diffusion in Ni–Cr alloys and implications for radiation induced segregation.* Journal of Nuclear Materials, 2014. **449**(1–3): p. 225-233.
108. Bongiorno, A. and A. Pasquarello, *Multiscale modeling of oxygen diffusion through the oxide during silicon oxidation.* Physical Review B, 2004. **70**(19): p. 195312.
109. Hao, S. and D.S. Sholl, *Self-diffusion and macroscopic diffusion of hydrogen in amorphous metals from first-principles calculations.* The Journal of Chemical Physics, 2009. **130**(24): p. 244705.
110. Tritsaris, G.A., et al., *Diffusion of Lithium in Bulk Amorphous Silicon: A Theoretical Study.* The Journal of Physical Chemistry C, 2012. **116**(42): p. 22212-22216.

111. Hao, S. and C. Wolverton, *Lithium transport in Amorphous $Al_2O_3$ and $AlF_3$ for discovery of battery coatings.* The Journal of Physical Chemistry C, 2013. **117**(16): p. 8009-8013.

112. Kong, N., et al., *Interstitial-based boron diffusion dynamics in amorphous silicon.* Applied Physics Letters, 2008. **93**(8): p. 082109.

113. Kuznetsov, A.Y. and B.G. Svensson, *Nickel atomic diffusion in amorphous silicon.* Applied Physics Letters, 1995. **66**(17): p. 2229.

114. Su, Y.S. and S. Pantelides, *Diffusion Mechanism of Hydrogen in Amorphous Silicon: Ab Initio Molecular Dynamics Simulation.* Physical Review Letters, 2002. **88**(16): p. 165503.

115. Liu, X.Y., et al., *First-principles study of phosphorus diffusion in silicon: Interstitial- and vacancy-mediated diffusion mechanisms.* Applied Physics Letters, 2003. **82**(12): p. 1839-1841.

116. Ahn, S. and J.A. Fessler, *Standard errors of mean, variance , and standard deviation estimators*. 2003, Univ. of Michigan, Ann Arbor: Univ. of Michigan, Ann Arbor. p. 1-2.

117. Norris, N., *The Standard Errors of the Geometric and Harmonic Means and Their Application to Index Numbers.* Ann. Math. Statist., 1940. **11**(4): p. 445-448.

118. Maclean, H.J., *Silver Transport in CVD Silicon Carbide*. 2004, Massachusetts Institute of Technology.

119. Leng, B., et al., *Effect of carbon irradiation on Ag diffusion in ion implanted SiC.* journal of Nuclear Materials, *In press*.

120. Dienes, G.J. and A.C. Damask, *Radiation Enhanced Diffusion in Solids.* Journal of Applied Physics, 1958. **29**(12): p. 1713-1721.

121. Sizmann, R., *The effect of radiation upon diffusion in metals.* Journal of Nuclear Materials, 1978. **69–70**: p. 386-412.

122. Leveque, P., et al., *Irradiation enhanced diffusion of boron in delta-doped silicon.* Journal of Applied Physics, 2001. **89**(10): p. 5400-5405.

123. Snead, L.L., et al., *Handbook of SiC properties for fuel performance modeling.* Journal of Nuclear Materials, 2007. **371**: p. 329-377.

124. Ko, H., et al., *Ag diffusion in SiC high-energy grain boundaries: kinetic Monte Carlo study with first-principle calculations.* Submitted to Acta Mater.

125. Bracht, H. and E.E. Haller, *Comment on ``Self-Diffusion in Silicon: Similarity between the Properties of Native Point Defects''.* Physical Review Letters, 2000. **85**(22): p. 4835-4835.

126. Amian, W. and D. Stover, *Diffusion of Silver and Cesium in SiC coating of TRISO fuel particle for HTGCR.* Nuclear Technology, 1983. **61**: p. 475-486.

127. Odette, G.R., T. Yamamoto, and D. Klingensmith, *On the effect of dose rate on irradiation hardening of RPV steels.* Philosophical Magazine, 2005. **85**(4-7): p. 779-797.

128. Watanabe, Y., K. Morishita, and Y. Yamamoto, *Nucleation and growth of self-interstitial atom clusters in $\beta$-SiC during irradiation: Kinetic Monte-Carlo modeling.* Nuclear Instruments and Methods in Physics Research Section B: Beam Interactions with Materials and Atoms, 2011. **269**(14): p. 1698-1701.

129. He, L., et al. *High-Resolution Scanning Transmission Electron Microscopy Study of Black Spot Defects in Ion Irradiated Silicon Carbide*. in *Microscopy and Microanalysis*. 2014.
130. Vitaly, V.S., *Kinetics of First Order Phase Transitions*. 2009.
131. Watanabe, Y., K. Morishita, and A. Kohyama, *Composition dependence of formation energy of self-interstitial atom clusters in β-SiC: Molecular dynamics and molecular statics calculations.* Journal of Nuclear Materials, 2011. **417**(1 – 3): p. 1119-1122.
132. Watanabe, Y., et al., *Energetics of defects in β-SiC under irradiation.* Nuclear Instruments and Methods in Physics Research Section B: Beam Interactions with Materials and Atoms, 2009. **267**(18): p. 3223-3226.
133. Jiang, C., D. Morgan, and I. Szlufarska, *Structures and stabilities of small carbon interstitial clusters in cubic silicon carbide.* Acta Materialia, 2014. **62**: p. 162-172.
134. IAEA, *Fuel performance and fission product behaviour in gas cooled reactors*. 1997, IAEA- TECDOC-978: International Atomic Energy Agency.
135. Bottiger, J., K. Pampus, and B. Torp, *Diffusion during Ion Irradiation in Amorphous PdCuSi.* Europhysics Letters, 1987. **4**(8): p. 915-919.
136. Dyrbye, K., et al., *Radiation-enhanced diffusion in amorphous Pd-Cu-Si.* Physical review B, 1988. **38**(13): p. 8562-8565.
137. Scharwaechter, P., W. Frank, and H. Kronmuller, *Diffusion in amorphous metallic alloys, particularly* $Co_{58}Fe_{5}Ni_{10}Si_{11}B_{16}$. Zeitschrift Fur Metallkunde, 1996. **87**(11): p. 892-897.
138. Priolo, F., et al., *Diffusion of Au in amorphous Si during ion-beam irradiation.* Fundamentals of Beam-Solid Interactions and Transient Thermal Processing. Symposium, 1988: p. 87-92.
139. Priolo, F., et al., *Radiation-enhanced diffuion of Au in amorphous Si.* Applied Physics Letters, 1988. **52**(15): p. 1213-1215.
140. Averback, R. and H. Hahn, *Radiation-enhanced diffusion in amorphous Ni-Zr alloys.* Physical Review B, 1988. **37**(17): p. 10383-10386.
141. Bellini, S., A. Montone, and M. Vittori-Antisari, *Radiation-enhanced diffusion in amorphous Ni-Zr studied by in situ electron irradiation in a transmission electron microscope.* Physical Review B, 1994. **50**(14): p. 9803-9809.
142. Schuler, T., et al., *Irradiation-enhanced self-diffusion in amorphous metallic alloys - experiments, molecular-dynamics simulations, interpretation.* Defect and diffusion forum 1997. **143**: p. 753-758.

# 9 Appendices

# Appendix A

## Summary of results for Task 4 “Co-incorporation of Ag with other elements”

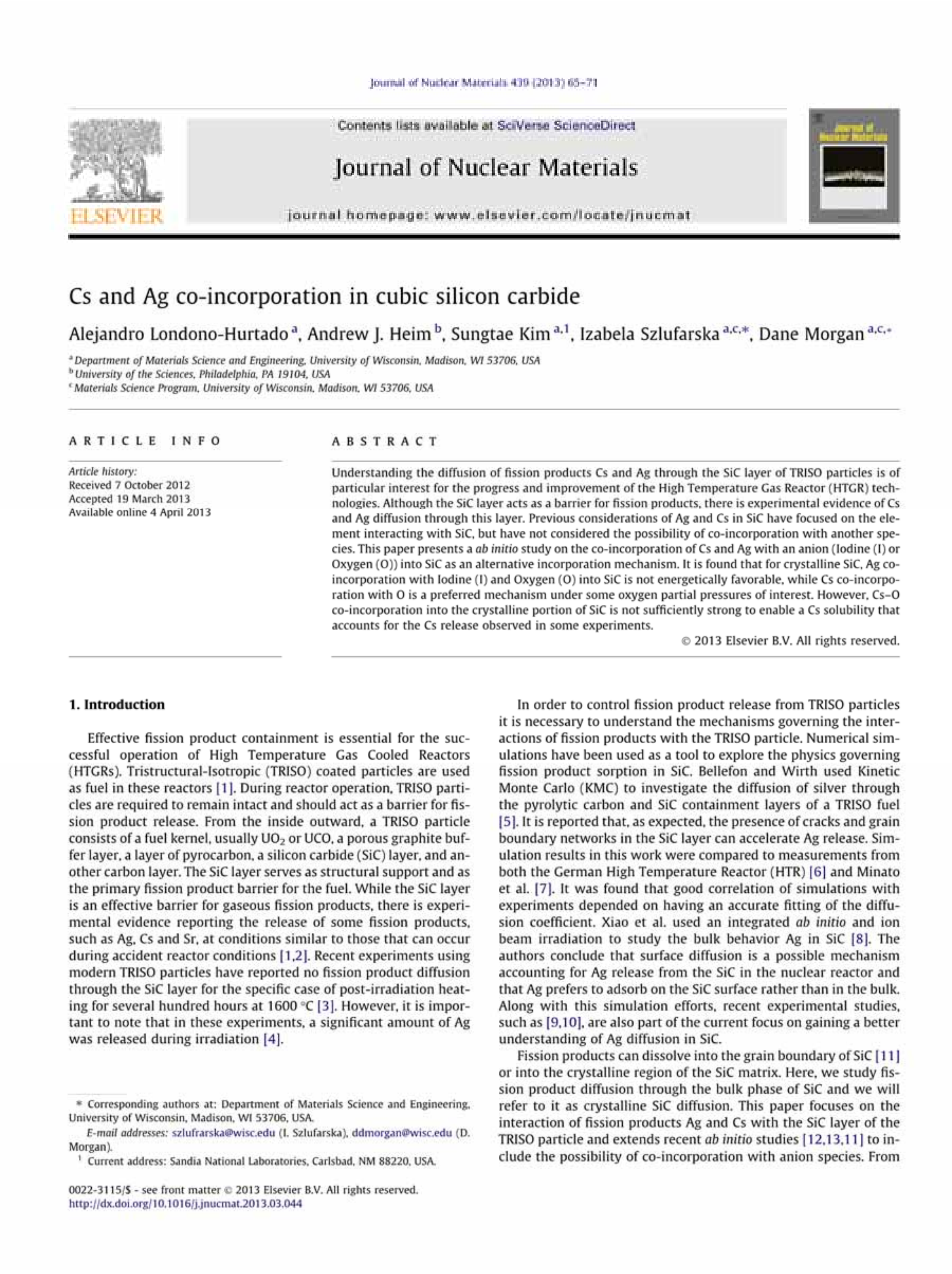

Journal of Nuclear Materials 439 (2013) 65–71

Contents lists available at SciVerse ScienceDirect

Journal of Nuclear Materials

journal homepage: www.elsevier.com/locate/jnucmat

# Cs and Ag co-incorporation in cubic silicon carbide

Alejandro Londono-Hurtado [a], Andrew J. Heim [b], Sungtae Kim [a,1], Izabela Szlufarska [a,c,*], Dane Morgan [a,c,*]

[a] Department of Materials Science and Engineering, University of Wisconsin, Madison, WI 53706, USA
[b] University of the Sciences, Philadelphia, PA 19104, USA
[c] Materials Science Program, University of Wisconsin, Madison, WI 53706, USA

ARTICLE INFO

*Article history:*
Received 7 October 2012
Accepted 19 March 2013
Available online 4 April 2013

ABSTRACT

Understanding the diffusion of fission products Cs and Ag through the SiC layer of TRISO particles is of particular interest for the progress and improvement of the High Temperature Gas Reactor (HTGR) technologies. Although the SiC layer acts as a barrier for fission products, there is experimental evidence of Cs and Ag diffusion through this layer. Previous considerations of Ag and Cs in SiC have focused on the element interacting with SiC, but have not considered the possibility of co-incorporation with another species. This paper presents a *ab initio* study on the co-incorporation of Cs and Ag with an anion (Iodine (I) or Oxygen (O)) into SiC as an alternative incorporation mechanism. It is found that for crystalline SiC, Ag co-incorporation with Iodine (I) and Oxygen (O) into SiC is not energetically favorable, while Cs co-incorporation with O is a preferred mechanism under some oxygen partial pressures of interest. However, Cs–O co-incorporation into the crystalline portion of SiC is not sufficiently strong to enable a Cs solubility that accounts for the Cs release observed in some experiments.

© 2013 Elsevier B.V. All rights reserved.

## 1. Introduction

Effective fission product containment is essential for the successful operation of High Temperature Gas Cooled Reactors (HTGRs). Tristructural-Isotropic (TRISO) coated particles are used as fuel in these reactors [1]. During reactor operation, TRISO particles are required to remain intact and should act as a barrier for fission product release. From the inside outward, a TRISO particle consists of a fuel kernel, usually $UO_2$ or UCO, a porous graphite buffer layer, a layer of pyrocarbon, a silicon carbide (SiC) layer, and another carbon layer. The SiC layer serves as structural support and as the primary fission product barrier for the fuel. While the SiC layer is an effective barrier for gaseous fission products, there is experimental evidence reporting the release of some fission products, such as Ag, Cs and Sr, at conditions similar to those that can occur during accident reactor conditions [1,2]. Recent experiments using modern TRISO particles have reported no fission product diffusion through the SiC layer for the specific case of post-irradiation heating for several hundred hours at 1600 °C [3]. However, it is important to note that in these experiments, a significant amount of Ag was released during irradiation [4].

In order to control fission product release from TRISO particles it is necessary to understand the mechanisms governing the interactions of fission products with the TRISO particle. Numerical simulations have been used as a tool to explore the physics governing fission product sorption in SiC. Bellefon and Wirth used Kinetic Monte Carlo (KMC) to investigate the diffusion of silver through the pyrolytic carbon and SiC containment layers of a TRISO fuel [5]. It is reported that, as expected, the presence of cracks and grain boundary networks in the SiC layer can accelerate Ag release. Simulation results in this work were compared to measurements from both the German High Temperature Reactor (HTR) [6] and Minato et al. [7]. It was found that good correlation of simulations with experiments depended on having an accurate fitting of the diffusion coefficient. Xiao et al. used an integrated *ab initio* and ion beam irradiation to study the bulk behavior Ag in SiC [8]. The authors conclude that surface diffusion is a possible mechanism accounting for Ag release from the SiC in the nuclear reactor and that Ag prefers to adsorb on the SiC surface rather than in the bulk. Along with this simulation efforts, recent experimental studies, such as [9,10], are also part of the current focus on gaining a better understanding of Ag diffusion in SiC.

Fission products can dissolve into the grain boundary of SiC [11] or into the crystalline region of the SiC matrix. Here, we study fission product diffusion through the bulk phase of SiC and we will refer to it as crystalline SiC diffusion. This paper focuses on the interaction of fission products Ag and Cs with the SiC layer of the TRISO particle and extends recent *ab initio* studies [12,13,11] to include the possibility of co-incorporation with anion species. From

---

[*] Corresponding authors at: Department of Materials Science and Engineering, University of Wisconsin, Madison, WI 53706, USA.

*E-mail addresses:* szlufrarska@wisc.edu (I. Szlufarska), ddmorgan@wisc.edu (D. Morgan).

[1] Current address: Sandia National Laboratories, Carlsbad, NM 88220, USA.

0022-3115/$ - see front matter © 2013 Elsevier B.V. All rights reserved.
http://dx.doi.org/10.1016/j.jnucmat.2013.03.044

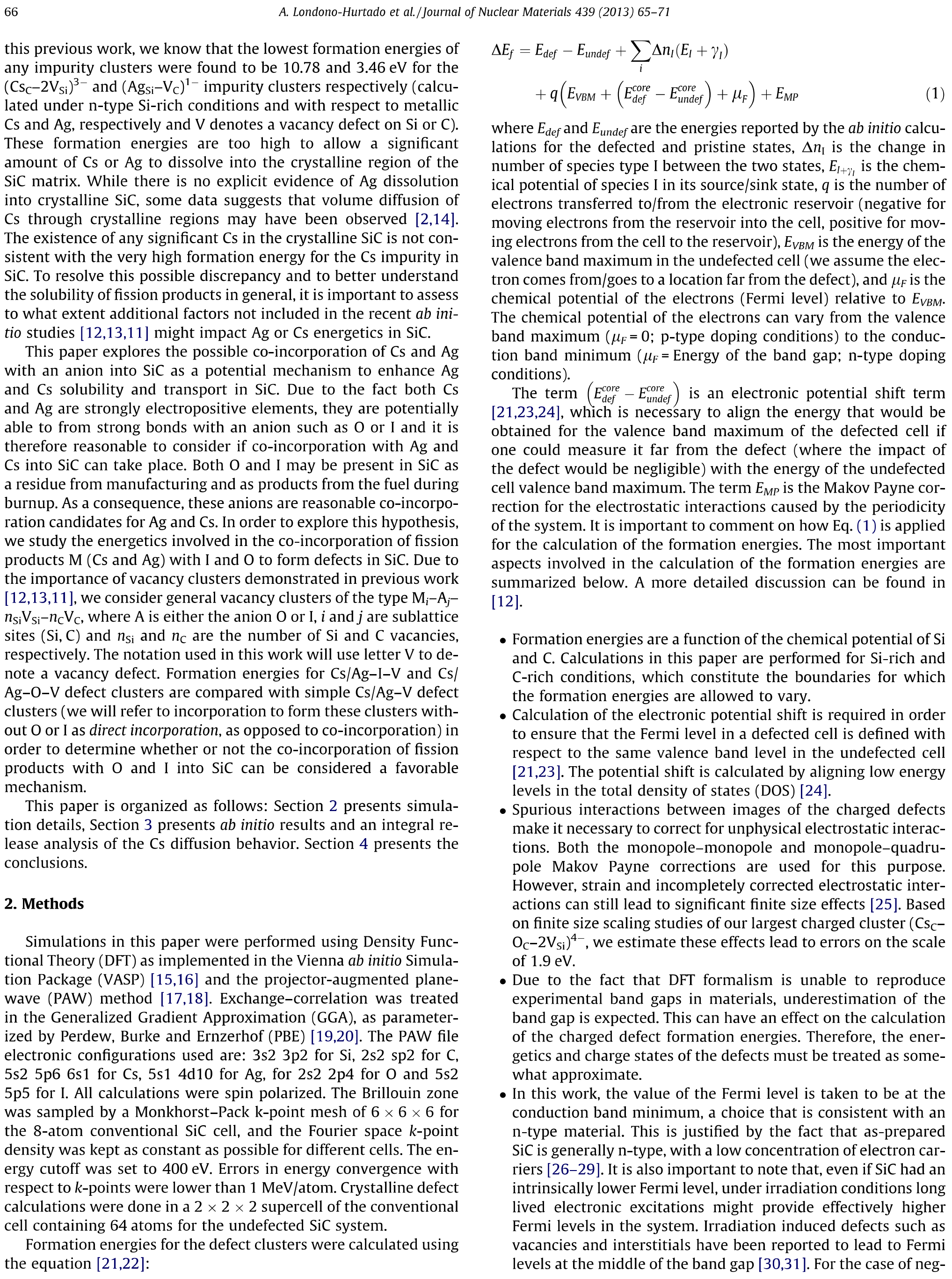

this previous work, we know that the lowest formation energies of any impurity clusters were found to be 10.78 and 3.46 eV for the $(Cs_C{-}2V_{Si})^{3-}$ and $(Ag_{Si}{-}V_C)^{1-}$ impurity clusters respectively (calculated under n-type Si-rich conditions and with respect to metallic Cs and Ag, respectively and V denotes a vacancy defect on Si or C). These formation energies are too high to allow a significant amount of Cs or Ag to dissolve into the crystalline region of the SiC matrix. While there is no explicit evidence of Ag dissolution into crystalline SiC, some data suggests that volume diffusion of Cs through crystalline regions may have been observed [2,14]. The existence of any significant Cs in the crystalline SiC is not consistent with the very high formation energy for the Cs impurity in SiC. To resolve this possible discrepancy and to better understand the solubility of fission products in general, it is important to assess to what extent additional factors not included in the recent *ab initio* studies [12,13,11] might impact Ag or Cs energetics in SiC.

This paper explores the possible co-incorporation of Cs and Ag with an anion into SiC as a potential mechanism to enhance Ag and Cs solubility and transport in SiC. Due to the fact both Cs and Ag are strongly electropositive elements, they are potentially able to from strong bonds with an anion such as O or I and it is therefore reasonable to consider if co-incorporation with Ag and Cs into SiC can take place. Both O and I may be present in SiC as a residue from manufacturing and as products from the fuel during burnup. As a consequence, these anions are reasonable co-incorporation candidates for Ag and Cs. In order to explore this hypothesis, we study the energetics involved in the co-incorporation of fission products M (Cs and Ag) with I and O to form defects in SiC. Due to the importance of vacancy clusters demonstrated in previous work [12,13,11], we consider general vacancy clusters of the type $M_i{-}A_j{-}n_{Si}V_{Si}{-}n_CV_C$, where A is either the anion O or I, $i$ and $j$ are sublattice sites (Si, C) and $n_{Si}$ and $n_C$ are the number of Si and C vacancies, respectively. The notation used in this work will use letter V to denote a vacancy defect. Formation energies for Cs/Ag–I–V and Cs/Ag–O–V defect clusters are compared with simple Cs/Ag–V defect clusters (we will refer to incorporation to form these clusters without O or I as *direct incorporation*, as opposed to co-incorporation) in order to determine whether or not the co-incorporation of fission products with O and I into SiC can be considered a favorable mechanism.

This paper is organized as follows: Section 2 presents simulation details, Section 3 presents *ab initio* results and an integral release analysis of the Cs diffusion behavior. Section 4 presents the conclusions.

## 2. Methods

Simulations in this paper were performed using Density Functional Theory (DFT) as implemented in the Vienna *ab initio* Simulation Package (VASP) [15,16] and the projector-augmented planewave (PAW) method [17,18]. Exchange–correlation was treated in the Generalized Gradient Approximation (GGA), as parameterized by Perdew, Burke and Ernzerhof (PBE) [19,20]. The PAW file electronic configurations used are: 3s2 3p2 for Si, 2s2 sp2 for C, 5s2 5p6 6s1 for Cs, 5s1 4d10 for Ag, for 2s2 2p4 for O and 5s2 5p5 for I. All calculations were spin polarized. The Brillouin zone was sampled by a Monkhorst–Pack k-point mesh of 6 × 6 × 6 for the 8-atom conventional SiC cell, and the Fourier space *k*-point density was kept as constant as possible for different cells. The energy cutoff was set to 400 eV. Errors in energy convergence with respect to *k*-points were lower than 1 MeV/atom. Crystalline defect calculations were done in a 2 × 2 × 2 supercell of the conventional cell containing 64 atoms for the undefected SiC system.

Formation energies for the defect clusters were calculated using the equation [21,22]:

$$\Delta E_f = E_{def} - E_{undef} + \sum_i \Delta n_I (E_I + \gamma_I) + q\left(E_{VBM} + \left(E^{core}_{def} - E^{core}_{undef}\right) + \mu_F\right) + E_{MP} \qquad (1)$$

where $E_{def}$ and $E_{undef}$ are the energies reported by the *ab initio* calculations for the defected and pristine states, $\Delta n_I$ is the change in number of species type I between the two states, $E_{I+\gamma_I}$ is the chemical potential of species I in its source/sink state, $q$ is the number of electrons transferred to/from the electronic reservoir (negative for moving electrons from the reservoir into the cell, positive for moving electrons from the cell to the reservoir), $E_{VBM}$ is the energy of the valence band maximum in the undefected cell (we assume the electron comes from/goes to a location far from the defect), and $\mu_F$ is the chemical potential of the electrons (Fermi level) relative to $E_{VBM}$. The chemical potential of the electrons can vary from the valence band maximum ($\mu_F = 0$; p-type doping conditions) to the conduction band minimum ($\mu_F$ = Energy of the band gap; n-type doping conditions).

The term $\left(E^{core}_{def} - E^{core}_{undef}\right)$ is an electronic potential shift term [21,23,24], which is necessary to align the energy that would be obtained for the valence band maximum of the defected cell if one could measure it far from the defect (where the impact of the defect would be negligible) with the energy of the undefected cell valence band maximum. The term $E_{MP}$ is the Makov Payne correction for the electrostatic interactions caused by the periodicity of the system. It is important to comment on how Eq. (1) is applied for the calculation of the formation energies. The most important aspects involved in the calculation of the formation energies are summarized below. A more detailed discussion can be found in [12].

- Formation energies are a function of the chemical potential of Si and C. Calculations in this paper are performed for Si-rich and C-rich conditions, which constitute the boundaries for which the formation energies are allowed to vary.
- Calculation of the electronic potential shift is required in order to ensure that the Fermi level in a defected cell is defined with respect to the same valence band level in the undefected cell [21,23]. The potential shift is calculated by aligning low energy levels in the total density of states (DOS) [24].
- Spurious interactions between images of the charged defects make it necessary to correct for unphysical electrostatic interactions. Both the monopole–monopole and monopole–quadrupole Makov Payne corrections are used for this purpose. However, strain and incompletely corrected electrostatic interactions can still lead to significant finite size effects [25]. Based on finite size scaling studies of our largest charged cluster $(Cs_C{-}O_C{-}2V_{Si})^{4-}$, we estimate these effects lead to errors on the scale of 1.9 eV.
- Due to the fact that DFT formalism is unable to reproduce experimental band gaps in materials, underestimation of the band gap is expected. This can have an effect on the calculation of the charged defect formation energies. Therefore, the energetics and charge states of the defects must be treated as somewhat approximate.
- In this work, the value of the Fermi level is taken to be at the conduction band minimum, a choice that is consistent with an n-type material. This is justified by the fact that as-prepared SiC is generally n-type, with a low concentration of electron carriers [26–29]. It is also important to note that, even if SiC had an intrinsically lower Fermi level, under irradiation conditions long lived electronic excitations might provide effectively higher Fermi levels in the system. Irradiation induced defects such as vacancies and interstitials have been reported to lead to Fermi levels at the middle of the band gap [30,31]. For the case of neg-

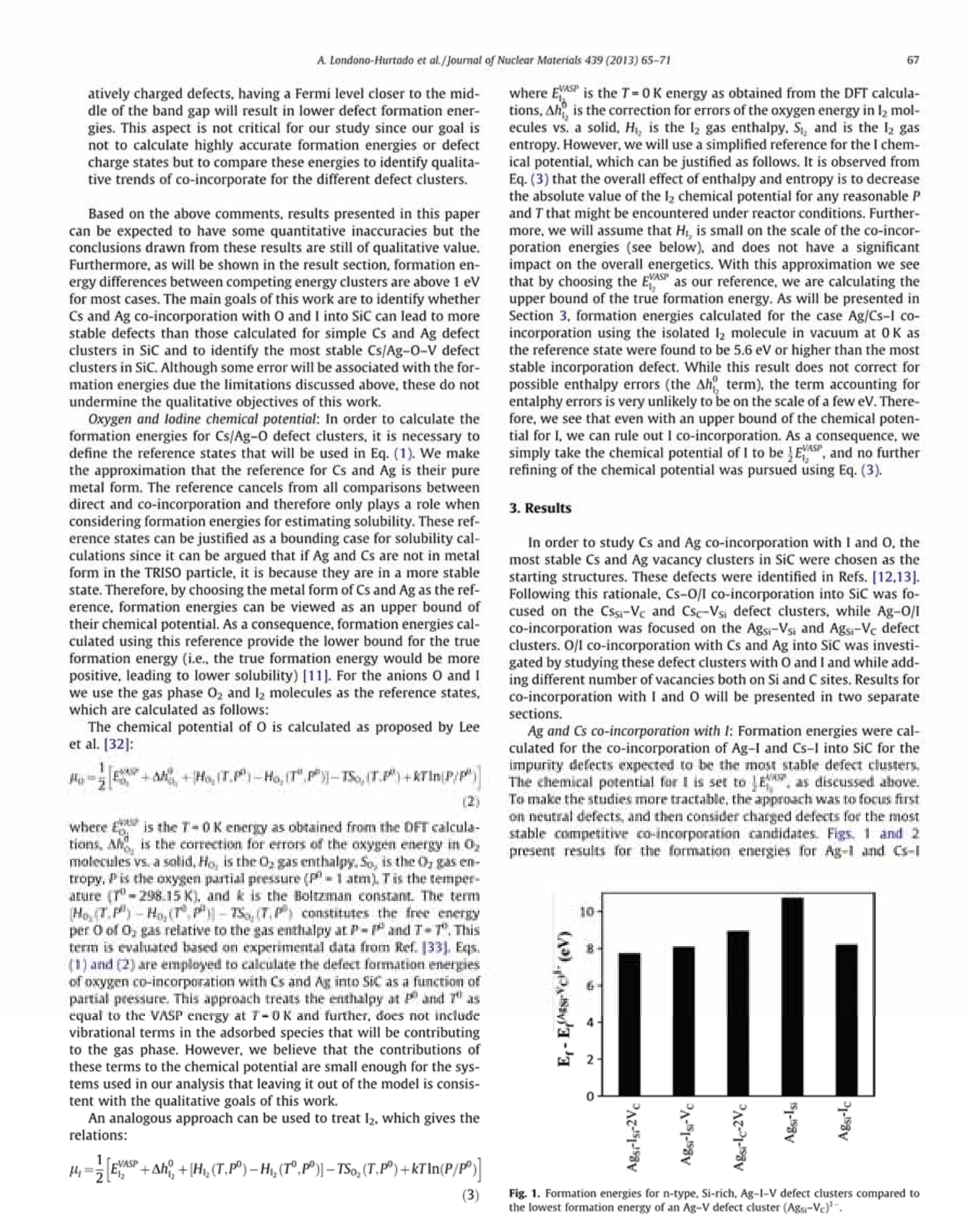

atively charged defects, having a Fermi level closer to the middle of the band gap will result in lower defect formation energies. This aspect is not critical for our study since our goal is not to calculate highly accurate formation energies or defect charge states but to compare these energies to identify qualitative trends of co-incorporate for the different defect clusters.

Based on the above comments, results presented in this paper can be expected to have some quantitative inaccuracies but the conclusions drawn from these results are still of qualitative value. Furthermore, as will be shown in the result section, formation energy differences between competing energy clusters are above 1 eV for most cases. The main goals of this work are to identify whether Cs and Ag co-incorporation with O and I into SiC can lead to more stable defects than those calculated for simple Cs and Ag defect clusters in SiC and to identify the most stable Cs/Ag–O–V defect clusters in SiC. Although some error will be associated with the formation energies due the limitations discussed above, these do not undermine the qualitative objectives of this work.

*Oxygen and Iodine chemical potential*: In order to calculate the formation energies for Cs/Ag–O defect clusters, it is necessary to define the reference states that will be used in Eq. (1). We make the approximation that the reference for Cs and Ag is their pure metal form. The reference cancels from all comparisons between direct and co-incorporation and therefore only plays a role when considering formation energies for estimating solubility. These reference states can be justified as a bounding case for solubility calculations since it can be argued that if Ag and Cs are not in metal form in the TRISO particle, it is because they are in a more stable state. Therefore, by choosing the metal form of Cs and Ag as the reference, formation energies can be viewed as an upper bound of their chemical potential. As a consequence, formation energies calculated using this reference provide the lower bound for the true formation energy (i.e., the true formation energy would be more positive, leading to lower solubility) [11]. For the anions O and I we use the gas phase $O_2$ and $I_2$ molecules as the reference states, which are calculated as follows:

The chemical potential of O is calculated as proposed by Lee et al. [32]:

$$\mu_O = \frac{1}{2}\left[E_{O_2}^{VASP} + \Delta h_{O_2}^0 + [H_{O_2}(T,P^0) - H_{O_2}(T^0,P^0)] - TS_{O_2}(T,P^0) + kT\ln(P/P^0)\right] \tag{2}$$

where $E_{O_2}^{VASP}$ is the $T = 0$ K energy as obtained from the DFT calculations, $\Delta h_{O_2}^0$ is the correction for errors of the oxygen energy in $O_2$ molecules vs. a solid, $H_{O_2}$ is the $O_2$ gas enthalpy, $S_{O_2}$ is the $O_2$ gas entropy, $P$ is the oxygen partial pressure ($P^0 = 1$ atm), $T$ is the temperature ($T^0 = 298.15$ K), and $k$ is the Boltzman constant. The term $[H_{O_2}(T,P^0) - H_{O_2}(T^0,P^0)] - TS_{O_2}(T,P^0)$ constitutes the free energy per O of $O_2$ gas relative to the gas enthalpy at $P = P^0$ and $T = T^0$. This term is evaluated based on experimental data from Ref. [33]. Eqs. (1) and (2) are employed to calculate the defect formation energies of oxygen co-incorporation with Cs and Ag into SiC as a function of partial pressure. This approach treats the enthalpy at $P^0$ and $T^0$ as equal to the VASP energy at $T = 0$ K and further, does not include vibrational terms in the adsorbed species that will be contributing to the gas phase. However, we believe that the contributions of these terms to the chemical potential are small enough for the systems used in our analysis that leaving it out of the model is consistent with the qualitative goals of this work.

An analogous approach can be used to treat $I_2$, which gives the relations:

$$\mu_I = \frac{1}{2}\left[E_{I_2}^{VASP} + \Delta h_{I_2}^0 + [H_{I_2}(T,P^0) - H_{I_2}(T^0,P^0)] - TS_{O_2}(T,P^0) + kT\ln(P/P^0)\right] \tag{3}$$

where $E_{I_2}^{VASP}$ is the $T = 0$ K energy as obtained from the DFT calculations, $\Delta h_{I_2}^0$ is the correction for errors of the oxygen energy in $I_2$ molecules vs. a solid, $H_{I_2}$ is the $I_2$ gas enthalpy, $S_{I_2}$ and is the $I_2$ gas entropy. However, we will use a simplified reference for the I chemical potential, which can be justified as follows. It is observed from Eq. (3) that the overall effect of enthalpy and entropy is to decrease the absolute value of the $I_2$ chemical potential for any reasonable $P$ and $T$ that might be encountered under reactor conditions. Furthermore, we will assume that $H_{I_2}$ is small on the scale of the co-incorporation energies (see below), and does not have a significant impact on the overall energetics. With this approximation we see that by choosing the $E_{I_2}^{VASP}$ as our reference, we are calculating the upper bound of the true formation energy. As will be presented in Section 3, formation energies calculated for the case Ag/Cs–I co-incorporation using the isolated $I_2$ molecule in vacuum at 0 K as the reference state were found to be 5.6 eV or higher than the most stable incorporation defect. While this result does not correct for possible enthalpy errors (the $\Delta h_{I_2}^0$ term), the term accounting for entalphy errors is very unlikely to be on the scale of a few eV. Therefore, we see that even with an upper bound of the chemical potential for I, we can rule out I co-incorporation. As a consequence, we simply take the chemical potential of I to be $\frac{1}{2}E_{I_2}^{VASP}$, and no further refining of the chemical potential was pursued using Eq. (3).

## 3. Results

In order to study Cs and Ag co-incorporation with I and O, the most stable Cs and Ag vacancy clusters in SiC were chosen as the starting structures. These defects were identified in Refs. [12,13]. Following this rationale, Cs–O/I co-incorporation into SiC was focused on the $Cs_{Si}$–$V_C$ and $Cs_C$–$V_{Si}$ defect clusters, while Ag–O/I co-incorporation was focused on the $Ag_{Si}$–$V_{Si}$ and $Ag_{Si}$–$V_C$ defect clusters. O/I co-incorporation with Cs and Ag into SiC was investigated by studying these defect clusters with O and I and while adding different number of vacancies both on Si and C sites. Results for co-incorporation with I and O will be presented in two separate sections.

*Ag and Cs co-incorporation with I*: Formation energies were calculated for the co-incorporation of Ag–I and Cs–I into SiC for the impurity defects expected to be the most stable defect clusters. The chemical potential for I is set to $\frac{1}{2}E_{I_2}^{VASP}$, as discussed above. To make the studies more tractable, the approach was to focus first on neutral defects, and then consider charged defects for the most stable competitive co-incorporation candidates. Figs. 1 and 2 present results for the formation energies for Ag–I and Cs–I

**Fig. 1.** Formation energies for n-type, Si-rich, Ag–I–V defect clusters compared to the lowest formation energy of an Ag–V defect cluster $(Ag_{Si}–V_C)^{1-}$.

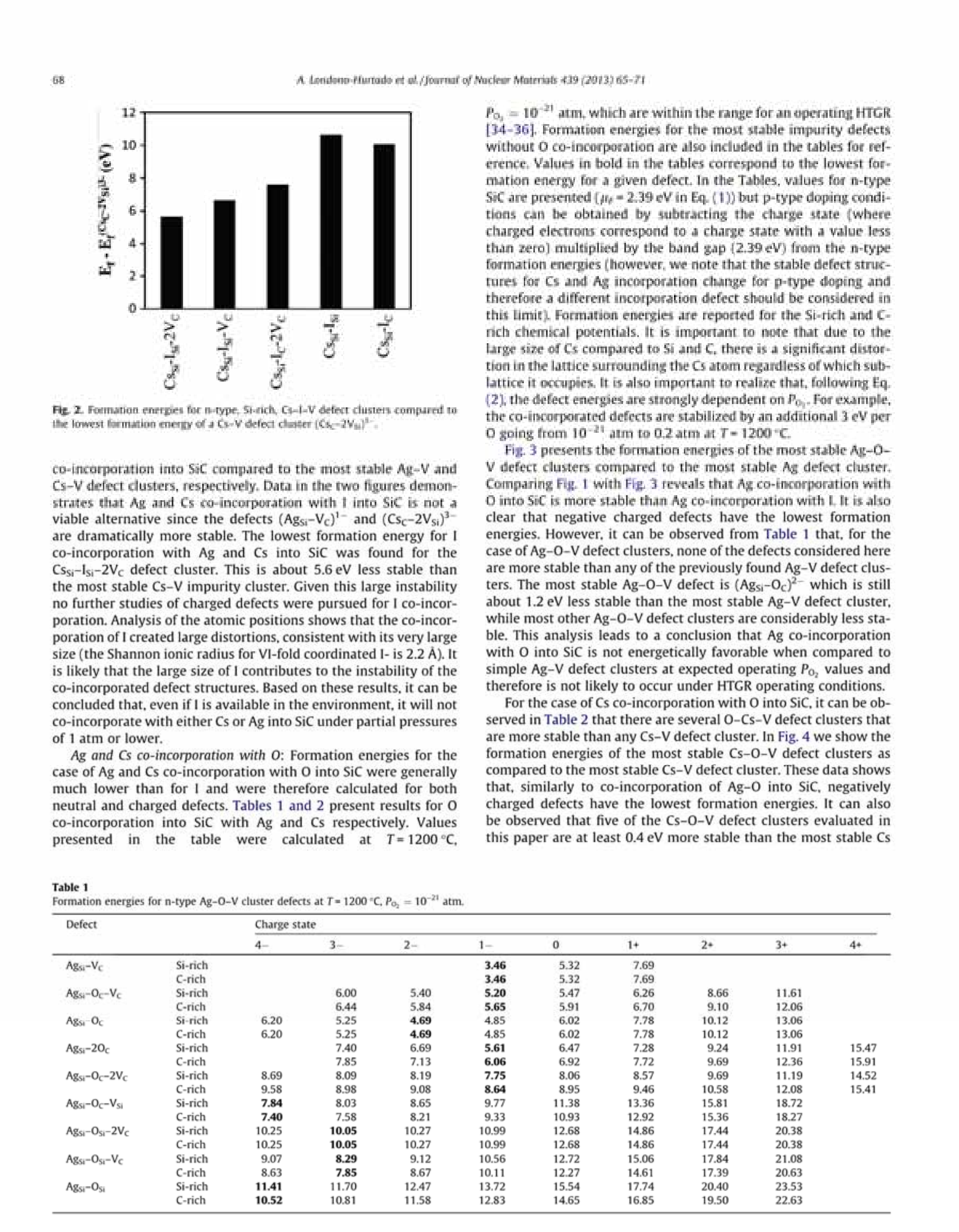
12
10
8
6
4
2
0
$E_f - E_f^{(Cs_C-2V_{Si})^{3-}}$ (eV)
$Cs_{Si}$-$I_{Si}$-$2V_C$
$Cs_{Si}$-$I_{Si}$-$V_C$
$Cs_{Si}$-$I_C$-$2V_C$
$Cs_{Si}$-$I_{Si}$
$Cs_{Si}$-$I_C$

**Fig. 2.** Formation energies for n-type, Si-rich, Cs–I–V defect clusters compared to the lowest formation energy of a Cs–V defect cluster $(Cs_C–2V_{Si})^{3-}$.

co-incorporation into SiC compared to the most stable Ag–V and Cs–V defect clusters, respectively. Data in the two figures demonstrates that Ag and Cs co-incorporation with I into SiC is not a viable alternative since the defects $(Ag_{Si}–V_C)^{1-}$ and $(Cs_C–2V_{Si})^{3-}$ are dramatically more stable. The lowest formation energy for I co-incorporation with Ag and Cs into SiC was found for the $Cs_{Si}–I_{Si}–2V_C$ defect cluster. This is about 5.6 eV less stable than the most stable Cs–V impurity cluster. Given this large instability no further studies of charged defects were pursued for I co-incorporation. Analysis of the atomic positions shows that the co-incorporation of I created large distortions, consistent with its very large size (the Shannon ionic radius for VI-fold coordinated I- is 2.2 Å). It is likely that the large size of I contributes to the instability of the co-incorporated defect structures. Based on these results, it can be concluded that, even if I is available in the environment, it will not co-incorporate with either Cs or Ag into SiC under partial pressures of 1 atm or lower.

*Ag and Cs co-incorporation with O*: Formation energies for the case of Ag and Cs co-incorporation with O into SiC were generally much lower than for I and were therefore calculated for both neutral and charged defects. Tables 1 and 2 present results for O co-incorporation into SiC with Ag and Cs respectively. Values presented in the table were calculated at $T = 1200$ °C, $P_{O_2} = 10^{-21}$ atm, which are within the range for an operating HTGR [34–36]. Formation energies for the most stable impurity defects without O co-incorporation are also included in the tables for reference. Values in bold in the tables correspond to the lowest formation energy for a given defect. In the Tables, values for n-type SiC are presented ($\mu_F = 2.39$ eV in Eq. (1)) but p-type doping conditions can be obtained by subtracting the charge state (where charged electrons correspond to a charge state with a value less than zero) multiplied by the band gap (2.39 eV) from the n-type formation energies (however, we note that the stable defect structures for Cs and Ag incorporation change for p-type doping and therefore a different incorporation defect should be considered in this limit). Formation energies are reported for the Si-rich and C-rich chemical potentials. It is important to note that due to the large size of Cs compared to Si and C, there is a significant distortion in the lattice surrounding the Cs atom regardless of which sublattice it occupies. It is also important to realize that, following Eq. (2), the defect energies are strongly dependent on $P_{O_2}$. For example, the co-incorporated defects are stabilized by an additional 3 eV per O going from $10^{-21}$ atm to 0.2 atm at $T = 1200$ °C.

Fig. 3 presents the formation energies of the most stable Ag–O–V defect clusters compared to the most stable Ag defect cluster. Comparing Fig. 1 with Fig. 3 reveals that Ag co-incorporation with O into SiC is more stable than Ag co-incorporation with I. It is also clear that negative charged defects have the lowest formation energies. However, it can be observed from Table 1 that, for the case of Ag–O–V defect clusters, none of the defects considered here are more stable than any of the previously found Ag–V defect clusters. The most stable Ag–O–V defect is $(Ag_{Si}–O_C)^{2-}$ which is still about 1.2 eV less stable than the most stable Ag–V defect cluster, while most other Ag–O–V defect clusters are considerably less stable. This analysis leads to a conclusion that Ag co-incorporation with O into SiC is not energetically favorable when compared to simple Ag–V defect clusters at expected operating $P_{O_2}$ values and therefore is not likely to occur under HTGR operating conditions.

For the case of Cs co-incorporation with O into SiC, it can be observed in Table 2 that there are several O–Cs–V defect clusters that are more stable than any Cs–V defect cluster. In Fig. 4 we show the formation energies of the most stable Cs–O–V defect clusters as compared to the most stable Cs–V defect cluster. These data shows that, similarly to co-incorporation of Ag–O into SiC, negatively charged defects have the lowest formation energies. It can also be observed that five of the Cs–O–V defect clusters evaluated in this paper are at least 0.4 eV more stable than the most stable Cs

**Table 1**
Formation energies for n-type Ag–O–V cluster defects at $T = 1200$ °C, $P_{O_2} = 10^{-21}$ atm.

| Defect | | Charge state | | | | | | | | |
|---|---|---|---|---|---|---|---|---|---|---|
| | | 4– | 3– | 2– | 1– | 0 | 1+ | 2+ | 3+ | 4+ |
| $Ag_{Si}–V_C$ | Si-rich | | | | **3.46** | 5.32 | 7.69 | | | |
| | C-rich | | | | **3.46** | 5.32 | 7.69 | | | |
| $Ag_{Si}–O_C–V_C$ | Si-rich | | 6.00 | 5.40 | **5.20** | 5.47 | 6.26 | 8.66 | 11.61 | |
| | C-rich | | 6.44 | 5.84 | **5.65** | 5.91 | 6.70 | 9.10 | 12.06 | |
| $Ag_{Si}–O_C$ | Si-rich | 6.20 | 5.25 | **4.69** | 4.85 | 6.02 | 7.78 | 10.12 | 13.06 | |
| | C-rich | 6.20 | 5.25 | **4.69** | 4.85 | 6.02 | 7.78 | 10.12 | 13.06 | |
| $Ag_{Si}–2O_C$ | Si-rich | | 7.40 | 6.69 | **5.61** | 6.47 | 7.28 | 9.24 | 11.91 | 15.47 |
| | C-rich | | 7.85 | 7.13 | **6.06** | 6.92 | 7.72 | 9.69 | 12.36 | 15.91 |
| $Ag_{Si}–O_C–2V_C$ | Si-rich | 8.69 | 8.09 | 8.19 | **7.75** | 8.06 | 8.57 | 9.69 | 11.19 | 14.52 |
| | C-rich | 9.58 | 8.98 | 9.08 | **8.64** | 8.95 | 9.46 | 10.58 | 12.08 | 15.41 |
| $Ag_{Si}–O_C–V_{Si}$ | Si-rich | **7.84** | 8.03 | 8.65 | 9.77 | 11.38 | 13.36 | 15.81 | 18.72 | |
| | C-rich | **7.40** | 7.58 | 8.21 | 9.33 | 10.93 | 12.92 | 15.36 | 18.27 | |
| $Ag_{Si}–O_{Si}–2V_C$ | Si-rich | 10.25 | **10.05** | 10.27 | 10.99 | 12.68 | 14.86 | 17.44 | 20.38 | |
| | C-rich | 10.25 | **10.05** | 10.27 | 10.99 | 12.68 | 14.86 | 17.44 | 20.38 | |
| $Ag_{Si}–O_{Si}–V_C$ | Si-rich | 9.07 | **8.29** | 9.12 | 10.56 | 12.72 | 15.06 | 17.84 | 21.08 | |
| | C-rich | 8.63 | **7.85** | 8.67 | 10.11 | 12.27 | 14.61 | 17.39 | 20.63 | |
| $Ag_{Si}–O_{Si}$ | Si-rich | **11.41** | 11.70 | 12.47 | 13.72 | 15.54 | 17.74 | 20.40 | 23.53 | |
| | C-rich | **10.52** | 10.81 | 11.58 | 12.83 | 14.65 | 16.85 | 19.50 | 22.63 | |

**Table 2**
Formation energies for n-type Cs–O–V cluster defects at $T = 1200\ ^\circ C$, $P_{O_2} = 10^{-21}$ atm.

| Defect | | Charge state | | | | | | | | |
|---|---|---|---|---|---|---|---|---|---|---|
| | | 5– | 4– | 3– | 2– | 1– | 0 | 1+ | 2+ | 3+ |
| $Cs_C–2V_{Si}$ | Si-rich | | | **10.78** | 11.27 | 12.22 | 13.59 | 15.39 | | |
| | C-rich | | | **10.34** | 10.83 | 11.78 | 13.15 | 14.95 | | |
| $Cs_{Si}–O_C–V_C$ | Si-rich | | | | **9.43** | 9.93 | 11.21 | 12.22 | 13.64 | 16.19 |
| | C-rich | | | | **9.87** | 10.37 | 11.65 | 12.66 | 14.09 | 16.64 |
| $Cs_{Si}–O_C$ | Si-rich | | | | **9.12** | 10.20 | 12.07 | 13.22 | 14.94 | 17.45 |
| | C-rich | | | | **9.12** | 10.20 | 12.07 | 13.22 | 14.94 | 17.45 |
| $Cs_{Si}–O_C–2V_C$ | Si-rich | | **8.73** | 8.76 | 9.21 | 10.03 | 11.39 | 12.36 | 13.74 | 15.41 |
| | C-rich | | **9.62** | 9.65 | 10.10 | 10.92 | 12.28 | 13.25 | 14.63 | 16.30 |
| $Cs_{Si}–O_{Si}–V_C$ | Si-rich | | 13.43 | **13.16** | 14.11 | 15.00 | 16.61 | 18.43 | 20.65 | 23.32 |
| | C-rich | | 12.98 | **12.71** | 13.67 | 14.56 | 16.17 | 17.98 | 20.20 | 22.87 |
| $Cs_{Si}–O_{Si}–2V_C$ | Si-rich | | 14.79 | **14.72** | 15.18 | 15.75 | 16.87 | 18.15 | 20.27 | 22.92 |
| | C-rich | | 14.79 | **14.72** | 15.18 | 15.75 | 16.87 | 18.15 | 20.27 | 22.92 |
| $Cs_{Si}–O_{Si}$ | Si-rich | | 16.95 | **16.82** | 17.46 | 18.60 | 20.37 | 22.33 | 24.71 | 27.60 |
| | C-rich | | 16.06 | **15.92** | 16.57 | 17.71 | 19.48 | 21.43 | 23.82 | 26.71 |
| $Cs_{Si}–O_{Si}–V_C–V_{Si}$ | Si-rich | | **14.66** | 17.09 | 18.69 | 19.47 | 21.19 | 22.83 | 25.05 | 26.95 |
| | C-rich | | **13.77** | 16.20 | 17.80 | 18.58 | 20.30 | 21.94 | 24.16 | 26.06 |
| $Cs_C–O_C$ | Si-rich | | | **13.31** | 13.40 | 13.89 | 14.92 | 15.67 | | |
| | C-rich | | | **14.20** | 14.29 | 14.79 | 15.82 | 16.56 | | |
| $Cs_C–O_C–V_{Si}$ | Si-rich | 16.25 | **12.08** | 12.37 | 13.16 | 14.29 | 15.71 | 16.47 | 17.82 | 19.73 |
| | C-rich | 15.80 | **11.64** | 11.92 | 12.71 | 13.84 | 15.27 | 16.02 | 17.37 | 19.28 |
| $Cs_C–O_C–2V_{Si}$ | Si-rich | | **8.09** | 8.83 | 10.19 | 11.98 | 14.25 | 15.81 | 17.95 | 20.55 |
| | C-rich | | **8.09** | 8.83 | 10.19 | 11.98 | 14.25 | 15.81 | 17.95 | 20.55 |
| $Cs_C–O_{Si}$ | Si-rich | | | **11.82** | 12.62 | 13.81 | 15.59 | 16.40 | 17.95 | 19.95 |
| | C-rich | | | **11.82** | 12.62 | 13.81 | 15.59 | 16.40 | 17.95 | 19.95 |
| $Cs_C–O_{Si}–V_{Si}$ | Si-rich | **10.41** | 10.52 | 11.15 | 12.55 | 14.32 | 16.62 | 18.34 | 20.27 | 21.76 |
| | C-rich | **9.96** | 10.08 | 10.71 | 12.10 | 13.87 | 16.17 | 17.89 | 19.83 | 21.32 |
| $Cs_C–O_{Si}–2V_{Si}$ | Si-rich | **13.21** | 13.65 | 14.49 | 15.76 | 17.38 | 19.45 | 21.30 | 23.59 | 26.31 |
| | C-rich | **12.32** | 12.76 | 13.60 | 14.87 | 16.49 | 18.56 | 20.41 | 22.70 | 25.42 |
| $Cs_C–O_{Si}–V_C–V_{Si}$ | Si-rich | | | | **14.11** | 15.17 | 16.74 | 17.77 | 19.65 | 22.08 |
| | C-rich | | | | **14.11** | 15.17 | 16.74 | 17.77 | 19.65 | 22.08 |

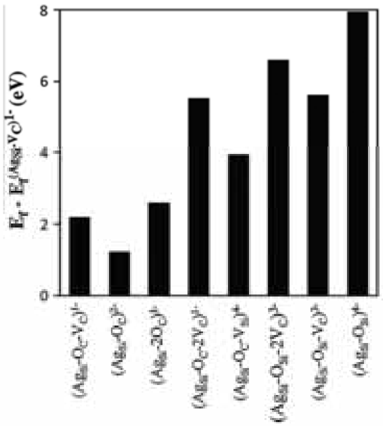

Fig. 3. Formation energies for n-type, Si-rich, Ag–O–V charged defect clusters relative to the most stable Ag–V defect cluster $(Ag_{Si}–V_C)^{1-}$. Values in figure are for $T = 1200\ ^\circ C$, $P_{O_2} = 10^{-21}$ atm.

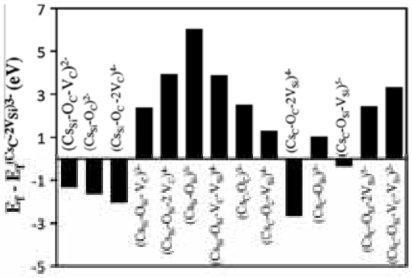

Fig. 4. Formation energies for n-type, Si-rich, Cs–O–V charged defect clusters compared to the lowest formation energy of a Cs–V defect cluster $(Cs_C–2V_{Si})^{3-}$. Values in figure are for $T = 1200\ ^\circ C$, $P_{O_2} = 10^{-21}$ atm.

defect cluster. The most stable Cs–O–V defect clusters is $(Cs_C–O_C–2V_{Si})^{4-}$ which is about 2.7 eV more stable than the most stable Cs–V defect cluster, followed by $(Cs_{Si}–O_C–2V_C)^{4-}$, a cluster with C vacancies which is 2.1 eV more stable. From studies reported in Ref. [13], it is known that the impurity defects $Cs_C–V_{Si}$ and $Cs_{Si}–V_C$ exhibit similar behavior, have equal formation energies and are the second most stable after $(Cs_C–2V_{Si})^{3-}$. Similarly to simple incorporation results, Cs–O co-incorporation results show that defect clusters both with Si and C vacancies can lead to the most stable configurations. This result is in contrast with results for Ag, where the most stable defect clusters were found for configurations having vacancies in C exclusively.

Fig. 5 presents the solubility of the most stable Cs–O complex in SiC ($(Cs_C–O_C–2V_{Si})^{4-}$) compared to that of the most stable Cs cluster $(Cs_C–2V_{Si})^{3-}$ as a function of pressure for three different temperatures. In Fig. 5, the solubility of a defect $C_i$ with a formation energy $E_f$ was calculated using the equation:

$$[C_i] = A\exp(-\beta E_f) \quad (4)$$

where $\beta$ is $1/(kT)$, $A$ is a prefactor assumed constant for Cs and Cs–O defects (which therefore cancels from the relative solubilities), and $E_f$ is the formation energy of the defect cluster.

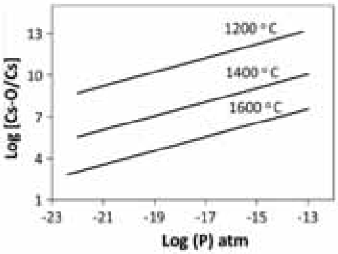

**Fig. 5.** Solubility of a Cs–O defect compared to that of a Cs defect in SiC.

One can see from Fig. 5 that for typical reactor operating conditions ($P_{O_2} = 10^{-21}$ atm, $T = 1200$ °C), the Cs–O complex is about 10 orders of magnitude more soluble than Cs in SiC. This result is an indication that Cs–O co-incorporation can play a significant role in Cs dissolution and diffusion in the SiC layer of the TRISO particle. Further work on the diffusion behavior of the Cs–O–V clusters has to be performed to assess to what extent Cs–O co-incorporation influences Cs diffusion.

Although Cs–O co-incorporation is predicted to occur, the co-incorporation defects are still very high in formation energy. A key question is whether the formation energies and associated predicted solubilities of co-incorporated Cs–O clusters can be high enough to be consistent with some integral release data suggesting fission product diffusion in SiC [1,2]. Integral release is increased by both higher solubility and higher diffusivity of Cs through the SiC coating, and the two factors must both be large enough to enable a significant amount of release. In order to determine if Cs–O co-incorporation can lead to solubilities consistent with integral release experiments, we will use the calculated solubilities in a simple integral release model to see whether the Cs–O cluster diffusion rates required to match the integral release are physically reasonable. We use the integral release model proposed in Ref. [11], which gives an estimate of fission product release rates from the TRISO particle's SiC layer for HTGR operating conditions assuming that the SiC provides the only diffusion barrier. In this case, the model assumes that Cs diffusion occurs along the crystalline regions of SiC. The integral release can be calculated as IR = $\Phi t A_f(4\pi r_i^2)$. In this expression $\Phi$ stands for the Cs flux, $t$ is the time, $A_f$ is the fractional area of the internal surface of SiC that is crystalline and $r_i$ is the inner radius of the SiC layer. The flux $\Phi$ is derived as follows. It is assumed that the SiC is a nearly spherical shell with an inner and outer surface. Ignoring the relatively small effects associated with its curvature on the transport, it is approximated as a flat layer. Furthermore, is assumed that the diffusion of Cs through the SiC has boundary conditions for Cs concentration $c$ being equal to the solubility limit and zero at the inner and outer surface of the SiC layer, respectively. With these assumptions, the steady state flux of Cs through the SiC is $\Phi = D_{eff}^{Cs}\Delta c = D_{eff}^{Cs}\Delta c_{Cs}/d_{th}$ where $D_{eff}^{Cs}$ is the Cs diffusion coefficient in the SiC, $c_{Cs}$ is the solubility limit of Cs in SiC and $d_{th}$ is the thickness of the SiC layer. It is also assumed that no time is spent diffusing through the TRISO components other than through the SiC (e.g., the fuel and carbon layers). If $n_{Cs}$ is the typical amount of Cs produced during the nuclear cycle, and assuming that a fraction $f_{rel}$ of the Cs is released in a period of time $t$, while all Cs is entirely mediated by the diffusion through the SiC layer, we can write the following equation:

$$f_{rel}n_{Cs} - \Phi t A_f(4\pi r_i^2) = 0 \tag{5}$$

**Table 3**
Parameters used in Cs integral release model, Eq. (6) [11].

| Property | Value |
|---|---|
| $f_{rel}$ | 0.04 |
| $n_{Cs}$ (mol) [37] | $1.1 \times 10^{-8}$ |
| $d_{th}$ (m) | $3.5 \times 10^{-5}$ |
| $\tau$ | 2 |
| $r_i$ | $3.15 \times 10^{-4}$ |
| $\rho$ (mol/m$^3$) | $1.6 \times 10^{5}$ |
| $t$ (s) | $8.64 \times 10^{5}$ (10 days) |
| $A_f$ | 0.998 |

Substituting $\Phi = D_{eff}^{Cs}\Delta c_{Cs}/d_{th}$ and $c_{Cs} = \rho \exp\left(-E_f^{Cs}/(kT)\right)$ into Eq. (5), the Cs diffusion coefficient in the SiC can be expressed as a function of measured and system parameters, including the Cs–O formation energy:

$$D_{eff}^{Cs} = \left(\frac{f_{rel}n_{Cs}d_{th}\tau}{4\pi r_i^2 \rho t A_f}\right)\exp\left(E_f^{Cs}/(kT)\right) \tag{6}$$

where $\tau$ is the TRISO particle's tortuosity and $\rho$ is the molar density of the SiC particle. Note that we are assessing only a release path through just the crystalline portion of the SiC as the above energetics are for a crystalline region. Terms $T$ and $k$ in the equation are the particle temperature and the Boltzman constant, respectively. Estimates performed using Eq. (6) are made assuming $t = 10$ days and $f_{rel} = 0.04$ for a temperature $T = 1600$ °C [6,7] while all remaining parameters are taken from Ref. [11] and summarized in Table 3.

Fig. 6 presents Cs formation energy in SiC as a function of the diffusion coefficient based on Eq. (6). In the figure, circles correspond to experimentally obtained diffusion coefficients [38,2,39]. It is observed from the figure that estimates for experimental Cs diffusion coefficients in SiC are on the order of $10^{-17}$–$10^{-18}$ m$^2$/s ($3.3 \times 10^{-17}$, $6.7 \times 10^{-17}$ and $4.4 \times 10^{-18}$ m$^2$/s), which according to Eq. (6) corresponds to a formation energy of about 0.3–0.7 eV. These values are about 8 eV lower than the ones found in this work. One can make a similar point by considering the $D$ values needed to match integral release measurements if we assume the predicted formation energies are correct. Based on the results presented in this work, at a temperature of 1600 °C, the formation energy for the most stable Cs–O defect cluster in SiC is $E_f^{Cs-O} = 9.43$ eV having bulk Cs as reference state or $E_f^{Cs-O} = 8.74$ eV if isolated Cs is taken instead as the reference state. The latter case, based on Eq. (6), could only match experimental release rates with a diffusion coefficient $D_{eff}^{Cs} = 1.5 \times 10^9$ m$^2$/s, which is many orders of magnitude higher than experimentally calculated diffusion coefficients or even any physically reasonable value (typically solid state diffusion coefficients in a bulk crystalline material are lower

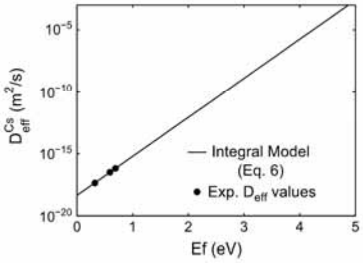

**Fig. 6.** Cs formation energy in SiC as a function of the effective diffusion coefficient $D_{eff}$. Line in figure corresponds to Eq. (6). Circles in figure denote formation energies calculated for experimental diffusion coefficients [38,2,39] using the same equation.

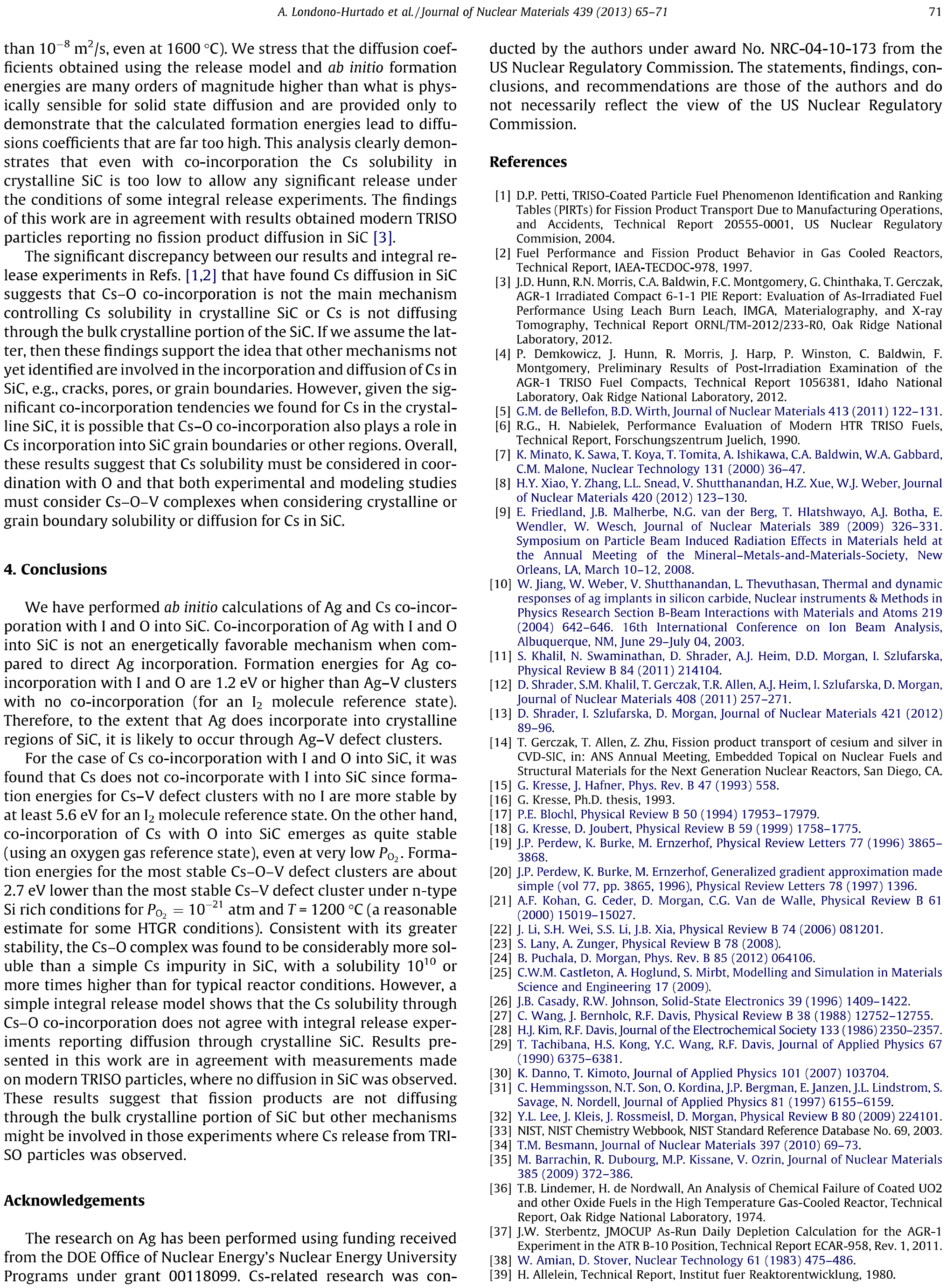

than $10^{-8}$ $m^2/s$, even at 1600 °C). We stress that the diffusion coefficients obtained using the release model and *ab initio* formation energies are many orders of magnitude higher than what is physically sensible for solid state diffusion and are provided only to demonstrate that the calculated formation energies lead to diffusions coefficients that are far too high. This analysis clearly demonstrates that even with co-incorporation the Cs solubility in crystalline SiC is too low to allow any significant release under the conditions of some integral release experiments. The findings of this work are in agreement with results obtained modern TRISO particles reporting no fission product diffusion in SiC [3].

The significant discrepancy between our results and integral release experiments in Refs. [1,2] that have found Cs diffusion in SiC suggests that Cs–O co-incorporation is not the main mechanism controlling Cs solubility in crystalline SiC or Cs is not diffusing through the bulk crystalline portion of the SiC. If we assume the latter, then these findings support the idea that other mechanisms not yet identified are involved in the incorporation and diffusion of Cs in SiC, e.g., cracks, pores, or grain boundaries. However, given the significant co-incorporation tendencies we found for Cs in the crystalline SiC, it is possible that Cs–O co-incorporation also plays a role in Cs incorporation into SiC grain boundaries or other regions. Overall, these results suggest that Cs solubility must be considered in coordination with O and that both experimental and modeling studies must consider Cs–O–V complexes when considering crystalline or grain boundary solubility or diffusion for Cs in SiC.

## 4. Conclusions

We have performed *ab initio* calculations of Ag and Cs co-incorporation with I and O into SiC. Co-incorporation of Ag with I and O into SiC is not an energetically favorable mechanism when compared to direct Ag incorporation. Formation energies for Ag co-incorporation with I and O are 1.2 eV or higher than Ag–V clusters with no co-incorporation (for an $I_2$ molecule reference state). Therefore, to the extent that Ag does incorporate into crystalline regions of SiC, it is likely to occur through Ag–V defect clusters.

For the case of Cs co-incorporation with I and O into SiC, it was found that Cs does not co-incorporate with I into SiC since formation energies for Cs–V defect clusters with no I are more stable by at least 5.6 eV for an $I_2$ molecule reference state. On the other hand, co-incorporation of Cs with O into SiC emerges as quite stable (using an oxygen gas reference state), even at very low $P_{O_2}$. Formation energies for the most stable Cs–O–V defect clusters are about 2.7 eV lower than the most stable Cs–V defect cluster under n-type Si rich conditions for $P_{O_2} = 10^{-21}$ atm and $T = 1200$ °C (a reasonable estimate for some HTGR conditions). Consistent with its greater stability, the Cs–O complex was found to be considerably more soluble than a simple Cs impurity in SiC, with a solubility $10^{10}$ or more times higher than for typical reactor conditions. However, a simple integral release model shows that the Cs solubility through Cs–O co-incorporation does not agree with integral release experiments reporting diffusion through crystalline SiC. Results presented in this work are in agreement with measurements made on modern TRISO particles, where no diffusion in SiC was observed. These results suggest that fission products are not diffusing through the bulk crystalline portion of SiC but other mechanisms might be involved in those experiments where Cs release from TRISO particles was observed.

## Acknowledgements

The research on Ag has been performed using funding received from the DOE Office of Nuclear Energy's Nuclear Energy University Programs under grant 00118099. Cs-related research was conducted by the authors under award No. NRC-04-10-173 from the US Nuclear Regulatory Commission. The statements, findings, conclusions, and recommendations are those of the authors and do not necessarily reflect the view of the US Nuclear Regulatory Commission.

## References

[1] D.P. Petti, TRISO-Coated Particle Fuel Phenomenon Identification and Ranking Tables (PIRTs) for Fission Product Transport Due to Manufacturing Operations, and Accidents, Technical Report 20555-0001, US Nuclear Regulatory Commision, 2004.
[2] Fuel Performance and Fission Product Behavior in Gas Cooled Reactors, Technical Report, IAEA-TECDOC-978, 1997.
[3] J.D. Hunn, R.N. Morris, C.A. Baldwin, F.C. Montgomery, G. Chinthaka, T. Gerczak, AGR-1 Irradiated Compact 6-1-1 PIE Report: Evaluation of As-Irradiated Fuel Performance Using Leach Burn Leach, IMGA, Materialography, and X-ray Tomography, Technical Report ORNL/TM-2012/233-R0, Oak Ridge National Laboratory, 2012.
[4] P. Demkowicz, J. Hunn, R. Morris, J. Harp, P. Winston, C. Baldwin, F. Montgomery, Preliminary Results of Post-Irradiation Examination of the AGR-1 TRISO Fuel Compacts, Technical Report 1056381, Idaho National Laboratory, Oak Ridge National Laboratory, 2012.
[5] G.M. de Bellefon, B.D. Wirth, Journal of Nuclear Materials 413 (2011) 122–131.
[6] R.G., H. Nabielek, Performance Evaluation of Modern HTR TRISO Fuels, Technical Report, Forschungszentrum Juelich, 1990.
[7] K. Minato, K. Sawa, T. Koya, T. Tomita, A. Ishikawa, C.A. Baldwin, W.A. Gabbard, C.M. Malone, Nuclear Technology 131 (2000) 36–47.
[8] H.Y. Xiao, Y. Zhang, L.L. Snead, V. Shutthanandan, H.Z. Xue, W.J. Weber, Journal of Nuclear Materials 420 (2012) 123–130.
[9] E. Friedland, J.B. Malherbe, N.G. van der Berg, T. Hlatshwayo, A.J. Botha, E. Wendler, W. Wesch, Journal of Nuclear Materials 389 (2009) 326–331. Symposium on Particle Beam Induced Radiation Effects in Materials held at the Annual Meeting of the Mineral–Metals-and-Materials-Society, New Orleans, LA, March 10–12, 2008.
[10] W. Jiang, W. Weber, V. Shutthanandan, L. Thevuthasan, Thermal and dynamic responses of ag implants in silicon carbide, Nuclear instruments & Methods in Physics Research Section B-Beam Interactions with Materials and Atoms 219 (2004) 642–646. 16th International Conference on Ion Beam Analysis, Albuquerque, NM, June 29–July 04, 2003.
[11] S. Khalil, N. Swaminathan, D. Shrader, A.J. Heim, D.D. Morgan, I. Szlufarska, Physical Review B 84 (2011) 214104.
[12] D. Shrader, S.M. Khalil, T. Gerczak, T.R. Allen, A.J. Heim, I. Szlufarska, D. Morgan, Journal of Nuclear Materials 408 (2011) 257–271.
[13] D. Shrader, I. Szlufarska, D. Morgan, Journal of Nuclear Materials 421 (2012) 89–96.
[14] T. Gerczak, T. Allen, Z. Zhu, Fission product transport of cesium and silver in CVD-SIC, in: ANS Annual Meeting, Embedded Topical on Nuclear Fuels and Structural Materials for the Next Generation Nuclear Reactors, San Diego, CA.
[15] G. Kresse, J. Hafner, Phys. Rev. B 47 (1993) 558.
[16] G. Kresse, Ph.D. thesis, 1993.
[17] P.E. Blochl, Physical Review B 50 (1994) 17953–17979.
[18] G. Kresse, D. Joubert, Physical Review B 59 (1999) 1758–1775.
[19] J.P. Perdew, K. Burke, M. Ernzerhof, Physical Review Letters 77 (1996) 3865–3868.
[20] J.P. Perdew, K. Burke, M. Ernzerhof, Generalized gradient approximation made simple (vol 77, pp. 3865, 1996), Physical Review Letters 78 (1997) 1396.
[21] A.F. Kohan, G. Ceder, D. Morgan, C.G. Van de Walle, Physical Review B 61 (2000) 15019–15027.
[22] J. Li, S.H. Wei, S.S. Li, J.B. Xia, Physical Review B 74 (2006) 081201.
[23] S. Lany, A. Zunger, Physical Review B 78 (2008).
[24] B. Puchala, D. Morgan, Phys. Rev. B 85 (2012) 064106.
[25] C.W.M. Castleton, A. Hoglund, S. Mirbt, Modelling and Simulation in Materials Science and Engineering 17 (2009).
[26] J.B. Casady, R.W. Johnson, Solid-State Electronics 39 (1996) 1409–1422.
[27] C. Wang, J. Bernholc, R.F. Davis, Physical Review B 38 (1988) 12752–12755.
[28] H.J. Kim, R.F. Davis, Journal of the Electrochemical Society 133 (1986) 2350–2357.
[29] T. Tachibana, H.S. Kong, Y.C. Wang, R.F. Davis, Journal of Applied Physics 67 (1990) 6375–6381.
[30] K. Danno, T. Kimoto, Journal of Applied Physics 101 (2007) 103704.
[31] C. Hemmingsson, N.T. Son, O. Kordina, J.P. Bergman, E. Janzen, J.L. Lindstrom, S. Savage, N. Nordell, Journal of Applied Physics 81 (1997) 6155–6159.
[32] Y.L. Lee, J. Kleis, J. Rossmeisl, D. Morgan, Physical Review B 80 (2009) 224101.
[33] NIST, NIST Chemistry Webbook, NIST Standard Reference Database No. 69, 2003.
[34] T.M. Besmann, Journal of Nuclear Materials 397 (2010) 69–73.
[35] M. Barrachin, R. Dubourg, M.P. Kissane, V. Ozrin, Journal of Nuclear Materials 385 (2009) 372–386.
[36] T.B. Lindemer, H. de Nordwall, An Analysis of Chemical Failure of Coated UO2 and other Oxide Fuels in the High Temperature Gas-Cooled Reactor, Technical Report, Oak Ridge National Laboratory, 1974.
[37] J.W. Sterbentz, JMOCUP As-Run Daily Depletion Calculation for the AGR-1 Experiment in the ATR B-10 Position, Technical Report ECAR-958, Rev. 1, 2011.
[38] W. Amian, D. Stover, Nuclear Technology 61 (1983) 475–486.
[39] H. Allelein, Technical Report, Institut fuer Reaktorentwicklung, 1980.

# Appendix B

## Summary of results for Task 6 “Continuum model of diffusion through polycrystalline SiC”

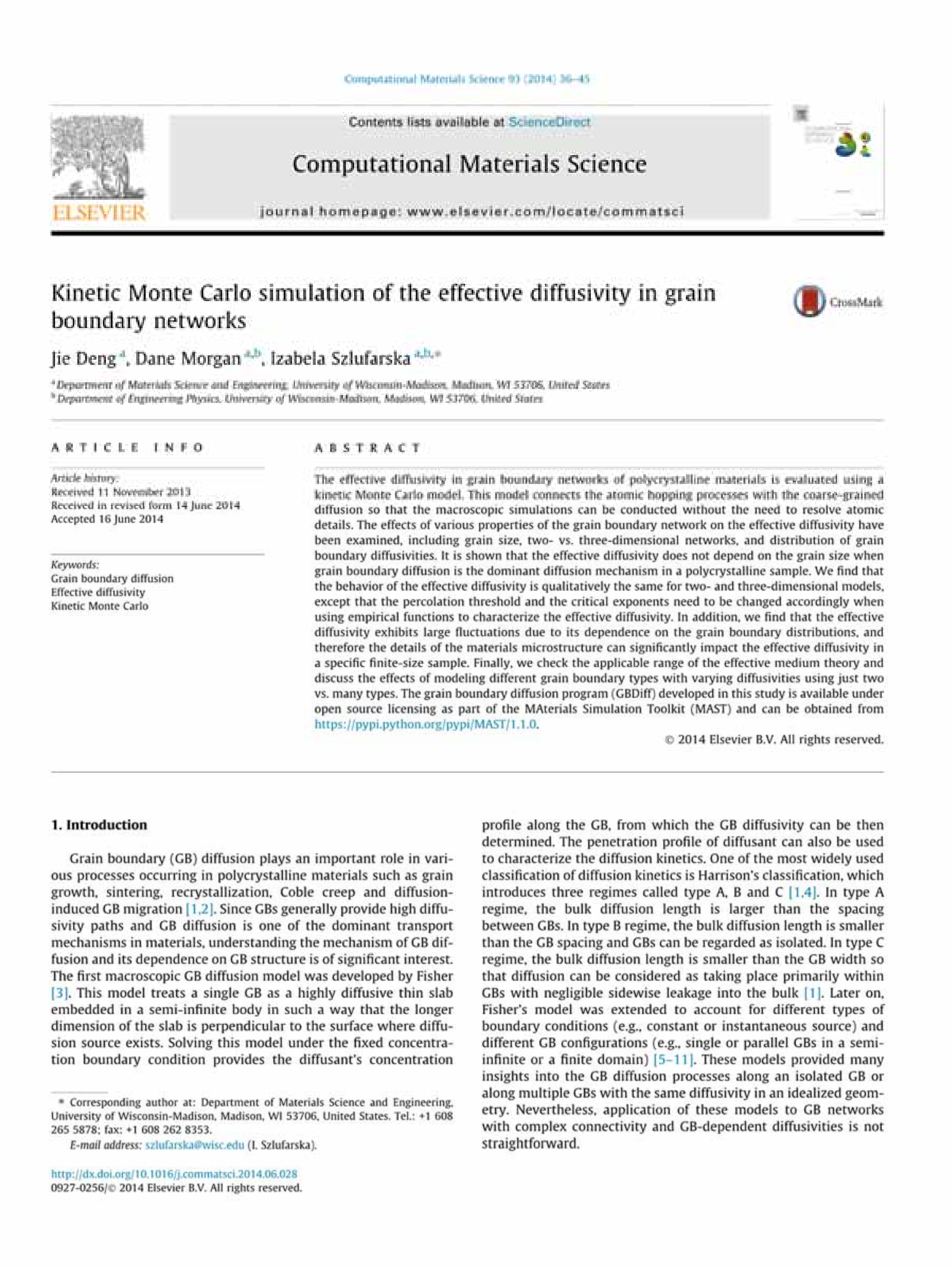

Computational Materials Science 93 (2014) 36–45

Contents lists available at ScienceDirect

Computational Materials Science

journal homepage: www.elsevier.com/locate/commatsci

# Kinetic Monte Carlo simulation of the effective diffusivity in grain boundary networks

Jie Deng [a], Dane Morgan [a,b], Izabela Szlufarska [a,b,*]

[a] Department of Materials Science and Engineering, University of Wisconsin-Madison, Madison, WI 53706, United States
[b] Department of Engineering Physics, University of Wisconsin-Madison, Madison, WI 53706, United States

ARTICLE INFO

*Article history:*
Received 11 November 2013
Received in revised form 14 June 2014
Accepted 16 June 2014

*Keywords:*
Grain boundary diffusion
Effective diffusivity
Kinetic Monte Carlo

ABSTRACT

The effective diffusivity in grain boundary networks of polycrystalline materials is evaluated using a kinetic Monte Carlo model. This model connects the atomic hopping processes with the coarse-grained diffusion so that the macroscopic simulations can be conducted without the need to resolve atomic details. The effects of various properties of the grain boundary network on the effective diffusivity have been examined, including grain size, two- vs. three-dimensional networks, and distribution of grain boundary diffusivities. It is shown that the effective diffusivity does not depend on the grain size when grain boundary diffusion is the dominant diffusion mechanism in a polycrystalline sample. We find that the behavior of the effective diffusivity is qualitatively the same for two- and three-dimensional models, except that the percolation threshold and the critical exponents need to be changed accordingly when using empirical functions to characterize the effective diffusivity. In addition, we find that the effective diffusivity exhibits large fluctuations due to its dependence on the grain boundary distributions, and therefore the details of the materials microstructure can significantly impact the effective diffusivity in a specific finite-size sample. Finally, we check the applicable range of the effective medium theory and discuss the effects of modeling different grain boundary types with varying diffusivities using just two vs. many types. The grain boundary diffusion program (GBDiff) developed in this study is available under open source licensing as part of the MAterials Simulation Toolkit (MAST) and can be obtained from https://pypi.python.org/pypi/MAST/1.1.0.

© 2014 Elsevier B.V. All rights reserved.

## 1. Introduction

Grain boundary (GB) diffusion plays an important role in various processes occurring in polycrystalline materials such as grain growth, sintering, recrystallization, Coble creep and diffusion-induced GB migration [1,2]. Since GBs generally provide high diffusivity paths and GB diffusion is one of the dominant transport mechanisms in materials, understanding the mechanism of GB diffusion and its dependence on GB structure is of significant interest. The first macroscopic GB diffusion model was developed by Fisher [3]. This model treats a single GB as a highly diffusive thin slab embedded in a semi-infinite body in such a way that the longer dimension of the slab is perpendicular to the surface where diffusion source exists. Solving this model under the fixed concentration boundary condition provides the diffusant's concentration profile along the GB, from which the GB diffusivity can be then determined. The penetration profile of diffusant can also be used to characterize the diffusion kinetics. One of the most widely used classification of diffusion kinetics is Harrison's classification, which introduces three regimes called type A, B and C [1,4]. In type A regime, the bulk diffusion length is larger than the spacing between GBs. In type B regime, the bulk diffusion length is smaller than the GB spacing and GBs can be regarded as isolated. In type C regime, the bulk diffusion length is smaller than the GB width so that diffusion can be considered as taking place primarily within GBs with negligible sidewise leakage into the bulk [1]. Later on, Fisher's model was extended to account for different types of boundary conditions (e.g., constant or instantaneous source) and different GB configurations (e.g., single or parallel GBs in a semi-infinite or a finite domain) [5–11]. These models provided many insights into the GB diffusion processes along an isolated GB or along multiple GBs with the same diffusivity in an idealized geometry. Nevertheless, application of these models to GB networks with complex connectivity and GB-dependent diffusivities is not straightforward.

---

[*] Corresponding author at: Department of Materials Science and Engineering, University of Wisconsin-Madison, Madison, WI 53706, United States. Tel.: +1 608 265 5878; fax: +1 608 262 8353.
*E-mail address:* szlufarska@wisc.edu (I. Szlufarska).

http://dx.doi.org/10.1016/j.commatsci.2014.06.028
0927-0256/© 2014 Elsevier B.V. All rights reserved.

In real materials, GB diffusion is sensitive to the GB atomic structure. The structure dependence of GB diffusion was first measured by Turnbull and Hoffman [12,13], where it was shown that the diffusion along the [001] tilt GBs in Ag is anisotropic and it depends on the misorientation between two grains. Since then, the misorientation dependence of GB diffusion has been found in many other systems. It is generally found that the diffusivity along high angle GBs is higher than along low angle or coincidence site lattice (CSL) GBs [14–17]. The structure dependence of GB diffusion arises from the atomic nature of diffusion. Specifically, GB diffusion generally depends on formation energies and migration energies of point defects and these properties strongly depend on the specific arrangements of atoms in the GB [18]. Because of this structure dependence, the diffusivities in individual GBs may vary by several orders of magnitude under typical testing conditions, which makes it challenging to describe the macroscopic diffusivity when mediated by GB diffusion in polycrystalline samples. In such cases, the effective diffusivity is one of the most important quantities used to characterize the macroscopic GB diffusion. The effective diffusivity is defined in such a way that the macroscopic diffusion through a heterogeneous GB network (where individual GBs have a wide range of diffusivities) is equivalent to the diffusion through a homogeneous system with a single value of the effective diffusivity. As the effective diffusivity is often correlated with various physical properties of structural materials related to GB diffusion, such as intergranular fracture, corrosion, and cavitation [19–23], understanding the dependence of the effective diffusivity on the details of the GB network is critical for design of materials with desirable properties.

One should note that the effective diffusivity through polycrystalline materials is a complex function of different properties of the GB network such as the GB distribution and the GB connectivity. Early investigations on the effective diffusivity were focused on developments of phenomenological diffusion models in the Harrison type-A kinetics regime [1,24–30]. These models account for the bulk diffusion and GB diffusion in different grain patterns (e.g., square grains with the same size surrounded by GB region uniformly distributed in the domain), but they generally consider only one GB type and simplified GB geometries, and therefore ignore the influence of GB variety and varied GB connectivity on the effective diffusivity. Here, we focus on the effective diffusivity in Harrison's type C kinetic regime where GB diffusion is much faster than bulk diffusion. One material science problem relevant to this regime may be the diffusion of Ag through polycrystalline silicon carbide (SiC) [31,32], where it has been suggested that the diffusivity of Ag in SiC GBs is several orders of magnitude larger than that in SiC bulk over a wide-range of temperature. In the type C kinetic regime, one can assume that the diffusion occurs along GBs only and that the properties of the GB network play a key role in determining the effective diffusivity. Recently, Chen and Schuh [33] provided new insights into the effective diffusivity in a two-dimensional (2D) honeycomb GB network. The authors investigated the role of a diffusivity contrast, defined as the ratio of the diffusivities along high-diffusivity and low-diffusivity GBs. The GB networks were categorized into high-contrast systems and low-contrast systems, where the diffusivity contrast is larger and smaller than $10^4$, respectively. It was shown that in high-contrast systems, the effective diffusivity is governed by the development of a percolating path of high-diffusivity GBs. In low-contrast systems, the effective diffusivity is less sensitive to the topology of the GB network and it can be described using composite averaging schemes.

The aim of our paper is twofold. First, we develop a kinetic Monte Carlo (kMC) model to calculate the effective diffusivity in static heterogeneous GB networks. This model is applicable for the case of impurity diffusion when the impurity has a strong tendency to segregate to GBs. In contrast to earlier kMC models that obtained the diffusivity in a single GB based on the jump rates of point defects [34–37], our model focuses on the long-range diffusion along GBs and determines the effective diffusivity by taking individual GB diffusivities as an input. Our model provides a connection between the coarse-grained motion of the diffusant and the atomic level processes underlying diffusion. This connection is validated numerically and it allows us to ignore the atomic details of GB diffusion in kMC simulations. Second, we extend the work of Chen and Schuh [33] to further account for the dependence of the effective diffusivity on various properties of the GB network. Instead of using a 2D honeycomb lattice, we use a three-dimensional (3D) Voronoi diagram to represent the GB network with non-uniform distributions of grain sizes and GB areas. Two or more types of GBs are assumed to be randomly distributed in the simulation domain. In a system with two types of GBs, we demonstrate the dependence of the effective diffusivity on diffusivity contrast, fraction of each GB type, GB distribution, and the average grain size. We also use our numerical models to test the validity of two ways of modeling the effective diffusivity, namely the effective medium theory (EMT) and the percolation theory. Finally, we discuss the effects of considering more than two types of GBs on the effective diffusivity.

## 2. Kinetic Monte Carlo model

In order to capture GB diffusion in 3D GB networks, we mesh each GB plane using the software Neper [38], which applies a widely-utilized bottom-up approach to generate mesh in Voronoi tessellation vertices, edges (GB junctions) and faces (GBs), successively. A typical 3D GB network with mesh in each GB is shown in Fig. 1a. For the sake of computational efficiency, our kMC model does not resolve the atomic hopping processes. Instead, a diffusing particle is assumed to perform a coarse-grained hop, i.e., it moves from one mesh node to another along an element edge instantaneously in each kMC step. Therefore the current model captures the motion of a particle on diffusive time scales and microscopic length scales, which is different from classic atomistic models where hops occur on the atomic scale. With the assumption of coarse-grained hop, the kMC calculation of the effective diffusivity can be carried out as follows.

A Voronoi diagram [38] with a specified number of grains is first generated in a 3D cubic domain to represent the GB network. In the Voronoi construction, grain centers are randomly distributed. Then each GB plane is meshed by triangular elements. Each GB is then randomly assigned to be one of two or more types, where each type has a different diffusivity. The diffusivity in a GB junction is assumed to be the same as the highest diffusivity in all GBs that connect to that GB junction. Then the diffusivity along each triangular element edge is set to be the diffusivity in the GB plane or GB junction it belongs to. Initially, a particle is located at a randomly selected mesh node, and it is allowed to diffuse in the domain via hops along element edges (i.e., from one mesh node to another). Periodic boundary conditions are applied in all spatial directions. In each kMC step, the particle chooses to move along a given element edge $i$ randomly based on the rate $\Gamma_i = \frac{D_i}{l_i^2}$, where $D_i$ and $l_i$ are the diffusivity and the length of element edge $i$, respectively. After each step, the total diffusion time $\tau$ and the total displacement $d$ (displacement between particle's initial position and its current position) are recorded. After a sufficiently long time (long enough to obtain converged results), the effective diffusivity can be calculated as $D_{eff} = \frac{d^2}{6\tau}$. This procedure is repeated for $5 \times 10^4$ polycrystalline samples, and the reported effective diffusivities are the average values. We also develop a model to calculate the effective diffusivity on a 2D Voronoi GB network. The simulation

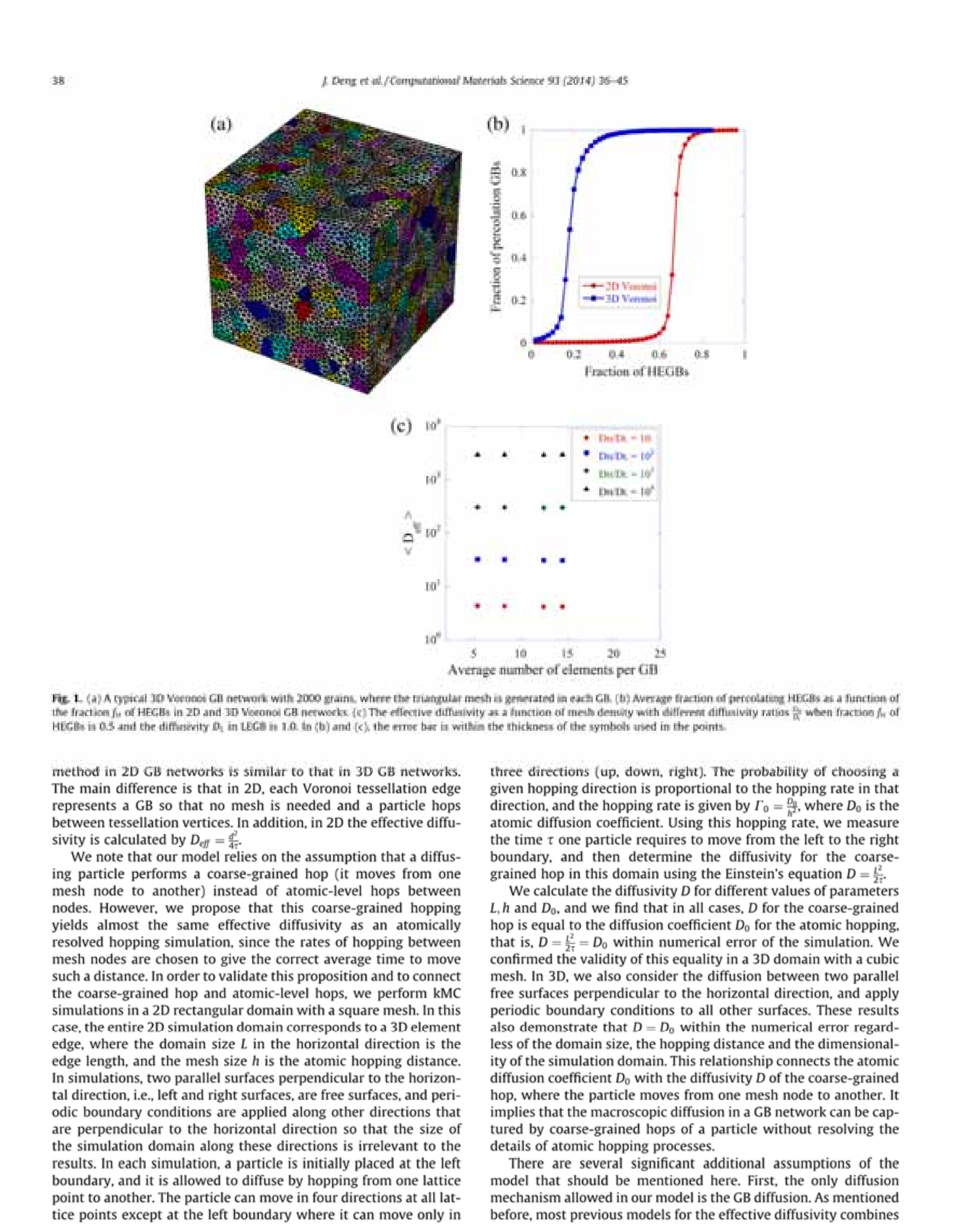

**Fig. 1.** (a) A typical 3D Voronoi GB network with 2000 grains, where the triangular mesh is generated in each GB. (b) Average fraction of percolating HEGBs as a function of the fraction $f_H$ of HEGBs in 2D and 3D Voronoi GB networks. (c) The effective diffusivity as a function of mesh density with different diffusivity ratios $\frac{D_H}{D_L}$ when fraction $f_H$ of HEGBs is 0.5 and the diffusivity $D_L$ in LEGB is 1.0. In (b) and (c), the error bar is within the thickness of the symbols used in the points.

method in 2D GB networks is similar to that in 3D GB networks. The main difference is that in 2D, each Voronoi tessellation edge represents a GB so that no mesh is needed and a particle hops between tessellation vertices. In addition, in 2D the effective diffusivity is calculated by $D_{eff} = \frac{d^2}{4\tau}$.

We note that our model relies on the assumption that a diffusing particle performs a coarse-grained hop (it moves from one mesh node to another) instead of atomic-level hops between nodes. However, we propose that this coarse-grained hopping yields almost the same effective diffusivity as an atomically resolved hopping simulation, since the rates of hopping between mesh nodes are chosen to give the correct average time to move such a distance. In order to validate this proposition and to connect the coarse-grained hop and atomic-level hops, we perform kMC simulations in a 2D rectangular domain with a square mesh. In this case, the entire 2D simulation domain corresponds to a 3D element edge, where the domain size $L$ in the horizontal direction is the edge length, and the mesh size $h$ is the atomic hopping distance. In simulations, two parallel surfaces perpendicular to the horizontal direction, i.e., left and right surfaces, are free surfaces, and periodic boundary conditions are applied along other directions that are perpendicular to the horizontal direction so that the size of the simulation domain along these directions is irrelevant to the results. In each simulation, a particle is initially placed at the left boundary, and it is allowed to diffuse by hopping from one lattice point to another. The particle can move in four directions at all lattice points except at the left boundary where it can move only in three directions (up, down, right). The probability of choosing a given hopping direction is proportional to the hopping rate in that direction, and the hopping rate is given by $\Gamma_0 = \frac{D_0}{h^2}$, where $D_0$ is the atomic diffusion coefficient. Using this hopping rate, we measure the time $\tau$ one particle requires to move from the left to the right boundary, and then determine the diffusivity for the coarse-grained hop in this domain using the Einstein's equation $D = \frac{L^2}{2\tau}$.

We calculate the diffusivity $D$ for different values of parameters $L, h$ and $D_0$, and we find that in all cases, $D$ for the coarse-grained hop is equal to the diffusion coefficient $D_0$ for the atomic hopping, that is, $D = \frac{L^2}{2\tau} = D_0$ within numerical error of the simulation. We confirmed the validity of this equality in a 3D domain with a cubic mesh. In 3D, we also consider the diffusion between two parallel free surfaces perpendicular to the horizontal direction, and apply periodic boundary conditions to all other surfaces. These results also demonstrate that $D = D_0$ within the numerical error regardless of the domain size, the hopping distance and the dimensionality of the simulation domain. This relationship connects the atomic diffusion coefficient $D_0$ with the diffusivity $D$ of the coarse-grained hop, where the particle moves from one mesh node to another. It implies that the macroscopic diffusion in a GB network can be captured by coarse-grained hops of a particle without resolving the details of atomic hopping processes.

There are several significant additional assumptions of the model that should be mentioned here. First, the only diffusion mechanism allowed in our model is the GB diffusion. As mentioned before, most previous models for the effective diffusivity combines

GB diffusion with other diffusion mechanisms (e.g., bulk or dislocation pipe diffusion) [1,24–30]. Our simulations are focused on long-range diffusion processes in a macroscopic domain where the GB diffusion is the dominant mechanism. The second assumption is that GBs with different characters are randomly distributed. It is known that GB types in experimental samples are correlated and subject to crystallographic constraints [39–41]. However, the only effect of GB correlation is a few percent shift in the percolation threshold, while the critical exponents in the percolation theory are not affected by the correlation [33]. Because of that, we ignore the GB correlation in this work. The reader should keep in mind that the percolation threshold in actual GB networks may be slightly different from the one predicted by our model. If needed, correlations in GB types can be added to our model framework relatively easily in future work. Finally, in our model the diffusion coefficient at the GB junction and the GB are taken as identical. While the diffusion along GB junctions is generally different from that in GBs, their difference depends on temperature and GB structure, and the relative magnitude of the diffusivity in GB junctions and GBs is still in debate [42,43]. As such, the diffusion coefficients along GB junctions are treated as equal to diffusion coefficients along GBs in the current model.

The GB diffusion model described above has been programmed into a tool called GBDiff. GBDiff is available under open source licensing as part of the MAterials Simulation Package [44] and can be obtained from https://pypi.python.org/pypi/MAST. The version of GBDiff used for this paper is GBDiff version 1.0 in MAST version 1.2.0. When using the GBDiff code please cite the present paper and any additional references given in the MAST citation file, which is generated automatically when MAST is run. GBDiff can also be used as on online application through the Materials Hub (materialhub.org (http://materialhub.org)) [45]. Please follow the citation guidelines given for this tool on the MaterialsHub.

## 3. Results for systems with two types of GBs

The kMC model introduced in Section 2 is first applied to calculate the effective diffusivity $D_{eff}$ in a system containing two types of GBs: high-energy GBs (HEGBs) with diffusivity $D_H$ and low energy GBs (LEGBs) with diffusivity $D_L$. These GB types are randomly distributed in the GB network. In order to determine the effect of system dimensionality on diffusion through GB networks, we consider two different GB topologies based on 2D and 3D Voronoi diagrams.

The GB network in our systems is characterized by the diffusivity contrast $\frac{D_H}{D_L}$, the fraction $f_H$ of HEGBs, the distribution of GB types and the average grain size. In addition to these properties, the connectivity of HEGBs can also play an important role in determining $D_{eff}$. The influence of the HEGB connectivity on macroscopic material properties has been shown in Refs. [19–23,33]. The effect of the HEGB connectivity is particularly apparent in systems with two types of GBs, as considered in our study, because HEGBs can form percolating paths for the diffusant and profoundly affect $D_{eff}$ [33]. Therefore, before we calculate $D_{eff}$ in our systems, we first evaluate the percolation threshold of the Voronoi GB networks. Following the method in Ref. [46], we investigate the percolation paths between two parallel free surfaces and apply periodic boundary conditions to all other surfaces. The final result of the percolation threshold is independent of which free surface we choose and instead, it depends on the connectivity of HEGBs in the system. Note that the boundary conditions used here for calculating the percolation threshold are different from the periodic boundary conditions applied when calculating the effective diffusivity. According to Ref. [46], a HEGB is called percolating if it is directly connected to the selected surface (the right boundary in our study) or if one of its nearest HEGB neighbors is percolating. With this criterion, we are able to identify the number of percolating HEGBs in the GB network, and then the fraction of percolating HEGBs can be obtained. Ideally, in a system with an infinite number of GBs, the fraction of percolating HEGBs will change from zero to unity when the fraction of HEGBs $f_H$ is equal to the percolation threshold $f_p$. In a system with finite number of GBs, when $f_H$ approaches $f_p$, the fraction of percolating HEGBs will change from zero to unity gradually but rapidly, and we can approximate $f_p$ from the change in the fraction of percolation HEGBs.

Since the fraction of percolating HEGBs is strongly dependent on the specific GB distribution for a finite system, in order to obtain statistically relevant results, we carry out a large number of simulations (typically $10^4$) for each value of $f_H$. The average value of the fraction of percolating HEGBs are reported. As shown in Fig. 1b, the percolation threshold $f_p$ is $0.67 \pm 0.01$ and $0.18 \pm 0.01$ for the 2D and 3D Voronoi GB networks, respectively. Here, $f_p$ is determined by the value of $f_H$ where the fraction of percolating GBs is 0.5, and the uncertainty is approximated by the range of $f_H$ where the fraction of percolation GBs varies from $\frac{1}{3}$ to $\frac{2}{3}$. The percolation threshold in 2D is consistent with the results of Monte Carlo simulations reported in Refs. [47,48], where the authors found $f_p = 0.66693$ in the 2D Voronoi network. In addition, $f_p$ can be used to estimate the effective coordination number Z according to the formula [49] $Zf_p = \frac{d}{d-1}$, where $d$ is the dimensionality. Using the values of $f_p$ and $d$, we find that $Z$ is about 3.0 and 8.3 for 2D and 3D Voronoi diagrams, respectively.

Before we evaluate the dependence of the effective diffusivity on the properties of the 3D GB network, we check the dependence of the effective diffusivity on the mesh density. Fig. 1c shows the effective diffusivity in a 3D GB network with $2 \times 10^3$ grains as a function of mesh density with different GB network properties. It can be seen that within the range of mesh density considered here, the effective diffusivity is not very sensitive to the mesh density. In the following, we carry out kMC diffusion simulations in a 3D Voronoi GB network with $4 \times 10^3$ grains where the average number of elements in one GB is approximately 9. In these simulations, $D_L$ is fixed at a constant value (which is 1 in our study), and we vary $D_H$ to change the diffusivity contrast $\frac{D_H}{D_L}$. As a result, the observed trends in the dependence of diffusion on $\frac{D_H}{D_L}$ are equivalent to the trends in the dependence on $D_H$. Moreover, in the following figures, $D_{eff}$ is normalized by $D_H$ so that the features of $D_{eff}$ observed in our study are not affected by the diffusivity unit. This normalization does not impact the dependence of $D_{eff}$ on the properties of the GB network.

### 3.1. Dependence of $D_{eff}$ on the diffusivity contrast $D_H/D_L$

Fig. 2 shows $\frac{D_{eff}}{D_H}$ as a function of $\frac{D_H}{D_L}$ for different values of $f_H$. In this figure, the solid lines and the dashed lines correspond to the cases when $f_H < f_p$ and $f_H > f_p$, respectively, where the percolation threshold $f_p = 0.18$ (see Fig. 1c). We find that the dependence of $D_{eff}$ on $\frac{D_H}{D_L}$ when $f_H < f_p$ is different from that when $f_H > f_p$. In particular, when $f_H < f_p, D_{eff}$ is nearly independent of $D_H$ so that $\frac{D_{eff}}{D_H}$ is proportional to $\left(\frac{D_H}{D_L}\right)^p$ with the power coefficient $p \approx -1$. This result means that when the fraction of HEGBs is lower than the percolation threshold, the effective diffusivity is governed primarily by the diffusivity along LEGBs. On the other hand, for the case of $f_H > f_p$ and when $\frac{D_H}{D_L}$ increases, the dependence of $D_{eff}$ on $D_H$ changes from a power law with exponent $p$ $(-1 < p < 0)$ to a linear function $(p \approx 0)$. The transition from a power law to a linear function depends on $f_H$ so that with higher $f_H, D_{eff}$ becomes linearly dependent on $D_H$ at smaller values of $\frac{D_H}{D_L}$. When the fraction of HEGBs exceeds the percolation threshold, $D_{eff}$ is dominated by $D_H$ and this

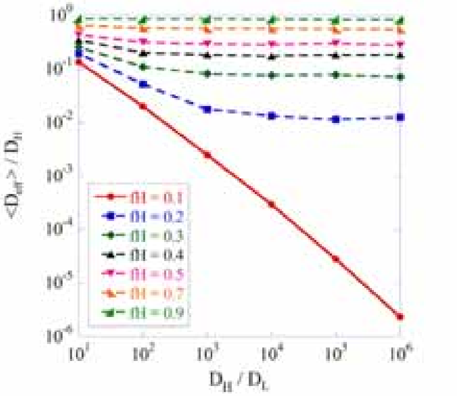

**Fig. 2.** Dependence of the effective diffusivity $D_{eff}$ on $\frac{D_H}{D_L}$ for different fractions $f_H$ of HEGBs. The solid lines and dashed lines correspond to the cases when $f_H$ is smaller and larger than the percolation threshold $f_p$, respectively.

dominance becomes more apparent as $\frac{D_H}{D_L}$ increases. This behavior is expected because above the percolation threshold, the diffusion through the polycrystalline samples is accomplished mainly by the diffusion along HEGBs. As $\frac{D_H}{D_L}$ increases, the probability of diffusing via LEGBs pathways is further decreased, and eventually $D_{eff}$ becomes a linear function of $D_H$. To summarize the trends in Fig. 2, $f_H$ determines how $D_{eff}$ depends on $\frac{D_H}{D_L}$. When $f_H < f_p, D_{eff}$ is governed by $D_L$ and is nearly independent of $\frac{D_H}{D_L}$. When $f_H > f_p, D_{eff}$ is approximately a linear function of $\frac{D_H}{D_L}$.

### 3.2. Dependence of $D_{eff}$ on the fraction of HEGB $f_H$

While $f_H$ determines the dependence of $D_{eff}$ on $\frac{D_H}{D_L}$ as illustrated in Fig. 2, the ratio $\frac{D_H}{D_L}$ affects how $D_{eff}$ depends on $f_H$. As shown in Ref. [33] for systems with a uniform grain size and uniform GB length, the dependence of $D_{eff}$ on $f_H$ follows different rules in high- and low-diffusivity contrast systems. Here we evaluate $D_{eff}$ as a function of $f_H$ for different values of $\frac{D_H}{D_L}$ in the GB network with non-uniform grain size and GB length distributions. The results of our simulations are shown in Fig. 3a. In the same figure, we also show predictions of the effective medium theory (EMT) [50], which is a widely used analytical model for describing macroscopic transport properties in heterogeneous media. As shown in Fig. 3a, predictions of EMT agree well with the results of kMC simulations for small values of $\frac{D_H}{D_L}$. However, deviations between two approaches are observed as $\frac{D_H}{D_L}$ increases. This trend is consistent with the conclusions from Ref. [33] that EMT fails to predict $D_{eff}$ in high contrast systems. The discrepancy between EMT and kMC is due to the fact that EMT averages the diffusivities of all GBs, but it does not take into account the GB connectivity. As some HEGBs may form high-diffusivity paths and the diffusion prefers to occur along these paths, the overall diffusivity is higher than that estimated by the EMT.

Two other interesting features are found in Fig. 3a. First, the deviation of EMT from kMC in this study is larger than the one reported in Ref. [33]. Specifically, the authors of Ref. [33] found that EMT works reasonably well when $\frac{D_H}{D_L} < 10^4$, while we find that EMT provides a poor approximation of the simulation data when $\frac{D_H}{D_L} > 10^2$. The difference in the range of applicability of EMT arises from the difference in the GB connectivity in the two studies. More specifically, the percolation threshold in the GB network considered in our study is lower than that in Ref. [33]. Consequently, in the present study, the formation of long-range connectivity of HEGBs is easier, leading to a failure of the EMT approximation at smaller values of $\frac{D_H}{D_L}$. Secondly, we find that the largest deviation between EMT and kMC occurs when $f_H \approx f_p$. To illustrate this deviation, in Fig. 3b we plot the ratio of $D_{eff}$ obtained from kMC to that predicted by EMT. It is clear from this plot that when $|f_H - f_p| > 0.2$, EMT works quite well even at large values of $\frac{D_H}{D_L}$. On the other hand, when $|f_H - f_p| < 0.2$, EMT and kMC predictions differ, and the difference reaches the maximum at $f_H = f_p$. We conclude that EMT provides a reasonable approximation for the effective diffusivity not only for low contrast systems, but also for high contrast systems when the absolute difference between $f_H$ and $f_p$ is large. This extension of the applicability of EMT makes it possible to use this theory to predict $D_{eff}$ in a wider range of GB structures than previously assumed.

As demonstrated in Fig. 3a and b, when $\frac{D_H}{D_L}$ increases, the percolating network of HEGBs begins to dominate diffusion and it is expected that $\frac{D_{eff}}{D_H}$ in high contrast systems can be approximated by the percolation theory. Based on the percolation theory described in detail in Refs. [50,51], $D_{eff}$ should exhibit a power-law dependence $D_{eff} \propto (f_H - f_p)^t$ when $f_H > f_p$ and $D_{eff} \propto (f_p - f_H)^{-s}$ when $f_H < f_p$, where $t$ and $s$ are critical exponents. Fig. 3c and d illustrate the dependence of $D_{eff}$ on $|f_p - f_H|$ for the cases of $f_H > f_p$ and $f_H < f_p$, respectively, where the solid lines represent the curve fitting using the above power-law functions. One can see that as $\frac{D_H}{D_L}$ increases, the relation between $D_{eff}$ and $|f_p - f_H|$ approaches the power laws shown above. In particular, when $\frac{D_H}{D_L} > 10^5$, all the $\frac{D_{eff}}{D_H}$ vs. $|f_p - f_H|$ functions can be well described by above power-law functions with exponents $t = 1.30 \pm 0.05$ and $s = 1.22 \pm 0.05$. This feature has also been observed in Ref. [33], but the critical exponents in that study were different from the ones reported here, presumably due to the difference in the type of GB network (e.g., 2D honeycomb lattice and 3D Voronoi diagram). The values of $t$ and $s$ found in our study are consistent with most of previous studies [50–58] on percolation systems, where the critical exponents are in the range of 1–2.

While EMT and the percolation theory can predict $D_{eff}$ when $\frac{D_H}{D_L}$ is low and high, respectively, a generalized effective medium (GEM) equation [59–61] has been often used to predict $D_{eff}$ in the entire range of $\frac{D_H}{D_L}$ values. This equation has been previously applied in Ref. [33] to fit $D_{eff}$ in a 2D honeycomb GB lattice. The GEM equation has the following form

$$(1 - f_H)\frac{D_L^{1/s} - D_{eff}^{1/s}}{D_L^{1/s} + \left(f_p^{-1} - 1\right)D_{eff}^{1/s}} + f_H\frac{D_H^{1/t} - D_{eff}^{1/t}}{D_H^{1/t} + \left(f_p^{-1} - 1\right)D_{eff}^{1/t}} = 0, \qquad (1)$$

where $f_H, f_p, D_H, D_L, s$ and $t$ have the same meanings as before. As shown earlier, in the case of our GB networks, $f_p = 0.18, t = 1.30$, and $s = 1.22$. By substituting these parameters into Eq. (1) we obtain the GEM prediction of $D_{eff}$. The comparison of GEM and kMC calculation of $D_{eff}$ is illustrated in Fig. 3a, which shows that two methods match quite well. This result indicates that $D_{eff}$ in a system with two types of GBs can be approximated by the GEM equation with the values for the percolation threshold and the critical exponents being appropriate for the given GB network. A combined analysis of Figs. 2 and 3 demonstrate that the effects of $f_H$ and $\frac{D_H}{D_L}$ on $D_{eff}$ are coupled to each other and are strongly dependent on the corresponding GB network.

### 3.3. Statistical distribution of $D_{eff}$

As discussed in Section 2, the effective diffusivities reported so far in Figs. 2 and 3 are the averages over $5 \times 10^4$ samples. The

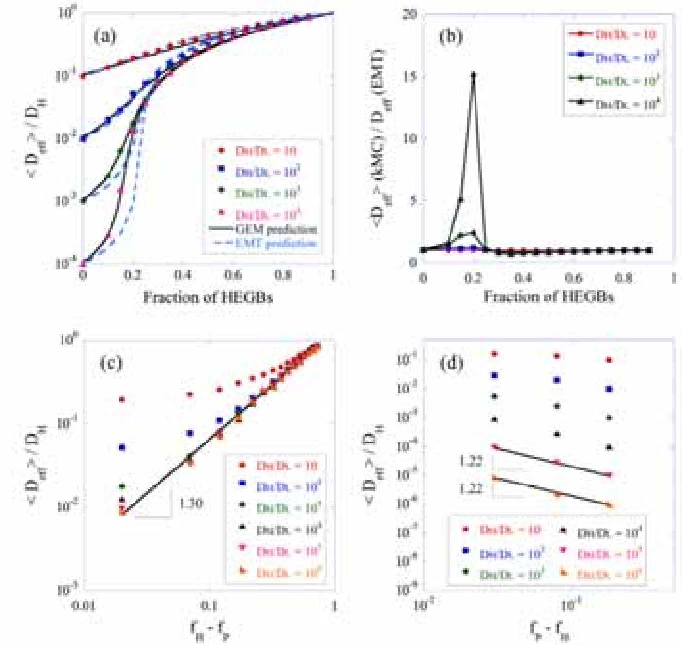

Fig. 3. (a) Dependence of $D_{eff}$ on $f_H$ for different ratios $\frac{D_H}{D_L}$. Symbols, dash lines and solid lines correspond to the results from kMC simulations, predictions of the EMT theory, and predictions of the GEM theory with $f_p = 0.18$, $t = 1.30$, and $s = 1.22$. (b) The ratio of $D_{eff}$ values calculated from kMC and from EMT for different values of $\frac{D_H}{D_L}$. $D_{eff}$ as a function of (c) $f_H - f_p$ when $f_H > f_p$ and (d) $f_p - f_H$ when $f_H < f_p$ calculated for different values of $\frac{D_H}{D_L}$. In (c) and (d), the solid lines are the curve fitting using the power-law functions described in text.

standard error (as estimated by the standard deviation divided by the mean) of the reported average $D_{eff}$ is around 1%. We note that the standard error decreases with both the number of samples, as to be expected, and the size of the system, as increasing the latter provides better averaging over a range of local environments (see Fig. 4a for an example). These results indicate that in order to have a more accurate measurement of the effective diffusivity in an experiment, we may either increase the system size or have more samples, which is as expected.

In addition to the standard error in the mean $D_{eff}$, the fluctuation in $D_{eff}$ among $5 \times 10^4$ samples is also of interested because it provides the spectrum of $D_{eff}$ that can be measured in a given sample and it reveals the dependence of $D_{eff}$ on the details of the microstructure. $D_{eff}$ exhibits fluctuations due to the statistical nature of GB distributions. Here we characterize the fluctuation in $D_{eff}$ using the coefficient of variation, $c_v = \frac{\sigma}{\mu}$, where $\mu = \langle D_{eff} \rangle$ is the average $D_{eff}$ and $\sigma$ is the standard deviation of $D_{eff}$. Fig. 4b and c shows the coefficient of variation of $D_{eff}$ for varying $\frac{D_H}{D_L}$ and $f_H$ as a function of the system size. One can see that $c_v$ (i.e., fluctuation in $D_{eff}$) generally decreases as the system size increases and the behavior of $c_v$ is not very sensitive to $\frac{D_H}{D_L}$ and $f_H$. Moreover, it is found that for the system size studied in this work (i.e., $10^2$–$10^4$ grains in 3D domain), $c_v$ is larger than 0.8, which demonstrates that the fluctuation in $D_{eff}$ can be significant even if we have more than $10^3$ grains in a system. The spread of the $D_{eff}$ indicates that although the macroscopic diffusion can be characterized by the mean value of $D_{eff}$, the details of the microstructure should be taken into account when trying to predict $D_{eff}$ if diffusion will occur through a specific polycrystalline sample.

### 3.4. Dependence of $D_{eff}$ on the model dimensionality

In order to examine the dependence of $D_{eff}$ on the dimensionality, we evaluate $D_{eff}$ on a 2D Voronoi GB network with $10^4$ grains. The simulation conditions in the 2D Voronoi GB network are the same as that in the 3D Voronoi GB network. The corresponding figures for 2D Voronoi GB networks are shown in the Supplemental document of the present paper.

We first analyze the dependence of $D_{eff}$ on $\frac{D_H}{D_L}$ for different values of $f_H$, and we find that the trends are similar to those found in 3D Voronoi GB network (shown in Fig. 2). Specifically, $D_{eff}$ in 2D Voronoi GB network is nearly independent of $\frac{D_H}{D_L}$ when $f_H$ is smaller than the percolation threshold $f_p$, which for 2D Voronoi diagram is equal to 0.67. When $f_H > f_p$, $D_{eff}$ becomes a linear function of $\frac{D_H}{D_L}$. We also find that the dependence of $D_{eff}$ on $f_H$ follows the same trend as that shown in Fig. 3. Specifically, the EMT is accurate for low-contrast systems and the power-law functions in the percolation theory provide a good model for $D_{eff}$ in high-contrast systems. Significant deviation of EMT predictions from kMC results are observed mainly when $f_H$ and $f_p$ are close in values. In addition, we find that, similarly as in 3D Voronoi GB network, the GEM theory (Eq. (1) with exponents $t = 1.6$ and $s = 1.3$) can be used to approximate $D_{eff}$ in 2D Voronoi GB network. The agreement between the kMC and GEM methods again demonstrates that with the appropriate percolation threshold and critical exponents, the GEM theory can predict $D_{eff}$ with a reasonable accuracy. We also analyze the coefficient of variation of $D_{eff}$. We find that, similarly as in a 3D GB network, the coefficient of variation of $D_{eff}$ in a 2D Voronoi GB network decreases as the system size increases, and

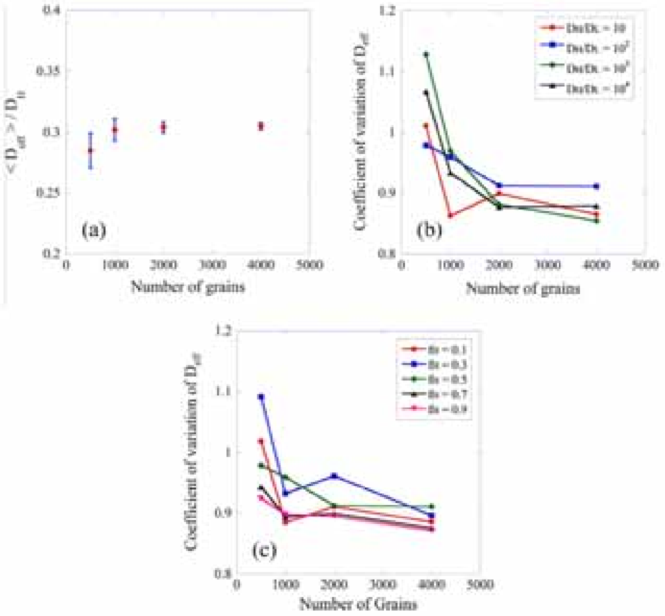

**Fig. 4.** (a) $\langle D_{eff} \rangle$ with error bar (estimated by the standard deviation divided by the mean) as a function of the system size when $\frac{D_H}{D_L} = 1000$ and $f_H = 0.5$. Coefficient of variation of $D_{eff}$ as a function of the system size for (b) different values of $\frac{D_H}{D_L}$ when $f_H = 0.5$ and (c) different values of $f_H$ when $\frac{D_H}{D_L} = 100$.

it does not strongly depend on $f_H$ and $\frac{D_H}{D_L}$. Moreover, the fluctuation of $D_{eff}$ in a 2D Voronoi GB network can also be significant for a system containing at lease up to $10^4$ grains.

In summary, the dependence of $D_{eff}$ on $\frac{D_H}{D_L}$ and $f_H$ as well as the fluctuation of $D_{eff}$ are nearly independent of the dimensionality of the simulation domain. The observed trends are similar in 2D and in 3D Voronoi GB networks. The main difference between 2D and 3D lies in the percolation threshold and the critical exponents in the percolation theory.

### 3.5. Grain size effect of $D_{eff}$

Grain size has been previously shown to affect diffusion through a polycrystalline sample, in cases where both GB diffusion and bulk diffusion are active [30]. As the grain size decreases, the fraction of GB region increases, which allows more diffusion to be conducted along GBs rather than through the crystalline grains. Since the GB diffusion is faster than the bulk diffusion, $D_{eff}$ increases as the grain size decreases. Here, we are interested in the kinetic regime where bulk diffusion through crystalline grains is negligible as compared to GB diffusion. It is interesting to ask whether the previously observed grain size effect will be present in this regime as well. We check three types of conditions: (1) the grain size is uniform and all GBs have the same character; (2) the grain size is uniform and GBs have two different characters; (3) the grain size is non-uniform and GBs have two different characters.

The grain size effect in the first case has been in fact already analyzed in Section 2, where the GB lattice is a square mesh in a 2D domain. We found that as the grain size decreases, the number of hopping steps across a certain distance increases. Meanwhile, the time spent in each hopping step decreases because the grain size decreases and so does the hopping distance. As a consequence, the total time over which one particle diffuses across a certain distance is independent of the grain size, and in this scenario $D_{eff}$ does not depend on the grain size. $D_{eff}$ in this case can actually be derived analytically following the steps shown in Ref. [62]. Specifically, the average square of the displacement of the diffusant after $n$ jumps can be expressed as $\langle d^2 \rangle = nl^2$, where $l$ is the distance in each jump. Since the total diffusion time $\tau$ is $\tau = n\Delta t$ (where $\Delta t$ is the time spent in each jump), it can be derived that $D_{eff} = \frac{\langle d^2 \rangle}{4\tau} = \frac{l^2}{4\Delta t}$, so the effective diffusivity is equal to the diffusivity in each GB, and therefore it is independent of the grain size.

The next step (case (2)) is to consider two types of GBs (HEGBs and LEGBs) with different diffusivities ($D_H$ and $D_L$). Analytical derivation of $D_{eff}$ in a system with two types of GBs is not straightforward since $D_{eff}$ depends on the GB connectivity as shown in Fig. 3, so we focus on numerical calculation of $D_{eff}$ here. We calculate the numerical values of $D_{eff}$ as a function of grain size, where the GB lattice is a square mesh and two types of GBs with diffusivity contrast $\frac{D_H}{D_L} = 10^3$ are randomly distributed. The results show that $D_{eff}$ still does not exhibit any grain size dependence within our error bars. We further evaluate $D_{eff}$ in a 2D Voronoi diagram with a non-uniform grain size and two types of GBs (case (3)), which again shows that $D_{eff}$ does not depend on the grain size.

Above results suggest that when GB diffusion is the only active mechanism of transport, $D_{eff}$ is independent of the grain size under quite general conditions. This finding is based on the assumption that the properties of the GB network (e.g., GB diffusivity, fraction of each type of GB) do not depend on the grain size. Therefore, if the grain size effect of $D_{eff}$ is observed in experiments on systems in the Type C regime, it will likely be induced by the relation between the grain size and the aforementioned properties of GBs. For instance, the authors of Ref. [63] have shown that the diffusion of hydrogen in pure nickel depends on grain size because the fraction of each type of GB and the density of trapping sites for hydrogen (and therefore GB diffusivity of hydrogen) change as grain size varies in the experiment.

## 4. Results for systems with multiple types of GBs

We extend our kMC simulations to investigate $D_{eff}$ in model systems that contain multiple types of GBs. These systems resemble closely the GB networks in actual polycrystalline materials. A comprehensive investigation of the dependence of $D_{eff}$ on the properties of GB networks, such as the diffusivity ratio and the fraction of each type of GB, is beyond the scope of this work. Here, we mainly demonstrate that our model is applicable to a system with multiple GB types and show the effects of including more types of GBs on the $D_{eff}$.

As an example, we investigate a system that contains ten types of GBs, where the fraction of each type is 10%. We consider 5 different cases for the GB diffusivities, as shown in Table 1. To enable a meaningful comparison, in all cases, the maximum and minimum diffusivities are the same, and so is the average diffusivity defined as $\overline{D} = \sum_{i=1}^{10} f_i D_i$, where $f_i$ and $D_i$ are the fraction and the diffusivity of the $i$-th GB, respectively. Moreover, GB diffusivities in each case can be categorized into three groups: low-diffusivity ($D_i < 50$), intermediate diffusivity ($D_i \approx 10^4$), and high-diffusivity ($D_i \approx 2 \times 10^4$). In order to make a comparison between the current simulations and the earlier simulations on systems containing two types of GBs (see Section 3), case 5 in Table 1 includes only low- and high-diffusivity GBs and therefore it is equivalent to a system with two types of GBs. The diffusivities in these 5 cases are chosen to have different diffusivity spread while keep the minimum, the maximum, and the average diffusivities the same. Here we again use the coefficient of variation $c_{vd} = \frac{\sigma}{\mu}$ to represent the diffusivity spread, where $\mu = \overline{D}$ is the mean GB diffusivity and $\sigma$ is the standard deviation of the GB diffusivity. Here the mean and standard deviations are taken over the 10 values for each case, and is not based on a KMC simulation. The coefficient of variation of the diffusity, $c_{vd}$, therefore differs greatly in meaning from the coefficient of variation of the effective diffusivity $c_v$ introduced in Section 3. Since $\mu$ is the same in all cases, $c_{vd}$ is proportional to $\sigma$. It can be seen from Table 1 that $c_{vd}$ is different in the five cases, and it has the largest value in case 5. One should note that the diffusivities in Table 1 can also be divided into two groups: one group with diffusivity on the order of 10 and the other on the order of $10^4$. For this reason, all 5 cases in Table 1 resemble systems with two GB types and they allow us to examine the qualitative behavior of $D_{eff}$ when multiple GB types instead of two GB types are considered.

Fig. 5a shows the effective diffusivity $D_{eff}$ calculated for each case as a function of $c_{vd}$, which is the measure of the spread in diffusivity values among the ten GB types. We find that $D_{eff}$ decreases with increasing $c_{vd}$. In addition, the system with only two types of GBs (case (5)) has generally a lower effective diffusivity than a system with more GB types, provided that the maximum, the minimum, and the average diffusivities are the same. The diffusivity spread in a system with multiple GB types reaches its minimum ($c_{vd} = 0$) when the GB diffusivity is uniform (i.e., $D_i = \overline{D}$). In this case, $D_{eff}$ has its maximum value, which is $\overline{D}$. From Fig. 5a we can also see that in a system with multiple GBs, low-diffusivity GBs have more impact on $D_{eff}$ than high-diffusivity GBs. Specifically, when the fraction of low-diffusivity GBs $f_L$ is the same as the fraction of high-diffusivity GBs $f_H$ (i.e., $f_L = f_H$), $D_{eff}$ decreases as $f_L$ $(= f_H)$ increases. The dominant role of low-diffusivity GBs in $D_{eff}$ is similar to systems with two types of GBs when the fraction of HEGBs is smaller than the percolation threshold (see Fig. 2).

For the sake of further comparison between the behavior of $D_{eff}$ in systems with two and more than two types of GBs, we also examine the EMT prediction of $D_{eff}$, the grain size effect, and fluctuation of $D_{eff}$. Fig. 5b gives the relative difference in $D_{eff}$ obtained from kMC and EMT (i.e., $\left(D_{eff}^{kMC} - D_{eff}^{EMT}\right)/D_{eff}^{EMT}$) as a function of the coefficient of variation $c_{vd}$. It shows that the deviation of EMT prediction from kMC results increases as $c_{vd}$ (i.e., the spread in diffusivity) increases. Since the physical meaning of the spread in diffusivity is the same in a system with multiple GB types and in a system with only two GB types, it is not surprising that in a system with multiple GB types, EMT works better for samples with smaller $c_{vd}$. The dependence of $D_{eff}$ on the average grain size in the five cases studied here is shown in Fig. 5c. It can be seen that, consistently with what we found in a system with two types of GBs, $D_{eff}$ in systems with multiple GB types does not depend on the grain size as long as only GB diffusion is activated. Including more types of GBs not only does not induce a grain size dependence of $D_{eff}$, but also does not have a strong effect on the fluctuation of $D_{eff}$, as shown in Fig. 5d. We find that although the coefficient of variation of $D_{eff}$ in systems with multiple GB types increases slightly as the diffusivity spread increases (from case 1 to case 5), the values of $c_v$ is similar in systems with two and multiple GB types. Consistently with the trend found in systems with two GB types (see Figs. 4b and c), the fluctuation of $D_{eff}$ decreases as the system size increases in a system with multiple GB types, and more importantly, the fluctuation can be significant even if a system has more than $10^3$ grains. The latter again demonstrates that the details of microstructure should be taken into account when the macroscopic diffusivity is measured in a specific polycrystalline sample.

In summary, extending the model systems to include more than two GB types does not have an impact on the existence or lack of grain size effects on diffusion and on fluctuation of diffusion coefficients among randomly generated microstructures with the same macroscopic parameters. When the minimum, the maximum and the average diffusivities of individual GBs are kept constant, including more than two GB types leads to a faster diffusion. For materials with multiple types of GBs, low-diffusivity GBs have more impact on $D_{eff}$ in the sense that when the fractions of low-diffusivity GBs and high-diffusivity GBs are kept the same (e.g., cases 1–5 in Table 1), $D_{eff}$ decreases as these fractions increase (e.g., from case 1 to case 5 in Table 1). We also find that the EMT model captures the diffusion behavior better in systems with a smaller spread in diffusivity values among the different GB types. Finally, one should note that the cases studied here are special because

**Table 1**
Diffusivities of the ten types of GBs in five different cases considered in this study. $c_{vd}$ is the coefficient of variation of the diffusivity for each case (see text for details).

| Case no. | $D_1$ | $D_2$ | $D_3$ | $D_4$ | $D_5$ | $D_6$ | $D_7$ | $D_8$ | $D_9$ | $D_{10}$ | $c_{vd}$ |
|---|---|---|---|---|---|---|---|---|---|---|---|
| 1 | 5 | 9980 | 9985 | 9990 | 9995 | 10005 | 10010 | 10015 | 10020 | 19995 | 0.471 |
| 2 | 5 | 10 | 9985 | 9990 | 9995 | 10005 | 10010 | 10015 | 19990 | 19995 | 0.667 |
| 3 | 5 | 10 | 15 | 9990 | 9995 | 10005 | 10010 | 19985 | 19990 | 19995 | 0.810 |
| 4 | 5 | 10 | 15 | 20 | 9995 | 10005 | 19980 | 19985 | 19990 | 19995 | 0.940 |
| 5 | 5 | 10 | 15 | 20 | 25 | 19975 | 19980 | 19985 | 19990 | 19995 | 1.053 |

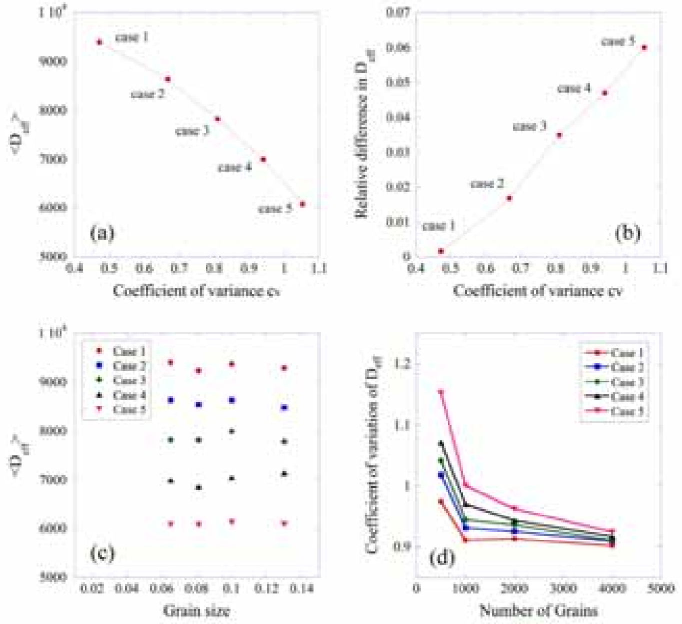

**Fig. 5.** Analysis of a system with more than two types of GB. (a) Effective diffusivity $D_{eff}$ calculated in the 5 cases (see Table 1); (b) a relative difference between kMC and EMT predictions as a function of the coefficient of variation of GB diffusivity; (c) dependence of $D_{eff}$ on the normalized grain size (ratio of the average grain size to the domain size); (d) coefficient of variation of $D_{eff}$ as a function of the system size.

all ten GB types are equally probable in the sample, which may not reflect the complexity in actual GB structure. Nevertheless, the properties of $D_{eff}$ shown above do not depend on the number of GB types or their fraction, and therefore they are expected to provide a general behavior of $D_{eff}$ in realistic GB systems with multiple GB characters.

## 5. Conclusions

We have developed a kinetic Monte Carlo model to evaluate the effective diffusivity in GB networks in polycrystalline materials. This model connects the atomic-level information of hopping processes with the coarse-grained diffusion on GB planes, which allows us to conduct macroscopic simulations without resolving atomic details. Several features of the effective diffusivity have been found from the numerical experiments. First, in the kinetic limit when GB diffusion is the dominant transport mechanism, the effective diffusivity through a polycrystalline sample does not depend on the grain size. Secondly, the dimensionality and the type of GB networks mainly affect the percolation threshold and the critical exponents in the percolation theory, and they do not change the qualitative dependence of the effective diffusivity on the diffusivity contrast and the fraction of GB types. We also find that the effective diffusivity exhibits fluctuations due to the statistical nature of GB distribution. In addition, our results show that EMT approximates the effective diffusivity with a reasonable accuracy not only in low-diffusivity contrast systems, but also in high-diffusivity contrast systems when the fraction of HEGBs is significantly different from the percolation threshold. In all cases, GEM can be used to predict the effective diffusivity if the percolation threshold and the critical exponents are known. Finally, including more types of GBs generally increases the effective diffusivity, provided that the maximum, the minimum and the average diffusivities, are kept the same.

Although the properties of the effective diffusivity shown above are based on simplified GB systems, these properties do not depend on specific materials or GB characters, and they shed light on the qualitative behavior of the effective diffusivity in systems containing two or more GB types. The presented modeling framework is flexible so that it will be straightforward to include additional effects such as the correlation of GB types. This model can be easily applied to specific materials systems with complex GB networks, realistic diffusivities, and with a variable fraction of each GB type.

## Acknowledgement

This research is being performed using funding received from the DOE Office of Nuclear Energy's Nuclear Energy University Programs Contract Number 00089350.

## Appendix A. Supplementary material

Supplementary data associated with this article can be found, in the online version, at http://dx.doi.org/10.1016/j.commatsci.2014.06.028.

## References

[1] I. Kaur, Y. Mishin, W. Gust, Fundamentals of Grain and Interphase Boundary Diffusion, Wiley, Chichester, UK, 1995.
[2] Y. Mishin, C. Herzig, Mater. Sci. Eng. A 260 (1999) 55.
[3] J. Fisher, J. Appl. Phys. 22 (1951) 74.

[4] L. Harrison, Trans. Faraday Soc. 57 (1961) 1191.
[5] R. Whipple, Philos. Mag. 45 (1954) 1225.
[6] A. Le Claire, Brit. J. Appl. Phys. 14 (1963) 351.
[7] T. Suzuoka, Trans. Jpn. Inst. Metals 2 (1961) 25.
[8] G. Gilmer, H. Farrel, J. Appl. Phys. 47 (1976) 3792.
[9] G. Gilmer, H. Farrel, J. Appl. Phys. 47 (1976) 4373.
[10] W. Preis, W. Sitte, J. Appl. Phys. 79 (1996) 2986.
[11] W. Preis, W. Sitte, J. Appl. Phys. 97 (2005) 093504.
[12] D. Turnbull, R. Hoffman, Acta Metall. 2 (1954) 419.
[13] R. Hoffman, Acta Metall. 4 (1956) 97.
[14] B. Straumal, B. Bokshtein, L. Klinger, L. Shvindlerman, Scripta Metall. 15 (1981) 1197.
[15] J. Sommer, C. Herzig, S. Mayer, W. Gust, Defect Diff. Forum 66-69 (1989) 843.
[16] E. Budke, C. Herzig, S. Prokofjev, L. Shvindlerman, Mater. Sci. Forum 207–209 (1996) 465.
[17] Q. Ma, R. Balluffi, Acta Metall. Mater. 41 (1993) 133.
[18] A. Suzuki, Y. Mishin, J. Mater. Sci. 40 (2005) 3155.
[19] L. Lim, T. Watanabe, Acta Metall. Mater. 38 (1990) 2507.
[20] V. Gertsman, K. Tangri, R. Valiev, Acta Metall. Mater. 42 (1994) 1785.
[21] L. Fionova, Mater. Chem. Phys. 37 (1994) 201.
[22] T. Watanabe, Mater. Sci. Eng. A 176 (1994) 39.
[23] V. Gertsman, M. Janecek, K. Tangri, Acta Mater. 44 (1996) 2869.
[24] W. Hart, Acta Metallogr. 5 (1957) 597.
[25] A. Mortlock, Acta Metallogr. 8 (1960) 132.
[26] J. Kalnins, E. Kotomin, J. Maier, J. Phys. Chem. Solids 63 (2002) 449.
[27] I. Belova, G. Murch, J. Phys. Chem. Solids 64 (2003) 873.
[28] I. Belova, G. Murch, Philos. Mag. 84 (2004) 17.
[29] I. Belova, G. Murch, J. Phys. Chem. Solids 66 (2005) 722.
[30] Y. Chen, C. Schuh, J. Appl. Phys. 101 (2007) 063524.
[31] D. Shrader, S. Khalil, T. Gerczak, T. Allen, A. Heim, I. Szlufarska, D. Morgan, J. Nucl. Mater. 408 (2011) 257.
[32] S. Khalil, N. Swaminathan, D. Shrader, A. Heim, D. Morgan, I. Szlufarska, Phys. Rev. B 84 (2011) 214104.
[33] Y. Chen, C. Schuh, Acta Mater. 54 (2006) 4709.
[34] A. Suzuki, Y. Mishin, Interface Sci. 11 (2003) 131.
[35] J. Harding, D. Harris, Phys. Rev. B 63 (2001) 094102.
[36] A. Pedersen, H. Jonsson, Acta Mater. 57 (2009) 4036.
[37] Y. Du, J. Rogal, R. Drautz, Phys. Rev. B 86 (2012) 174110.
[38] R. Quey, P. Dawson, F. Barbe, Comput. Methods Appl. Mech. Eng. 200 (2011) 1729–1745.
[39] M. Frary, C. Schuh, Appl. Phys. Lett. 83 (2003).
[40] M. Frary, C. Schuh, Phys. Rev. B 69 (2004) 134115.
[41] M. Frary, C. Schuh, Philos. Mag. 85 (2005) 1123.
[42] B. Bokstein, V. Ivanov, O. Oreshina, A. Peteline, S. Peteline, Mater. Sci. Eng. A 302 (2001) 151.
[43] T. Frolov, Y. Mishin, Phys. Rev. B 79 (2009) 174110.
[44] T. Angsten, T. Mayeshiba, H. Wu, D. Morgan, New J. Phys. 16 (2014) 015018.
[45] https://materialshub.org/resources/diffcalc.
[46] P. Millett, M. Tonks, S. Biner, J. Nucl. Mater. 424 (2012) 176.
[47] A. Becker, R. Ziff, Phys. Rev. E 80 (2009) 041101.
[48] V. Vyssotsky, S. Gordon, H. Frisch, J. Hammersley, Phys. Rev. 123 (1961) 1566.
[49] A. Hunt, Percolation Theory for Flow in Porous Media, Springer, Berlin, 2005.
[50] S. Kirkpatrick, Rev. Mod. Phys. 45 (1973) 574.
[51] D. Stauffer, A. Aharony, Introduction to Percolation Theory, CRC Press, Philadelphia, USA, 1994.
[52] M. Isichenko, Rev. Mod. Phys. 64 (1992) 961.
[53] J. Clerc, G. Giraud, J. Laugier, J. Luck, Adv. Phys. 39 (1990) 191.
[54] P. Li, W. Strieder, J. Phys. C 15 (1982) L1235.
[55] M. Sahimi, J. Phys. A 17 (1984) L601.
[56] J. Straley, Phys. Rev. B 15 (1977) 5733.
[57] I. Webman, J. Jortner, M. Cohen, Phys. Rev. B 16 (1977) 2593.
[58] M. Sahimi, B. Hughes, L. Scriven, H. Davis, J. Phys. C 16 (1983) L521.
[59] D. McLachlan, J. Phys. C 20 (1987) 865.
[60] D. McLanchlan, M. Blaskiewicz, R. Newnham, J. Am. Ceram. Soc. 73 (1990) 2187.
[61] J. Wu, D. McLachlan, Phys. Rev. B 56 (1997) 1236.
[62] H. Berg, Random Walks in Biology, Princeton University Press, Princeton, NJ, 1993.
[63] A. Oudriss, J. Creus, J. Bouhattate, E. Conforto, C. Berziou, C. Savall, X. Feaugas, Acta Mater. 60 (2012) 6814.

Journal of Nuclear Materials 467 (2015) 332–340

Contents lists available at ScienceDirect

Journal of Nuclear Materials

journal homepage: www.elsevier.com/locate/jnucmat

# Grain boundary diffusion of Ag through polycrystalline SiC in TRISO fuel particles

Jie Deng [a], Hyunseok Ko [a], Paul Demkowicz [b], Dane Morgan [a, c], Izabela Szlufarska [a, c, *]

[a] Department of Materials Science and Engineering, University of Wisconsin-Madison, Madison, WI 53706, USA
[b] Idaho National Laboratory, P.O. Box 1625, Idaho Falls, ID 83414, USA
[c] Department of Engineering Physics, University of Wisconsin-Madison, Madison, WI 53706, USA

## HIGHLIGHTS

- Developed models for the effective diffusivity and release fraction of Ag in polycrystalline SiC in TRISO fuel particles.
- Showed dependence of Ag diffusivity and release fraction on various grain boundary network properties.
- Demonstrated a non-negligible contribution of GB structure variation to the scatter in Ag diffusivity and release fraction.

## ARTICLE INFO

*Article history:*
Received 9 May 2015
Received in revised form
30 September 2015
Accepted 30 September 2015
Available online 9 October 2015

*Keywords:*
Grain boundary diffusion
TRISO fuel particles
Fission product release

## ABSTRACT

The effective diffusivity and release fraction of Ag in polycrystalline SiC are evaluated using a kinetic Monte Carlo model. The effects of various grain boundary network properties on the transport of Ag across the SiC layer have been examined, including fraction of grain boundary type, spread in grain boundary diffusivities and distribution of grain boundary types. It is shown that the effective diffusivity and release fraction of Ag can exhibit a large variability due to changes in the GB structure of SiC, and this variability is almost independent of temperature fluctuation. The present results suggest that the variation in properties of grain boundary networks in SiC may contribute to the spread in the Ag diffusivity and release fraction measured in TRISO particles. It is also found that the grain boundary diffusion alone may be insufficient to account for the Ag diffusivities and release fractions measured in integral release experiments. Additional factors such as irradiation and temperature distribution may also play an important role in Ag transport across the SiC layer.

© 2015 Elsevier B.V. All rights reserved.

## 1. Introduction

The tristructural-isotropic (TRISO) fuel particle is one of the main fuel forms used in the very high temperature reactors (VHTR) [1]. A fuel particle consists of a spherical fuel kernel surrounded by a porous graphite buffer layer and three coating layers [2,3]: inner pyrolytic carbon layer, SiC layer, and outer pyrolytic carbon layer. Each coating layer has its own functionality, and one of the main functions of the SiC layer is to prevent the radioactive fission products from diffusing out into the coolant [4]. It has been observed in reactor experiments that although the SiC layer can retain most fission products, some species such as Ag can escape from fuel particles [5–10]. For example, Nabielek et al. [5] carried out in-pile experiments in the Dragon reactor and found that the content of Ag retained in individual fuel particles after irradiation has drastic variations. In addition Ag release was found to be significantly increased at fuel operating temperatures above 1200 °C. Amian et al. [6] and Verfondern et al. [7] conducted post-irradiation annealing tests on coated particles at temperatures between 1000 °C and 2100 °C, where the coated particles had been irradiated in a wide range of temperature, burnup and fluence. It was found that Ag was released in all cases considered, and that there was a large scatter in the Ag diffusivity in individual fuel particles. Bullock et al. [8] carried out post-irradiation annealing tests on different types of TRISO fuel particles at three different temperatures (1200 °C, 1350 °C and 1500 °C). It was shown that for SiC coated particles, Ag was released at 1500 °C only and, as in the earlier experiments, Ag release varied strongly from particle to particle. Recently Demkowicz et al. [9] and Baldwin et al. [10]

---

* Corresponding author. Department of Materials Science and Engineering, University of Wisconsin-Madison, Madison, WI 53706, USA.
*E-mail address:* szlufarska@wisc.edu (I. Szlufarska).

http://dx.doi.org/10.1016/j.jnucmat.2015.09.054
0022-3115/© 2015 Elsevier B.V. All rights reserved.

presented results of post-irradiation examination of the Advanced Gas Reactor (AGR) TRISO fuel compacts that experienced a wide range of irradiation temperatures and a significant spatial variation in temperature within a single compact. It was shown that the fractional release of Ag from particles can be quite significant. Individual compacts within a single capsule exhibited significantly different Ag retention, and within a single compact individual particles exhibited a wide range of Ag release. These experimental results suggest that the release of Ag can be significant in TRISO fuel elements at high temperatures (above approximately 1000 °C–1100 °C) and moreover, that there is a high variability in the release fraction and diffusivity of Ag in individual fuel particles. The release of Ag from fuel has safety implications related to plant maintenance, as it can deposit on surfaces in the helium coolant circuit. In order to better design the TRISO fuel particles, it is critical to understand transport mechanisms of Ag across the SiC layer and to identify the causes of variability in the degree of Ag release.

The mechanisms of Ag moving across the SiC layer are still under debate [11–24]. One proposed mechanism is that Ag escapes from fuel particles via vapor diffusion along cracks in the SiC layer [12,13]. This argument was presented for example by MacLean et al. who investigated transport of Ag implanted into polycrystalline $\beta$-SiC [12,13]. As the authors did not observe any Ag diffusion through SiC in their experiments, they concluded that in reactor conditions Ag may diffuse along cracks in SiC. These cracks could be generated during fabrication or irradiation exposure. The mechanism of diffusion along cracks is consistent with results of *ab initio* calculations based on the density functional theory (DFT) [14], which showed that Ag prefers to absorb on the SiC surface rather than remain in the bulk and that the mobility of Ag on the SiC surface is high. However, there might be other reasons why Ag did not diffuse in the experiments reported in Refs. [12,13] and yet be possible in reactor conditions. For instance, in the laboratory experiments implantation introduced a highly amorphous layer in SiC and it is possible that this amorphization led to Ag being trapped in precipitates. An amorphous implantation layer is unlikely to occur under reactor conditions. In addition, recent experiments by Minato et al. [15] and Lopez-Honorato et al. [16] showed that the release behavior of Ag cannot be explained only by the presence or absence of the cracks in the SiC layer because some particles with no cracks in the SiC have very poor Ag retention. The above findings indicate that although the presence of cracks could accelerate Ag transport, cracks are not the only transport pathway, and perhaps not even the dominant one. Another proposed mechanism for fast Ag release is the chemical degradation of SiC by fission products such as Pd [17–19]. Neethling et al. [17–19] showed that Pd can react with SiC and form palladium silicides along grain boundaries (GBs) of SiC. These palladium silicides can interact with Ag and form a Pd, Ag, and Si solution that is capable of migrating along GBs in SiC over time. These results suggest that the presence of Pd may facilitate the migration of Ag in SiC. On the other hand, Minato et al. [20] found high Ag release in fuel particles where Pd attack was not observable using optical microscopy, which may indicate that Ag can transport in SiC without assistance of Pd.

In addition to vapor diffusion and chemical degradation, GB diffusion is another potential mechanism for Ag transport in SiC [16,21–24]. Friedland et al. [21,22] implanted Ag in SiC and compared migration of Ag in single crystal SiC and polycrystalline SiC at 1300 °C. Ag diffusion was observed to take place in the latter but not the former structure, which implies that Ag can be transported in SiC via GB diffusion. In addition, Lopez-Honorato et al. [16,23] developed a method of trapping thin layers of Ag between two SiC layers in actual coated fuel particles. In their experiments, Ag was clearly detected at GBs, which shows that migration of Ag is at least partially governed by GB diffusion. Recently, Gerczak et al. [24] compared the transport of Ag implanted into single crystal 4H–SiC and polycrystalline chemical-vapor-deposited 3C–SiC at 1500 °C, 1535 °C, 1569 °C and 1625 °C. The penetration of Ag into the bulk past the primary implantation peak is not observed in 4H–SiC, but is found in 3C–SiC after thermal exposure above 1535 °C. These results imply that the presence of GBs may facilitate Ag diffusion above 1535 °C. In addition to the experimental investigations, DFT calculations demonstrated that in SiC the diffusivity of Ag along GBs [25–27] is much higher than that in bulk [28], which suggests that GBs in SiC may provide fast-diffusion paths for Ag migration. Moreover, microstructures of SiC in TRISO fuel particles have been examined by electron back scatter diffraction [29–31], where it was shown that GB characters in SiC can vary significantly among different particles. Since the diffusivity of Ag in GBs presumably depends on the characters of GBs, it is expected that different distributions of GB character may lead to fluctuation in the overall transport of Ag across the SiC layer. Therefore, these previous studies suggest that GB diffusion may not only account for fast Ag transport in SiC, but also be responsible for at lease some of the variability in diffusivity and release fraction of Ag measured in integral release experiments shown in Refs. [5–10].

The present study focuses on GB diffusion of Ag in the SiC layer and aims to test two hypotheses: (i) the variation in GB structures may be the origin of some or all of the scatter in diffusivity and release fraction of Ag in TRISO fuel particles; (ii) GB diffusion in polycrystalline SiC is fast enough to explain experimentally observed Ag release. To test these hypotheses, we use our recently developed kinetic Monte Carlo (kMC) model [32] for diffusion through polycrystalline materials and calculate the effective diffusivity of Ag in heterogeneous GB networks in SiC. The model is also further extended to evaluate the release fraction of Ag in fuel particles with time-dependent generation of Ag. We demonstrate the dependence of the effective diffusivity and release fraction of Ag on various properties of GB networks such as GB distribution and fraction of each GB type. We also examine the role of GB structure and temperature variation in the fluctuation of Ag transport and discuss additional factors that may affect GB diffusion of Ag in actual fuel particles, such as irradiation damage and temperature distribution.

## 2. Kinetic Monte Carlo model

In our kMC model, the GB network of SiC is represented by a three-dimensional (3D) Voronoi diagram [33]. In order to approximate the spherical shell structure of the SiC layer with a simpler geometry, the simulation domain is assumed to be a rectilinear

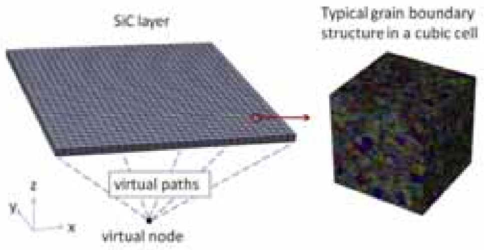

**Fig. 1.** Schematic view of the simulation domain. The SiC layer consists of 32 × 32 connected cubic cells, and each cell has the same Voronoi diagram but different grain boundary distributions. Virtual node and virtual paths are used when calculating the release fraction of Ag. See details in text.

block where the dimensions in the x and y directions (denoted by Lx and Ly, respectively) are much larger than that in the z direction (denoted by Lz), see Fig. 1 for a schematic diagram. Here x, y and z directions represent three orthogonal directions in a 3D space, where the x and y directions are parallel to the tangent of the coating surface, and the z direction is normal to the coating surface. In a typical fuel particle, the SiC layer has a thickness of 35 $\mu$m with the inner surface area around 1–2 mm$^2$. Thus the simulation domain is set to be Lz = 35 $\mu$m and Lx = Ly = 32 Lz. In an ideal simulation we would generate a Voronoi diagram directly in this domain, and then mesh each GB plane by triangular elements so that a Ag atom can hop along an element edge (from one mesh node to another neighboring node) along GBs. However, considering the typical grain size (0.5 $\mu$m–2.5 $\mu$m) in a SiC layer, the number of GBs in the simulation domain is more than $10^7$ and meshing all of them is not numerically practical. Therefore, to simplify the numerical problem in this study, we assume that the simulation domain consists of 32 × 32 = 1024 connected cubic boxes, each with the edge size equal to Lz. We first generate a Voronoi diagram in one box and mesh each GB within this box using triangular elements. Subsequently we assume that the same Voronoi diagram represents well the GB topology in each of the 1024 boxes, and simply replicate the Voronoi diagram across all of the boxes. Having assigned the Voronoi diagram in all boxes, we then assign a random diffusivity to each GB in the entire simulation domain. In other words, each of the 1024 boxes share the same Voronoi diagram but have different distributions of GB diffusivities. In order to test how a specific assignment of the Voronoi diagram influences the effective diffusivity in a single box, we calculated the effective diffusivity (see below for method of calculation) in a cubic box of size Lz with different Voronoi diagrams. In all these test simulations we kept the average grain size constant. We found that the magnitude and distribution of the effective diffusivity is almost independent of the Voronoi diagram used in the box, with variations in effective diffusivity among different Voronoi diagrams being lower than 5%. Thus from the perspective of our diffusion study, the procedure of using a single Voronoi diagram for all the boxes is an excellent approximation of the more realistic case where GB topology varies among the boxes.

With the GB networks of SiC built as described above, the effective diffusivity of Ag moving across such networks is calculated as follows. A Ag atom is placed at a randomly selected mesh node at the beginning of the simulation, and then it diffuses in the domain via hops along element edges. In each kMC step, the Ag atom randomly chooses to move along an element edge $i$ based on the rate $\Gamma_i = \frac{D_i}{l_i}$, where $D_i$ and $l_i$ are the diffusivity and length of the element edge $i$, respectively. After each kMC step, the total diffusion time $t$ and the total displacement $d_z$ along the z direction are recorded. Displacement $d_z$ is calculated as a projection on the z direction of the distance between the current and the initial positions of the Ag atom. Periodic boundary conditions are applied in all spatial directions. After a sufficiently long time (long enough to obtain converged results), the effective diffusivity can be calculated as $D_{\text{eff}} = \frac{d_z^2}{2t}$. Note that this is technically the effective diffusivity along just the z direction. Given that diffusion along the z direction is the relevant parameter for Ag release we take this as the effective diffusivity in this work. In addition, the effective diffusivity is largely isotropic, with very minor anisotropy emerging from the modeling approach, and the z diffusivity is therefore very close to the full isotropic effective diffusion coefficient. We repeat this procedure for $10^4$ samples (each sample has 1024 boxes, and they share the same Voronoi diagram but have different GB distributions) and then we obtain the average effective diffusivity $\langle D_{\text{eff}} \rangle$ of Ag through polycrystalline SiC. A more detailed description of our model can be found in Ref. [32].

The model described above can be applied both to the case where temperature is constant and where it changes as a function of time. The model can also be extended to evaluate the release fraction of Ag when the generation rate of Ag is time-dependent. When calculating the release fraction of Ag, periodic boundary conditions are applied along x and y directions only. We further denote the z- and z + planes (two boundary planes in the z direction) as the inner and outer surface of the SiC layer, respectively. The diffusivity of a Ag atom along the SiC surface or in the inner region of a fuel particle (e.g., the porous buffer layer) is generally larger than the GB diffusivity in SiC. In order to capture the fast transport of Ag on the inner surface of SiC (or within the inner buffer layer), we add a virtual node and place it outside the SiC layer. The virtual node is connected to each node in the z-plane by virtual paths so that a Ag atom can diffuse back and forth between any node on the z-plane through the virtual node (see Fig. 1 for a simplified illustration). The Ag diffusivity along each virtual path is assumed to be the same and much larger than the GB diffusivity of Ag in the SiC layer, thus effectively connecting all the nodes on the z-plane with a fast diffusion path. In each simulation, a Ag atom starts at the virtual node, and the atom is assumed to be released if it can reach the z + plane within its diffusion time. Let us assume that Ag is generated (with some known dependence of the generation rate on time) between time 0 and time $\tau$, where $\tau$ represents the total time of an in-pile experiment for a fuel. The release fraction of Ag at time $\tau$ can be calculated as follows. We first divide $\tau$ into $m$ intervals, i.e., the first interval $[t_0, t_1]$, the second interval $[t_1, t_2]$, …, the $m$-th interval $[t_{m-1}, t_m]$, where $t_0 = 0$, $t_m = \tau$ and $t_i - t_{i-1} = \tau/m$ for $i = 1, \ldots, m$. Denote $n_i$ as the number of Ag atoms generated in the $i$-th interval $[t_{i-1}, t_i]$. For the sake of numerical efficiency, we assume that $n_i$ Ag atoms are generated at a specific time, which we take as $\langle t_i \rangle = (t_i + t_{i-1})/2$. Then the release fraction of Ag at $\tau$ can be expressed as $F = \sum_{i=1}^{m}(f_i n_i)/\sum_{i=1}^{m} n_i$, where $f_i$ is the release fraction of the Ag atoms generated at the $i$-th interval. $f_i$ represents the probability of moving more than the thickness of the SiC layer in the z direction (i.e., reaching the z + plane) during the diffusion time $\tau - \langle t_i \rangle$.

We note that there are several assumptions in our model. First, the only active transport mechanism of Ag in the model is GB diffusion. Bulk diffusion is not considered because Ag has a strong tendency to segregate to SiC GBs and the GB diffusivity of Ag is much higher than its bulk diffusivity [25,26,28]. Secondly, the hop of Ag atoms is coarse-grained (from one mesh node to another) rather than atomic. However, it has been demonstrated in Ref. [32] that with the appropriate hopping rate, the kMC model with coarse-grained hops yields the same effective diffusivity as a model with atomic resolution. Thirdly, the difference between the diffusion of Ag along GB junctions and within GB planes is ignored here. While diffusion along the GB junction is generally different from diffusion within GB planes, their difference depends on temperature and GB structure, and there is currently no quantitative data for Ag diffusivity along GB junctions of SiC that would allow us to include this distinction in our model. As such, in the current model the diffusion coefficient for transport along a GB junction is set to be the highest diffusion coefficient in all GBs that connect to that GB junction. The most significant approximation in the model is likely the use of just two GB diffusivities whose values are adapted as best as possible from modeling and experimental results, as described in Sec. 3. This approximation is necessitated by the fact that the Ag diffusion coefficients are not known for general GB types.

We note that kMC models have been previously applied by other researchers to examine transport of Ag across the three coating layers in TRISO fuel particles [34]. The model developed in Ref. [34] assumes that Ag has a single diffusivity in each coating layer and each layer consists of rectangular grains. The influence of a number of microstructural features (such as reflective interfaces, cracks and radiation-induced cavities) on Ag transport were taken into account using parametric functions that may either accelerate or retard Ag diffusion. The results showed that it is possible to fit integral release experimental data by varying parameters in the model. In contrast to this earlier study, in our model we focus on GB diffusion in the SiC layer and we consider a 3D GB network with properties similar to those measured in experimental SiC samples. No other types of defects or microstructural features are included, which isolates other influences on Ag diffusion and allows us to test whether GB diffusion alone may account for fast Ag diffusion in SiC as well as the variability in Ag release behavior.

## 3. Grain boundary diffusion of Ag in SiC

The kMC model introduced in Section 2 is applied to evaluate the effective diffusivity and release fraction of Ag in polycrystalline SiC. In order to provide insights into Ag transport in fuel particles, the properties of GB networks in the SiC layer in actual TRISO fuel particles shown in Refs. [29,35] are used in our model. Specifically, the simulation domain is a rectilinear block, where the surface area is similar to the area of the inner surface of the SiC coating in TRISO and the domain thickness is 35 $\mu$m, which is a typical thickness of the SiC layer. The domain contains about $4.1 \times 10^6$ grains and the average grain size is 2.2 $\mu$m, which is within the range of typical grain size (0.5 $\mu$m − 2.5 $\mu$m) found in TRISO particles. The GB character in the SiC layer has a wide distribution, which includes various coincidence site lattice (CSL) GBs, low- and high-angle GBs. Although a few simulation studies reported diffusion coefficients along specific GBs in SiC [25–27], a general dependence of Ag diffusion coefficient on GB type is still unknown. As such, in our model we assume that two types of GBs, low-energy GB (LEGB) and high-energy GB (HEGB), are randomly distributed throughout the sample. The diffusivities of Ag along LEGB and HEGB, denoted by $D_{\rm L}$ and $D_{\rm H}$, respectively, represent the lower and upper limit of Ag diffusion along GBs in SiC.

The range of the fraction of LEGB, $f_{\rm L}$, is determined as follows. The electron backscatter diffraction measurement on AGR-1 fuel particles shows that the range of the fraction of CSL GBs, low-angle GBs and high-angle GBs in the SiC layer is 0.3–0.45, 0.1–0.15, and 0.4–0.6, respectively [35]. We assume that these values are at least approximately representative of other TRISO particle SiC grown by chemical vapor deposition in previous integral release experiments. In the case when only CSL GBs can be counted as LEGBs (a lower bound for LEGB fraction), the minimum $f_{\rm L}$ is 0.3. In the case when only high-angle GBs can be counted as HEGBs (an upper bound for LEGB fraction), the maximum $f_{\rm L}$ is 0.6. Therefore, the range of $f_{\rm L}$ can be approximated as 0.3–0.6. Correspondingly, the fraction of HEGB, $f_{\rm H}$, varies from 0.4 to 0.7 in our model.

The values of $D_{\rm L}$ and $D_{\rm H}$ in the present study are assumed to be $D_{\rm L} = 10^{-9} \times \exp\left(\frac{-2.7}{kT}\right)$ m$^2$/s, and $D_{\rm H} = 10^{-9} \times \exp\left(\frac{-2.04}{kT}\right)$ m$^2$/s. These values are chosen to meet the following constraints and assumptions:

1. The values are such that in the relevant temperature range 900 °C–1400 °C, the diffusivity ratio $\frac{D_{\rm H}}{D_{\rm L}}$ varies from $10^2$ to $10^3$, which is reasonable for impurity diffusion in polycrystalline materials [36].
2. The variation in values are due to activation energies, rather than attempt frequencies, as the latter are not expected to vary dramatically with GB type. The attempt frequencies are set to values from fitted D values for integral release in Refs. [5–7].
3. The activation energies should be close to 2.2 eV, which is approximately the value observed in integral release experiments [5–7].
4. The specific values of the activation energies for $D_{\rm L}$ and $D_{\rm H}$ are then selected to ensure that when $f_{\rm H}$ varies from 0.4 to 0.7, the effective diffusivities of Ag are between the lower and upper limits of the Ag diffusivity measured in Refs. [5–7]. This approach assures that our overall predicted D values are consistent with the average integral release experiments. It also allows us to assess the variation in diffusivity with variation of the specific spatial distributions of GB types for fixed $f_{\rm H}$, which is the focus of Sections 3.1 and 3.2.

It is emphasized here that although the diffusivity ratio in our model can be as large as $10^2$ or $10^3$, it does not mean that the effective diffusivity $D_{\rm eff}$ will vary 2 or 3 orders of magnitude. The actual fluctuation of $D_{\rm eff}$, which is one of the main interests of this study, remains to be examined because $D_{\rm eff}$ is not only dependent on $D_{\rm L}$ and $D_{\rm H}$, but it is also affected by $f_{\rm H}$, as well as by the connectivity of GBs [32,37]. We note that by fitting the values of diffusivities to release data from Refs. [5–7] we can assess our first hypothesis, that GB structure may be a significant source of variation in integral release values, but we cannot assess our second hypothesis, that Ag integral release can be explained by GB diffusion, as our release will be reasonably consistent with experiments by construction. These fitted diffusivity values will therefore only be used to assess the first hypothesis, as done in Sec. 3.1–3.3. The second hypothesis will be tested in Sec. 3.4 using GB diffusivities estimated from published quantitative data distinct from integral release based estimates.

### 3.1. Effect of GB network properties on the effective diffusivity at constant temperature

With the GB diffusivities of Ag and properties of GB networks in SiC shown above, we first examine the effective diffusivity of Ag at a constant temperature. Because temperature is constant throughout the simulation time, the diffusivities $D_{\rm L}$ and $D_{\rm H}$ are independent of time as well. In the following figures, $\langle D_{\rm eff}\rangle$ is normalized by $D_{\rm L}$ so that the features of $\langle D_{\rm eff}\rangle$ are not affected by the diffusivity unit. Normalization of $\langle D_{\rm eff}\rangle$ does not alter its dependence on properties of GB networks.

Fig. 2a shows $\frac{\langle D_{\rm eff}\rangle}{D_{\rm L}}$ as a function of $f_{\rm H}$ with different diffusivity ratios $\frac{D_{\rm H}}{D_{\rm L}}$. It can be seen that for larger values of $\frac{D_{\rm H}}{D_{\rm L}}$, $\langle D_{\rm eff}\rangle$ increases more rapidly with $f_{\rm H}$. The dependence of $\langle D_{\rm eff}\rangle$ on $\frac{D_{\rm H}}{D_{\rm L}}$ for different values of $f_{\rm H}$ is shown in Fig. 2b. We find that in most cases $D_{\rm eff}$ is strongly dependent on $\frac{D_{\rm H}}{D_{\rm L}}$ and that this dependence is almost linear. Fig. 2a and b show that the effective diffusivity of Ag may vary significantly as the properties of GB networks in SiC change. This result suggests that decreasing the variability in GB characters may reduce the scatter in Ag diffusivity.

As mentioned in Section 2, the effective diffusivities shown in Fig. 2 are averaged over $10^4$ samples with different GB distributions. $D_{\rm eff}$ exhibits fluctuations among these samples because of the statistical nature of GB distributions. It is instructive to investigate the fluctuation of $D_{\rm eff}$ since it reveals the dependence of $D_{\rm eff}$ on the randomly sampled microstructure and gives an estimate of the range of $D_{\rm eff}$ values that can be measured in different samples with the same dimensions, with the same $f_{\rm H}$ and the same $\frac{D_{\rm H}}{D_{\rm L}}$. Here, we characterize the fluctuation of $D_{\rm eff}$ using the coefficient of variation, $c_v = \frac{\sigma}{\mu}$, where $\mu$ is the average effective diffusivity and $\sigma$ is the standard deviation of $D_{\rm eff}$. Fig. 3a shows how $c_v$ depends on the values of $f_{\rm H}$ and $\frac{D_{\rm H}}{D_{\rm L}}$. Two main conclusions can be drawn from this

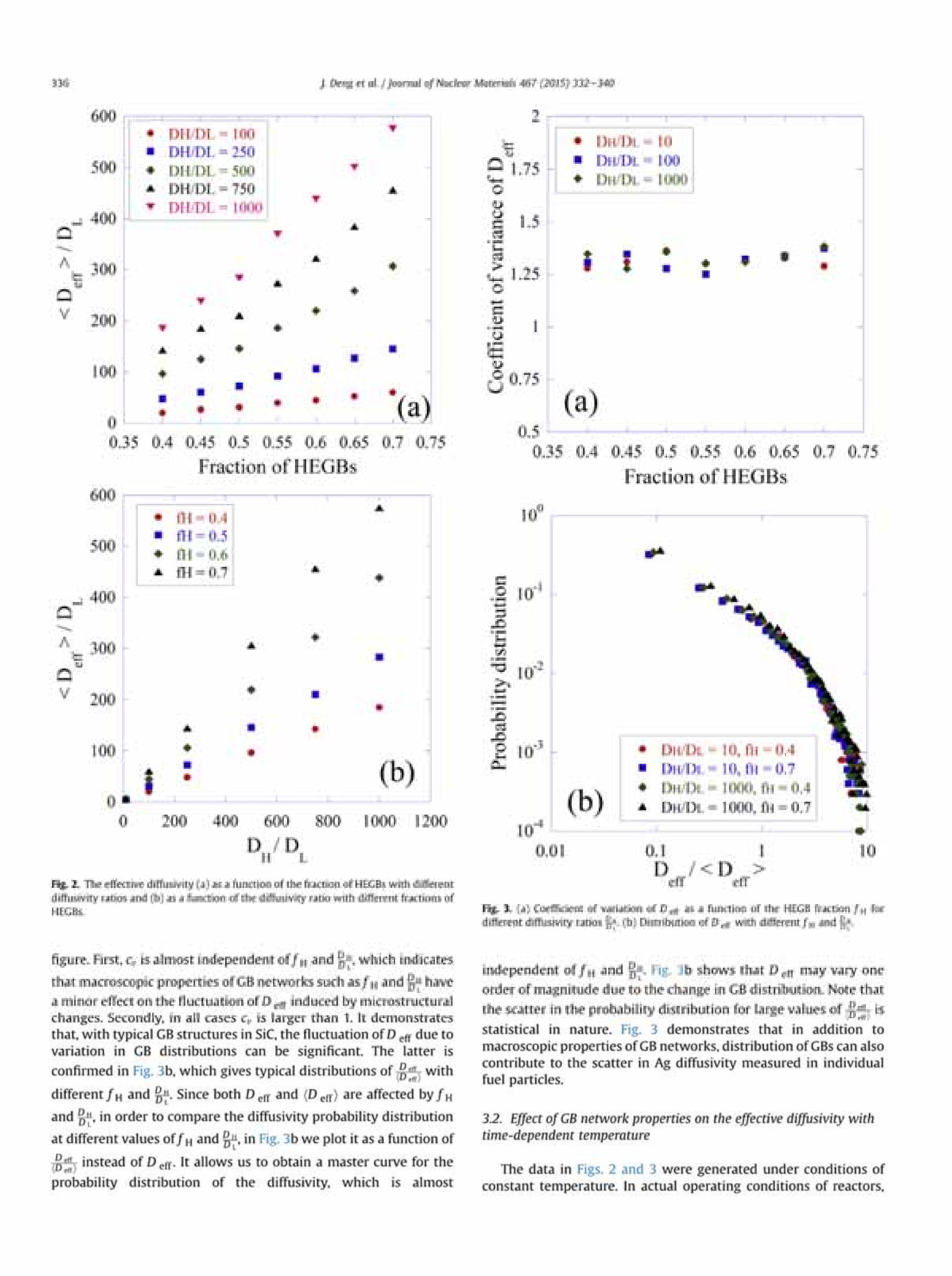
600
500
400
300
200
100
0
0.35 0.4 0.45 0.5 0.55 0.6 0.65 0.7 0.75
Fraction of HEGBs
< D_eff > / D_L
DH/DL = 100
DH/DL = 250
DH/DL = 500
DH/DL = 750
DH/DL = 1000
(a)
2
1.75
1.5
1.25
1
0.75
0.5
Coefficient of variance of D_eff
DH/DL = 10
DH/DL = 100
DH/DL = 1000
(a)
0 200 400 600 800 1000 1200
D_H / D_L
fH = 0.4
fH = 0.5
fH = 0.6
fH = 0.7
(b)
10^0
10^-1
10^-2
10^-3
10^-4
0.01 0.1 1 10
D_eff / < D_eff >
Probability distribution
DH/DL = 10, fH = 0.4
DH/DL = 10, fH = 0.7
DH/DL = 1000, fH = 0.4
DH/DL = 1000, fH = 0.7
(b)

336 *J. Deng et al. / Journal of Nuclear Materials 467 (2015) 332–340*

**Fig. 2.** The effective diffusivity (a) as a function of the fraction of HEGBs with different diffusivity ratios and (b) as a function of the diffusivity ratio with different fractions of HEGBs.

**Fig. 3.** (a) Coefficient of variation of $D_{\mathrm{eff}}$ as a function of the HEGB fraction $f_H$ for different diffusivity ratios $\frac{D_H}{D_L}$. (b) Distribution of $D_{\mathrm{eff}}$ with different $f_H$ and $\frac{D_H}{D_L}$.

figure. First, $c_v$ is almost independent of $f_H$ and $\frac{D_H}{D_L}$, which indicates that macroscopic properties of GB networks such as $f_H$ and $\frac{D_H}{D_L}$ have a minor effect on the fluctuation of $D_{\mathrm{eff}}$ induced by microstructural changes. Secondly, in all cases $c_v$ is larger than 1. It demonstrates that, with typical GB structures in SiC, the fluctuation of $D_{\mathrm{eff}}$ due to variation in GB distributions can be significant. The latter is confirmed in Fig. 3b, which gives typical distributions of $\frac{D_{\mathrm{eff}}}{\langle D_{\mathrm{eff}}\rangle}$ with different $f_H$ and $\frac{D_H}{D_L}$. Since both $D_{\mathrm{eff}}$ and $\langle D_{\mathrm{eff}}\rangle$ are affected by $f_H$ and $\frac{D_H}{D_L}$, in order to compare the diffusivity probability distribution at different values of $f_H$ and $\frac{D_H}{D_L}$, in Fig. 3b we plot it as a function of $\frac{D_{\mathrm{eff}}}{\langle D_{\mathrm{eff}}\rangle}$ instead of $D_{\mathrm{eff}}$. It allows us to obtain a master curve for the probability distribution of the diffusivity, which is almost independent of $f_H$ and $\frac{D_H}{D_L}$. Fig. 3b shows that $D_{\mathrm{eff}}$ may vary one order of magnitude due to the change in GB distribution. Note that the scatter in the probability distribution for large values of $\frac{D_{\mathrm{eff}}}{\langle D_{\mathrm{eff}}\rangle}$ is statistical in nature. Fig. 3 demonstrates that in addition to macroscopic properties of GB networks, distribution of GBs can also contribute to the scatter in Ag diffusivity measured in individual fuel particles.

### *3.2. Effect of GB network properties on the effective diffusivity with time-dependent temperature*

The data in Figs. 2 and 3 were generated under conditions of constant temperature. In actual operating conditions of reactors,

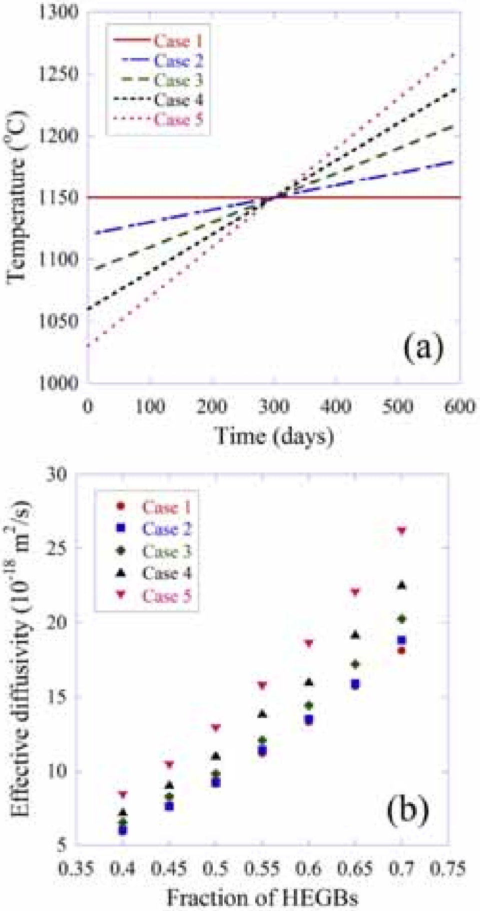

**Fig. 4.** (a) Temperature as a linear function of time with different slopes. In case 1, the temperature is a constant. (b) The effective diffusivity as a function of the fraction of HEGBs with different temperature profiles shown in (a).

temperature fluctuates with time. Therefore, it is important to examine the dependence of the effective diffusivity of Ag on GB structures when temperature (and thus GB diffusivity) is time-dependent. In order to show the effect of temperature fluctuation clearly, we assume that temperature changes as a linear function of time, and the initial values are chosen so as to yield the same average temperature for all cases. Fig. 4a shows temperature profiles for 5 different cases we studied, where the temperature change from time 0–600 days is 0 °C, 60 °C, 120 °C, 180 °C, and 240 °C. The range of time-averaged, volume-averaged irradiation temperatures in AGR-1 fuel compacts is approximately 200 °C [9], which is within the range of temperature variation considered here. The total simulation time (600 days) is also similar to the total operation time in the AGR-1 irradiation test [38].

In Fig. 4b we plot the dependence of the effective diffusivity on $f_H$ with the different temperature profiles shown in Fig. 4a. It can be seen that both the temperature history and GB structures affect the effective diffusivity of Ag. In particular, $\langle D_{eff} \rangle$ increases as temperature variation increases, which is expected due to the Arrhenius (exponential) dependence of $\langle D_{eff} \rangle$ on temperature. Specifically, $D_{eff}$ is larger in the case when the operating temperature is higher in the high-temperature regime (the region where time is larger than 300 days), in spite of the fact that the operating temperature is reduced by the same magnitude in the low-temperature regime (the region where time is smaller than 300 days). It shows that keeping the maximum temperature low is more important for reducing the overall Ag release than keeping the minimum temperature low. This data also shows that it is undesirable to have the temperature fluctuation that leads to temporary excursions to high temperatures because it may have a detrimental effect on Ag release. In order to confirm the effect of temperature variation on $D_{eff}$, we calculate $D_{eff}$ when temperature decreases linearly as a function of time in 5 cases. The magnitude of temperature variation in these 5 cases is the same as that shown in Fig. 4a, and the only difference is that the temperature slope is negative such that the highest temperature occurs at the beginning instead of the end. We find that the results of $\langle D_{eff} \rangle$ in these 5 cases are the same as that shown in Fig. 4b, which demonstrates that the direction (increase or decrease) of temperature change does not affect the dependence of $\langle D_{eff} \rangle$ on temperature variation. In addition to the influence of temperature variation, we find that $D_{eff}$ changes rapidly as $f_H$ varies from 0.4 to 0.7 in all cases. This result indicates that $D_{eff}$ is still strongly affected by the properties of GB networks even when temperature is time-dependent. Moreover, we also find that temperature variation does not dramatically affect the fluctuation and distribution of $D_{eff}$ due to microstructural changes (see Fig. 5a and b). Therefore, based on Figs. 4 and 5 we conclude that, irrespectively of whether temperature is constant or time-dependent, the variation in GB structures can induce significant fluctuation in the effective diffusivity of Ag.

### 3.3. *Effect of GB network properties on the Ag release fraction with time-dependent temperature and Ag generation rate*

Up to this point we have focused on the dependence of the effective Ag diffusivity on GB structures. Another property of interest is the release fraction of Ag because it is directly related to the ability of SiC to retain Ag inside of fuel particles. As discussed in Section 2, when calculating the release fraction of Ag, we consider the generation rate of Ag to be time-dependent in order to be consistent with actual operating conditions. Fig. 6a shows the normalized generation rate of Ag-110 m as a function of time used in our simulations, which is obtained from the Ag inventory generation in one compact of the AGR-1 test [39]. The trend shown in Fig. 6a (i.e., more Ag is generated at a later stage) is typically observed during irradiation due to several factors, including the higher yield of Ag-109 from plutonium fission [39]. We note that different Ag isotopes may have different generation rates. Here, we mainly focus on qualitative trends in Ag release resulting from a non-linear source generate rate and we do not investigate any quantitative effects of generation rate on Ag transport. We use temperature profiles shown in Fig. 4a to provide a meaningful comparison between our calculations of the effective diffusivities (reported in Sec. 3.2) and results of the release fraction of Ag studied here.

The release fraction is calculated by the methods described in Sec. 2. In simulations, we denote the diffusivity along virtual paths as $D_V$, where virtual paths connect a virtual node outside the SiC layer with nodes in the z-plane of the SiC TRISO layer (see Section 2). We then examine the dependence of Ag release fraction on the

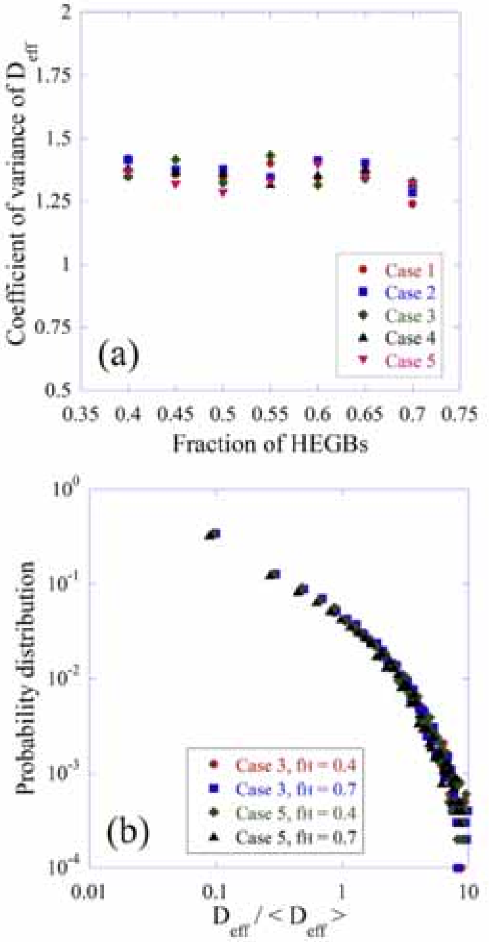

**Fig. 5.** (a) Coefficient of variation of $D_{eff}$ as a function of the HEGB fraction $f_H$ with different temperature profiles shown in Fig. 3a. (b) Distribution of $D_{eff}$ with different temperature profiles and $f_H$.

ratio $\frac{D_V}{D_H}$, where we vary $D_V$ while keeping $D_H$ constant. Fig. 6b shows the Ag release fraction as a function of the ratio $\frac{D_V}{D_H}$ with different $f_H$ in the Case 1 (shown in Fig. 4a). It is found that as $\frac{D_V}{D_H}$ increases, the Ag release fraction first increases, and then approaches a constant. The former (initial increase of Ag release fraction) is expected because higher $D_V$ helps the Ag atom select a faster path to diffuse among the different GB paths. The latter (Ag release approaches a constant) indicates that the Ag release will saturate for large $\frac{D_V}{D_H}$. Since $\frac{D_V}{D_H}$ does not affect the Ag release fraction significantly when it is larger than 10, we set $\frac{D_V}{D_H} = 10$ in the following simulations. Fig. 6c shows the release fraction of Ag at the 600th day as a function of $f_H$ with different temperature profiles. It is clear that with all temperature profiles the release fraction has a wide range of values when $f_H$ changes from 0.4 to 0.7. Comparison of Figs. 6c and 4b shows that the dependence of the release fraction of Ag on $f_H$ is consistent with the trend in the effective diffusivity, which is expected because the release of Ag is governed by its effective diffusivity in GB networks.

Fig. 6 together with Figs. 2–5 shows that variation in properties of GB networks (including $\frac{D_H}{D_L}$, $f_H$ and distribution of GBs) can induce fluctuation in the effective diffusivity and release fraction of Ag when temperature is either constant or time-dependent. It suggests that changes in GB structures in the SiC layer may have significant contributions to the scatter in the effective diffusivity and release fraction of Ag measured in experiments.

### *3.4. Effects of irradiation and temperature distribution on Ag diffusion*

Calculations in Sections 3.1–3.3 demonstrate that the transport of Ag across the SiC layer is sensitive to the variation of GB structures when the diffusivities of Ag in HEGB and LEGB are consistent with the integral release experimental data. In order to further test the hypothesis that GB diffusion is the dominant transport mechanism of Ag in SiC, we now analyze kMC simulations where the GB diffusivities were taken to match published quantitative data, instead of fitting the diffusivities to the release measurements. Through this analysis we can estimate if the release experiments can be quantitatively explained through GB diffusion alone. As discussed in Section 3, there is not enough data to map all the GB types onto Ag diffusivities, however there are a few experimental ion implantation studies [12,21,22,35] and DFT simulations [25,26] that provide reasonable bounds to consider in our simulations. The results from ion implantation experiments and DFT calculations, together with integral release experimental measurements [5–7,40], are summarized in Fig. 7. In the same figure, we also show the effective diffusivity obtained by the present kMC model when LEGB and HEGB, respectively, are represented by Σ 3 GB and amorphous GB with diffusivities ($D_L = 1.6 \times 10^{-7} \times \exp\left(\frac{-3.95}{kT}\right)$ m²/s, and $D_H^{max} = 2.39 \times 10^{-10} \times \exp\left(\frac{-2.61}{kT}\right)$ m²/s) obtained from Refs. [25] and [26]. Symbols in the figure correspond to experimental data and lines correspond to results from simulations. It can be seen that the diffusivities calculated in our model (red solid and red dotted lines) fall in the same range as the ones measured in ion-implantation experiments (black symbols). Interestingly, the diffusivity calculated in our model as well as those measured in ion-implantation experiments are visibly lower than those obtained from integral release experiments. The difference in the diffusivities between the calculated values and the integral release experimental data suggest that additional mechanisms or factors, which are not considered in the present model, may play an important role in Ag transport through SiC.

One potential factor is that Ag diffusion could be affected by radiation. Radiation effects have not been so far included in DFT calculations and ion-implantation experiments of Ag transport, but fuel particles are all irradiated during integral release experiments. Although the influence of a number of microstructural features on Ag transport are considered in Refs. [34], their effects are modeled by parametric functions where parameters are selected to fit experimental data, so the quantitative mechanism of the Ag transport under irradiation remains to be understood. A full investigation of radiation effects is beyond the scope of the current paper.

In addition to irradiation effects, another potential factor that could explain the difference between the diffusivities measured in reactor experiments and that measured in diffusion couple experiments (and predicted by DFT and our model) is the spatial and

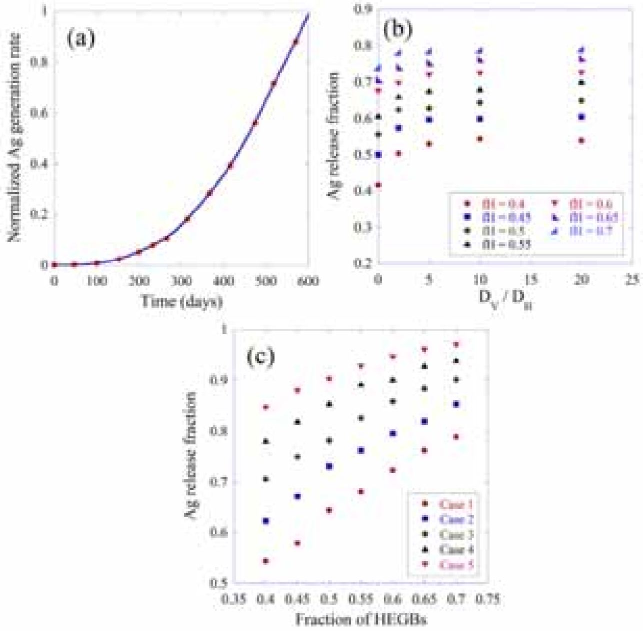

**Fig. 6.** (a) Normalized Ag generation rate as a function of time. (b) The Ag release fraction as a function of $\frac{D_V}{D_H}$ with different $f_H$ in the Case 1 shown in Fig. 3a. (c) The Ag release fraction as a function of the $f_H$ with different temperature profiles shown in Fig. 3a.

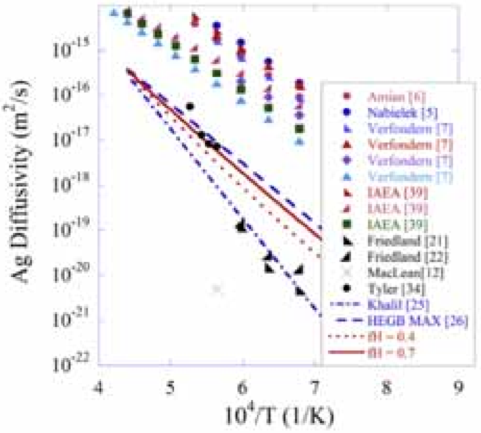

**Fig. 7.** Comparison of the Ag diffusivities measured in integral release experiments [5–7,39], ion implantation experiments [12,20,21,34] and DFT calculations [25,26]. The blue dash-dot line and blue dash line are the diffusivities in Σ 3 GB [25] and the upper limit of the diffusivity in amorphous GB [26] obtained from DFT calculations without consideration of irradiation effect. The red dotted line and the red solid line are $D_{eff}$ obtained from the present kMC model when $f_H$ is 0.4 and 0.7, respectively, where LEGB and HEGB are represented by Σ 3 GB and amorphous GB, respectively. (For interpretation of the references to color in this figure legend, the reader is referred to the web version of this article.)

temporal fluctuations of temperature in reactors. It was shown in Ref. [9] that within a single AGR-1 capsule, the time average-volume average temperatures in compacts can differ by as much as 130 °C, and within certain compacts, the temperature distribution may have a range of as much as 300 °C (the difference between the minimum and the maximum temperature) due to the geometry of the irradiation capsule. It was also shown in Ref. [39] that the volume average temperature in compacts could vary over several hundred degrees Celsius over the course of the irradiation. The effect of temporal variation in temperature on the Ag diffusivity is demonstrated in Fig. 4b. It is expected that the spatial fluctuation of temperature may enhance the Ag diffusivity as well. In addition to increasing the magnitude of the Ag diffusivity, the temperature fluctuation in both space and time may also affect the spread the Ag diffusivity. We have shown in Fig. 7 that when the temperature changes by 300 °C the effective diffusivity may vary by one or two orders of magnitude. Finally, it is also possible that fission products such as Pd may additionally accelerate Ag diffusion as discussed in Refs. [17–19].

There are other factors that may contribute to the scatter in Ag diffusivity observed in integral release experiments. The Ag diffusivity fluctuation shown in Fig. 3 corresponds to the contribution of GB distribution under constant temperature, $f_H$ and $\frac{D_H}{D_L}$. In actual reactors, in addition to spatial and temporal temperature fluctuation mentioned above, $f_H$ and $\frac{D_H}{D_L}$ may also vary amount fuel particles. As shown in Fig. 2, variation in $f_H$ and $\frac{D_H}{D_L}$ may change Ag diffusivity by more than one order of magnitude. Moreover, finite size of the sample may further contribute to the scatter in Ag diffusivity. By combining all these factors, the spread in the effective diffusivity is likely to be similar to that measured in integral release experiments.

## 4. Concluding remarks

We have developed a kinetic Monte Carlo model to evaluate the effective diffusivity and release fraction of Ag through polycrystalline SiC. It is found that the transport of Ag across the SiC layer is sensitive to the variation in GB network properties such as fraction of each GB type, spectrum in GB diffusivity and GB distributions. In particular, as properties of GB networks vary, the effective diffusivity and release fraction of Ag change significantly. Moreover, we find that the variation of the effective diffusivity and release fraction of Ag due to changes in GB structures is almost independent of temperature fluctuations. These results suggest that the variation in properties of GB networks in the SiC layer may contribute to the scatter in Ag diffusivity and release fraction measured in experiments.

Comparisons of laboratory experiments and modeling results with release from irradiated fuel particles strongly suggests that in actual fuel particles, diffusion of Ag is not only dependent on GB structures in SiC, but it is also affected by other factors such as irradiation and temperature distribution. In particular, various defect structures developed in SiC during irradiation may have a pronounced impact on Ag diffusion. Non-uniform temperature distribution may enhance the spread in the diffusivity and release fraction of Ag in individual fuel particles. Understanding the effects of irradiation and temperature distribution on Ag transport may help to resolve the discrepancy in the literature data on Ag diffusivities and is currently in progress.

## Acknowledgment

This research is being performed using funding received from the DOE Office of Nuclear Energy's Nuclear Energy University Programs contract number 00089350.

## References

[1] D. Olander, Nuclear fuels — present and future, J. Nucl. Mater. 389 (2009) 1–22.

[2] D. Petti, J. Buongiorno, J. Maki, R. Hobbins, G. Miller, Key difference in the fabrication, irradiation and high temperature accident testing of US and German TRISO-coated particle fuel, and their implications on fuel performance, Nucl. Eng. Des. 222 (2003) 281–297.

[3] N. van der Berg, J. Malherbe, A. Botha, E. Friedland, SEM analysis of the microstructure of the layers in triple-coated isotropic (TRISO) particles, Surf. Interface Anal. 42 (2010) 1156–1159.

[4] J. Malherbe, Diffusion of fission products and irradiation damage in SiC, J. Phys. D. Appl. Phys. 46 (2013) 473001.

[5] H. Nabielek, P. Brown, P. Offermann, Silver release from coated particle fuel, Nucl. Tech. 35 (1977) 483–493.

[6] W. Amian, D. Stover, Diffusion of silver and cesium in silicon-carbide coatings of fuel particles for high-temperature gas-cooled reactors, Nucl. Tech. 61 (1983) 475–486.

[7] K. Verfondern, R. Martin, R. Moormann, Methods and Data for HTGR Fuel Performance and Radionuclide Release Modeling during Normal Operation and Accidents for Safety Analyese, Jul-2722, Forschungzentrum Julich GmbH, January 1993.

[8] R. Bullock, Fission-product release during post-irradiation annealing of several types of coated fuel particles, J. Nucl. Mater. 125 (1984) 304–319.

[9] P. Demkowicz, J. Hunn, R. Morris, J. Harp, P. Winston, C. Baldwin, F. Montgomery, Preliminary results of post-irradiation examination of the AGR-1 TRISO fuel compacts, HTR2012-3-027, in: Proceedings of the HTR 2012, Tokyo, Japan October 28-November 1, 2012.

[10] C. Baldwin, J. Hunn, R. Morris, F. Montgomery, C. Silva, P. Demkowicz, First elevated-temperature performance testing of coated particle fuel compacts from the AGR-1 irradiation experiment, Nucl. Eng. Des. 271 (2014) 131–141.

[11] Y. Katoh, L. Snead, I. Szlufarska, W. Weber, Radiation effects in SiC for nuclear structural applications, Curr. Opin. Solid State Mater. Sci. 16 (2012) 143–152.

[12] H. MacLean, R. Ballinger, L. Kolaya, S. Simonson, N. Lewis, M. Hanson, The effect of annealing at 1500C on migration and release of ion implanted silver in CVD silicon carbide, J. Nucl. Mater. 357 (2006) 31–47.

[13] H. MacLean, Silver Transport in CVD Silicon Carbide (Ph.D. thesis), MIT, Department of Nuclear Engineer, 2004.

[14] H. Xiao, Y. Zhang, L. Snead, V. Shutthanandan, H. Xue, W. Weber, Near-surface and bulk behavior of Ag in SiC, J. Nucl. Mater. 420 (2012) 123–130.

[15] K. Minato, K. Sawa, T. Koya, T. Tomita, A. Ishikawa, Fission product release behavior of individual coated fuel particles for high-temperature gas-cooled reactors, Nucl. Technol. 131 (2000) 36–47.

[16] E. Lopez-Honorato, H. Zhang, D. Yang, P. Xiao, Silver diffusion in silicon carbide coatings, J. Am. Ceram. Soc. 94 (2011) 3064–3071.

[17] E. Olivier, J. Neethling, Palladium transport in SiC, Nucl. Eng. Des. 244 (2012) 25–33.

[18] J. Neethling, J. O'Connell, E. Olivier, Palladium assisted silver transport in polycrystalline SiC, Nucl. Eng. Des. 251 (2012) 230–234.

[19] E. Olivier, J. Neethling, The role of Pd in the transport of Ag in SiC, J. Nucl. Mater. 432 (2013) 252–260.

[20] K. Minato, T. Ogawa, K. Fukuda, H. Sekino, H. Miyanishi, S. Kado, I. Takahashi, Release behavior of metallic fission products from HTGR fuel particles at 1600 to 1900C, J. Nucl. Mater. 202 (1993) 47–53.

[21] E. Friedland, J. Malherbe, N. van der Berg, T. Hlatshwayo, A. Botha, E. Wendler, W. Wesch, Study of silver diffusion in silicon carbide, J. Nucl. Mater. 389 (2009) 326–331.

[22] E. Friedland, N. van der Berg, J. Malherbe, J. Hancke, J. Barry, E. Wendler, W. Wesch, Investigation of silver and iodine transport through silicon carbide layers prepared for nuclear fuel element cladding, J. Nucl. Mater. 410 (2011) 24–31.

[23] E. Lopez-Honorato, D. Yang, J. Tan, P. Meadows, P. Xiao, Silver diffusion in coated fuel particles, J. Am. Ceram. Soc. 93 (2010) 3076–3079.

[24] T. Gerczak, B. Leng, K. Sridharan, J. Hunter Jr, A. Giordani, T. Allen, Observations of Ag diffusion in ion implanted SiC, to be published.

[25] S. Khalil, N. Swaminathan, D. Shrader, A. Heim, D. Morgan, I. Szlufarska, Diffusion of Ag along $\Sigma$ 3 grain boundaries in 3C-SiC, Phys. Rev. B 84 (2011) 214104.

[26] H. Ko, J. Deng, I. Szlufarska, D. Morgan, Ag diffusion in SiC high energy grain boundaries: kinetic Monte Carlo study with first-principle calculations, in preparation.

[27] J. Rabone, E. Lopez-Honorato, P. van Uffelen, Silver and cesium diffusion dynamics at the β-SiC $\Sigma$ 5 grain boundary investigated with density functional theory molecular dynamics and metadynamics, J. Phys. Chem. A 118 (2014) 915–926.

[28] D. Shrader, S. Khalil, T. Gerczak, T. Allen, A. Heim, I. Szlufarska, D. Morgan, Ag diffusion in cubic silicon carbide, J. Nucl. Mater. 408 (2011) 257–271.

[29] R. Kirchhofer, J. Hunn, P. Demkowicz, J. Cole, B. Gorman, Microstructure of TRISO coated particles from the AGR-1 experiment: SiC grain size and grain boundary character, J. Nucl. Mater. 432 (2013) 127–134.

[30] L. Tan, T. Allen, J. Hunn, J. Miller, EBSD for microstructure and property characterization of the SiC-coating in TRISO fuel particles, J. Nucl. Mater. 372 (2008) 400–404.

[31] D. Helary, O. Dugne, X. Bourrat, P. Jouneau, F. Cellier, EBSD investigation of SiC for HTR fuel particles, J. Nucl. Mater. 350 (2006) 332–335.

[32] J. Deng, D. Morgan, I. Szlufarska, Kinetic Monte Carlo simulation of the effective diffusivity in grain boundary networks, Comp. Mater. Sci. 93 (2014) 36–45.

[33] https://en.wikipedia.org/wiki/Voronoi_diagram.

[34] G. Meric de Bellefon, B. Wirth, Kinetic Monte Carlo (KMC) simulation of fission product silver transport through TRISO fuel particles, J. Nucl. Mater. 413 (2011) 122–131.

[35] T. Gerczak, Understanding Ag Release from TRISO Fuel through Surrogate Diffusion Experiments and Fuel Analysis, Dissertation, University of Wisconsin — Madison, 2013.

[36] I. Kaur, Y. Mishin, W. Gust, Fundamentals of Grain and Interphase Boundary Diffusion, Wiley, Chichester, 1995.

[37] Y. Chen, C. Schuh, Diffusion on grain boundary networks: percolation theory and effective medium approximations, Acta Mater. 54 (2006) 4709–4720.

[38] B. Collin, AGR-1 Irradiation Test Final as-run Report, INL-EXT-10-18097 Revision 3, 2015.

[39] P. Demkowicz, B. Collin, AGR-1 silver release: comparison of experiment with PARFUME predictions, in: Presentation in Very High Temperature Reactor Research and Development 2013 Technical Review Meeting, 2013.

[40] IAEA-TECDOC-978, Fuel Performance and Fission Product Behavior in Gas Cooled Reactors, 1997.